Max-Planck-Institut für Metallforschung
Stuttgart

Mechanics of Robust and Releasable Adhesion in Biology

Haimin Yao

Dissertation
an der
Universität Stuttgart

Bericht Nr. 188
Juni 2006

Mechanics of Robust and Releasable Adhesion in Biology

Von der Fakultät Chemie der Universität Stuttgart
zur Erlangung der Würde eines Doktors der
Naturwissenschaften (Dr. rer. nat.) genehmigte Abhandlung

Vorgelegt von

Haimin Yao

aus Zhejiang/China

Hauptberichter:	Prof. Dr. Huajian Gao
Mitberichter:	Prof. Dr. phil. Eduard Arzt
Tag der Einreichung:	27. März 2006
Tag der mündlichen Prüfung:	27. Juni 2006

Max-Planck-Institut für Metallforschung, Stuttgart

Juni 2006

To my parents, wife and unborn kid

Max-Planck-Institut für Metallforschung, Stuttgart, 2006
163 Pages, 70 Figures, 4 Tables.

Copyright © 2006, By Haimin Yao.
All Rights Reserved.
No part of this publication may be reproduced or transmitted in any form or by any means, electronic or mechanical, including photocopy, recording, or any information storage and retrieval system, without permission in writing from the publisher.

All manuscripts are printed in Germany.

Acknowledgements

First of all, I wish to express my deepest appreciation to Prof. Dr. Huajian Gao, who accepted me as his doctoral student and provided me a precious opportunity to work on some of the most interesting problems in biomechanics. I am deeply indebted for the guidance, support and encouragement that he provided unselfishly during my years at Max Planck Institute for Metals Research in Stuttgart.

At the same time, I have benefited much from stimulating discussions and collaboration with Dr. Stanislav Gorb and Prof. Dr. Eduard Arzt on the problems related to biological adhesion systems. I am also greatly indebted to Dr. Xiang Wang, Dr. Yong Kong, Dr. Baohua Ji, Dr. Xu Guo, Dr. Shaohua Chen, Dr. Markus Buehler and Dr. Ji Chen for their encouragement as well as scientific discussions. Of course, this endeavor would not have been possible without the help of other colleagues and friends like Dr. Jizeng Wang, Jin Qian, Xiaojun Fan, Nils Brödling, Xinghua Shi, Wendong Shi, Chun Li, Yinghong Xie, Shuyu Wei and Dr. Ernst-Helmut Brandt, as well as all other colleagues in our group who helped me toward my goal of completing my PhD research. I would like to thank Igor Kanter and Giovani Estrada for their technical support. I would like to acknowledge our departmental secretary, Silvia Casanova for her always being very helpful and providing much encouragement.

I thank my thesis committee members, Prof. Eduard Arzt for agreeing on assuming the "Mitbericht" for my dissertation, and Prof. Fritz Aldinger for agreeing on assuming the "Prüfungsvorsitz". I am also grateful to the Max Planck Society for the Advancement of Science for providing me the scholarship. The work reported in this thesis was performed at the Max Planck Institute for Metals Research between January 2003 and June 2006.

Last but not least, I acknowledge the help and support of my parents and my wife.

Abstract

Nature has found, through billions years of natural evolution, many ingenious ways to produce materials with superior mechanical properties. It would be a convenient and practical way for us to explore the existing biological systems for the ideas of designing novel materials. In this thesis, our attention will be focused on dry adhesion, a specific phenomenon observed frequently in many animal species like gecko, fly and insects. Our goal is to elucidate the adhesion mechanism behind these professional climbers. The prospective results may provide a useful guideline for the fabrication of the novel materials and devices in engineering.

The whole thesis can be broadly divided into three parts. In part one, which consists of Chapter 1-3, we begin by introducing the motivation and overview of this work. Then, in Chapter 2 the theory of contact mechanics is reviewed briefly. It is followed by Chapter 3 in which the useful research methods are introduced with emphasis on the mathematical preliminaries and computational methods.

For animals like gecko, the robustness and releasability of the attachment systems are two essential features ensuring their locomotion on vertical walls or ceilings. The second part of this thesis (Chapter 4-6) is entirely devoted to the investigation on these two seemingly contradictive characteristics. While the adhesion robustness is treated in Chapters 4 and 5, adhesion releasability is the subject of Chapter 6.

Given contact area, adhesion strength is commonly measured by the magnitude of the pull-off force, i.e., the force required to pull two bonded objects apart. The higher the pull-off force, the stronger is the adhesive joint. How to increase the adhesion strength as much as possible is what we are interested in. In Chapter 4, we start with study on the adhesion between two single contact asperities. It is found that the adhesion strength is strongly dependent on the geometric shape and size of the contact surfaces and limited by the theoretical strength. There exists a specific shape termed optimal shape, by which theoretical adhesion strength can be achieved. A general methodology for determining the optimal shape is developed, by which analytical expressions of the

optimal shapes for several example cases are obtained. However, shape optimization design for optimum adhesion is found to be unreliable especially at the macroscopic scale because the pull-off force then is quite sensitive to the small variations in the contact shape. A robust design of shape-insensitive optimal adhesion becomes possible only when the characteristic size of the contact area is reduced to a length scale on the order of 100 nm. In general, optimal adhesion could be achieved by a combination of size reduction and shape optimization. The smaller the size, the less important the shape. It is basically for this reason that the fibrillar nanostructures in biology possess high adhesion strength.

The results obtained in Chapter 4 imply that materials have intrinsic ability to tolerate quite small contact flaws. In reality, however, contact surfaces tend to be rough in a variety of length scales, leading to multi-scale contact flaws. Optimizing adhesion at the level of single asperities or fibrils does not automatically address the problem of robust adhesion on rough surfaces at macroscopic scales. To solve this problem, we study, in Chapter 5, the adhesion strength between rough surfaces. Instead of directly modeling adhesive contact on random or fractal rough surfaces, we follow a different approach by considering the behavior of an interfacial crack representing random contact flaws due to surface roughness or contaminants. By investigating the conditions under which the representative crack does not grow, we effectively treat, in a statistically average sense, the problem of how to prevent randomly occurring poor contact regions from triggering crack-like adhesive failure. So that a state of flaw-tolerance is achieved in which preexisting cracks do not propagate even as the material is stretched to failure near its theoretical strength. In Chapter 5, various strategies for achieving flaw tolerant adhesion are discussed. It is found that in traditional homogeneous materials, flaw tolerance can only be achieved on condition that the structure dimension is reduced to below a critical length scale. To achieve the generalized flaw tolerance in which crack-like flaws of all sizes can be tolerated, we have to appeal to the graded material or hierarchical design. Both theoretical modeling and numerical simulation show that a graded material in conjunction with hierarchical energy dissipation mechanism can be designed to suppress the growth of interfacial cracks of all sizes so as to achieve the flaw tolerance from the smallest dimension up to macroscopic length scales. Such design philosophy also agrees well with the common structural features observed from a variety of biological attachment systems.

For most animals, however, only having robust adhesion ability can not sufficiently ensure them to move on the vertical and even reverse surfaces. The releasability of the

attachment devices is just as important as the robustness. Our discussion of Chapter 6 is dedicated to the problem of how to release the robust adhesion with ease. Inspired by the common structural features of the biological attachment systems, we study the effect of the material anisotropy on the orientation dependence of adhesion strength. It is found that materials with strong anisotropy allow the adhesion strength to vary strongly with the direction of pulling. The resulting orientation-dependent pull-off force enables robust attachment in the stiff direction of the material to be released just by pulling in the soft direction, achieving an orientation-controlled switch between attachment and detachment.

Biological adhesion devices are sophisticated systems which provide a rich source of ideas for development of industrial applications. The concept developed in this thesis should be of general value in understanding the biological attachment devices and the design of synthetic adhesive systems in engineering. In the last part of this thesis, Chapter 7, the most important results obtained in this thesis are summarized and the whole thesis is concluded by providing an outlook to the future work.

Contents

List of Figures

List of Tables

Chapter 1. Introduction

Nature, through billions years of natural selection, has found many ingenious ways to produce materials with superior mechanical properties. Understanding of the mechanisms behind these natural materials will be of great value to the design of the novel materials in engineering. A handy example of biomimicking material is the recently developed self-cleaning material whose advent can be attributed to the understanding of the principle of lotus-effect [9]. It would be a convenient and practical way for man to explore the existing biological systems for the ideals of material designs. In this thesis, our attention is focused on dry adhesion, a specific phenomena in biology. Our objective is to elucidate the adhesion mechanism from the viewpoint of mechanics. Although the investigations are inspired by the biological adhesion systems, the revealed mechanical principles can be extensively treated as the general rules of interfacial adhesion.

1.1. Biological attachment systems: motivations

It is widely observed in nature that many animal species like gecko, fly, spider and some insects possess extraordinary ability to move rapidly on vertical walls or ceilings with unpredictable surface roughness and material properties. From the robustness point of view, these biological attachment systems must be insensitive to the adhesion flaws induced by roughness, contaminants, trapped air bubbles and skewed contact angles. On the other hand, the survivability of animals not only necessitates the robustness of adhesion but also an ability to rapidly switch between attachment and detachment during animal's locomotion. How can an adhesion system designed for robust attachment allow easy detachment simultaneously? Clearly, this problem has been solved successfully by nature. The remaining task for us is to reveal the ingenious design principles behind these existing biological materials or structures.

During last century, much effort has been invested in the adhesion principle in biological attachment systems and a variety of adhesion mechanisms have been brought forward, such as mechanical interlocking, suction, adhesive secretion, capillary forces

and so on [70]. More recently, the development of MEMS and nano-technology makes it possible to obtain new insights into the biological attachments. For example, strong evidence has been provided that the adhesion ability of geckos is basically owing to the van der Waals interaction [56] between the contacting surface and hundreds of thousands of keratinous hairs or setae on the gecko's foot [3, 5]. Each seta is 110 μm long and contains hundreds of 200-500 nm projections called spatulae (Figure 1.1a). This finding may appear somewhat surprising because van der Waals interaction is so weak ($\approx 0.01 - 0.05$ J/m^2) that people commonly disregard it in the macroscopic scale. How can such a weak interaction be applied to support the appreciable weight of an animal? Obviously, the fibrillar structure of gecko plays an important role. A question thus arises. Are there any other alternative adhesion systems in nature? Comparative

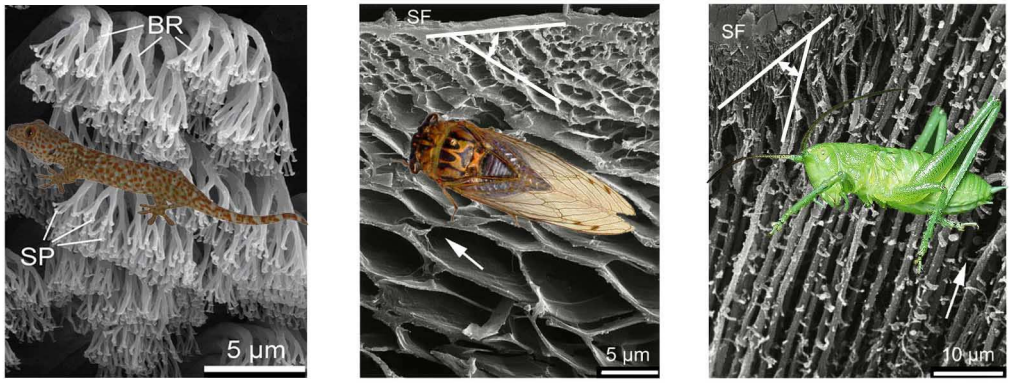

Figure 1.1.: Biological attachment systems of (a) gecko (b) cicada and (c) *Tettigonia viridissima*(Photograph courtesy of S. Gorb, Max Planck Institute for Metals Research).

studies of hundreds of insects and animal species [10] revealed that biological attachment systems show convergent evolution into two principal designs. While species like gecko, fly, spider and beetle exhibit "hairy" protruding fibrils on their feet, others like cicada, bee and bush cricket (*Tettigonia viridissima*) adopt smooth membranes covering some finely structured tissues. Scanning electron microscopy has been particularly useful in revealing the ultrastructures of biological attachment pads [41, 72, 84]. The ultrastructure on gecko's feet shows a hairy hierarchical structure with hundreds of thousands of setae; each seta further branches into hundreds of submicron protrusions called spatulae (Figure 1.1 a). On the other hand, the attachment pad of cicada exhibits a smooth top membrane covering an anisotropic foam-like microstructure with varying cell size and wall thickness (Figure 1.1 b). The pad of bush cricket shows a smooth membra-

nous layer covering arrays of cross-linked rod-like fibers that are branches of thicker principle located deeper in the cuticle and oriented at some angle to the cuticle surface (Figure 1.1 c). It can be noted that the common features shared by all these biological ultrastructures are nothing but the nonhomogeneous and strongly anisotropic material properties accomplished via a variety of microstructure designs. We believe correlations must exist between the superior adhesion properties of biological attachment systems and their common structural features. The main purpose of this thesis is to uncover these correlations within the framework of continuum mechanics. After our study, we hope to find the answers to the following questions:

- How can we increase the adhesion strength?
- How can we achieve the robust (flaw tolerant) adhesion on rough surface?
- How can we release a robust attachment system easily?

1.2. Overview

In the remainder of this dissertation, we investigate the mechanics of robust and releasable adhesion in biology. In Chapter 2, we first present some fundamental concepts of the intermolecular force which is actually the physical root of dry adhesion. Then, we briefly review the classical theories of contact mechanics, including Hertz model, JKR (Johnson-Kendall-Roberts) model [62], DMT (Derjaguin-Muller-Toporov) model [21] and M-D (Maugis-Dugdale) model [67]. Next, in Chapter 3 we introduce the research methods that will be used in the subsequent chapters with emphasis placed on the mathematical preliminaries and computational methods. Throughout Chapter 2 and 3, the necessary preliminaries of this thesis are prepared.

As the backbone of this thesis, Chapters 4, 5 and 6 approach our principle topic, mechanics of robust and releasable adhesion. While the former two chapters are devoted to answering the question of how to maximize the adhesion strength, the later one is dedicated to the reverse question of how to release the strong adhesion readily. In Chapter 4, our attention is focused on the adhesion strength between a single asperity and a substrate. The effect of the geometric shape upon the adhesion strength is investigated in an attempt to find the optimal shape through which the maximum adhesion strength can be achieved. However, optimal shape does not sufficiently ensure that optimum adhesion can occur spontaneously. Condition for spontaneous optimum adhesion then is developed by investigating the variation of adhesive force in the approaching-receding

procedure between an optimal-shaped solid and a substrate. Since optimal strength on the level of individual contact elements does not automatically address flaws on scales larger than single asperities, in Chapter 5 we investigate the adhesion between rough surfaces. The concept of flaw tolerance is introduced, in which the contact region around a crack-like flaw fails not by crack propagation but by uniform detachment at the theoretical strength of adhesion. Within the framework of continuum mechanics, various strategies for flaw tolerance are discussed. In Chapter 6, we turn our attention to the opposite question of how to release the strong adhesion with ease. Orientation dependence of adhesion strength induced by severe anisotropy is proved to be a reasonable solution to the releasable adhesion.

In Chapter 7, we summarize the most important results obtained in this thesis, whose potential applications get discussed subsequently. Lastly, the whole thesis is closed with an outlook to the future research.

Chapter 2. Theoretical background

Although this thesis is not primarily concerned with the intermolecular forces, it is nevertheless appropriate to start it by reviewing some fundamental principles about intermolecular forces without which a mere knowledge of surface forces may not always be very meaningful. In the first section of this chapter, we begin by introducing some fundamental concepts of the intermolecular forces. Then based on the Lennard-Jones pair potential for two molecules, the stress-separation law of two surfaces is derived. In the second section, several classical contact models are reviewed, such as Hertz model [49], JKR (Johnson-Kendall-Roberts) model [62], DMT (Derjaguin-Muller-Toporov) [21] model and M-D (Maugis-Dugdale) model [67].

2.1. Intermolecular and surface forces

2.1.1. Force between molecules

It is well established that there are four distinct forces in nature, which are, in decreasing order of intensity, strong interactions, electromagnetic force, weak interaction and gravitation. The forces between atoms and molecules belong to the category of electromagnetic force.

Forces binding atoms in a molecule are due to chemical bonding. The energy required to break a bond is referred to *bond-energy*. The force holding molecules together are generally called *intermolecular forces*. The energy required to break molecules apart is much smaller than a typical bond-energy. But intermolecular forces play important roles in determining the properties of a substance, such as melting point, vapor pressure, evaporation, viscosity, surface tension and solubility. In addition, intermolecular forces pin gigantic molecules like enzymes, proteins and DNA into the shapes required for biological activity.

The intermolecular forces may be either attractive or repulsive in nature. In general, the attractive forces can be divided into several categories by their origins. The four

prominent types are: ionic attraction forces, dipole-dipole forces, Hydrogen bonding forces and London dispersion forces. The forces between neutral (uncharged) molecules include dipole-dipole forces, Hydrogen bonding forces, London dispersion forces. Typically, dipole-dipole forces and London dispersion forces are grouped together and termed as *van der Waals* forces (sometimes the hydrogen bonding forces are also included within this group). The forces related to ions or the ionic attraction force can be subdivided into two types: ion-dipole force and ionic bonding, depending on the presence of polar molecules. Figure 2.1 summarizes the classification of the intermolecular forces.

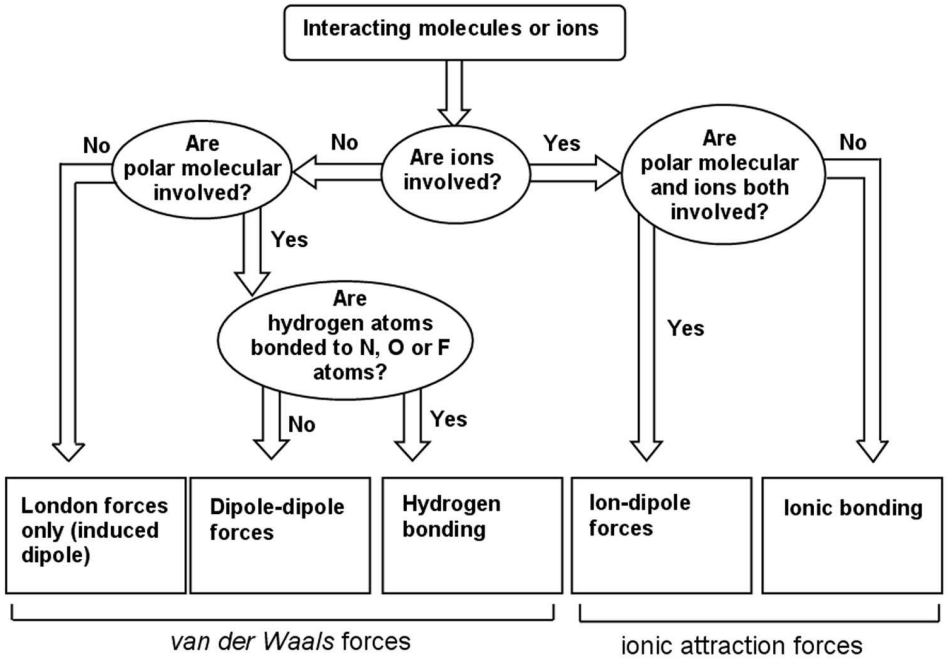

Figure 2.1.: Classification of the intermolecular forces.

The van der Waals forces between polar molecules consists of three distinct contributions: the orientation force, the induction force and the dispersion force, each of which has an interaction free energy that is inversely proportional to the sixth power of intermolecular separation r. The orientation force is the interaction of two permanent dipoles which depends on their relative orientation, and might be expected to be zero overall for a compound if all orientations are possible. The interaction energy due to orientation effect varies as $1/r^6$, the force between the dipoles as $1/r^7$. The induction force also varies as $1/r^7$ and its magnitude depends on the polarizability of the molecule. As the weakest intermolecular force, the dispersion force is the only force of interaction

in non-polar molecules, and arises from a temporary dipole induced by a complementary dipole in an adjacent molecule. Therefore, this force is sometimes called an induced dipole-induced dipole attraction. These dipoles are always shifting, but are induced in phase and give a net attraction. They depend on the polarizability of the molecule, and also vary as $1/r^7$.

The repulsive forces are of much shorter range than the attractive ones. Its physical origin is related to the Pauli principle: when the electronic clouds surrounding the atoms start to overlap, the energy of the system increases abruptly. The three most common potentials are the *hard sphere potential*, the *inverse power-law potential* and the *exponential potential*.

The hard sphere model gives the potential as

$$U(r) = (r_0/r)^n, \text{where } n = \infty. \tag{2.1}$$

Since for $r > r_0$ the value of $U(r)$ is effectively zero while for $r < r_0$ it is infinite, this expression nicely describes the hard sphere repulsion where r_0 is the hard sphere diameter of a molecule.

While the *power-law potential* is given by $U(r) = (r_0/r)^n$ the exponential potential can be expressed as $U(r) = c \cdot \exp(-r/r_0)$, where n is an integer (normally taken as a number between 9 and 16, say, 12), c and r_0 are adjustable constants. Both of these two potentials are more realistic than the hard sphere model since they allow finite compressibility of the molecules. Actually, on physical grounds, the exponential potential is more appropriate than the power-law potential, but due to mathematical convenience the power-law potential is used more frequently.

Knowing the attractive and repulsive intermolecular potentials, the total intermolecular pair potential is obtained by summing up all the attractive and repulsive potentials. As the most well-known potential, *Lennard-Jones* or '$6-12$' potential describes the total pair potential as

$$U_{\mathrm{LJ}}(r) = A/r^{12} - B/r^6, \tag{2.2}$$

where A, B are two constants chosen to fit the material properties. In Equation (2.2) term A/r^{12} represents the repulsion between molecules when they are brought very close to each other, while term B/r^6 describes the long-distance attractive interaction.

2.1.2. Force between surfaces

Having obtained the pair interaction between two molecules, let us now consider the interactions between a molecule and a solid surface and further between two solid surfaces. Related results were firstly obtained by de Boer [19] and Hamaker [48]. Suppose

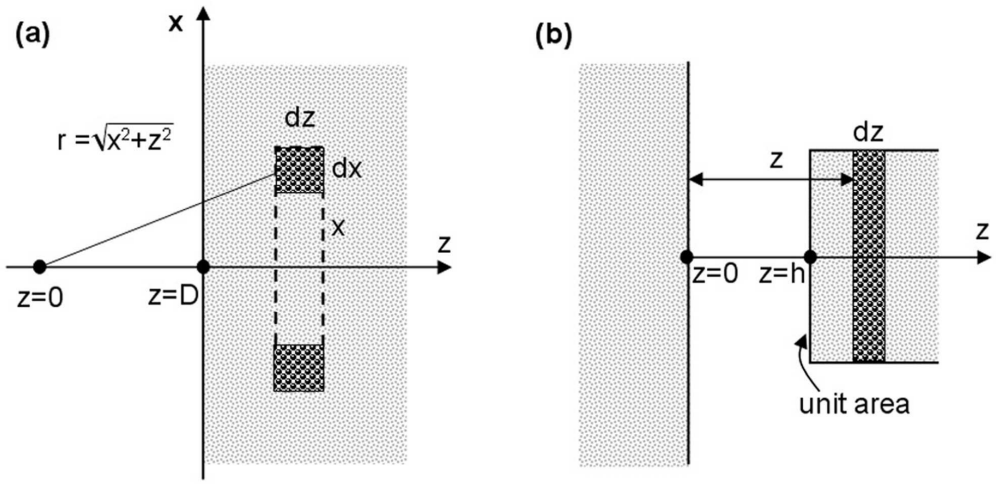

Figure 2.2.: Scheme for calculating the interaction energies between (a) a molecule and a solid surface, and (b) two solid surfaces by integrating the interaction energies between molecules in solids (adapted from [56]).

that the pair potential between two molecules separated by distance r has the form $U(r) = A/r^{12} - B/r^6$. With additional assumption of additivity, the net interaction energy between a molecule and a planar surface of a solid made up of same molecules will be the sum of its interactions with all the molecules in the body. As shown in Figure 2.2(a), for molecules in a circular ring of cross-sectional area $\mathrm{d}x\mathrm{d}z$ and radius x, the ring volume is $2\pi x\mathrm{d}x\mathrm{d}z$, and the number of molecules in the ring will be $2\pi\rho x\mathrm{d}x\mathrm{d}z$, where ρ is the number of molecules per unit volume in the solid. The net interaction energy for a molecule at distance D away from the surface can be calculated by

$$U(D) = 2\pi\rho \int_D^\infty \mathrm{d}z \int_0^\infty \left[\frac{A}{(z^2+x^2)^6} - \frac{B}{(z^2+x^2)^3}\right] x dx = x\rho\left(\frac{A}{45D^9} - \frac{B}{6D^3}\right). \quad (2.3)$$

Based on this result, now let us calculate the interaction energy between two planar surfaces at distance h apart (Figure 2.2b). For two infinite surfaces, the result must be infinity, and so we have to consider the energy per unit surface area. Let us start

with a thin sheet of molecules of unit area and thickness $\mathrm{d}z$ at a distance z away from an extended surface of large area. According to Equation (2.3) the interaction energy between this sheet and the surface is

$$\pi\rho\left[\frac{A}{45z^9}-\frac{B}{6z^3}\right]\rho'\mathrm{d}z,$$

where ρ' is the number of molecules per unit volume in the thin sheet. The energy between two surfaces thus can be immediately written as

$$U(h)=\int_h^\infty \pi\rho\rho'\left(\frac{A}{45z^9}-\frac{B}{6z^3}\right)\mathrm{d}z=\pi\rho\rho'\left(\frac{A}{360h^8}-\frac{B}{12h^2}\right). \tag{2.4}$$

Therefore, the interaction force per unit area, or the interaction stress, between two surfaces is given by

$$\sigma(h)=\frac{\partial U}{\partial h}=\pi\rho\rho'\left(\frac{B}{6h^3}-\frac{A}{45h^9}\right). \tag{2.5}$$

Here we define the stress as $\partial U/\partial h$ rather than $-\partial U/\partial h$ so as to make the sign of the interaction stress consistent with the convention in elasticity theory, i.e. tensile is positive. Denoting the equilibrium separation by z_0 at which the interaction stress of Equation (2.5) vanishes, we have

$$A=\frac{15}{2}Bz_0^6 \tag{2.6}$$

Substituting Equation (2.6) back into Equation (2.5) to eliminate parameter A, the interaction stress thus can be rewritten as

$$\sigma(h)=\frac{\pi B\rho\rho'}{6z_0^3}\left[\left(\frac{z_0}{h}\right)^3-\left(\frac{z_0}{h}\right)^9\right]. \tag{2.7}$$

Hence, the work required to separate two surfaces from the equilibrium separation to infinity, which is normally termed *work of adhesion* (units of $\mathrm{J/m^2}$), is given by

$$W_{\mathrm{ad}}=\int_{z_0}^\infty \sigma(h)\mathrm{d}h=\frac{3z_0}{8}\frac{\pi B\rho\rho'}{6z_0^3}. \tag{2.8}$$

On the other hand, the creation of new surface in a solid is obtained by breaking the bonds which ensure the cohesion of that condensed phase. In this regard, the work of adhesion should equal the differential surface energy $\Delta\gamma=\gamma_1+\gamma_2-\gamma_{12}$, where γ_1,γ_2 are the surface energy of two solids and γ_{12} is their interfacial energy. But this is not always the case. For some circumstances in which the break of adhesive bonds is accompanied

by irreversible energy dissipation process like work hardening or viscous losses, the work of adhesion would be much greater than the surface energy $\Delta\gamma$. In this thesis, the adhesion failure processes, except those specified particularly, are assumed reversible, i.e. $W_{\text{ad}} = \Delta\gamma$. Equating Equation (2.8) to $\Delta\gamma$ gives rise to

$$\frac{\pi B\rho\rho'}{6z_0^3} = \frac{8\Delta\gamma}{3z_0}. \tag{2.9}$$

Substituting Equation (2.9) into Equation (2.7), we have

$$\sigma(h) = \frac{8\Delta\gamma}{3z_0}\left[\left(\frac{z_0}{h}\right)^3 - \left(\frac{z_0}{h}\right)^9\right]. \tag{2.10}$$

Equation (2.10) gives the surface-surface interaction stress in terms of equilibrium separation z_0, work of adhesion $\Delta\gamma$ and interfacial separation h. Given $\Delta\gamma$ and z_0, the maximum tensile stress, or the *theoretical strength* of adhesion σ_{th}, occurs at $h = 3^{1/6}z_0$ and equals $16\Delta\gamma/9\sqrt{3}z_0$. Figure 2.3 plots the variation of the normalized interaction stress as a function of separations h. The shape of the $\sigma - h$ curves is related to the

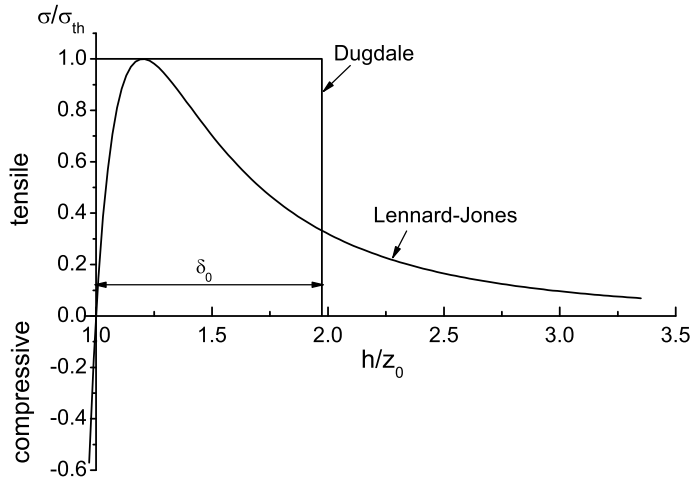

Figure 2.3.: Lennard-Jones and Dugdale laws for interaction between two surfaces.

competition between the attractive and repulsive forces. The interactive range of the attractive force is longer than that of the repulsive one, and for $h > z_0$ the long-ranged force dominates the interfacial interaction and draws the surfaces closer together with a concurrent reduction in potential energy. On the other hand, for separations less than

z_0, the repulsive forces, which arises primarily from electron-electron overlap of the inner electron shells of the individual atoms, dominates. Hence, the attractive and repulsive forces are equal and opposite at $h = z_0$. The net force at equilibrium is zero, which is associated with the minimum in potential energy since $\sigma = \partial U/\partial h$. Thus, in the absence of externally applied forces, two flat solid surfaces are two parallel planes with an equilibrium interfacial separation of z_0.

Although Equation (2.10) depicts the interaction between two planar surfaces, it is often applied to the interaction between two unparallel solid surfaces [43]. Actually, this argument was first proposed by Derjaguin [20] in terms of energy rather than forces. The *Derjaguin approximation* stated that the interaction energy between two small solid surfaces, which may be curved and slightly inclined to each other, is the same as the energy per unit area between two parallel planes. In our studies, especially in the numerical calculations, Equation (2.10) and Derjaguin approximation are adopted.

However, the Lennard-Jones law of Equation (2.10) appears too complex especially for the theoretical analysis. Under this circumstance, a simpler approximate law like Dugdale model [23] becomes quite useful in which the attractive force is assumed to be a constant and equal to the theoretical strength σ_{th} if the separation falls in the range of $z_0 \leq h \leq z_0 + \delta_0$ with δ_0 being the effective interaction range of adhesion (Figure 2.3). As the work of adhesion should not be altered after the approximation, δ_0 then is determined by $\delta_0 = \Delta\gamma/\sigma_{\text{th}} = 0.974 z_0$. It has been pointed out that use of a more realistic interaction law like Lennard-Jones law generally yields results qualitatively similar to those derived based on the Dugdale model provided that the theoretical strength and the work of adhesion remain unchanged [8, 67].

2.2. Classical theories of contact mechanics

In the preceding section, we have introduced the intermolecular and surface forces that inevitably occur when two solids are brought into contact. As a consequence, deformation of the solids will take place. Contact mechanics is just such a subject that is aimed to study the stresses and deformation arising from the contact. In this section, we will briefly review some classical models in the theory of contact mechanics. These models can be thought of the fundamental of contact mechanics and some of them are still used broadly.

2.2.1. Hertz theory: a non-adhesive contact model

The history of contact mechanics theory can be traced back to 1882 [49] when Hertz published his famous paper *"On the contact of elastic solids"*. In this paper, Hertz solved the contact problem between two elastic spheres compressed by externally applied forces P, as shown by Figure 2.4(a). The basic assumptions introduced by Hertz allowed him

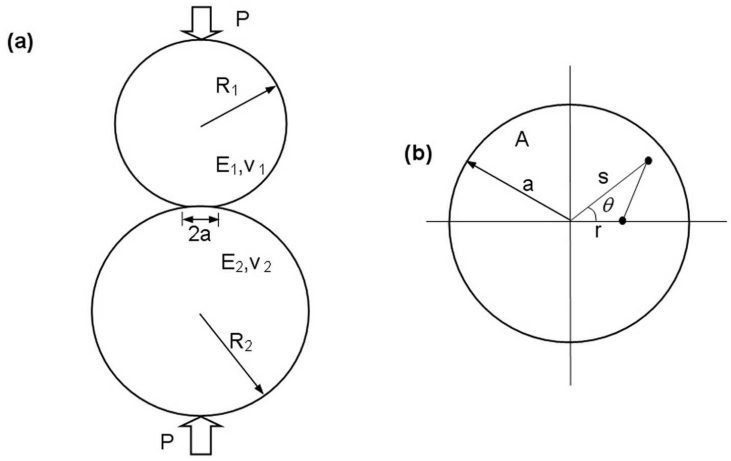

Figure 2.4.: (a) Two elastic spheres are pressed together by force P, resulting in contact area with radius a. (b) Integration scheme for calculating the displacement of the contact area.

to deal with the problem in an analytical manner and obtain the solutions with very simple forms. These assumptions can be summarized as follows:

- Two spheres are assumed to be frictionless so that only normal pressure is transmitted between them.
- In contrast to the spheres radii, the contact size is quite small, i.e., $a \ll R_{1,2}$.
- Each sphere can be considered as an elastic half-space.
- Profiles of the spheres can be approximated by parabola $r^2/2R_{1,2}$.

In elasticity theory, the problem of determining the deformation in an elastic half-space due to a point force applied normally to the surface is termed *Boussinesq*'s problem [11]. According to the solution of Boussinesq's problem, the vertical displacement of surface w induced by a unit concentrated force acting normally to the half-space surface at the origin $r = 0$ can be expressed as

$$w(r) = (1 - \nu^2)/\pi E r, \tag{2.11}$$

where E and ν denote the Young's modulus and Poisson's ratio of the half-space respectively. For the contact between two spheres, based on the assumptions proposed above, the surface deflections of two contacting spheres can be expressed by

$$\begin{aligned} w_i(r) &= \frac{1-\nu_i^2}{\pi E_i}\int_0^a sp(s)\mathrm{d}s\int_0^{2\pi}\left(r^2+s^2-2rs\cos\theta\right)^{-1/2}\mathrm{d}\theta \\ &= \frac{4(1-\nu_i^2)}{\pi E_i}\int_0^a \frac{s}{r+s}\mathbf{K}\left(\frac{2(rs)^{1/2}}{r+s}\right)p(s)\mathrm{d}s, \quad (i=1,2) \end{aligned} \tag{2.12}$$

where function p is the pressure acting on the contact area, s and θ are coordinates parameters as defined in Figure 2.4(b) and $\mathbf{K}(\cdot)$ is the complete elliptical integral of first kind.

On the other hand, the geometric conformability within the contact region requires

$$w_1 + w_2 = \delta - \frac{r^2}{2R}, \quad (r < a) \tag{2.13}$$

where $R = [1/R_1 + 1/R_2]^{-1}$ is the reduced radius of the spheres and δ denotes the relative approach of distant points in these two spheres. The contact problem between two spheres now can be stated as such that the mutual axisymmetric pressure distribution $p(r)$ acting over the circular contact area A on the surface of two elastic half-spaces is required which will produce deflections satisfying following condition within the contact area

$$w_1 + w_2 = \frac{4}{\pi E^*}\int_0^a \frac{s}{r+s}\mathbf{K}\left(\frac{2(rs)^{1/2}}{r+s}\right)p(s)\mathrm{d}s = \delta - \frac{r^2}{2R}, \quad (r < a) \tag{2.14}$$

where the combined elastic modulus of the spheres $E^* = [(1-\nu_1^2)/E_1 + (1-\nu_2^2)/E_2]^{-1}$. Equation (2.14) implies that the contact pressure $p(r)$ only depends on R, E^*. That is, for a given δ the pressure distribution in an elastic-sphere/rigid-plane contact system is identical to that in a rigid-sphere/elastic-plane system as long as R, E^* are the same for both cases. Actually, it is the common feature of the classical contact models concerning two elastic spheres.

By assuming an elliptical distribution of pressure in the contact area, Hertz proposed the solution of Equation (2.14) as

$$p(r) = \frac{2aE^*}{\pi R}\left[1-(r/a)^2\right]^{1/2}. \quad (r < a) \tag{2.15}$$

Due to Newton's third law, integration of Equation (2.15) over the contact area A gives rise to the external load applied on the stationary spheres as

$$P = \frac{4E^* a^3}{3a}. \tag{2.16}$$

Substitution of Equation (2.15) into Equation (2.14) yields the penetration

$$\delta = \frac{a^2}{R}. \tag{2.17}$$

Hertz theory has been proved a good description in macroscopic scale although the intermolecular adhesion between two solid surfaces has not been considered as we can see from the nonnegative pressure of Equation (2.15). However, as the size decreases the surface-to-bulk ratio will become more and more significant and the surfaces adhesion induced by the intermolecular interactions can not be neglected any more. After 1930 when the London theory of van der Waals forces was established, a great deal of efforts were made for understanding the interact forces between small particles like colloids. In the following, we will introduce several theoretical models, in which the adhesive forces are taken into account on the basis of various assumptions.

2.2.2. Adhesive contact models

In 1932, Bradley [12] assessed the attractive force between two rigid (nondeforming) spheres in contact by integration

$$F = 2\pi \int_0^\infty r\sigma(h)\mathrm{d}r, \tag{2.18}$$

where $\sigma(h)$ is the adhesive stress which is a function of the surface separation h. By using the parabola expression to approximate the spherical profile, the separation between two surfaces can be written as $h(r) = h_0 + r^2/2R$, where R is the reduced radius of the spheres and h_0 is the surface-surface separation at $r = 0$. Taking derivative of h with respect to r yields

$$R\mathrm{d}h = r\mathrm{d}r. \tag{2.19}$$

Substituting Equation (2.19) into Equation (2.18), we obtain the adhesive force in terms of h_0 as

$$F(h_0) = 2\pi R \int_{h_0}^\infty \sigma(h)\mathrm{d}h. \tag{2.20}$$

In fact, the integral on the right-hand side of Equation (2.20) stands for the area enclosed by the $\sigma(h) - h$ curve ranging from $h = h_0$ to $h = \infty$. Recalling the definition of work of adhesion, the maximum of this integral will occur at $h_0 = z_0$ and equal the work of adhesion $\Delta\gamma$. Therefore, the maximum adhesion force between two rigid spheres can be immediately written as

$$F^{\mathrm{f}} = 2\pi R\Delta\gamma, \tag{2.21}$$

a result actually independent of the exact form of the interaction law. This maximum value represents the force required to separate two spheres from adhesive contact and therefore is commonly called *pull-off* force.

Obviously, the Bradley model did not consider the deformation of the spheres induced by the contacting forces. To solve this problem, Johnson *et al.* [62] investigated the adhesive contact problem between two elastic spheres. Their theory, commonly termed JKR (Johnson-Kendall-Roberts) model, is based on the Griffith energy argument [45] in which equilibrium state is achieved when the strain energy release rate equals the work of adhesion, i.e. $\mathcal{G} = \Delta\gamma$. The resulting pressure within the contact area is given by

$$p(r) = \frac{2aE^*}{\pi R}\left[1 - (r/a)^2\right]^{1/2} - \left(\frac{2\Delta\gamma E^*}{\pi a}\right)^{1/2}\left[1 - (r/a)^2\right]^{-1/2}. \quad (r < a) \tag{2.22}$$

In comparison with the Hertzian result of Equation (2.15), Equation (2.22) contains an additional adhesive (negative) term with a square root singularity near the contact periphery $r = a$, by which one may be immediately reminded of the similar stress singularity occurring at the crack tip in fracture mechanics. This resemblance exhibits the similarity between contact problem and fracture problem in mathematics.

Integrating Equation (2.22) over the contact area gives rise to the external load applied on the stationary spheres as

$$P = 2\pi\int_0^a p(r)\mathrm{d}r = \frac{4E^*a^3}{3R} - \sqrt{8\pi\Delta\gamma E^*a^3}. \tag{2.23}$$

Equation (2.23) has a non-zero root $a = (9\pi R^2\Delta\gamma/2E^*)^{1/3}$ for $P = 0$, suggesting that two spheres can adhere to each other even under zero external force. This behaviour can not be seen from the Hertz model because it is derived on the basis of nonadhesive contact. The minimum of Equation (2.23) occurs at the contact radius

$$a = a_{\mathrm{c}} = (9\pi\Delta\gamma R^2/8E^*)^{1/3}, \tag{2.24}$$

which gives the pull-off force as

$$F^{\mathrm{f}} = -P_{\min} = \frac{3}{2}\pi R\Delta\gamma. \tag{2.25}$$

This is really an astonishing result because of its independence on the elastic properties of the spheres. In that case, in the limit of two rigid spheres, the pull-off force between two rigid spheres should be $\frac{3}{2}\pi R\Delta\gamma$ rather than $2\pi R\Delta\gamma$ as predicted by the Bradley model. Same contradiction also exists between JKR model and DMT model [21] in which the interaction forces outside the "contact area" are considered but are assumed not to deform the profile so that the net load is expressed by

$$P = \frac{4E^* a^3}{3R} - 2\pi R\Delta\gamma, \tag{2.26}$$

giving pull-off force $2\pi R\Delta\gamma$. This conflict hadn't been solved until the introduction of the Tabor number [93]

$$\mu \equiv \left(\frac{R\Delta\gamma^2}{E^{*2} z_0^3}\right)^{1/3}, \tag{2.27}$$

where z_0 is the equilibrium interfacial separation as in Equation (2.6). It was pointed out by Tabor that the JKR theory applied to the cases with large μ while the DMT model held for the cases with small μ. For the intermediate range between JKR and DMT models, an analytical solution was obtained by Maugis [67] on the basis of Dugdale's model [23]. The contact pressure and net load predicted by M-D (Maugis-Dugdale) model are

$$p(r) = \begin{cases} \dfrac{2aE^*}{\pi R}\left[1-(r/a)^2\right]^{1/2} - \dfrac{\sigma_{\mathrm{th}}}{\pi}\cos^{-1}\left(\dfrac{2a^2-c^2-r^2}{c^2-r^2}\right), & (r \le a) \\ -\sigma_{\mathrm{th}}, & (a \le r \le c) \end{cases} \tag{2.28}$$

$$P = \frac{4E^* a^3}{3R} - 2\sigma_{\mathrm{th}} a\left[a\sqrt{c^2-a^2} + c^2\sec^{-1}(c/a)\right], \tag{2.29}$$

where c is the outer radius of the cohesive zone determined by following equation

$$\frac{a^2\sigma_{\mathrm{th}}}{\pi R\Delta\gamma}\left[(m^2-2)\sec^{-1}m + \sqrt{m^2-1}\right] + \frac{4\sigma_{\mathrm{th}}^2 a}{\pi\Delta\gamma E^*}\left[\sqrt{m^2-1}\sec^{-1}m + 1 - m\right] = 1 \tag{2.30}$$

with $m = c/a$. The pull-off force given by M-D model ranges from $\frac{3}{2}\pi R\Delta\gamma$ to $2\pi R\Delta\gamma$, depending on the Tabor number. This result have been confirmed by the numerical results based on the more realistic Lennard-Jones law [43, 61]. Although M-D theory gives

the analytical solutions, the results are still presented in an implicit form. To overcome this inconvenience in the practical applications, some simpler experiential formulae with a very good approximation to the M-D solutions were developed [16, 80].

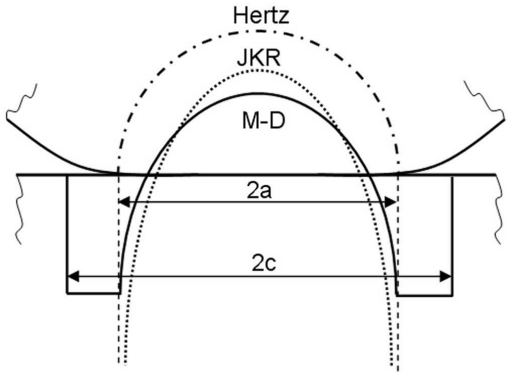

Figure 2.5.: Contact pressure distributions predicted by different contact models (adapted from [61]).

Figure 2.5 schematically shows the distribution of the contact stress predicted by various models in the classical contact theory. The absence of the corresponding curve for DMT model is due to its identical pressure with Hertz theory within the contact area, while out the contact area no exact expression has been given. For comparison, Table 2.1 tabulates the external load P and the pull-off force F^{f} given by different models.

Table 2.1.: Summary of the classic contact models for two elastic spheres

Models	External load	Pull-off force
Hertz	$P = 4E^*a^3/3R$	$F^{\mathrm{f}} = 0$
JKR	$P = 4E^*a^3/3R - \sqrt{8\pi\Delta\gamma E^*a^3}$	$F^{\mathrm{f}} = \frac{3}{2}\pi R\Delta\gamma$
DMT	$P = 4E^*a^3/3R - 2\pi R\Delta\gamma$	$F^{\mathrm{f}} = 2\pi R\Delta\gamma$
M-D	$P = 4E^*a^3/3R - 2\sigma_{\mathrm{th}}a\left[a\sqrt{c^2-a^2} + c^2\sec^{-1}(c/a)\right]$	$F^{\mathrm{f}} \in (\frac{3}{2}\pi R\Delta\gamma,\ 2\pi R\Delta\gamma)$

In essence, the difference between these theories can be attributed to the different stress-separation laws [16] that they are based on. Figure 2.6 shows the stress-separation laws applied in Hertz, JKR, DMT and M-D models. It can be seen that no attractive force exists in the Hertz model at all. While the JKR model employs a short-range/high-strength adhesion law which is essentially a delta function with strength $\Delta\gamma$, the DMT model adopts a long-range/low-strength interaction. In M-D model, Dugdale law is adopted so that the adhesive stress is constant within the interaction range. Given work of adhesion $\Delta\gamma$, Dugdale law will approach a delta function as the interaction range decreases. Reversely, if the interaction range increases, it will get close to the DMT

model. Figure 2.6 shows that the M-D model describes the transition from JKR model to DMT model nicely.

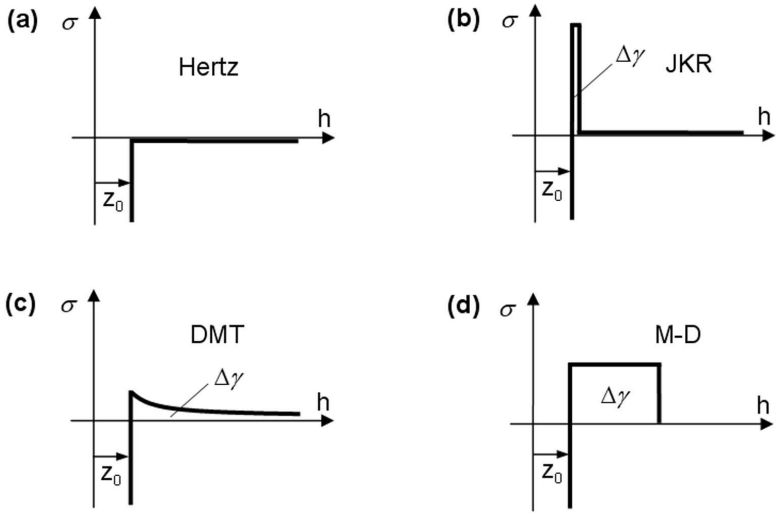

Figure 2.6.: Stress-separation laws applied respectively in (a) Hertz model, (b) JKR model, (c) DMT model and (d) M-D model (adapted from [16]).

In addition to the above-mentioned contact models for spheres (three-dimensional), corresponding theories also have been developed for the cylinders (two-dimensional). For example, Barquins [7] obtained the JKR-like solutions for the contact between a rigid cylinder and elastic flat surface. According to his results, the contact pressure can be given by

$$p(x) = \frac{E^*}{2R}(a^2 - x^2)^{1/2} - \sqrt{\frac{2E^*\Delta\gamma}{\pi}}(a^2 - x^2)^{-1/2}. \tag{2.31}$$

The externally applied load per unit cylinder length is

$$P = \pi E^* a^2/4R - \sqrt{2E^*\pi a\Delta\gamma}. \tag{2.32}$$

The minimum load occurs at the half-width of contact

$$a = a_c = \left(\frac{2\Delta\gamma R^2}{\pi E^*}\right)^{1/3}, \tag{2.33}$$

which gives the pull-off force per unit cylinder length

$$F^f = 3\left(\frac{\pi E^*\Delta\gamma^2 R}{16}\right)^{1/3}. \tag{2.34}$$

The counterpart of the M-D theory in two-dimensional case was proposed by Baney and Hui [6]. More recent endeavors have extended the contact theories to the periodic contact asperities [54], coupled normal and shear loads [64], viscoelastic materials [46, 51] and biological attachments [1, 2, 5, 33, 34, 50, 78, 89].

Chapter 3. Research methods

Theoretical modeling, computational simulation and experiment are referred to as three basic approaches of scientific research. In this thesis, our studies are carried out mainly by means of the former two methods. In order to build up a successful theoretical model, some simplifications and assumptions have to be made on condition that no essence of the problem is lost. For instance, in the classical contact theories, contact solids are usually treated as elastic half-spaces so as to make it possible to calculate the deformation of the solids analytically. However, for most contact problems it is still impossible to get the solution in an analytical form. Under these circumstances, computational simulation becomes very useful because it is capable of handling more realistic but complicated cases. It is basically for this reason that computational simulation is often used as the benchmark to verify the prediction of the theoretical model. In this regard, computational simulation is usually called computational experiment.

3.1. Theoretical modeling: application of Hankel transform in contact mechanics

According to the classical elasticity theory, the general solution to the Láme-Navier equation can be constructed by harmonic or bi-harmonic strain functions [88, 96]. Particularly, for an axisymmetric problem, the number of such strain functions is reduced to one for bi-harmonic function or two for harmonic functions. On the other hand, any harmonic function can be expressed in terms of Hankel transforms with respect to two unknown functions. Therefore, the general solution for any axisymmetric problem can be given by Hankel transforms with respect to four unknown functions. After applying the boundary conditions, these unknown functions can be determined by solving a pair of dual integral equations. This Hankel-transform-based method has been systematically discussed by Sneddon [88] and widely used in contact mechanics. In the following, we first present a brief introduction to the expression of harmonic function in terms of Hankel transforms. It is followed by the formulation of the axisymmetric problem in an

elastic half-space via Hankel transforms. Then, general solutions to some special dual integral equations are introduced. Finally, application of this approach is illustrated by solving a typical contact problem.

3.1.1. Expression of harmonic function in terms of Hankel transforms

Hankel transforms are widely used especially in the axisymmetric problems in elasticity theory. Given function $f(r)$, the nth order Hankel transform is defined as

$$F(\xi) \equiv \mathcal{H}_n[f(r); r \to \xi] \equiv \int_0^\infty r f(r) J_n(r\xi) \mathrm{d}r, \tag{3.1}$$

where $J_n(r\xi)$ is the nth order Bessel function of the first kind. The inversion of Hankel transform is defined as:

$$f(r) \equiv \mathcal{H}_n^{-1}[F(\xi); \xi \to r] \equiv \int_0^\infty \xi F(\xi) J_n(\xi r) \mathrm{d}\xi. \tag{3.2}$$

Apparently, Equations (3.1) and (3.2) shows that Hankel transform and its inversion describe the same operation, namely, $\mathcal{H}_n^{-1} = \mathcal{H}_n$.

Since the nth order Bessel functions are more frequently defined as the solutions to the differential equation

$$\frac{\mathrm{d}^2 y}{\mathrm{d}x^2} + \frac{\mathrm{d}y}{x\mathrm{d}x} + \left(1 - \frac{n^2}{x^2}\right) y = 0,$$

function $J_n(r\xi)$ must satisfy equation

$$\left(\frac{\partial^2}{\partial r^2} + \frac{1}{r}\frac{\partial}{\partial r} - \frac{n^2}{r^2} + \xi^2\right) J_n(r\xi) = 0. \tag{3.3}$$

Letting operator $\mathcal{B}_n \equiv \dfrac{\partial^2}{\partial r^2} + \dfrac{1}{r}\dfrac{\partial}{\partial r} - \dfrac{n^2}{r^2}$, rearrangement of Equation (3.3) gives rise to

$$\mathcal{B}_n[J_n(r\xi)] = -\xi^2 J_n(r\xi). \tag{3.4}$$

Performing operator $\mathcal{B}_n$ on both sides of Equation (3.2) leads to

$$\mathcal{B}_n[f(r)] = \mathcal{B}_n\left[\int_0^\infty \xi F(\xi) J_n(r\xi) \mathrm{d}\xi\right] = \int_0^\infty \xi F(\xi) \mathcal{B}_n[J_n(r\xi)] \mathrm{d}\xi. \tag{3.5}$$

On substituting Equation (3.4) into the far right-hand side of Equation (3.5), we have

$$\mathcal{B}_n[f(r)] = -\int_0^\infty \xi\xi^2 F(\xi) J_n(r\xi)\mathrm{d}\xi = -\mathcal{H}_n^{-1}\left[\xi^2 F(\xi); \xi \to r\right]. \tag{3.6}$$

Perform Hankel transform on both sides of Equation (3.6) to get

$$\mathcal{H}_n[\mathcal{B}_n f(r); r \to \xi] = -\xi^2 F(\xi) = -\xi^2 \mathcal{H}_n[f(r); r \to \xi]. \tag{3.7}$$

In cylindrical coordinates (r, θ, z), the *Laplace* operator can be expressed as

$$\nabla^2 = \frac{\partial^2}{\partial r^2} + \frac{1}{r}\frac{\partial}{\partial r} + \frac{1}{r^2}\frac{\partial^2}{\partial \theta^2} + \frac{\partial^2}{\partial z^2}.$$

For an arbitrary quantity $f(r, z)$ associated with an axisymmetric problem, owing to its independence of angle θ, we have

$$\nabla^2 f(r,z) = \left(\frac{\partial^2}{\partial r^2} + \frac{1}{r}\frac{\partial}{\partial r} + \frac{\partial^2}{\partial z^2}\right) f(r,z) = (\mathcal{B}_0 + \frac{\partial^2}{\partial z^2}) f(r,z). \tag{3.8}$$

Performing Hankel transform $\mathcal{H}_0$ on Equation (3.8) and then applying Equation (3.7) with $n = 0$ yield

$$\mathcal{H}_0[\nabla^2 f(r,z); r \to \xi] = (D_z^2 - \xi^2) F(\xi, z) \tag{3.9}$$

where $D_z = \partial/\partial z$ and

$$F(\xi, z) \equiv \mathcal{H}_0[f(r,z); r \to \xi] = \int_0^\infty r f(r) J_0(r\xi)\mathrm{d}r.$$

Equation (3.9) indicates that $f(r, z)$ is a harmonic function with $\nabla^2 f(r, z) = 0$ only if its 0th order Hankel transform $F(\xi, z)$ satisfies

$$(D_z^2 - \xi^2) F(\xi, z) = 0, \tag{3.10}$$

and vice versa. Since the general solution to the differential Equation (3.10) is

$$F(\xi, z) = A_1(\xi)\exp(-\xi z) + A_2(\xi)\exp(\xi z) \tag{3.11}$$

with $A_1(\xi)$ and $A_2(\xi)$ being two arbitrary functions of ξ,, inversion of Equation (3.11) immediately leads to the expression of the arbitrary axisymmetric harmonic function

$f(r,z)$ in terms of Hankel transform as:

$$f(r,z) = \mathcal{H}_0[A_1(\xi)\exp(-\xi z) + A_2(\xi)\exp(\xi z); \xi \to r]. \tag{3.12}$$

3.1.2. Formulation of axisymmetric half-space problems via Hankel transforms

In classical elasticity theory, the Papkovich-Neuber solution [71, 75] provides a general solution to the Láme-Navier equation. Following Papkovich-Neuber solution, the displacement components for an axisymmetric problem can be given by

$$u_r = -\frac{1}{2G}\frac{\partial}{\partial r}(z\,\Psi + \Phi), \tag{3.13}$$

$$u_z = \frac{1}{2G}\left[4(1-\nu)\,\Psi - \frac{\partial}{\partial z}(z\,\Psi + \Phi)\right], \tag{3.14}$$

$$u_\theta = 0, \tag{3.15}$$

where G is the shear modulus and Ψ, Φ are two strain functions to be determined by boundary conditions. If no body force is considered, strain functions Ψ, Φ must be harmonic, i.e.,

$$\nabla^2\,\Psi = 0, \tag{3.16}$$

$$\nabla^2\,\Phi = 0. \tag{3.17}$$

On the other hand, for the axisymmetric problem in elastic half-space $z \geq 0$, harmonic functions Ψ, Φ should be independent of angle θ. Considering the limited displacements at $z = \infty$, harmonic functions Ψ, Φ must be finite at $z = \infty$ and, in the light of Equation (3.12), can be expressed in terms of Hankel transforms as

$$\Psi(r,z) = \mathcal{H}_0[\xi^{-1}A(\xi)\exp(-\xi z); \xi \to r], \tag{3.18}$$

$$\Phi(r,z) = \mathcal{H}_0[\xi^{-2}C(\xi)\exp(-\xi z); \xi \to r], \tag{3.19}$$

where $A(\xi)$, $C(\xi)$, functions of ξ, will be determined through the boundary conditions of the problem.

Substituting Equations (3.18, 3.19) into Equations (3.13, 3.14) and then applying the relationship between Hankel transforms $\mathcal{H}_0$ and $\mathcal{H}_1$ for arbitrary function $g(\xi)$

$$\frac{\partial}{\partial r}\mathcal{H}_0[g(\xi); \xi \to r] \equiv -\mathcal{H}_1[\xi g(\xi); \xi \to r], \tag{3.20}$$

the displacement and accordingly the stress solutions can be expressed in terms of Hankel transforms as

$$u_r(r,z) = \mathcal{H}_1[Y(\xi,z);\xi \to r], \tag{3.21}$$

$$u_z(r,z) = \mathcal{H}_0[V(\xi,z);\xi \to r], \tag{3.22}$$

$$\tau_{rz}(r,z) = \mathcal{H}_1[S(\xi,z);\xi \to r], \tag{3.23}$$

$$\sigma_{zz}(r,z) = \mathcal{H}_0[T(\xi,z),\xi \to r], \tag{3.24}$$

with

$$\begin{bmatrix} 2GY \\ 2GV \\ -S \\ -T \end{bmatrix} = \begin{bmatrix} (\xi z A + C)\xi^{-1} \\ [(3-4\nu)A + \xi z A + C]\xi^{-1} \\ (1-2\nu)A + \xi z A + C \\ (2-2\nu)A + \xi z A + C \end{bmatrix} \exp(-\xi z). \tag{3.25}$$

Equations (3.21-3.25) summarize the general solution to an axisymmetric problem of an elastic half-space in terms of Hankel-transforms. Similar expressions were firstly presented by Harding and Sneddon [47].

3.1.3. Dual integral equations

We have expressed the general solutions to the axisymmetric problem of half-space in terms of Hankel transforms with respect to two unknown functions. The determination of these two functions by using boundary conditions finally converges on the solution of a pair of dual integral equations of type

$$\int_0^\infty \xi^{-2\alpha}\phi(\xi)J_n(\rho\xi)\mathrm{d}\xi = \mathrm{F}_1(\rho), \qquad (0 \le \rho \le 1) \tag{3.26}$$

$$\int_0^\infty \phi(\xi)J_n(\rho\xi)\mathrm{d}\xi = \mathrm{G}_2(\rho), \qquad (\rho > 1) \tag{3.27}$$

where $\mathrm{F}_1(\rho)$ and $\mathrm{G}_2(\rho)$ are two known functions correlated with the specific boundary conditions. In mathematics, the solution to such kind of dual integral Equations has been systematically discussed by Titchmarsh [99] and Sneddon[88]. Following the general solutions given by Sneddon, here we just synopsize[1] the solutions to four special cases with different combinations of α and n. A frequent use of these general solutions will be made in our later discussions on the axisymmetric contact problems.

[1]The errors that occur in the formulae given by Sneddon [88] have been corrected here.

Case(a):

If $\alpha = \frac{1}{2}$, $n = 0$, Equations (3.26) and (3.27) can be rewritten as

$$\int_0^\infty \xi^{-1}\phi(\xi)J_0(\rho\xi)\mathrm{d}\xi = \mathrm{F}_1(\rho), \qquad (0 \le \rho \le 1) \tag{3.28}$$

$$\int_0^\infty \phi(\xi)J_0(\rho\xi)\mathrm{d}\xi = \mathrm{G}_2(\rho), \qquad (\rho > 1) \tag{3.29}$$

The solution to these dual integral equations is given by (see Equation 4.4.4 in [88])

$$\begin{aligned}\phi(\xi) \;=\; & \frac{2\xi}{\pi}\left\{\cos\xi\int_0^1 \frac{t\mathrm{F}_1(t)\mathrm{d}t}{\sqrt{1-t^2}} + \xi\int_0^1 \frac{s\mathrm{d}s}{\sqrt{1-s^2}}\int_0^1 t\sin(\xi t)\mathrm{F}_1(st)\mathrm{d}t\right. \\ & \left. + \int_1^\infty t\cos(\xi t)\mathrm{d}t\int_1^\infty \frac{s\mathrm{G}_2(st)\mathrm{d}s}{\sqrt{s^2-1}}\right\}.\end{aligned} \tag{3.30}$$

Denoting

$$\mathrm{F}_2(\rho) \equiv \int_0^\infty \xi^{-1}\phi(\xi)J_0(\rho\xi)\mathrm{d}\xi, \qquad (\rho > 1)$$

$$\mathrm{G}_1(\rho) \equiv \int_0^\infty \phi(\xi)J_0(\rho\xi)\mathrm{d}\xi, \qquad (0 \le \rho \le 1)$$

we have

$$\mathrm{F}_2(\rho) = \frac{2}{\pi}\int_1^\rho \frac{\mathrm{G}^{**}(\xi)\mathrm{d}\xi}{\sqrt{\rho^2-\xi^2}} + \frac{2\sqrt{\rho^2-1}}{\pi}\int_0^1 \frac{t\mathrm{F}_1(t)\mathrm{d}t}{(\rho^2-t^2)\sqrt{1-t^2}}, \tag{3.31}$$

$$\mathrm{G}_1(\rho) = -\frac{2}{\pi\rho}\frac{\mathrm{d}}{\mathrm{d}\rho}\int_\rho^1 \frac{\xi\mathrm{F}^{**}(\xi)\mathrm{d}\xi}{\sqrt{\xi^2-\rho^2}} - \frac{2}{\pi\sqrt{1-\rho^2}}\int_1^\infty \frac{t\sqrt{t^2-1}\mathrm{G}_2(t)\mathrm{d}t}{t^2-\rho^2}, \tag{3.32}$$

where

$$\mathrm{F}^{**}(\xi) = \frac{\mathrm{d}}{\mathrm{d}\xi}\int_0^\xi \frac{s\mathrm{F}_1(s)\mathrm{d}s}{\sqrt{\xi^2-s^2}},\ \mathrm{G}^{**}(\xi) = \int_\xi^\infty \frac{s\mathrm{G}_2(s)\mathrm{d}s}{\sqrt{s^2-\xi^2}}. \tag{3.33}$$

Case(b):

If $\alpha = -\frac{1}{2}$, $n = 0$, Equations (3.26)(3.27) can be rewritten as

$$\int_0^\infty \xi\phi(\xi)J_0(\rho\xi)\mathrm{d}\xi = \mathrm{F}_1(\rho), \qquad (0 \le \rho \le 1) \tag{3.34}$$

$$\int_0^\infty \phi(\xi)J_0(\rho\xi)\mathrm{d}\xi = \mathrm{G}_2(\rho), \qquad (\rho > 1) \tag{3.35}$$

The solution to these dual integral equations is given by (see Equation 4.4.12 in [88])

$$\begin{aligned}\phi(\xi) &= \frac{2}{\pi}\int_0^1 \sin(\xi t)\mathrm{d}t \int_0^t \frac{\tau \mathrm{F}_1(\tau)\mathrm{d}\tau}{\sqrt{t^2-\tau^2}} \\ &\quad -\frac{2}{\pi}\sin\xi \int_1^\xi \frac{\tau \mathrm{G}_2(\tau)\mathrm{d}\tau}{\sqrt{\tau^2-1}} + \frac{2\xi}{\pi}\int_1^\infty \cos(\xi t)\mathrm{d}t \int_t^\infty \frac{\tau \mathrm{G}_2(\tau)\mathrm{d}\tau}{\sqrt{\tau^2-t^2}}. \end{aligned} \tag{3.36}$$

Letting

$$\begin{aligned}\mathrm{F}_2(\rho) &\equiv \int_0^\infty \xi\phi(\xi)J_0(\rho\xi)\mathrm{d}\xi, \qquad (\rho>1) \\ \mathrm{G}_1(\rho) &\equiv \int_0^\infty \phi(\xi)J_0(\rho\xi)\mathrm{d}\xi, \qquad (0\le\rho\le 1)\end{aligned}$$

we have

$$\mathrm{F}_2(\rho) = \frac{2}{\pi}\frac{\mathrm{d}}{\mathrm{d}\rho}\int_1^\rho \frac{\xi \mathrm{G}^*(\xi)\mathrm{d}\xi}{\sqrt{\rho^2-\xi^2}} - \frac{2}{\pi\sqrt{\rho^2-1}}\int_0^1 \frac{t\sqrt{1-t^2}\mathrm{F}_1(t)\mathrm{d}t}{\rho^2-t^2}, \tag{3.37}$$

$$\mathrm{G}_1(\rho) = \frac{2}{\pi}\int_\rho^1 \frac{\mathrm{F}^*(\xi)\mathrm{d}\xi}{\sqrt{\xi^2-\rho^2}} + \frac{2\sqrt{1-\rho^2}}{\pi}\int_1^\infty \frac{t\mathrm{G}_2(t)\mathrm{d}t}{(t^2-\rho^2)\sqrt{t^2-1}}, \tag{3.38}$$

where

$$\mathrm{F}^*(\xi) = \int_0^\xi \frac{s\mathrm{F}_1(s)\mathrm{d}s}{\sqrt{\xi^2-s^2}},\ \mathrm{G}^*(\xi) = -\frac{\mathrm{d}}{\mathrm{d}\xi}\int_\xi^\infty \frac{s\mathrm{G}_2(s)\mathrm{d}s}{\sqrt{s^2-\xi^2}}. \tag{3.39}$$

Case(c):

If $\alpha = -\frac{1}{2}$, $n=1$, by Equations (3.26) and (3.27) we have

$$\int_0^\infty \xi\phi(\xi)J_1(\rho\xi)\mathrm{d}\xi = \mathrm{F}_1(\rho), \qquad (0\le\rho\le 1) \tag{3.40}$$

$$\int_0^\infty \phi(\xi)J_1(\rho\xi)\mathrm{d}\xi = \mathrm{G}_2(\rho), \qquad (\rho>1) \tag{3.41}$$

In this case, the solutions can derived from Equation 4.2.21 in [88] as

$$\begin{aligned}\phi(\xi) &= \frac{\sqrt{2\xi}}{\sqrt{\pi}}\int_0^1 \frac{1}{\sqrt{t}}J_{3/2}(\xi t)\mathrm{d}t \int_0^t \frac{\tau^2}{\sqrt{t^2-\tau^2}}\mathrm{F}_1(\tau)\mathrm{d}\tau \\ &\quad -\frac{\sqrt{2\xi}}{\sqrt{\pi}}\int_1^\infty t\sqrt{t}J_{3/2}(\xi t)\mathrm{d}t\frac{\mathrm{d}}{\mathrm{d}t}\int_t^\infty \frac{1}{\sqrt{\tau^2-t^2}}\mathrm{G}_2(\tau)\mathrm{d}\tau \end{aligned} \tag{3.42}$$

Similarly, letting

$$\mathrm{F}_2(\rho) \equiv \int_0^\infty \xi\phi(\xi)J_1(\rho\xi)\mathrm{d}\xi, \qquad (\rho > 1)$$
$$\mathrm{G}_1(\rho) \equiv \int_0^\infty \phi(\xi)J_1(\rho\xi)\mathrm{d}\xi, \qquad (0 \le \rho \le 1)$$

we have (see Equations 4.3.13 and 4.3.14 in [88])

$$\mathrm{F}_2(\rho) = \frac{2}{\rho^2\pi}\frac{\mathrm{d}}{\mathrm{d}\rho}\int_1^\rho \frac{\xi^3\mathrm{G}^*(\xi)\mathrm{d}\xi}{\sqrt{\rho^2-\xi^2}} - \frac{2}{\pi\rho\sqrt{\rho^2-1}}\int_0^1 \frac{t^2\sqrt{1-t^2}\mathrm{F}_1(t)\mathrm{d}t}{\rho^2-t^2}, \tag{3.43}$$

$$\mathrm{G}_1(\rho) = \frac{2\rho}{\pi}\int_\rho^1 \frac{\mathrm{F}^*(\xi)\mathrm{d}\xi}{\xi^2\sqrt{\xi^2-\rho^2}} + \frac{2\rho\sqrt{1-\xi^2}}{\pi}\int_1^\infty \frac{\mathrm{G}_2(t)\mathrm{d}t}{(t^2-\rho^2)\sqrt{t^2-1}}, \tag{3.44}$$

where

$$\mathrm{F}^*(\xi) = \int_0^\xi \frac{s^2\mathrm{F}_1(s)\mathrm{d}s}{\sqrt{\xi^2-s^2}},\ \mathrm{G}^*(\xi) = -\frac{\mathrm{d}}{\mathrm{d}\xi}\int_\xi^\infty \frac{\mathrm{G}_2(s)\mathrm{d}s}{\sqrt{s^2-\xi^2}}. \tag{3.45}$$

Case(d):

If $\alpha = \frac{1}{2}$, $n = 1$, Equations (3.26, 3.27) turn to be

$$\int_0^\infty \xi^{-1}\phi(\xi)J_1(\rho\xi)\mathrm{d}\xi = \mathrm{F}_1(\rho), \qquad (0 \le \rho \le 1) \tag{3.46}$$

$$\int_0^\infty \phi(\xi)J_1(\rho\xi)\mathrm{d}\xi = \mathrm{G}_2(\rho), \qquad (\rho > 1) \tag{3.47}$$

In this case, the solutions can be derived from Equation 4.2.27 in [88] as

$$\begin{aligned}\phi(\xi) \;=\; & \frac{2\xi}{\pi}\left\{\sin(\xi)\int_0^1 (1-t^2)^{-1/2}t^2\mathrm{F}_1(t)\mathrm{d}t\right. \\ & + \int_0^1 (1-\tau^2)^{-1/2}\tau^2\mathrm{d}\tau\int_0^1 [\sin(\xi t) - \xi t\cos(\xi t)]\mathrm{F}_1(\tau t)\mathrm{d}t \\ & \left. + \int_1^\infty t\sin(\xi t)\mathrm{d}t\int_1^\infty (\tau^2-1)^{-1/2}\mathrm{G}_1(t\tau)\mathrm{d}\tau\right\}. \end{aligned} \tag{3.48}$$

Letting

$$\mathrm{F}_2(\rho) \equiv \int_0^\infty \xi^{-1}\phi(\xi)J_1(\rho\xi)\mathrm{d}\xi, \qquad (\rho > 1)$$
$$\mathrm{G}_1(\rho) \equiv \int_0^\infty \phi(\xi)J_1(\rho\xi)\mathrm{d}\xi, \qquad (0 \le \rho \le 1)$$

we have (see Equations 4.3.19, 4.3.20 in [88])

$$\mathrm{F}_2(\rho) = \frac{2}{\pi\rho}\int_1^\rho \frac{\xi^2 \mathrm{G}^{**}(\xi)\mathrm{d}\xi}{\sqrt{\rho^2-\xi^2}} + \frac{2\sqrt{\rho^2-1}}{\pi\rho}\int_0^1 \frac{t^2\mathrm{F}_1(t)\mathrm{d}t}{\sqrt{1-t^2}(\rho^2-t^2)}, \tag{3.49}$$

$$\mathrm{G}_1(\rho) = -\frac{2}{\pi}\frac{\mathrm{d}}{\mathrm{d}\rho}\int_\rho^1 \frac{\mathrm{F}^{**}(t)\mathrm{d}t}{t\sqrt{t^2-\rho^2}} - \frac{2\rho}{\pi\sqrt{1-\rho^2}}\int_1^\infty \frac{\sqrt{t^2-1}\mathrm{G}_2(t)\mathrm{d}t}{(t^2-\rho^2)}, \tag{3.50}$$

where

$$\mathrm{F}^{**}(t) = \frac{\mathrm{d}}{\mathrm{d}t}\int_0^t \frac{s^2\mathrm{F}_1(s)\mathrm{d}s}{\sqrt{t^2-s^2}},\ \mathrm{G}^{**}(t) = \int_t^\infty \frac{\mathrm{G}_2(s)\mathrm{d}s}{\sqrt{s^2-t^2}}. \tag{3.51}$$

3.1.4. Application example

Having introduced the Hankel transform and the dual integral equations, now let us try to apply them to an example problem involving an axisymmetric rigid punch in contact with an elastic half-space. The solution to this problem was first given by Sneddon [87].

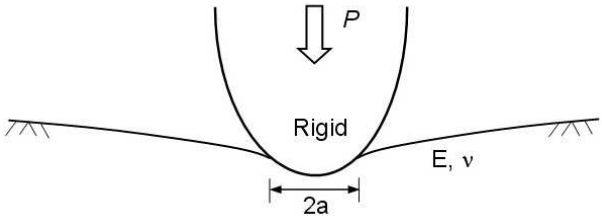

Figure 3.1.: Schematic of a rigid punch in contact with an elastic half-space.

As shown in Figure 3.1, an axisymmetric rigid punch is in contact with an elastic half-space $z \geq 0$. If friction forces are neglected, one can immediately write the boundary conditions as

$$u_{z|z=0} = \delta - f(r/a), \quad (0 \leq r \leq a) \tag{3.52}$$

$$\tau_{zr|z=0} = 0, \qquad (r \geq 0) \tag{3.53}$$

$$\sigma_{zz|z=0} = 0, \qquad (r > a) \tag{3.54}$$

where δ is penetration of the punch tip, $f(r/a)$ is the shape of the punch profile with $f(0) = 0$ and a denotes the radius of the contact area.

By using Equations (3.21-3.25), the general solutions to the axisymmetric problem in half-space, boundary conditions (3.52-3.54) can be rewritten in terms of Hankel transforms as

$$u_{z|z=0} = \frac{1}{2G}\mathcal{H}_0\left[\xi^{-1}[(3-4\nu)A+C];\xi\to r\right] = \delta - f(r/a),\ (0\le r\le a) \quad (3.55)$$

$$\tau_{rz|z=0} = -\mathcal{H}_1\left[(1-2\nu)A+C;\xi\to r\right] = 0, \quad (r\ge 0) \quad (3.56)$$

$$\sigma_{zz|z=0} = -\mathcal{H}_0\left[(2-2\nu)A+C;\xi\to r\right] = 0. \quad (r>a) \quad (3.57)$$

Equation (3.56) implies that

$$(1-2\nu)A + C = 0 \text{ or } C = (2\nu-1)A. \quad (3.58)$$

Substituting Equation (3.58) into Equations (3.55) and (3.57) results in

$$\mathcal{H}_0\left[\xi^{-1}A;\xi\to r\right] = \frac{E^*}{2}\left[\delta - f(r/a)\right], \quad (0\le r\le a) \quad (3.59)$$

$$\mathcal{H}_0\left[A;\xi\to r\right] = 0, \quad (r>a) \quad (3.60)$$

where $E^* = 2G/(1-\nu) = E/(1-\nu^2)$.

Now denoting $\psi(\xi) = A(\xi/a)$, Equations (3.59) and (3.60) can be normalized to be

$$\mathcal{H}_0\left[\xi^{-1}\psi(\xi);\xi\to r\right] = \int_0^\infty \psi(\xi)J_0(\xi\rho)\mathrm{d}\xi = \frac{aE^*}{2}[\delta - f(\rho)],\ (0\le\rho\le 1) \quad (3.61)$$

$$\mathcal{H}_0\left[\psi(\xi);\xi\to r\right] = \int_0^\infty \psi(\xi)\xi J_0(\xi\rho)\mathrm{d}\xi = 0, \quad (\rho>1) \quad (3.62)$$

where $\rho = r/a$. It is evident that Equations (3.61-3.62) are just a special case of standard dual integral equations (3.28-3.29) with $\mathrm{F}_1 = \frac{aE^*}{2}[\delta - f(\rho)]$ and $\mathrm{G}_2 = 0$. Actually, what we are interested in here is not the solution of $\psi(\xi)$ but G_1, i.e., the expression of $\mathcal{H}_0[\psi(\xi);\xi\to r]$ within $0\le\rho\le 1$, by which the contact stress can be expressed as

$$\sigma_{zz|z=0} = -\mathcal{H}_0[A;\xi\to r] = -\frac{1}{a^2}\int_0^\infty \xi\psi(\xi)J_0(\xi\rho)\mathrm{d}\xi = -\frac{1}{a^2}\mathrm{G}_1(\rho). \quad (0\le\rho\le 1) \quad (3.63)$$

Substitute $\mathrm{F}_1 = \frac{aE^*}{2}[\delta - f(\rho)]$ and $\mathrm{G}_2 = 0$ directly into Equation (3.32) to get

$$\mathrm{G}_1(\rho) = -\frac{2}{\pi\rho}\frac{\mathrm{d}}{\mathrm{d}\rho}\int_\rho^1 \frac{\xi\mathrm{F}^{**}(\xi)\mathrm{d}\xi}{\sqrt{\xi^2-\rho^2}} = \frac{2}{\pi}\left[\frac{\mathrm{F}^{**}(1)}{\sqrt{1-\rho^2}} - \int_\rho^1 \frac{\mathrm{F}'^{**}(\xi)\mathrm{d}\xi}{\sqrt{\xi^2-\rho^2}}\right], \quad (3.64)$$

where

$$\mathrm{F}^{**}(\xi) = \frac{aE^*}{2}\frac{\mathrm{d}}{\mathrm{d}\xi}\int_0^\xi \frac{s[\delta - f(s)]\mathrm{d}s}{\sqrt{\xi^2-s^2}} = \frac{aE^*}{2}\left[\delta - \xi\int_0^\xi \frac{f'(s)\mathrm{d}s}{\sqrt{\xi^2-s^2}}\right]. \quad (3.65)$$

Inserting Equation (3.64) into (3.63) gives rise to

$$\sigma_{zz|z=0} = -\frac{E^*}{2a}\left[\frac{\chi(1)}{\sqrt{1-r^2/a^2}} - \int_{r/a}^{1}\frac{\chi'(\xi)\mathrm{d}\xi}{\sqrt{\xi^2-r^2/a^2}}\right], \quad (0 \le r \le a) \tag{3.66}$$

where

$$\chi(\xi) = \frac{4}{\pi a E^*}F^{**}(\xi) = \frac{2}{\pi}\left[\delta - \xi\int_0^{\xi}\frac{f'(s)\mathrm{d}s}{\sqrt{\xi^2-s^2}}\right]. \tag{3.67}$$

One can note that the stress in Equation (3.66) contains two parts: one is the compressive part with vanishing value at $r = a$ and the other is attractive part with an inverse-square-root singularity at the contact periphery $r = a$, similar to the JKR model. We therefore call this solution as JKR-like solution.

Equation (3.67) indicates that the penetration

$$\delta = \frac{\pi}{2}\chi(1) + \int_0^1\frac{f'(s)\mathrm{d}s}{\sqrt{1-s^2}}. \tag{3.68}$$

Due to the Newton's third law, the load P required to achieve such a penetration is

$$P = -2\pi a^2\int_0^1\sigma_{zz|z=0}\rho\mathrm{d}\rho = \pi a E^*\int_0^1\chi(\xi)\mathrm{d}\xi = 2aE^*\left[\delta - \int_0^1\frac{sf(s)\mathrm{d}s}{\sqrt{1-s^2}}\right]. \tag{3.69}$$

In particular, for a spherical punch with profile function

$$f(\rho) = a^2\rho^2/2R,\ \rho = r/a, \tag{3.70}$$

Equation (3.67) gives

$$\chi(\xi) = \frac{2}{\pi}\left[\delta - \frac{a^2\xi^2}{R}\right], \tag{3.71}$$

$$\chi(1) = \frac{2}{\pi}\left[\delta - \frac{a^2}{R}\right]. \tag{3.72}$$

If we take $\chi(1) = 0$ to have stresses finite at $r = a$, we have

$$\delta = \frac{a^2}{R}, \tag{3.73}$$

$$P = \frac{4a^3E^*}{3R}, \tag{3.74}$$

$$\sigma_{zz|z=0} = -\frac{2aE^*}{\pi R}\left[1-(r/a)^2\right]^{1/2}, \quad (0 \le r \le a) \tag{3.75}$$

which actually are the Hertzian results. If we take $\chi(1) \neq 0$, we have

$$\delta = \frac{a^2}{3R} + \frac{P}{2aE^*}, \tag{3.76}$$

$$\sigma_{zz|z=0} = \frac{K_{\mathrm{I}}}{\sqrt{\pi a}}\left[1-(r/a)^2\right]^{-1/2} - \frac{2aE^*}{\pi R}\left[1-(r/a)^2\right]^{1/2}, \tag{3.77}$$

where $K_{\mathrm{I}} = -\dfrac{E^*}{2}\chi(1)\sqrt{\dfrac{\pi}{a}}$ is the stress intensity factor. The Griffith fracture criterion [45] correlates it with the surface energy $\Delta\gamma$ by

$$K_{\mathrm{I}} = \sqrt{2\Delta\gamma E^*},$$

therefore

$$\sigma_{zz|z=0} = \left(\frac{2\Delta\gamma E^*}{\pi a}\right)^{1/2}\left[1-(r/a)^2\right]^{-1/2} - \frac{2aE^*}{\pi R}\left[1-(r/a)^2\right]^{1/2}, \tag{3.78}$$

$$P = \frac{4E^*a^3}{3R} - \sqrt{8\pi\Delta\gamma E^* a^3}, \tag{3.79}$$

which are actually the results as given by JKR theory.

In fact, it can be shown that Equations (3.66-3.69) also apply to two elastic solids just by taking $f(r/a) = f_1(r/a) + f_2(r/a)$ and $E^* = [(1-\nu_1^2)/E_1 + (1-\nu_2^2)/E_2]^{-1}$, provided that the half-space assumption is still valid for each elastic solid.

3.2. Computational methods

We have derived the JKR-like solutions for contact problem between an arbitrary-shaped rigid punch and an elastic plane on the basis of Hankel transforms. The results, say Equation (3.66), involve a repeated integral associated with the profile function $f(r/a)$. Hence, if the punch has a complex profile, it would be not easy to get an explicit result due to the mathematical intractability. Additionally, like the JKR theory these solutions are also based on a delta-function-like force-separation law (Figure 2.6b). It has been pointed out that such a force-separation law is not always applicable especially for the cases with small Tabor number. We therefore develop some numerically computational methods, by which we can handle more complex profiles and more realistic stress-separation laws. These methods will be very useful in understanding the effect of the contact shape on the adhesion strength, which is actually the topic of the next

chapter. Before we start the discussion on the computational approaches, it would be better to explore some basic correlations in the typical contact problems.

3.2.1. Self-consistent correlations in contact problems

When two solids come into contact, their surfaces will experience tractions due to the intermolecular forces. In the contact region, the local traction stress σ could be compressive or tensile or zero, depending on the local surface-surface separation h at that point. As a consequence, deformation of the surfaces would occur if the materials are deformable. Although the magnitude of the surface deformation u might be very small in comparison with the dimension of the solids, it is still capable of causing some changes in the interfacial separation h and in turn leading to an appreciable change in the stress field σ owning to the dependence of σ on h. Therefore, as shown in Figure 3.2, traction

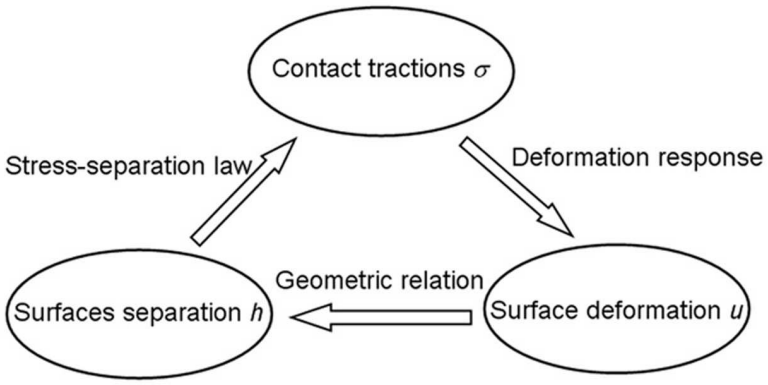

Figure 3.2.: Self-consistent relationships in contact problems.

σ, deformation u and interfacial separation h are correlated to one another. At the equilibrium state all these three quantities should be self-consistent. That is, all interrelations among them should be met simultaneously. These relations include the stress-separation law between h and σ, the deformation response correlating u and σ and the geometric relation between u and h. In our preceding Hankel-transform-based approach, the stress-separation law is assumed as a delta-function with strength $\Delta\gamma$ and the deformation is calculated by using the Boussinesq's solution as the Green's function. In the coming section, we will use the Lennard-Jones potential to describe the surface interaction. But we will still keep the half-space assumption for the moment, so that the surface deformation can be calculated numerically by using Boussinesq's solution as the Green's function.

3.2.2. Green's function method

Consider a rigid cylinder punch contacting with and elastic half-space $z \leq 0$, as shown in Figure 3.3. Lennard-Jones law is adopted to describe the stress between two surfaces

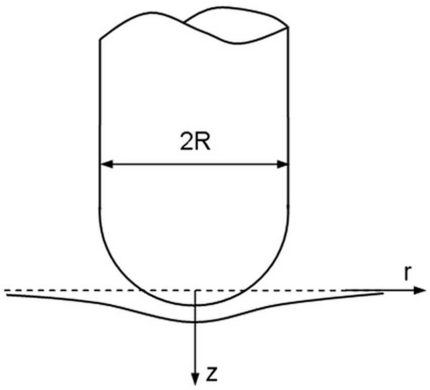

Figure 3.3.: Schematic of an axisymmetric rigid punch in contact with an elastic plane.

separated by distance h even though two surfaces are inclined or curved:

$$\sigma(h) = -p(h) = \frac{8\Delta\gamma}{3z_0}\left[\left(\frac{z_0}{h}\right)^3 - \left(\frac{z_0}{h}\right)^9\right]. \tag{3.80}$$

On the other hand, using Boussinesq's solution, the normal displacement of the plane surface caused by an axisymmetric pressure distribution $p(r)$ can be expressed as

$$w(r) = u_{z|z=0} = \frac{4}{\pi E^*}\int_0^R \frac{r_0 p(r_0)}{r + r_0}\mathbf{K}\left(\frac{2(rr_0)^{1/2}}{r + r_0}\right)\mathrm{d}r_0, \tag{3.81}$$

where $\mathbf{K}(\cdot)$ is the complete elliptic integral of the fist kind. One can see that the integrand in Equation (3.81) has singularity as $r = r_0$ since $\mathbf{K}(1) = \infty$. Denoting the punch profile by function $f(r)$, the geometric relation that correlates the separation $h(r)$ and deformation $w(r)$ can be written as

$$h(r) = -\delta + w(r) + f(r) + z_0, \tag{3.82}$$

where δ is the penetration of the punch with respect to the zero force position $h(0) = z_0$. Since $\sigma(r) = -p(r)$, Equations (3.80-3.82) formulate the contact problem by three intercoupling equations with respect to three unknown functions $p(r)$, $h(r)$ and $w(r)$, whose solutions can be calculated numerically as follows.

Introducing non-dimensional parameters

$$x = \frac{2r}{R} - 1, \bar{H}(x) = \frac{h(r) - z_0}{z_0}, \bar{P}(\bar{H}) = p(h)\frac{z_0}{\Delta\gamma}, \bar{\Delta} = \frac{\delta}{z_0}, \overline{W}(x) = \frac{w(r)}{z_0}, \bar{F}(x) = \frac{f(r)}{R},$$

Equations (3.80-3.82) can be normalized to be

$$\bar{P}(\bar{H}) = \frac{8}{3}\left[\left(\frac{1}{1+\bar{H}}\right)^9 - \left(\frac{1}{1+\bar{H}}\right)^3\right], \tag{3.83}$$

$$\overline{W}(x) = \frac{2\lambda\eta}{\pi}\int_{-1}^{1}\frac{(x_0+1)\bar{P}(\bar{H}(x_0))}{x+x_0+2}\mathbf{K}\left(\frac{2\sqrt{(x+1)(x_0+1)}}{x+x_0+2}\right)\mathrm{d}x_0, \tag{3.84}$$

$$\bar{H}(x) = -\bar{\Delta} + \overline{W}(x) + \lambda\bar{F}(x), \tag{3.85}$$

where $\lambda = \frac{R}{z_0}$, $\eta = \frac{\Delta\gamma}{E^* z_0}$. The general strategy to calculate the singular integration in Equation (3.84) is to employ the *Gauss-Chebyshev* numerical quadrature [25, 26] which results in

$$\overline{W}(x_i^*) = \frac{4\lambda\eta}{(2n+1)}\sum_{k=1}^{n}\frac{\sqrt{1-x_k^2}(1+x_k)}{x_i^*+x_k+2}\bar{P}(\bar{H}(x_k))\mathbf{K}\left(\frac{2\sqrt{(x_i^*+1)(x_k+1)}}{x_i^*+x_k+2}\right), \tag{3.86}$$

where x_k and x_i^* are integration points and collocation points defined respectively by

$$x_k = \cos\left(\frac{2k-1}{2n+1}\pi\right), \quad (k = 1, 2, \cdots, n) \tag{3.87}$$

$$x_i^* = \cos\left(\frac{2i\pi}{2n+1}\right). \quad (i = 1, 2, \cdots, n) \tag{3.88}$$

Denoting

$$\overline{W}_i^* = \overline{W}(x_i^*),\ \bar{H}_k = \bar{H}(x_k),\ \bar{P}_k = \bar{P}(\bar{H}_k),\ \bar{F}_k = \bar{F}(x_k),$$

$$K_{ik} = \frac{4}{(2n+1)}\frac{\sqrt{1-x_k^2}(1+x_k)}{x_i^*+x_k+2}\mathbf{K}\left(\frac{2\sqrt{(x_i^*+1)(x_k+1)}}{x_i^*+x_k+2}\right),$$

Equations (3.83-3.85) thus can be discretized to be

$$\bar{P}_k = \frac{8}{3}\left[\frac{1}{(1+\bar{H}_k)^9} - \frac{1}{(1+\bar{H}_k)^3}\right], \tag{3.89}$$

$$\overline{W}_i^* = \lambda\eta\sum_{k=1}^{n}K_{ik}\bar{P}_k, \tag{3.90}$$

$$\bar{H}_k = -\bar{\Delta} + \overline{W}_k + \lambda\bar{F}_k. \tag{3.91}$$

For a given $\bar{\Delta}$, Equations (3.89-3.91) can be solved by numerical iterations process as shown in Figure 3.4.

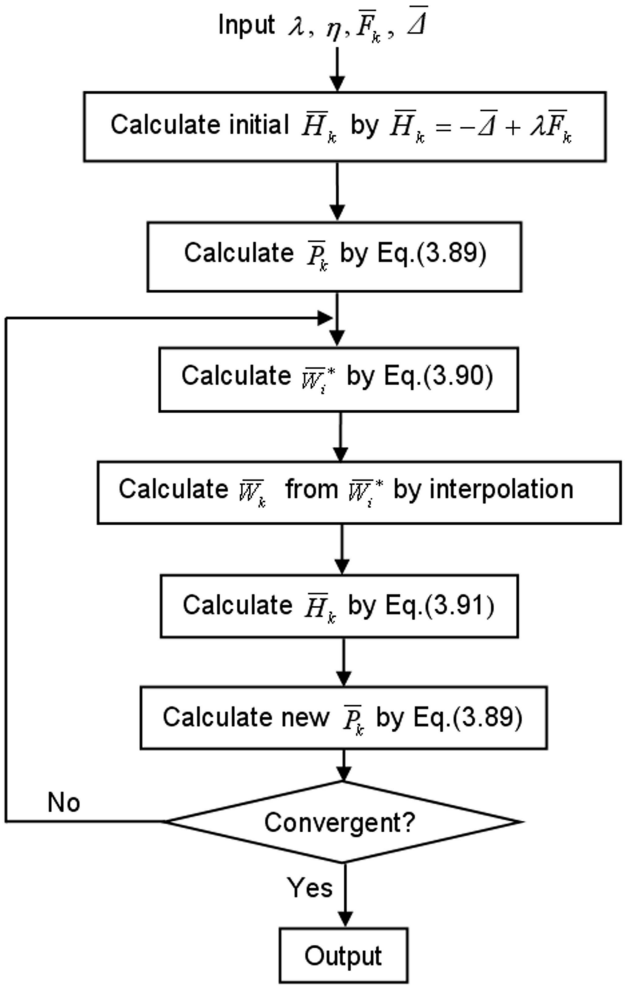

Figure 3.4.: Iteration process for solving Equations (3.89-3.91).

After getting the convergent normalized pressure $\bar{P}_k$, we then can calculate the load force via numerical integration

$$P = \int_0^R 2\pi r p(r)\mathrm{d}r = \frac{\pi R^2}{2}\int_{-1}^{1}(x+1)p(h(x))\mathrm{d}x = \frac{\pi^2 R^2 \Delta\gamma}{(2n+1)z_0}\sum_{k=1}^{n}(1+x_k)\sqrt{1-x_k^2}\bar{P}_k. \tag{3.92}$$

By repeating this process for a series of $\bar{\Delta}$'s, we can track the variation of the adhesion force as the punch approaches the substrate. Generally, this iteration process is initiated with a sufficiently small $\bar{\Delta}$ corresponding to a large separation, so that the interfacial tractions are weak and the calculation convergence is easy to get. Once convergence is

reached for a separation $\bar{\Delta}_n$, we let the punch have a small increment, arriving at a new $\bar{\Delta}_{n+1}$. Then a new round of iterations is triggered by taking the $\bar{H}_k$ that results from the previous round as the initial value. Similarly, we can simulate the adhesion force in a receding process just by changing the sign of the increment of $\bar{\Delta}$, as we will show in section 4.3.

3.2.3. Finite element simulation

The Green's function method introduced in the above is based on the half-space assumption which is appropriate only if the contact area is much smaller than the overall dimension of the contacting solids. Obviously, it is not always the case. If the contact area is comparable to the solid dimension, the solid deformation has to be calculated by using real numerical method (e.g. Finite Element Method). *Tahoe*[2] is such a finite element code that can fulfill this function via its specific cohesive surface elements. Since, most computational simulations in this thesis are performed on Tahoe, it is worthwhile to introduce some immediately relevant concepts in Tahoe here.

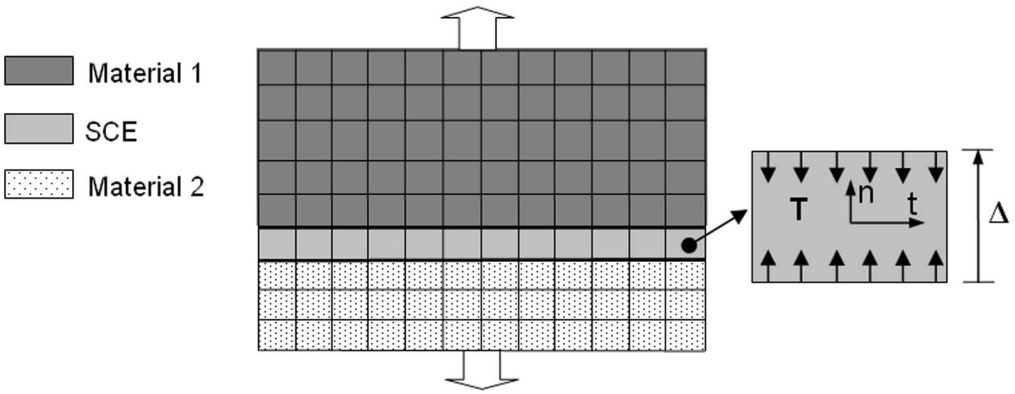

Figure 3.5.: Meshing implementation of an adhesion problem in Tahoe.

The process of solving an adhesion problem in Tahoe is also aimed to find the equilibrium point at which all the self-consistent relationships (Figure 3.2) are satisfied. What distinguishes it from the preceding methods is that in Tahoe the deformation is calculated by using finite element method and the surface-surface interaction is accomplished by the constitutive relation of the Surface Cohesive Elements (SCE). Consider an adhesion problem between two materials, Figure 3.5 schematically shows the meshing

[2]http://tahoe.ca.sandia.gov

implementation by Tahoe. Here, the elastic solids are simulated by the traditional finite elements, whereas the interface is modeled by the SCE with specific constitutive relation. Tahoe supports many SCE constitutive relations, including Tvergaard-Hutchinson model [100], Xu-Needleman model [103], Lennard-Jones model and etc. In the simulations presented in this thesis, we adopt the Tvergaard-Hutchinson model due to its simplicity and preservation of adhesion energy regardless of the separation direction. In the following, we will give a brief introduction to it.

Like any other SCE constitutive relations, Tvergaard-Hutchinson model also specifies a relationship between the traction vector $\mathbf{T}$ and the interface separation vector $\boldsymbol{\Delta}$ (Figure 3.5). The interface separation in Tvergaard-Hutchison model is characterized by a dimensionless scalar

$$\bar{\lambda} = \sqrt{\left(\frac{\Delta_{\mathrm{n}}}{\delta_{\mathrm{cn}}}\right)^2 + \left(\frac{\Delta_{\mathrm{t}}}{\delta_{\mathrm{ct}}}\right)^2},$$

where Δ_{n} and Δ_{t} are the components of $\boldsymbol{\Delta}$ in normal and tangential directions respectively; δ_{cn} and δ_{ct} are two parameters denoting the critical opening for complete failure. The potential function U is defined by

$$U(\bar{\lambda}) = \delta_{\mathrm{cn}} \int_0^{\bar{\lambda}} \varphi(\tilde{\lambda}) \mathrm{d}\tilde{\lambda}.$$

The force function $\varphi(\bar{\lambda})$ is taken to be tri-linear,

$$\varphi(\bar{\lambda}) = \begin{cases} \sigma_{\max}\bar{\lambda}/\Lambda_1, & (\bar{\lambda} < \Lambda_1) \\ \sigma_{\max}, & (\Lambda_1 < \bar{\lambda} < \Lambda_2) \\ \sigma_{\max}(1-\bar{\lambda})/(1-\Lambda_2), & (\Lambda_2 < \bar{\lambda} < 1) \end{cases}$$

with Λ_1 and Λ_2 being the values of $\bar{\lambda}$ at which the cohesive force stress reaches the peak $\sigma_{\max}$, as shown in Figure 3.6.

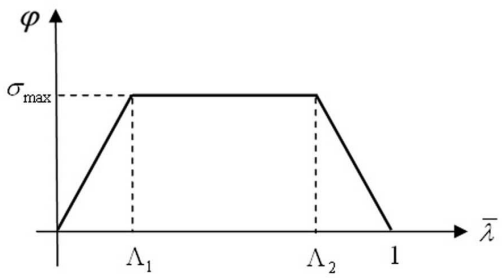

Figure 3.6.: Force function in Tvergaard-Hutchinson model.

Taking partial derivatives of the potential with respect to the normal and tangential separations respectively gives the normal and tangential tractions as

$$T_{\mathrm{n}} = \frac{\partial U}{\partial \Delta_{\mathrm{n}}} = \frac{\Delta_{\mathrm{n}}}{\delta_{\mathrm{cn}}} \frac{\varphi(\bar{\lambda})}{\bar{\lambda}}, \quad T_{\mathrm{t}} = \frac{\partial U}{\partial \Delta_{\mathrm{t}}} = \frac{\delta_{\mathrm{cn}}}{\delta_{\mathrm{ct}}} \frac{\Delta_{\mathrm{t}}}{\delta_{\mathrm{ct}}} \frac{\varphi(\bar{\lambda})}{\bar{\lambda}}.$$

It is clear that Tvergaard-Hutchinson model not only takes account of the normal tractions but also the tangential tractions. Knowledge of all five parameters δ_{cn}, δ_{ct}, $\sigma_{\max}$, Λ_1, Λ_2 completely determines the constitutive relation. The work of adhesion thus can be calculated by

$$\Delta\gamma = 0.5(1 + \Lambda_2 - \Lambda_1)\sigma_{\max}\delta_{\mathrm{cn}}.$$

For example, if we take $\sigma_{\max} = 10$ MPa, $\Lambda_1 = 0.1$, $\Lambda_2 = 0.9$, $\delta_{\mathrm{cn}} = \delta_{\mathrm{ct}} = 5$ nm, the work of adhesion can be immediately given by

$$\Delta\gamma = 0.5(1 + \Lambda_2 - \Lambda_1)\sigma_{\max}\delta_{\mathrm{cn}} = 45 \text{ mJ/m}^2.$$

Actually, what we have introduced above is just the two-dimensional Tvergaard-Hutchinson model. It is easy to extend it to three dimension by defining

$$\bar{\lambda} = \sqrt{\left(\frac{\Delta_{\mathrm{n}}}{\delta_{\mathrm{cn}}}\right)^2 + \left(\frac{\Delta_{\mathrm{t1}}}{\delta_{\mathrm{ct}}}\right)^2 + \left(\frac{\Delta_{\mathrm{t2}}}{\delta_{\mathrm{ct}}}\right)^2}$$

where Δ_{n}, Δ_{t1}, Δ_{t2} are components of $\boldsymbol{\Delta}$ in normal and two tangential directions of the mid-plane respectively. Under this circumstance, the tractions components are given by

$$T_{\mathrm{n}} = \frac{\partial U}{\partial \Delta_{\mathrm{n}}} = \frac{\Delta_{\mathrm{n}}}{\delta_{\mathrm{cn}}} \frac{\varphi(\bar{\lambda})}{\bar{\lambda}}, \; T_{\mathrm{t1}} = \frac{\partial U}{\partial \Delta_{\mathrm{t1}}} = \frac{\delta_{\mathrm{cn}}}{\delta_{\mathrm{ct}}} \frac{\Delta_{\mathrm{t1}}}{\delta_{\mathrm{ct}}} \frac{\varphi(\bar{\lambda})}{\bar{\lambda}}, \; T_{\mathrm{t2}} = \frac{\partial U}{\partial \Delta_{\mathrm{t2}}} = \frac{\delta_{\mathrm{cn}}}{\delta_{\mathrm{ct}}} \frac{\Delta_{\mathrm{t2}}}{\delta_{\mathrm{ct}}} \frac{\varphi(\bar{\lambda})}{\bar{\lambda}}.$$

In this chapter, we have mainly introduced the research methods, including the Hankel-transform-based approach, Green's function method and FEM (Finite Element Method). A frequent use of these approaches will be made in the subsequent chapters.

Chapter 4. Shape-insensitive optimal adhesion

Having introduced the necessary preliminaries, now let us turn our attention to the theme of this thesis. In this chapter, we will firstly consider the effect of surface shape on the adhesion strength. By investigating the adhesion strength for the power-law shape $z = r^n/nR^{n-1}$ $(n > 0)$, we will find that the adhesion strength between two solid surfaces is dependent on their geometric shapes. This result motivates us to seek for the optimal shape by which the adhesion strength can be maximized. A general methodology for determining the optimal shape is developed, by which various examples of optimal shapes are presented. However, optimal shape does not necessarily ensure spontaneous optimal adhesion. The condition for spontaneous optimal adhesion is investigated by exploring the variation of the adhesion force in an approaching/receding process between an optimal-shaped punch and a flat substrate.

4.1. Shape effect on adhesion strength

Recalling the classical adhesive contact theories such as JKR, DMT and M-D models, we note that the spheres in all these models are approximated by a parabola function $z = r^2/2R_i$ $(i = 1, 2)$, where R_1, R_2 are the radii of two spheres respectively. Under this circumstance, the pull-off force falls in the range between $\frac{3}{2}\pi R\Delta\gamma$ and $2\pi R\Delta\gamma$ with $R = (1/R_1 + 1/R_2)^{-1}$, depending on the Tabor number of the case. It should be of great interest to investigate the pull-off force for solids (or punches) with other profile shapes.

4.1.1. JKR-like solution for punch with power-law shape

Consider an axisymmetric elastic punch with profile $f(r/a)$ in frictionless contact with an elastic plane. According to the result of subsection 3.1.4, the stress underneath the

punch is given by

$$\sigma_{zz|z=0} = -\frac{E^*}{2a}\left[\frac{\chi(1)}{\sqrt{1-r^2/a^2}} - \int_{r/a}^{1}\frac{\chi'(\xi)}{\sqrt{\xi^2-r^2/a^2}}\mathrm{d}\xi\right], \quad (0 \le r \le a) \tag{4.1}$$

where

$$\chi(\xi) = \frac{2}{\pi}\left[\delta - \xi\int_0^{\xi}\frac{f'(s)\mathrm{d}s}{\sqrt{\xi^2-s^2}}\right], \quad E^* = \left[\frac{1-\nu_\mathrm{s}^2}{E_\mathrm{s}} + \frac{1-\nu_\mathrm{p}^2}{E_\mathrm{p}}\right]^{-1}, \tag{4.2}$$

with a being the radius of the contact region; E_p, ν_p, E_s, ν_s the Young's moduli and Poisson's ratios of punch and substrate, respectively. We can note that the stress in Equation (4.1) contains two parts: one is the compressive part with vanishing value at $r = a$ and the other is attractive part with an inverse-square-root singularity at the contact periphery $r = a$. This is quite similar to the JKR model. Applying Griffith's energy balance [45] to the singularity term at the contact edge leads to

$$K_\mathrm{I} = \lim_{r\to a}\sqrt{2\pi(a-r)}\sigma_{zz}(r) = -\frac{E^*\chi(1)\sqrt{\pi}}{2\sqrt{a}}, \tag{4.3}$$

$$\mathcal{G} = \frac{K_\mathrm{I}^2}{2E^*} = \frac{E^*\pi}{8a}[\chi(1)]^2, \tag{4.4}$$

$$\mathcal{G} = W_\mathrm{ad}, \tag{4.5}$$

where W_ad denotes the work of adhesion which is taken to be the surface energy $\Delta\gamma$ in the absence of bulk energy dissipation. Combining Equation (4.4) and Equation (4.5) yields

$$\chi(1) = -\sqrt{\frac{8\Delta\gamma a}{\pi E^*}}. \tag{4.6}$$

Inserting Equation (4.6) into Equation (4.1) and then integrating the contact stress over the entire contact area $r \le a$ give the applied pulling force as

$$F = \sqrt{8\pi a^3\Delta\gamma E^*} - 2aE^*\int_0^1\frac{s^2 f'(s)\mathrm{d}s}{\sqrt{1-s^2}}. \tag{4.7}$$

Equation (4.7) generalizes the JKR model to the adhesive contact between elastic bodies with arbitrary axisymmetric surface profiles.

Consider the power-law profile

$$z = f(r/a) = f(\rho) = \frac{r^n}{nR^{n-1}} = \frac{a^n\rho^n}{nR^{n-1}}, \quad (n > 0) \tag{4.8}$$

where R is the characteristic length and n is the shape index. Different n's lead to different surface shapes as shown in Figure 4.1. The case $n = 2$ corresponds to the parabola shape used in most of the classical contact mechanics models to approximate a sphere of radius R.

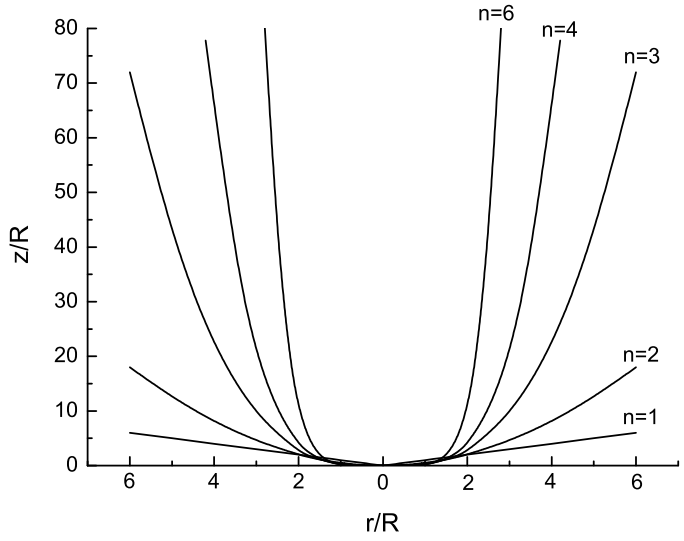

Figure 4.1.: Power-law surfaces $z = r^n/nR^n$. The parabolic case $n = 2$ is most widely used in classical contact mechanics theories.

Substituting Equation (4.8) into (4.7) and then making use of the integral

$$\int_0^1 \frac{s^{n+1}}{\sqrt{1-s^2}}\mathrm{d}s = \frac{\Gamma(1+n/2)}{(n+1)\Gamma(1/2+n/2)} \tag{4.9}$$

result in

$$F = \sqrt{8\pi a^3 E^* \Delta\gamma} - \frac{2\sqrt{\pi}a^{n+1}\Gamma(1+n/2)E^*}{(n+1)R^{n-1}\Gamma(1/2+n/2)}, \tag{4.10}$$

where $\Gamma(\cdot)$ is the Gamma function. Given E^*, $\Delta\gamma$, n, Equation (4.10) expresses the applied pulling force as a function of the contact radius a. The maximum of the pulling force occurs at the contact radius

$$a = a_\mathrm{c} = \left[\frac{3\Gamma(1/2+n/2)}{\sqrt{2}\Gamma(1+n/2)}\right]^{2/(2n-1)} R^{2(n-1)/(2n-1)}(\Delta\gamma/E^*)^{1/(2n-1)}, \tag{4.11}$$

which gives the pull-off force as

$$F^{\mathrm{f}} = \sqrt{2\pi}\left(\frac{2n-1}{n+1}\right)\left[\frac{3\Gamma(1/2+n/2)}{\sqrt{2}\Gamma(1+n/2)}\right]^{3/(2n-1)} E^{*(n-2)/(2n-1)} R^{3(n-1)/(2n-1)} \Delta\gamma^{(n+1)/(2n-1)}. \tag{4.12}$$

Equation (4.12) indicates that the pull-off force F^{f} depends on the index n and accordingly on the surface shape. For the parabolic case $n = 2$, the exponent of E^* in Equation (4.12) vanishes and the pull-off force is reduced to the JKR prediction $F^{\mathrm{f}} = \frac{3}{2}\pi R\Delta\gamma$. Therefore, the absence of Young's modulus in the JKR pull-off force can be attributed to the assumption of a parabolic surface profile. In the limit of $n = \infty$, the pull-off force is reduced to $F^{\mathrm{f}} = \sqrt{8\pi R^3 E^* \Delta\gamma}$, a solution associated with an external circumferential crack with radius R. Variation of the pull-off force with $RE^*/\Delta\gamma$ for different shape indexes n is shown in Figure 4.2. Further discussions of the effect of contact shapes on adhesion strength can be found in the work by Spolenak *et al.* [89].

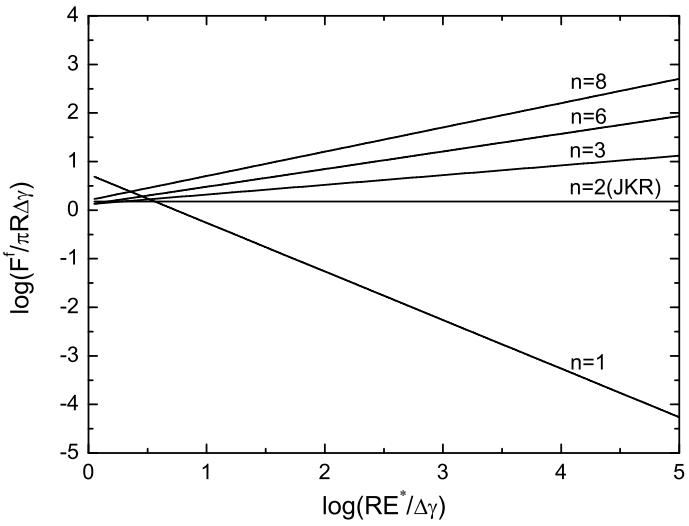

Figure 4.2.: Variation of the normalized pull-off force with parameter $RE^*/\Delta\gamma$ for different shape indexes n.

The shape effect on the adhesion suggests that the parabolic approximation in the JKR model may not always be appropriate to describe the behavior of adhesion between two spheres. In order to evaluate the possible error induced by such parabolic approximation in the JKR model, we calculate the pull-off force between a rigid sphere with exactly spherical shape and a flat elastic substrate.

4.1.2. JKR-like solution for exact sphere

Consider a rigid punch with exactly spherical profile

$$f(\rho) = R - \sqrt{R^2 - a^2\rho^2},\ \rho = r/a, \tag{4.13}$$

where R denotes the radius of the sphere. On substituting Equation (4.13) into (4.2), we have

$$\begin{aligned}
\chi(\xi) &= \frac{2}{\pi}\left[\delta - \xi\int_0^\xi \frac{f'(s)\mathrm{d}s}{\sqrt{\xi^2 - s^2}}\right] = \frac{2}{\pi}\left\{\delta - \xi\int_0^\xi \frac{a^2 s\mathrm{d}s}{\sqrt{R^2 - a^2 s^2}\sqrt{\xi^2 - s^2}}\right\} \\
&= \frac{2}{\pi}\left\{\delta - a\xi\left[\frac{1}{2}\ln\left(R^2/a^2 + \xi^2 - 2s^2 - 2\sqrt{R^2/a^2 - s^2}\sqrt{\xi^2 - s^2}\right)\Big|_0^\xi\right]\right\} \\
&= \frac{1}{\pi}\left\{2\delta - a\xi\ln\left[\frac{R + a\xi}{R - a\xi}\right]\right\}.
\end{aligned} \tag{4.14}$$

It follows that

$$\chi'(\xi) = -\frac{a}{\pi}\ln\left[\frac{R + a\xi}{R - a\xi}\right] - \frac{\xi}{\pi}\left[\frac{2R}{R^2/a^2 - \xi^2}\right]. \tag{4.15}$$

Substituting Equation (4.15) into (4.1) and then applying (4.6) give the contact stress as

$$\begin{aligned}
\sigma_{zz|z=0}(r) = \sqrt{\frac{2E^*\Delta\gamma}{\pi a}}\frac{1}{\sqrt{1 - r^2/a^2}} - \frac{E^*}{2\pi}\Bigg\{&\int_{r/a}^1 \ln\left[\frac{R + a\xi}{R - a\xi}\right]\frac{\mathrm{d}\xi}{\sqrt{\xi^2 - r^2/a^2}} \\
&+ \frac{2R}{a}\int_{r/a}^1 \frac{\xi\mathrm{d}\xi}{(R^2/a^2 - \xi^2)\sqrt{\xi^2 - r^2/a^2}}\Bigg\}.
\end{aligned} \tag{4.16}$$

Then the external load force can be calculated by integrating

$$\begin{aligned}
F =& 2\pi\int_0^a r\sigma_{zz|z=0}\mathrm{d}r \\
=& \sqrt{8\pi a^3 E^*\Delta\gamma} - \pi E^*\int_0^a r\mathrm{d}r\int_{r/a}^1 \ln\left[\frac{R + a\xi}{R - a\xi}\right]\frac{\mathrm{d}\xi}{\pi\sqrt{\xi^2 - r^2/a^2}} \\
&- \frac{2E^*R}{a}\int_0^a r\mathrm{d}r\int_{r/a}^1 \frac{\xi\mathrm{d}\xi}{(R^2/a^2 - \xi^2)\sqrt{\xi^2 - r^2/a^2}}.
\end{aligned} \tag{4.17}$$

Interchanging the integration order in Equation (4.17) gives rise to

$$
\begin{aligned}
F =& \sqrt{8\pi a^3 E^* \Delta\gamma} - a^2 E^* \int_0^1 \ln\left[\frac{R+a\xi}{R-a\xi}\right] \mathrm{d}\xi \int_0^\xi \frac{s\mathrm{d}s}{\sqrt{\xi^2 - s^2}} \\
& - 2aRE^* \int_0^1 \frac{\xi \mathrm{d}\xi}{(R^2/a^2 - \xi^2)} \int_0^\xi \frac{s\mathrm{d}s}{\sqrt{\xi^2 - s^2}} \\
=& \sqrt{8\pi a^3 E^* \Delta\gamma} - a^2 E^* \left[\frac{\xi R}{a} + \frac{1}{2}\left(\xi^2 - \frac{R^2}{a^2}\right) \ln\left(\frac{R+a\xi}{R-a\xi}\right)\right]_{|0}^{1} \\
& - 2aRE^* \left[\frac{R}{a}\tanh^{-1}\left(\frac{a}{R}\right) - 1\right] \\
=& \sqrt{8\pi a^3 E^* \Delta\gamma} - aRE^* \left[\left(\frac{a}{2R} - \frac{R}{2a}\right) \ln\left(\frac{R+a}{R-a}\right) + \frac{2R}{a}\tanh^{-1}\left(\frac{a}{R}\right) - 1\right]. \qquad (4.18)
\end{aligned}
$$

Denoting $\bar{a} = a/R$, Equation (4.18) can be normalized to be

$$
\frac{F}{\pi R\Delta\gamma} = \sqrt{\frac{8RE^*}{\pi\Delta\gamma}}\bar{a}^{3/2} - \frac{RE^*}{\pi\Delta\gamma}\left[\frac{(\bar{a}^2+1)}{2}\ln\left(\frac{1+\bar{a}}{1-\bar{a}}\right) - \bar{a}\right], \qquad (4.19)
$$

where Equation (A.17) has been used.

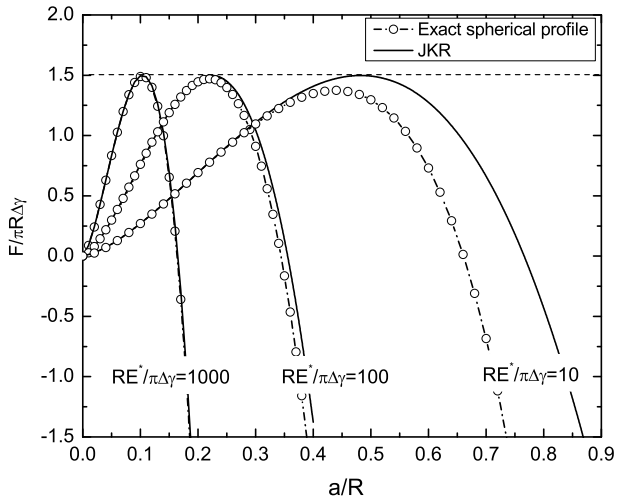

Figure 4.3.: Variation of adhesive force with the contact radius for different $RE^*/\pi\Delta\gamma$.

Figure 4.3 plots the variation of $F/\pi R\Delta\gamma$ as a function of a/R for various $RE^*/\pi\Delta\gamma$ in contrast to the JKR results. It can be seen that for larger $RE^*/\pi\Delta\gamma$, say 1000, parabola assumption exhibits a very good approximation to the spherical surface, whereas for the

case with small $RE^*/\pi\Delta\gamma$ considerable deviation occurs as the contact radius increases. Even so, the parabola is still a quite good approximation when the contact radius is small, say $a/R < 0.2$. Therefore, even in the JKR regime characterized by large Tabor number, JKR theory is applicable only when the contact area is small in comparison with the radius R. Another interesting observation from Figure 4.3 is that the pull-off force for the exact spheres varies with $RE^*/\pi\Delta\gamma$ instead of being an invariant $\frac{3}{2}\pi R\Delta\gamma$ as predicted by JKR theory. It is reconfirmed that the absence of Young's modulus in the pull-off force of JKR theory is just owing to the parabola approximation for the spherical profile.

4.1.3. JKR-like solution for a ring-shaped punch: numerical results

It will be also interesting to investigate the pull-off force between a rigid circular cylinder and an elastic substrate, as shown in Figure 4.4(a). The associated theoretical investigations in contact mechanics theory [38] show that it is not easy to get a simple expression for the adhesive force. Here we therefore develop a numerical method to compute the adhesive force between a rigid ring-shaped punch and an elastic substrate.

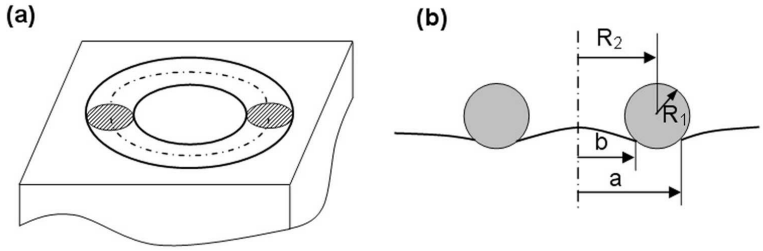

Figure 4.4.: Schematic of a rigid ring-shaped punch in contact with an elastic half-space substrate.

As shown in Figure 4.4(b), the outer and inner radii of the contact region is denoted by a and b. According to the Boussinesq's solution, the normal surface displacement of the elastic substrate (half-space) under the axisymmetric pressure $p(r)$ can be expressed in terms of integral as

$$w(r) = \frac{4}{\pi E^*}\int_b^a \frac{r_0 p(r_0)}{(r+r_0)}\mathbf{K}\left(\frac{2(r_0 r)^{1/2}}{r+r_0}\right)\mathrm{d}r_0, \tag{4.20}$$

where $\mathbf{K}(\cdot)$ is the complete elliptical integral of first kind and $E^* = E/(1-\nu^2)$ with E, ν being the Young's modulus and Poisson's ratio of the substrate.

JKR theory implies that the contact stress $p(r_0)$ tends to be infinite in a square root singular manner as r_0 approaches a^- and b^+. We therefore assume that $p(r_0)$ can be expressed as the product of a fundamental solution $[(1-r_0/a)(r_0/b-1)]^{-1/2}$ and an unknown regular function $\dfrac{a-b}{2\sqrt{ab}}\phi(r_0)$, i.e.,

$$p(r_0)=\frac{1}{\sqrt{(1-r_0/a)}\sqrt{(r_0/b-1)}}\frac{a-b}{2\sqrt{ab}}\phi(r_0). \tag{4.21}$$

Denoting

$$x_0=\frac{2(r_0-a)}{a-b}+1, \tag{4.22}$$

Equation (4.21) can be rewritten as

$$p\left(a+\frac{(a-b)(x_0-1)}{2}\right)=\frac{1}{\sqrt{1-x_0}\sqrt{1+x_0}}\phi\left(a+\frac{(a-b)(x_0-1)}{2}\right). \tag{4.23}$$

On substituting Equation (4.23) into Equation (4.20), we have

$$w(r)=\frac{2(a-b)}{\pi E^*}\int_{-1}^{1}\frac{1}{\sqrt{1-x_0^2}}\phi\left(a+\frac{(a-b)(x_0-1)}{2}\right)\frac{r_0}{r+r_0}\mathbf{K}\left(\frac{2(r_0r)^{1/2}}{r+r_0}\right)\mathrm{d}x_0. \tag{4.24}$$

By using *Gauss-Chebyshev* quadrature [25, 26], the integral in Equation (4.24) can be calculated numerically as

$$w(r_i')=\frac{2(a-b)}{nE^*}\sum_{k=1}^{n}\phi(r_k)\frac{r_k}{r_i'+r_k}\mathbf{K}\left(\frac{2(r_kr_i')^{1/2}}{r_i'+r_k}\right). \tag{4.25}$$

with integration points and collocation points given by

$$r_k=a+\frac{(a-b)(x_k-1)}{2},\ x_k=\cos\frac{(2k-1)\pi}{2n}\ (k=1,2,\cdots,n), \tag{4.26a}$$

$$r_i'=a+\frac{(a-b)(x_i'-1)}{2},\ x_i'=\cos\left(\frac{i\pi}{n}\right)\quad (i=1,2,\cdots,n-1). \tag{4.26b}$$

Letting

$$\varepsilon=\frac{b}{a},\ y=1+\frac{(1-\varepsilon)(x-1)}{2}, \tag{4.27}$$

Equation (4.25) can be recast into

$$w(ay_i') = \frac{2(1-\varepsilon)a}{nE^*}\sum_{k=1}^{n}\phi(r_k)\frac{y_k}{y_i'+y_k}\mathbf{K}\left(\frac{2(y_k y_i')^{1/2}}{y_i'+y_k}\right). \tag{4.28}$$

In addition, the square-root singularity of the contact stress at the contact edge suggests that

$$\lim_{r\to a^-} p(r) = -\frac{K_{\mathrm{I}}}{\sqrt{2\pi(a-r)}}, \quad \lim_{r\to b^+} p(r) = -\frac{K_{\mathrm{I}}}{\sqrt{2\pi(r-b)}}, \tag{4.29}$$

where stress intensity factor K_{I}, according to the Griffith fracture criterion, is given by

$$K_{\mathrm{I}} = \sqrt{2E^*\Delta\gamma},$$

with $\Delta\gamma$ being the adhesion energy. From Equation (4.26a), one can see that $r_1 \approx a$, $r_n \approx b$ for large n. Hence, combination of Equation (4.23) with Equation (4.29) leads to

$$\phi(r_1) = -\frac{\sqrt{2E^*\Delta\gamma}\sqrt{1+x_1}}{\sqrt{\pi a(1-\varepsilon)}}, \tag{4.30}$$

$$\phi(r_n) = -\frac{\sqrt{2E^*\Delta\gamma}\sqrt{1-x_n}}{\sqrt{\pi a(1-\varepsilon)}}, \tag{4.31}$$

Denoting

$$\Phi_k = \phi(r_k)\sqrt{\frac{a}{E^*\Delta\gamma}}, \; W_i = w(ay_i')\sqrt{\frac{E^*}{\Delta\gamma a}}, \tag{4.32}$$

Equations (4.30)(4.31)(4.28) then can be normalized to be

$$\Phi_1 = \phi(r_1)\sqrt{\frac{a}{E^*\Delta\gamma}} = -\sqrt{\frac{2(1+x_1)}{\pi(1-\varepsilon)}}, \tag{4.33}$$

$$\Phi_n = \phi(r_n)\sqrt{\frac{a}{E^*\Delta\gamma}} = -\sqrt{\frac{2(1-x_n)}{\pi(1-\varepsilon)}}, \tag{4.34}$$

$$W_i = \sum_{k=1}^{n} K_{ik}\Phi_k, \tag{4.35}$$

where

$$K_{ik} = \frac{2(1-\varepsilon)}{n}\frac{y_k}{y_i'+y_k}\mathbf{K}\left(\frac{2(y_k y_i')^{1/2}}{y_i'+y_k}\right). \tag{4.36}$$

On the other hand, the geometric compatibility within the contact region $b < r < a$ indicates that

$$w(r_i') = \delta - f(r_i'), \quad (i = 1, 2, \cdots, n-1) \tag{4.37}$$

where δ is the penetration of the punch tip and $f(r)$ is the function describing the profile of the punch. For the circular annulus, we have

$$f(r) = R_1 - \sqrt{R_1^2 - (r - R_2)^2}, \tag{4.38}$$

where R_1, R_2 are two principal radii at the annulus bottom, as shown in Figure 4.4(b). Denoting

$$\bar{\Delta} = \delta\sqrt{\frac{E^*}{\Delta\gamma a}},\ \bar{F}_i = f(r_i')\sqrt{\frac{E^*}{\Delta\gamma a}} = \sqrt{\frac{E^*}{\Delta\gamma a}}R_1\left[1 - \sqrt{1 - \left(\frac{ay_i'}{R_1} - \frac{R_2}{R_1}\right)^2}\right], \tag{4.39}$$

Equation (4.37) can be expressed in a normalized form as

$$W_i = \bar{\Delta} - \bar{F}_i. \tag{4.40}$$

On substituting Equation (4.40) into Equation (4.35), we have

$$\begin{bmatrix} \bar{\Delta} - \bar{F}_1 \\ \bar{\Delta} - \bar{F}_2 \\ \vdots \\ \bar{\Delta} - \bar{F}_{n-1} \end{bmatrix}_{(n-1)\times 1} = \begin{bmatrix} K_{11} & K_{12} & \cdots & K_{1n} \\ K_{21} & & & \\ \vdots & \ddots & & \vdots \\ K_{n-1,1} & & \cdots & K_{n-1,n} \end{bmatrix}_{(n-1)\times n} \begin{bmatrix} \Phi_1 \\ \Phi_2 \\ \vdots \\ \Phi_n \end{bmatrix}_{n\times 1}. \tag{4.41}$$

Given ε and n, in Equation (4.41), Φ_1, Φ_n and matrix K can be determined easily by Equations (4.33)(4.34)(4.36), respectively. So we have n unknown variables $\bar{\Delta}$, a, Φ_2, $\cdots$, Φ_{n-1} whereas $n-1$ equations. In order to solve these equations, an additional assumed condition is introduced that

$$a + b = a(1 + \varepsilon) = 2R_2,$$

namely,

$$a = \frac{2R_2}{1 + \varepsilon}. \tag{4.42}$$

This assumption is appropriate when the contact region is quite small in contrast to the radius R_1. Substituting Equation (4.42) into Equation (4.39) results in

$$\bar{F}_i = \frac{\varsigma\sqrt{1 + \varepsilon}}{\vartheta}\left[1 - \sqrt{1 - \vartheta^2\left[\frac{2y_i'}{(1 + \varepsilon)} - 1\right]^2}\right], \tag{4.43}$$

where

$$\varsigma = \sqrt{\frac{E^* R_2}{2\Delta\gamma}},\ \vartheta = \frac{R_2}{R_1}. \tag{4.44}$$

The externally applied force P then can be calculated as

$$P = 2\pi \int_b^a rp(r)\mathrm{d}r = \frac{4(1-\varepsilon)\pi^2 R_2}{n(1+\varepsilon)} \sqrt{\frac{E^* \Delta\gamma R_2}{2(1+\varepsilon)}} \sum_{k=1}^{n} y_k \Phi_k,$$

which can be normalized to be

$$\bar{P} = \frac{P}{\pi R_2 \Delta\gamma} = \frac{4\pi(1-\varepsilon)\varsigma}{n(1+\varepsilon)^{3/2}} \sum_{k=1}^{n} y_k \Phi_k. \tag{4.45}$$

Combination Equation (4.45) with Equation (4.41) results in

$$\begin{bmatrix} \bar{\Delta} - \bar{F}_1 \\ \bar{\Delta} - \bar{F}_2 \\ \vdots \\ \bar{\Delta} - \bar{F}_{n-1} \\ \bar{P} \end{bmatrix}_{n\times 1} = \begin{bmatrix} K_{11} & K_{12} & \cdots & K_{1n} \\ K_{21} & & & \\ \vdots & \ddots & & \vdots \\ K_{n-1,1} & & \cdots & K_{n-1,n} \\ \dfrac{4\pi\varsigma(1-\varepsilon)y_1}{n(1+\varepsilon)^{3/2}} & & \cdots & \dfrac{4\pi\varsigma(1-\varepsilon)y_n}{n(1+\varepsilon)^{3/2}} \end{bmatrix}_{n\times n} \begin{bmatrix} \Phi_1 \\ \Phi_2 \\ \vdots \\ \Phi_n \end{bmatrix}_{n\times 1}. \tag{4.46}$$

Given ε, ς, ϑ, in Equation (4.46) we have n unknown variables $\Phi_2, \cdots, \Phi_{n-1}$, $\bar{\Delta}$, $\bar{P}$ and

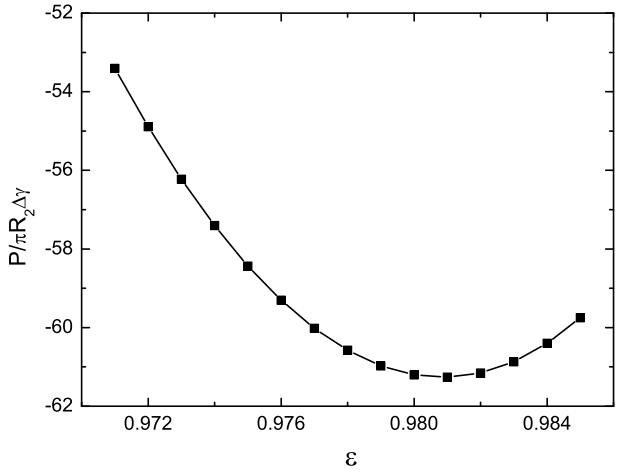

Figure 4.5.: Variation of the adhesive force with ε for a ring-shaped punch.

n equations. It can be solved by general linear algebra approach. For instance, taking $R_1 = 0.05$ μm, $R_2 = 0.25$ μm, $E = 1.0$ GPa, ν =0.3 and $\Delta\gamma = 10$ mJ/m^2, Figure 4.5 shows the variation of the adhesive force $P/\pi R_2\Delta\gamma$ as a function of ε. One can see that the pull-off force for such a ring-like punch is about $61\pi R_2\Delta\gamma$, which is much higher than $\frac{3}{2}\pi R_2\Delta\gamma$, the JKR value corresponding to a spherical punch with radius R_2.

4.2. Optimal shape

It has been pointed out that the pull-off force is dependent on the profile shape of the contact surfaces. For the adhesive contact between two elastic solids, the *adhesion strength* is commonly measured by the pull-off force per unit contact area. For the above-mentioned case associated with a power-law-shaped punch in contact with a plane, Equations (4.11-4.12) give the adhesion strength as

$$\begin{aligned}\sigma_{\mathrm{c}} &= F^{\mathrm{f}}/\pi {a_{\mathrm{c}}}^2 \\ &= \sqrt{\frac{2}{\pi}}\left(\frac{2n-1}{n+1}\right)\left[\frac{\sqrt{2}\Gamma(1+n/2)}{3\Gamma(1/2+n/2)}\right]^{1/(2n-1)} E^{*n/(2n-1)}\left(\frac{\Delta\gamma}{R}\right)^{(n-1)/(2n-1)},\end{aligned} \tag{4.47}$$

which is also a function of shape index n. In general, the adhesion strength given in Equation (4.47) is much smaller than the theoretical adhesion strength σ_{th} unless the characteristic size R is reduced to below a nanoscale threshold. Given the shape effect described in Equations (4.12, 4.47), we will advance further to see whether there exist surface shapes that can have the adhesion strength to reach the theoretical adhesion strength σ_{th}.

4.2.1. Definition of optimal shape

In conventional engineering, if two elastic bodies are jointed together (Figure 4.6a) by adhesion and then subjected to a pulling load, stress concentration is expected to occur near the edge of the joint. As the load increases, the intensity of stress concentration ultimately reaches a critical level to drive a crack to propagate and break the joint(Figure 4.6b). Under this circumstance, the carrying capacity of the joint is not used most efficiently because only a small fraction of material is highly stressed at any instant of loading, and failure occurs by incremental crack propagation. Clearly, in order to achieve the utmost adhesion strength, it is necessary to homogenize the distribution of the adhesive stress so as to achieve such an ideal scenario that at pull-off the stress

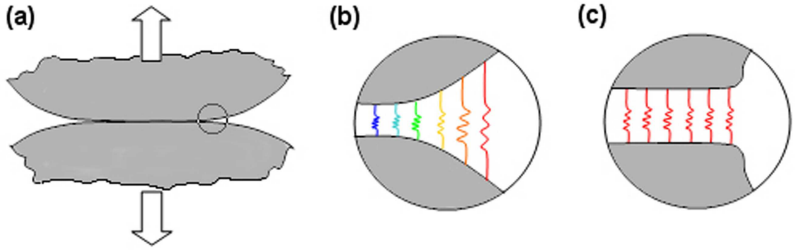

Figure 4.6.: Shape effect on the adhesive stress distribution.

is uniformly distributed over the contact region with magnitude equal to the theoretical adhesion strength σ_{th}(Figure 4.6c). We call this perfect adhesion state as *optimal adhesion*. In theory, it is always possible to achieve optimal adhesion via shape optimization. The *optimal shape* of two objects in adhesive contact over a surface area A is defined as such that the stress distribution is uniform and equal to the theoretical strength σ_{th} of adhesion at pull-off. In contrast to the *optimal shape*, the *singular shape* of two contacting objects over a surface area A is defined as such that the stress distribution is equivalent to the singular stress distribution associated with a crack external to the connecting area A at pull-off.

4.2.2. Methodology for determining the optimal shape

Now let us see how to determine the optimal shape and singular shape in practice. In Chapter 2, it has been addressed that the molecular adhesion force between two contacting surfaces relies on the surface-surface separation. There exists a unique separation h_{c} at which the maximum (theoretical) adhesion strength σ_{th} can be reached. For optimal shape, since the adhesive stress at pull-off is uniformly equal to the theoretical strength over the entire contact area, the separation between two surfaces are uniform and equal to h_{c}. That is, the deformed contact surfaces are complementary to each other, as shown in Figure 4.7(a).

Provided that the configuration in Figure 4.7(a) is known, to determine the optimal shape free of stress, a uniform pressure with magnitude equal to σ_{th} is applied separately on the contact region of the two objects which will deform as depicted in Figure 4.7(b). Superposing Figure 4.7(a) and (b) leads to the optimal shape before deformation. Here, we can use two arbitrary complementary surfaces to determine the undeformed configurations of the optimal shape by the superposition theorem in elasticity [96]. If the deformed configuration of the conforming interface (Figure 4.7a) is not prescribed in ad-

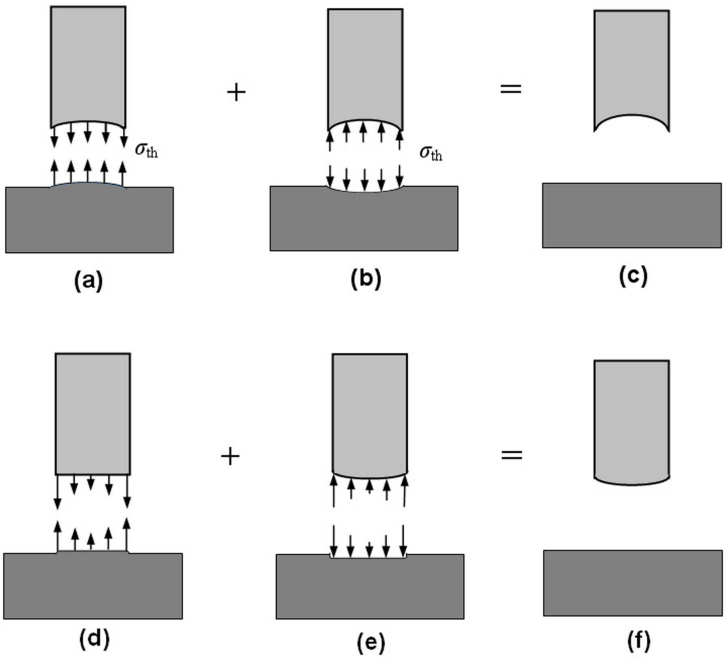

Figure 4.7.: Methodology for determining the optimal and singular shapes.

vance, we can in principle find an infinite number of solutions for the optimally shaped contacting surfaces which give rise to the theoretical pull-off force. The solution is unique only when the deformed configuration of the contact interface is known or the undeformed configuration of one solid is prescribed. For example, assuming that the undeformed shape of the substrate in Figure 4.7(c) is prescribed, we can find the optimal shape for the other solid as follows. Firstly, by applying the uniform tensile stress with magnitude σ_{th} on the substrate, we can calculate its deformed shape (Figure 4.7a). Then according to the conformability condition, the deformed contacting area shape for the other solid is determined. Superposing a uniform pressure with magnitude σ_{th} (Figure 4.7b) on this deformed configuration finally gives rise to the optimal shape of the solid free of stress (Figure 4.7c).

Similarly, Figure 4.7(d-e) describes the procedure that can be used to determine the singular shapes for the contacting objects. Instead of a uniform stress, now the adhesive stress has singular stress distribution associated with an external crack. Two contact surfaces are always bonded together before pull-off and therefore complementary to each other even though the adhesive stress is not uniform any more (Figure 4.7d). At first glance, it seems incompatible with the stress-separation law which implies that uniform separation gives rise to uniform stress. However, the presence of the singular

stress implies that the stress-separation law we face here is a delta-function, as shown in Figure 2.6(b). Under this circumstance, surface conformability or uniform separation does not necessarily lead to uniform stress.

The procedure illustrated in Figure 4.7 can be used as the methodology for determining the optimal shape and singular shape for general adhesive joint. A critical step in this methodology is to solve the boundary value problem defined in Figure 4.7(b) and (e). Assuming the deformation of the solids is small (linear elastic) at pull-off, the existence and uniqueness theorems of elasticity guarantee that the solution can be determined uniquely. Now let us apply the above-mentioned methodology to determine the optimal shapes for some special cases.

4.2.3. Optimal shape for frictionless adhesion

We first consider a case of a cylindrical fiber in contact with a half-space. Assuming that the half-space is flat, the optimal shape of the fiber tip is expected to maximize the adhesion strength. For simplicity, frictions are neglected at the moment.

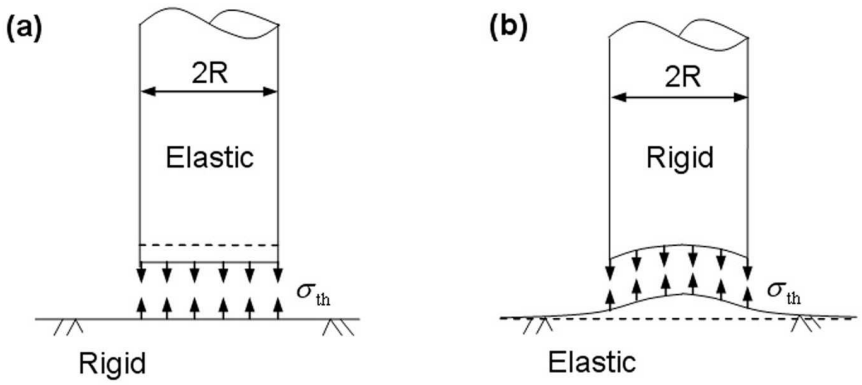

Figure 4.8.: Schematic illustrations of the optimal shapes for (a) elastic punch/rigid substrate and (b) rigid punch/elastic substrate.

If the fiber is elastic and the substrate is rigid. One can immediately realize that the optimal shape is flat because the tip shape of a flat-ended cylinder keeps flat under uniform traction (Figure 4.8a), which makes it conform to the rigid substrate plane. In this case, however, the singular shape can not be determined in closed form.

In contrast, if the fiber is rigid while the substrate is elastic, we find that the flat turns to be the singular shape. The associated pull-off force can be calculated according to

the Griffith condition for crack initiation as

$$F_{\text{crack}}^{\text{f}} = \sqrt{8\pi R^3 E^* \Delta\gamma} = \pi R^2 \sqrt{\frac{8}{\pi}} \left(\frac{E^* \Delta\gamma}{R} \right)^{1/2}, \tag{4.48}$$

where R is the radius of the cylinder fiber, E^* is defined as $E^* = E/(1-\nu^2)$, E, ν being Young's modulus and Poisson's ratio of the substrate, $\Delta\gamma$ is the work of adhesion. On the other hand, since the punch is nondeforming, the optimal-shaped tip must be conformal to the deformed elastic substrate under uniform traction σ_{th} (Figure 4.8b). Assuming the substrate is an elastic half-space, the surface deflection due to the uniform tensile σ_{th} acting on the circular area $r \leq R$ is given by [60]

$$w(r) = -\frac{4\sigma_{\text{th}} R}{\pi E^*} \mathbf{E}(r/R), \quad (r \leq R) \tag{4.49}$$

where $\mathbf{E}(\cdot)$ is the complete elliptic integral of the second kind. Therefore, the optimal shape of the rigid fiber can be described by shape function

$$f_{\text{opt}}(r) = \frac{\sigma_{\text{th}} R}{E^*} \left[\frac{4}{\pi} \mathbf{E}(r/R) - 2 \right], \quad (r \leq R) \tag{4.50}$$

where a constant has been added to make $f(0) = 0$. As shown in Figure 4.9, it is a concave with depth $0.726\sigma_{\text{th}} R/E^*$. Normally, the ratio σ_{th}/E^* is quite small $(1 - 2\%)$

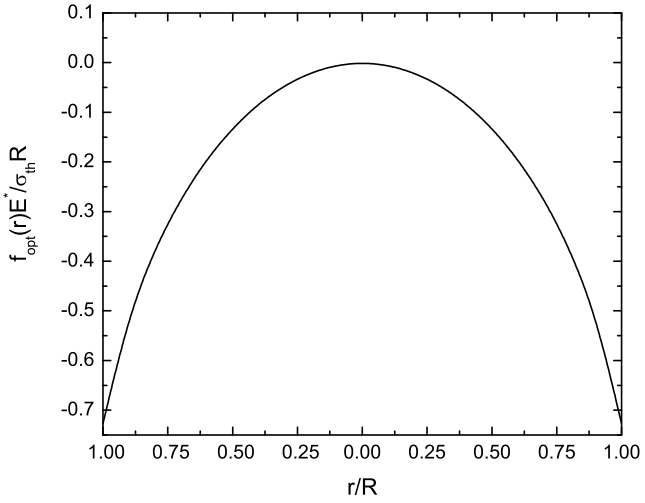

Figure 4.9.: Optimal shapes for rigid punch in contact with a planar elastic substrate.

and so is the concave depth, suggesting that the difference of the optimal shape and singular shape is small. Clearly, the pull-off force associated with the optimal shape is

$$F^{\mathrm{f}}_{\mathrm{opt}} = \pi R^2 \sigma_{\mathrm{th}}. \tag{4.51}$$

In fact, Equations (4.48)(4.51) also apply to an elastic fiber on a rigid substrate when E^* is interpreted as the modulus of the fiber. More generally, for an elastic fiber with Young's modulus E_{f} and Poisson's ratio ν_{f} in contact with an elastic substrate with Young's modulus E_{s} and Poisson's ratio ν_{s}, the pull-off force associated with the singular shape would still be given by Equation (4.48) if E^* is properly generalized according to

$$\frac{1}{E^*} = \frac{1-\nu_{\mathrm{f}}^2}{E_{\mathrm{f}}} + \frac{1-\nu_{\mathrm{s}}^2}{E_{\mathrm{s}}}.$$

The pull-off force for the optimal shape is always defined by Equation (4.51).

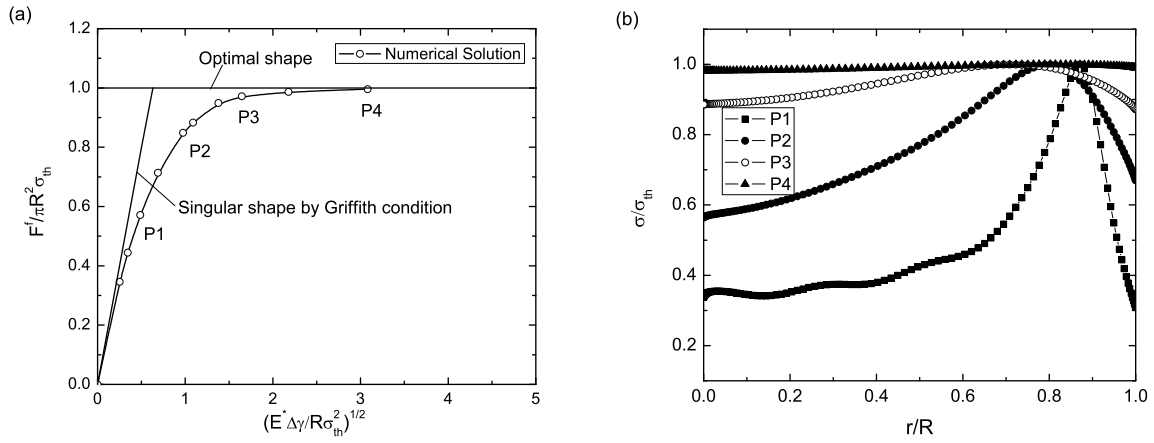

Figure 4.10.: Saturation of adhesion strength for the singular-shaped punch. (a) The variation of the normalized pull-off force with the nondimensional parameter $(E^*\Delta\gamma/R\sigma_{\mathrm{th}}^2)^{1/2}$. (b)The distribution of the adhesive stress along the contact radius for various punch radii.

Figure 4.10(a) plots the normalized adhesive strength $F^{\mathrm{f}}/\pi R^2\sigma_{\mathrm{th}}$ as a function of the non-dimensional parameter $(E^*\Delta\gamma/R\sigma_{\mathrm{th}}^2)^{1/2}$. The predictions of Equation (4.48) and (4.51) are plotted as two straight solid lines labeled by "Singular shape by Griffith condition" and "Optimal shape" respectively. In addition, we used the numerical Green's function method developed in subsection 3.2.2 to study the pull-off force associated with a rigid singular-shaped fiber in contact with an elastic substrate. The computational results of the pull-off force for the singular shape, as shown in Figure 4.10(a), agrees

well with the prediction by Griffith criterion for large fiber sizes but asymptotically approaches the theoretical adhesion strength as the fiber size decreases. This is because the theoretical strength is the upper limit of adhesion. The Griffith condition assumes that failure always occurs by crack propagation, i.e. a crack is assumed to nucleate at the edge of the contact and propagates to break the joint. This assumption breaks down for very small fibers. The results of Figure 4.10(a) shows that the theoretical adhesion strength can be achieved in two ways: The first is by accurately adopting the optimal shape of the tip of the fiber and the second is by reducing the diameter of the fiber. If theoretical strength is achieved, failure occurs no longer by crack propagation, but by a uniform detachment over the entire contact region. For very small sizes, the condition for crack propagation can not be satisfied before the theoretical strength is reached. The calculated pull-off force associated with the singular shape shows a smooth transition between two failure modes: crack propagation at large sizes and uniform detachment at small sizes. Figure 4.10(b) shows the distribution of adhesive traction at pull-off for the singular shape with different punch sizes, corresponding to the four date points in Figure 4.10(a). It is quite clear that the adhesive traction becomes more and more uniform as the fiber size decreases, eventually becoming uniform at a critical size.

On the other hand, at macroscopic sizes the pull-off force is quite sensitive to the variation in the tip shape of the fiber. For example, taking $\Delta\gamma = 10$ mJ/m^2, $\sigma_{\text{th}} = 20$ MPa and $E^* = 1$ GPa (the case of a keratinous fiber in contact with a rigid substrate) and fiber radius equal to 1 mm, the pull-off force for the optimal shape is estimated to be 62.8 N and that for the singular shape is only 0.5 N. The design of optimal shape, although theoretically feasible, is unrealizable in practice at macroscopic scale. Interestingly, Figure 4.11 shows that the difference between the adhesive strength of the optimal shape and that of the singular shape decreases as the size of the fiber is reduced. At the critical size

$$R_{\text{cr}} = \frac{8}{\pi}\frac{E^*\Delta\gamma}{\sigma_{\text{th}}^2}, \tag{4.52}$$

the strength of the singular shape predicted by Equation (4.48) becomes equal to that of the optimal shape predicted by Equation (4.51). Taking $\Delta\gamma = 10$ mJ/m^2, $\sigma_{\text{th}} = 20$ MPa and $E^* = 1$ GPa, we estimate $R_{\text{cr}} \approx 64$ nm. From these results we can conclude that the sensitivity of adhesion strength to tip geometry of the fiber decreases as the fiber diameter is reduced, and a robust design of optimal adhesion becomes possible around a critical size at which the pull-off force is no longer sensitive to variations in tip geometry. This length scale is around 100 nanometers, suggesting that the nanometer size of the fibrillar ultra-structure (spatula) of gecko and many insects may be the

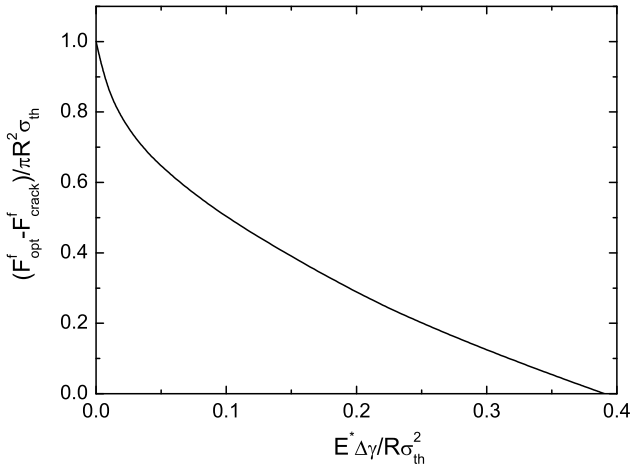

Figure 4.11.: The shape sensitivity of adhesion strength. As $E^*\Delta\gamma/R\sigma_{\rm th}^2$ increases, or the punch radius decreases, the difference between the adhesive strength of the singular shape and that of the optimal shape decrease, eventually vanishes at the critical length on the order of 100 nm.

result of optimization for reliable and optimal adhesion. It has recently [32] been shown that the nanometer size of mineral particles in bone-like biological materials may have been selected to ensure optimum fracture strength and maximum tolerance of crack-like flaws. The present result shows that the nanoscale dimension may play a crucial role in achieving reliable adhesion in a fibrillar structure, agreeing with the recently discovered fact that adhesion strength can be enhanced by splitting the contact area [1, 2].

The optimal adhesion strength described here can be compared with the JKR solution for a fiber having radius of curvature R at the tip in contact with a flat surface. The ratio of the optimal solution to that of JKR is

$$\frac{F^{\rm f}_{\rm opt}}{F^{\rm f}_{\rm JKR}} = \frac{2}{3}\frac{R\sigma_{\rm th}}{\Delta\gamma}. \tag{4.53}$$

Taking $\Delta\gamma = 10$ mJ/m^2, $\sigma_{\rm th} = 20$ MPa, this ratio is evaluated to be as large as 10^6 for a fiber of radius around 1 mm and 10^3 for that around 1 μm. Therefore, a huge magnification of pull-off force can be achieved by modification of the tip shape (shape optimization). Depending on animal species and convenience, optimal adhesion could be achieved by a combination of size reduction and shape optimization. The smaller the size, the less important the shape. At large sizes, the optimal adhesion could still be

achieved if the shape could be manufactured to a sufficiently high precision.

So far, our discussion about optimal shape has always been limited in the frictionless case. Generally, owing to the asymmetry of two solids with respect to the interface, either in material or in structure, interfacial friction will occur between two surfaces. Is it still possible to find the optimal shape in the presence of friction stresses? Will the friction force affect the optimal shape drastically or slightly? To answer these questions, the concept of optimal shape will be discussed in the following within the context of frictional adhesion [105].

4.2.4. Optimal shape for frictional adhesion

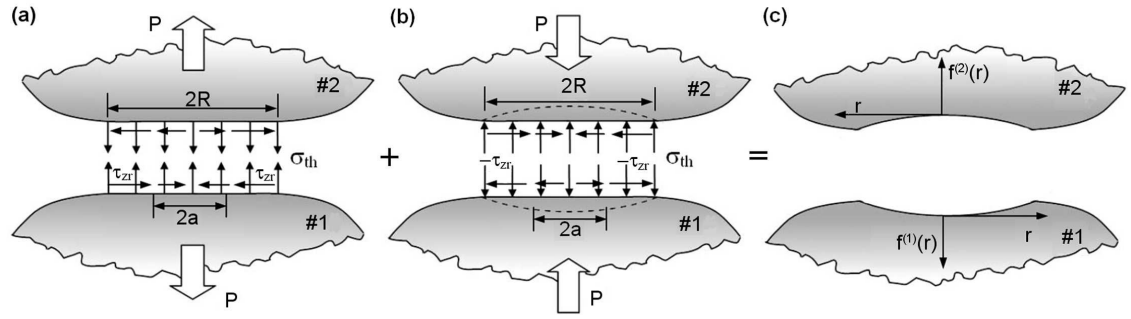

Figure 4.12.: Methodology for determining the optimal shapes for adhesive binding of two elastic bodies over a prescribed contact area. (a) The optimal-shaped surfaces should achieve conformal contact at pull-off with uniform normal traction equal to the theoretical strength of interactive forces. Tangential traction exists if the contact interface has finite shear strength. (b) Superposition of a uniform pressure σ_{th} and inverse shear stress $-\tau_{zr}$ over the contact region results in the optimal shapes under traction-free conditions, as depicted in (c).

Consider two axisymmetric elastic bodies in adhesive binding over a circular patch of radius R (Figure 4.12). The interactive forces are restricted to within the binding region in which the optimal shapes will be determined. The contact interface is assumed to have a finite shear strength τ_{f} so that shear traction also exists along the interface, as shown in Figure 4.12(a). Two special cases, $\tau_{\mathrm{f}} = 0$ or $\tau_{\mathrm{f}} = \infty$, correspond to frictionless or perfectly bonded conditions respectively. We seek to determine optimal surface shapes that lead to uniform separation h_{c} corresponding to uniform adhesion stress σ_{th} at pull-off.

Since the contact interface has finite shear strength, the tractions within the contact region at pull-off consist of a uniform tension σ_{th} and a distribution of shear stress $\tau_{zr}(r)$. If the deformed configuration of the contact interface is known (Figure 4.12a), the optimal shape can be determined via superposition of a uniform pressure σ_{th} and an inverse

tangential traction field $-\tau_{zr}(r)$ over the contact region, as depicted in Figure 4.12(b). Superposition of Figures 4.12(a) and (b) then gives the optimal surface shapes free of tractions, as in Figure 4.12(c). The reasoning in the above indicates that it is the gap between the two solid surfaces which determines the pull-off force. For two contacting bodies, there should be a family of optimal shapes that all lead to the same theoretical adhesion strength as long as the gap between the two surfaces is appropriately selected. In other words, the solution of the optimal shapes is unique only when the deformed configuration of the contact interface is prescribed. The superposition procedure in Figure 4.12 provides a useful strategy to determine the optimal shapes as soon as the distribution of shear stress $\tau_{zr}(r)$ at pull-off is known.

Following the classical contact models, we assume that the contact region is much smaller than the characteristic dimensions of both contacting bodies so that each body can be effectively treated as an elastic half-space. Slip between the contacting surfaces is allowed whenever the local shear stress reaches the interfacial shear strength τ_{f}. This causes the contact region to be divided into a slipping region ($a \leq r \leq R$) in which the shear stress is equal to τ_{f} and a non-slipping region ($0 \leq r \leq a$) in which the relative tangential displacement between the two surfaces vanishes (Figure 4.13a,b).

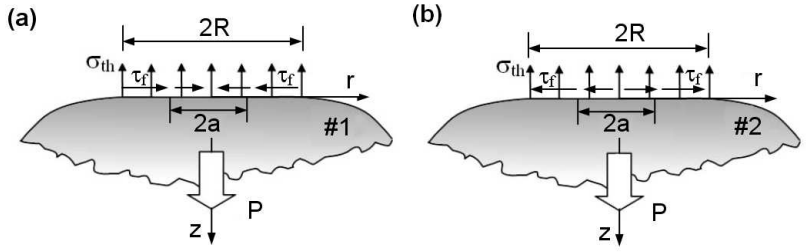

Figure 4.13.: Surface tractions on optimal-shaped solids #1 and #2 at pull-off. The normal traction is uniform and equal to the theoretical adhesion strength σ_{th}. The shear traction is equal to the interfacial shear strength τ_{f} in the slipping region while slip vanishes in the non-slipping region. The directions of shear stresses in (a) and (b) are plotted assuming positive Dundurs' constant.

According to the general solution to the axisymmetric problems associated with an elastic half-space (see subsection 3.1.2), the displacement and stress components on the half-space surface (Figure 4.13a,b) can be expressed in terms of Hankel transform as

$$\begin{cases} u_r^{(1)}(r,0) = \dfrac{1}{2G_1}\mathcal{H}_1\left[\xi^{-1}C_1;\xi\to r\right] \\ \tau_{zr}^{(1)}(r,0) = -\mathcal{H}_1\left[(1-2\nu_1)A_1 + C_1;\xi\to r\right] \\ \sigma_{zz}^{(1)}(r,0) = -\mathcal{H}_0\left[(2-2\nu_1)A_1 + C_1;\xi\to r\right], \end{cases} \tag{4.54a}$$

for solids #1 and

$$\begin{cases} u_r^{(2)}(r,0) = \dfrac{1}{2G_2}\mathcal{H}_1\left[\xi^{-1}C_2;\xi\to r\right] \\ \tau_{zr}^{(2)}(r,0) = -\mathcal{H}_1\left[(1-2\nu_2)A_2 + C_2;\xi\to r\right] \\ \sigma_{zz}^{(2)}(r,0) = -\mathcal{H}_0\left[(2-2\nu_2)A_2 + C_2;\xi\to r\right], \end{cases} \tag{4.54b}$$

for solids #2, where G_1, G_2 are shear moduli, ν_1, ν_2 are Poisson's ratios and A_1, A_2, C_1, C_2, generally functions of ξ, will be determined through the boundary conditions; superscripts '(1)'and '(2)' are used to denote the quantities pertaining to the materials #1 and #2. Note that the components in Equations (4.54a,b) are referred to the respective coordinate system of each material with z-axis pointing into the material (Figure 4.13a,b).

It is clear that when two solids are brought into contact, the continuity of traction across the interface requires

$$\sigma_{zz}^{(1)}(r,0) = \sigma_{zz}^{(2)}(r,0),\ \tau_{zr}^{(1)}(r,0) = -\tau_{zr}^{(2)}(r,0). \tag{4.55}$$

For an optimal-shaped surface, the stresses at pull-off should satisfy

$$\sigma_{zz}^{(1)}(r,0) = \sigma_{zz}^{(2)}(r,0) = T(r/a), \quad (0 \le r < \infty) \tag{4.56}$$

$$\tau_{zr}^{(1)}(r,0) = -\tau_{zr}^{(2)}(r,0) = Q(r/a), \quad (a \le r < \infty) \tag{4.57}$$

where

$$T(r/a) = \begin{cases} \sigma_{\text{th}}, & (0 \le r \le R) \\ 0, & (R < r < \infty) \end{cases} \tag{4.58}$$

and

$$Q(r/a) = \begin{cases} \tau_{\text{f}}, & (a \le r \le R) \\ 0, & (R < r < \infty) \end{cases} \tag{4.59}$$

Substituting Equations (4.54a,b) into Equation (4.55), one can obtain the relationship between functions A_1, C_1 and A_2, C_2 as

$$(2-2\nu_1)A_1 + C_1 = (2-2\nu_2)A_2 + C_2, \tag{4.60}$$

$$(1-2\nu_1)A_1 + C_1 = -(1-2\nu_2)A_2 - C_2. \tag{4.61}$$

Eliminating A_2 in Equations (4.60) and (4.61), one can express C_2 in terms of A_1 and

C_1 as

$$C_2 = -\left[\frac{A_1}{2}(\kappa_1\kappa_2 - 1) + \kappa_2 C_1\right], \tag{4.62}$$

where $\kappa_i \equiv 3 - 4\nu_i$ $(i = 1, 2)$. Similarly, by using Equation (4.54a) boundary conditions of Equations (4.56) and (4.57) can be rewritten in terms of Hankel transforms as

$$-\mathcal{H}_0[(2 - 2\nu_1)A_1 + C_1; \xi \to r] = T(r/a), \quad (0 \le r < \infty) \tag{4.63}$$

$$-\mathcal{H}_1[(1 - 2\nu_1)A_1 + C_1; \xi \to r] = Q(r/a). \quad (a \le r < \infty) \tag{4.64}$$

On the other hand, in the non-slipping region the displacement continuity indicates

$$u_r^{(1)}(r, 0) - u_r^{(2)}(r, 0) = 0. \quad (0 \le r \le a) \tag{4.65}$$

Substituting the expression for $u_r^{(1)}$ and $u_r^{(2)}$ of Equations (4.54a,b) into (4.65) and then invoking Equation (4.62) lead to

$$\mathcal{H}_1\left[\xi^{-1}(C_1 + \omega A_1); \xi \to r\right] = 0, \quad (0 \le r \le a) \tag{4.66}$$

where

$$\omega = \frac{(\kappa_1\kappa_2 - 1)G_1}{2(G_2 + G_1\kappa_2)}. \tag{4.67}$$

Denoting

$$\psi(\xi) = A_1(\xi/a), \quad \phi(\xi) = C_1(\xi/a), \tag{4.68}$$

Equations (4.63) (4.64) and (4.66) then can be normalized to be

$$\mathcal{H}_0\left[(2 - 2\nu_1)\psi(\xi) + \phi(\xi); \xi \to \rho\right] = -a^2 T(\rho), \quad (\rho \ge 0) \tag{4.69a}$$

$$\mathcal{H}_1\left[(1 - 2\nu_1)\psi(\xi) + \phi(\xi); \xi \to \rho\right] = -a^2 Q(\rho), \quad (\rho \ge 1) \tag{4.69b}$$

$$\mathcal{H}_1\left[\xi^{-1}[\phi(\xi) + \omega\psi(\xi)]; \xi \to \rho\right] = 0, \quad (0 \le \rho < 1) \tag{4.69c}$$

where $\rho = r/a$. With Equation (4.58), inversion of Equation (4.69a) yields

$$(2 - 2\nu_1)\psi(\xi) + \phi(\xi) = -aR\sigma_{\text{th}}\frac{J_1(R\xi/a)}{\xi}. \tag{4.70}$$

Inserting Equation (4.70) back into Equations (4.69b,c) to eliminate function $\phi(\xi)$ yields

$$\mathcal{H}_1\left[\xi^{-1}\psi(\xi);\xi\to\rho\right]=\frac{a^2\sigma_{\rm th}\rho}{2[\omega-(2-2\nu_1)]},\quad(0\le\rho<1) \tag{4.71a}$$

$$\mathcal{H}_1\left[\psi(\xi);\xi\to\rho\right]=a^2Q(\rho)-aR\sigma_{\rm th}\mathcal{H}_1\left[\frac{J_1(R\xi/a)}{\xi};\xi\to\rho\right].\quad(\rho\ge1) \tag{4.71b}$$

Equation (4.71b) suggests that function $\psi(\xi)$ must have the form

$$\psi(\xi)=-aR\sigma_{\rm th}\frac{J_1(R\xi/a)}{\xi}+\bar{\psi}(\xi), \tag{4.72}$$

where $\bar{\psi}(\xi)$ is determined, according to Equations (4.71a,b), by dual integral equations

$$\mathcal{H}_1\left[\xi^{-1}\bar{\psi}(\xi);\xi\to\rho\right]=\frac{a^2\sigma_{\rm th}\beta\rho}{2},\quad(0\le\rho<1) \tag{4.73a}$$

$$\mathcal{H}_1\left[\bar{\psi}(\xi);\xi\to\rho\right]=a^2Q(\rho),\quad(\rho\ge1) \tag{4.73b}$$

with

$$\beta=\frac{(\kappa_1-1)/G_1-(\kappa_2-1)/G_2}{(\kappa_1+1)/G_1+(\kappa_2+1)/G_2} \tag{4.74}$$

being the Dundurs' constant [24]. Without loss of generality, we assume $\beta\ge0$, i.e. $(\kappa_1-1)/G_1\ge(\kappa_2-1)/G_2$. It can be seen that Equations (4.73a,b) is just a special case of standard dual integral equations (3.46-3.47) with $\mathrm{F}_1(\rho)=a^2\sigma_{\rm th}\beta\rho/2$ and $\mathrm{G}_2(\rho)=a^2Q(\rho)$. Following Equation (3.48), the solution to Equations (4.73a,b) is given by

$$\bar{\psi}(\xi)=\frac{2}{\pi}a^2\tau_{\rm f}\int_1^{R/a}t\ln\left[\frac{R}{at}+\sqrt{\frac{R^2}{a^2t^2}-1}\right]\sin(\xi t)\mathrm{d}t+\frac{2}{\pi}a^2\sigma_{\rm th}\beta\left(\frac{\sin\xi}{\xi^2}-\frac{\cos\xi}{\xi}\right). \tag{4.75}$$

Meanwhile, the shear stress $\tau_{zr}^{(1)}(r,0)$, according to Equations (4.54a, 4.68, 4.72), can be expressed in terms of $\bar{\psi}(\xi)$ as

$$\tau_{zr}^{(1)}(r,0)=\frac{1}{a^2}\mathcal{H}_1\left[\bar{\psi}(\xi);\xi\to\rho\right]. \tag{4.76}$$

Substituting Equation (4.75) into (4.76) yields

$$\tau_{zr}^{(1)}(r,0)=\frac{2}{\pi}\left[\sigma_{\rm th}\beta\frac{\rho}{\sqrt{1-\rho^2}}-\frac{\tau_{\rm f}\rho}{\sqrt{1-\rho^2}}\int_1^{R/a}\frac{(t^2-1)^{1/2}\mathrm{d}t}{t^2-\rho^2}\right],\quad(0\le\rho<1) \tag{4.77}$$

where integral (A.8) and relationship (A.15) (see Appendix A) have been used.

The continuity of the frictional stress at the edge of the slipping region $\rho = 1$ requires that the stress singularity in Equation (4.77) vanishes, i.e.,

$$\lim_{\rho\to 1}\frac{2}{\pi}\sqrt{1-\rho}\left[\sigma_{\mathrm{th}}\beta\frac{\rho}{\sqrt{1-\rho^2}}-\frac{\tau_{\mathrm{f}}\rho}{\sqrt{1-\rho^2}}\int_1^{R/a}\frac{(t^2-1)^{1/2}\mathrm{d}t}{t^2-\rho^2}\right]=0. \tag{4.78}$$

This yields the following equation

$$\frac{R+\sqrt{R^2-a^2}}{a}=\exp\left(\frac{\sigma_{\mathrm{th}}\beta}{\tau_{\mathrm{f}}}\right), \tag{4.79}$$

to determine the size of the non-slipping region as a function of the Dundurs' constant β, the theoretical adhesion strength σ_{th} and the interfacial shear strength τ_{f}. Taking $\tau_{\mathrm{f}} = \sigma_{\mathrm{th}}$, $\nu_1 = 0.3$, $G_2 \to \infty$ in Equation (4.79) yields $a \approx 0.96R$. The variation of a/R with $\sigma_{\mathrm{th}}\beta/\tau_{\mathrm{f}}$ is plotted in Figure 4.14. As expected, a approaches 0 in the limit of frictionless contact $\tau_{\mathrm{f}} \to 0$ ($\sigma_{\mathrm{th}}\beta/\tau_{\mathrm{f}} \to \infty$) and approaches R in the limit of perfect bonding $\tau_{\mathrm{f}} \to \infty$ ($\sigma_{\mathrm{th}}\beta/\tau_{\mathrm{f}} = 0$).

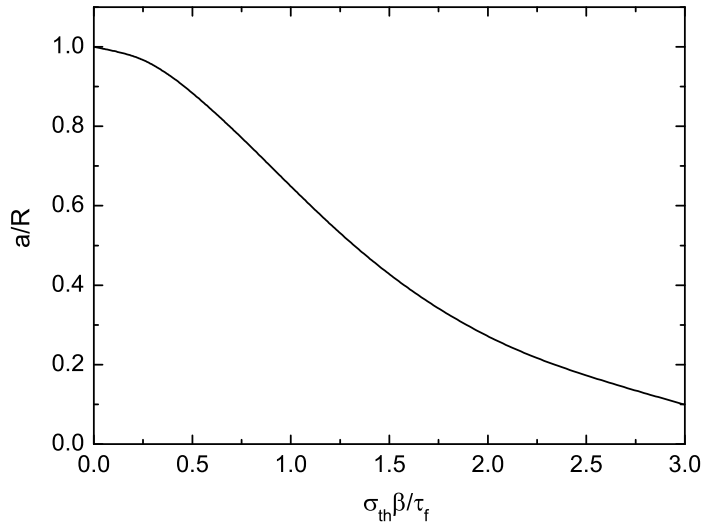

Figure 4.14.: The normalized radius of the non-slipping region a/R as a function of the dimensionless parameter $\sigma_{\mathrm{th}}\beta/\tau_{\mathrm{f}}$

Substituting Equation (4.79) into (4.77) gives rise to the shear stress in the non-

slipping region ($0 \le r < a$) as

$$\tau_{\mathrm{f}}^{(1)}(r,0) = \frac{2}{\pi}\frac{\rho\tau_{\mathrm{f}}}{\sqrt{1-\rho^2}}\left[\ln\left(R/a+\sqrt{R^2/a^2-1}\right) - \int_1^{R/a}\frac{(t^2-1)^{1/2}\mathrm{d}t}{t^2-\rho^2}\right]. \tag{4.80}$$

Since

$$\ln\left(R/a+\sqrt{R^2/a^2-1}\right) = \int_1^{R/a}\left(t^2-1\right)^{-1/2}\mathrm{d}t,$$

Equation (4.80) can be reduced further to be

$$\begin{aligned}
\tau_{zr}^{(1)}(r,0) &= \frac{2}{\pi}\frac{\rho\tau_{\mathrm{f}}}{\sqrt{1-\rho^2}}\left[\int_1^{R/a}\frac{\mathrm{d}t}{(t^2-1)^{1/2}} - \int_1^{R/a}\frac{(t^2-1)^{1/2}\mathrm{d}t}{t^2-\rho^2}\right] \\
&= \frac{2}{\pi}\rho\tau_{\mathrm{f}}\sqrt{1-\rho^2}\int_1^{R/a}\frac{1}{(t^2-\rho^2)\sqrt{t^2-1}}\mathrm{d}t \\
&= \frac{\tau_{\mathrm{f}}}{\pi}\sqrt{1-\rho^2}\int_1^{R/a}\left[\frac{1}{(t-\rho)\sqrt{t^2-1}} - \frac{1}{(t+\rho)\sqrt{t^2-1}}\right]\mathrm{d}t \\
&= \frac{\tau_{\mathrm{f}}}{\pi}\left[\sin^{-1}\frac{Rr-a^2}{(R-r)a} + \sin^{-1}\frac{Rr+a^2}{(R+r)a}\right],
\end{aligned} \tag{4.81}$$

where integrals of (A.9) and (A.10) have been applied. Taking $a = 0.96R$, friction stress is plotted in Figure 4.15. As expected, the friction stress distribution is continuous at the edge of the non-slipping region $r = a$.

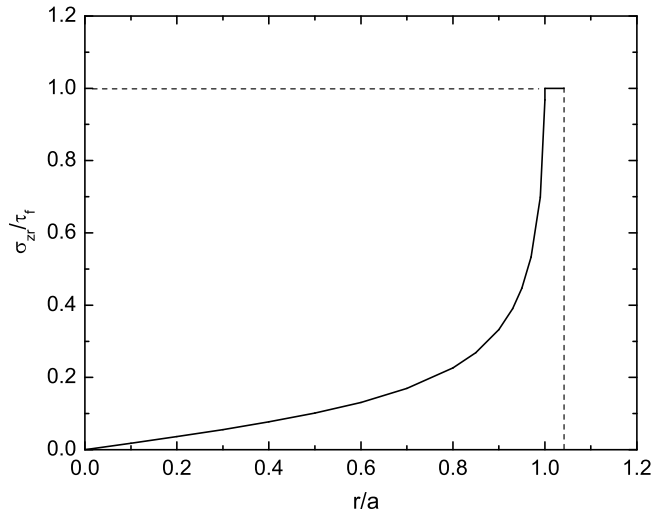

Figure 4.15.: Distribution of friction stress within the contact region for $a/R = 0.96$.

The normal and tangential tractions applied on the contact area now can be summarized as follows,

$$\sigma_{zz}^{(1)}(r,0) = \sigma_{zz}^{(2)}(r,0) = \sigma_{\text{th}}, \quad (0 \le r \le R) \tag{4.82a}$$

$$\tau_{zr}^{(1)}(r,0) = -\tau_{zr}^{(2)}(r,0) = \frac{\tau_{\text{f}}}{\pi}\left[\sin^{-1}\frac{Rr-a^2}{(R-r)a} + \sin^{-1}\frac{Rr+a^2}{(R+r)a}\right], \quad (0 \le r < a) \tag{4.82b}$$

$$\tau_{zr}^{(1)}(r,0) = -\tau_{zr}^{(2)}(r,0) = \tau_{\text{f}}, \quad (a \le r \le R) \tag{4.82c}$$

The associated surface displacements in the normal direction is calculated [60]

$$\begin{aligned} u_z^{(1)}(r,0) = &-\frac{4\sigma_{\text{th}}R}{\pi E_1^*}\mathbf{E}\left(\frac{r}{R}\right) - \frac{2(\kappa_1-1)\tau_{\text{f}}(R-a)}{\pi(\kappa_1+1)E_1^*} \\ &- \frac{2(\kappa_1-1)\tau_{\text{f}}a}{\pi^2(\kappa_1+1)E_1^*}\left[\pi - \frac{r}{a}\sin^{-1}\frac{Rr-a^2}{(R-r)a}\right. \\ &\left.-\frac{r}{a}\sin^{-1}\frac{Rr+a^2}{(R+r)a} - 2\frac{R}{a}\sin^{-1}\sqrt{\frac{a^2-r^2}{R^2-r^2}}\right], \quad (0 \le r < a) \end{aligned} \tag{4.83a}$$

$$u_z^{(1)}(r,0) = -\frac{4\sigma_{\text{th}}R}{\pi E_1^*}\mathbf{E}\left(\frac{r}{R}\right) - \frac{2(\kappa_1-1)\tau_{\text{f}}(R-r)}{\pi(\kappa_1+1)E_1^*}, \quad (a \le r \le R) \tag{4.83b}$$

$$\begin{aligned} u_z^{(2)}(r,0) = &-\frac{4\sigma_{\text{th}}R}{\pi E_2^*}\mathbf{E}\left(\frac{r}{R}\right) + \frac{2(\kappa_2-1)\tau_{\text{f}}(R-a)}{\pi(\kappa_2+1)E_2^*} \\ &+ \frac{2(\kappa_2-1)\tau_{\text{f}}a}{\pi^2(\kappa_2+1)E_2^*}\left[\pi - \frac{r}{a}\sin^{-1}\frac{Rr-a^2}{(R-r)a}\right. \\ &\left.-\frac{r}{a}\sin^{-1}\frac{Rr+a^2}{(R+r)a} - 2\frac{R}{a}\sin^{-1}\sqrt{\frac{a^2-r^2}{R^2-r^2}}\right], \quad (0 \le r < a) \end{aligned} \tag{4.84a}$$

$$u_z^{(2)}(r,0) = -\frac{4\sigma_{\text{th}}R}{\pi E_2^*}\mathbf{E}\left(\frac{r}{R}\right) + \frac{2(\kappa_2-1)\tau_{\text{f}}(R-r)}{\pi(\kappa_2+1)E_2^*}, \quad (a \le r \le R) \tag{4.84b}$$

where $\mathbf{E}(\cdot)$ is the complete elliptic integral of the second kind and $E_1^* = E_1/(1-\nu_1^2)$, $E_2^* = E_2/(1-\nu_2^2)$. Following the superposition procedure outlined in Figure 4.12, the optimal shapes for solid #1 and #2 are obtained as

$$\begin{aligned} f_{\text{opt}}^{(1)}(r) = &\frac{\sigma_{\text{th}}R}{E_1^*}\left[\frac{4}{\pi}\mathbf{E}\left(\frac{r}{R}\right) - 2\right] + \frac{2(\kappa_1-1)\tau_{\text{f}}a}{\pi^2(\kappa_1+1)E_1^*}\left[\frac{2R}{a}\sin^{-1}\left(\frac{a}{R}\right) - \frac{r}{a}\sin^{-1}\frac{Rr-a^2}{(R-r)a}\right. \\ &\left.-\frac{r}{a}\sin^{-1}\frac{Rr+a^2}{(R+r)a} - \frac{2R}{a}\sin^{-1}\sqrt{\frac{a^2-r^2}{R^2-r^2}}\right] + \tilde{f}(r), \quad (0 \le r < a) \end{aligned} \tag{4.85a}$$

$$\begin{aligned} f_{\text{opt}}^{(1)}(r) = &\frac{\sigma_{\text{th}}R}{E_1^*}\left[\frac{4}{\pi}\mathbf{E}\left(\frac{r}{R}\right) - 2\right] + \frac{2(\kappa_1-1)\tau_{\text{f}}a}{\pi^2(\kappa_1+1)E_1^*}\left[\frac{2R}{a}\sin^{-1}\left(\frac{a}{R}\right) - \frac{r\pi}{a}\right] + \tilde{f}(r), \\ &(a \le r \le R) \end{aligned} \tag{4.85b}$$

$$f_{\text{opt}}^{(2)}(r) = \frac{\sigma_{\text{th}} R}{E_2^*}\left[\frac{4}{\pi}\mathbf{E}\left(\frac{r}{R}\right) - 2\right] - \frac{2(\kappa_2-1)\tau_{\text{f}} a}{\pi^2(\kappa_2+1)E_2^*}\left[\frac{2R}{a}\sin^{-1}\left(\frac{a}{R}\right) - \frac{r}{a}\sin^{-1}\frac{Rr-a^2}{(R-r)a}\right.$$
$$\left. -\frac{r}{a}\sin^{-1}\frac{Rr+a^2}{(R+r)a} - \frac{2R}{a}\sin^{-1}\sqrt{\frac{a^2-r^2}{R^2-r^2}}\right] - \tilde{f}(r), \quad (0 \le r < a) \tag{4.86a}$$

$$f_{\text{opt}}^{(2)}(r) = \frac{\sigma_{\text{th}} R}{E_2^*}\left[\frac{4}{\pi}\mathbf{E}\left(\frac{r}{R}\right) - 2\right] - \frac{2(\kappa_2-1)\tau_{\text{f}} a}{\pi^2(\kappa_2+1)E_2^*}\left[\frac{2R}{a}\sin^{-1}\left(\frac{a}{R}\right) - \frac{r\pi}{a}\right] - \tilde{f}(r),$$
$$(a \le r \le R) \tag{4.86b}$$

where $\tilde{f}(r)$ is an arbitrary function representing the deformed configuration of the contact interface at pull-off. Equations (4.85a,b) and (4.86a,b) define the optimal shapes for adhesive binding of two elastic bodies over the circular patch ($0 \le r \le R$). The second term of each equation corresponds to the effect of finite interfacial shear strength. Since the pull-off force only depends on the summation $f_{\text{opt}}^{(1)}(r) + f_{\text{opt}}^{(2)}(r)$, an arbitrary function $\tilde{f}(r)$ has been included without affecting the optimized adhesion strength.

It therefore suffices to consider the special solution when the deformed contact area at pull-off is a perfectly flat circular patch, namely, $\tilde{f}(r) = 0$. A few special cases can be discussed to give some insight into the problem. In the frictionless limit of $\tau_{\text{f}} = 0$ or $\beta = 0$, Equations (4.85a,b) and (4.86a,b) are reduced to be

$$f_{\text{FL}}^{(1)}(r) = \frac{\sigma_{\text{th}} R}{E_1^*}\left[\frac{4}{\pi}\mathbf{E}\left(\frac{r}{R}\right) - 2\right], \quad (0 \le r \le R) \tag{4.87a}$$

$$f_{\text{FL}}^{(2)}(r) = \frac{\sigma_{\text{th}} R}{E_2^*}\left[\frac{4}{\pi}\mathbf{E}\left(\frac{r}{R}\right) - 2\right]. \quad (0 \le r \le R) \tag{4.87b}$$

In the perfect bonding limit of $\tau_{\text{f}} \to \infty$, rearranging Equation (4.79) as

$$\tau_{\text{f}} = \frac{\sigma_{\text{th}}\beta}{\ln\left[\frac{R+\sqrt{R^2+a^2}}{a}\right]}, \tag{4.88}$$

substituting Equation (4.88) into Equations (4.85a,b) (4.86a,b) and then letting lead to the optimal shape as

$$f_{\text{PB}}^{(1)}(r) = \frac{\sigma_{\text{th}} R}{E_1^*}\left[\frac{4}{\pi}\mathbf{E}\left(\frac{r}{R}\right) - 2\right] + \frac{4(\kappa_1-1)\beta\sigma_{\text{th}} R}{(\kappa_1+1)\pi^2 E_1^*}\left[\sqrt{1-r^2/R^2} - 1\right], \tag{4.89a}$$

$$f_{\text{PB}}^{(2)}(r) = \frac{\sigma_{\text{th}} R}{E_2^*}\left[\frac{4}{\pi}\mathbf{E}\left(\frac{r}{R}\right) - 2\right] - \frac{4(\kappa_2-1)\beta\sigma_{\text{th}} R}{(\kappa_2+1)\pi^2 E_2^*}\left[\sqrt{1-r^2/R^2} - 1\right]. \tag{4.89b}$$

Since

$$\beta = \frac{(\kappa_1 - 1)/G_1 - (\kappa_2 - 1)/G_2}{(\kappa_1 + 1)/G_1 + (\kappa_2 + 1)/G_2},\ \frac{\kappa_1 - 1}{\kappa_1 + 1} = \frac{1 - 2\nu_1}{2(1 - \nu_1)},\ \frac{\kappa_2 - 1}{\kappa_2 + 1} = \frac{1 - 2\nu_2}{2(1 - 2\nu_2)},$$

for positive Poisson's ratios, the largest deviation between the perfect bonding solution (4.89a,b) and the frictionless solution (4.87a,b) occurs when $\beta = \dfrac{\kappa_1 - 1}{\kappa_1 + 1} = \dfrac{\kappa_2 - 1}{\kappa_2 + 1} = \dfrac{1}{2}$, in which case

$$f_{\mathrm{PB}}^{(1)}(r) = \frac{\sigma_{\mathrm{th}} R}{E_1^*}\left[\frac{4}{\pi}\mathbf{E}\left(\frac{r}{R}\right) - 2\right] + \frac{\sigma_{\mathrm{th}} R}{\pi^2 E_1^*}\left[\sqrt{1 - r^2/R^2} - 1\right], \tag{4.90a}$$

$$f_{\mathrm{PB}}^{(2)}(r) = \frac{\sigma_{\mathrm{th}} R}{E_2^*}\left[\frac{4}{\pi}\mathbf{E}\left(\frac{r}{R}\right) - 2\right] - \frac{\sigma_{\mathrm{th}} R}{\pi^2 E_2^*}\left[\sqrt{1 - r^2/R^2} - 1\right]. \tag{4.90b}$$

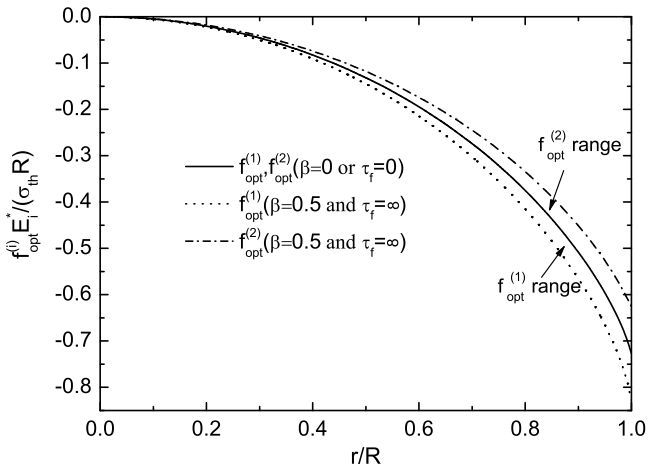

Figure 4.16.: The normalized optimal shapes for frictionless and perfect bonding contact interfaces. For other cases with moderate frictional effect, the optimal shapes must lies in the ranges confined by them. In this plot, the deformed configuration of the contact interface is assumed to be a perfectly flat circular patch. An arbitrary function can be added to modify both surfaces at the same time without affecting the adhesion strength.

For other cases with moderate frictional effect, the optimal shapes $f_{\mathrm{opt}}^{(1)}$, $f_{\mathrm{opt}}^{(2)}$ must lie in the ranges confined by Equations (4.87a, 4.90a) and (4.87b, 4.90b) respectively, as shown in Figure 4.16. The relative difference between the frictionless solution and perfect bonding solution

$$\mathfrak{R} = \left|\frac{f_{\mathrm{PB}}^{(i)}(r) - f_{\mathrm{FL}}^{(i)}(r)}{f_{\mathrm{FL}}^{(i)}(r)}\right| = \frac{\sqrt{1 - r^2/R^2} - 1}{\pi^2\left[4\mathbf{E}(r/R)/\pi - 2\right]},\quad (i = 1,\ 2) \tag{4.91}$$

is plotted in Figure 4.17 as a function of r/R. The result indicates that the effect of interfacial shear strength can cause up to 14% variation in the optimal shape.

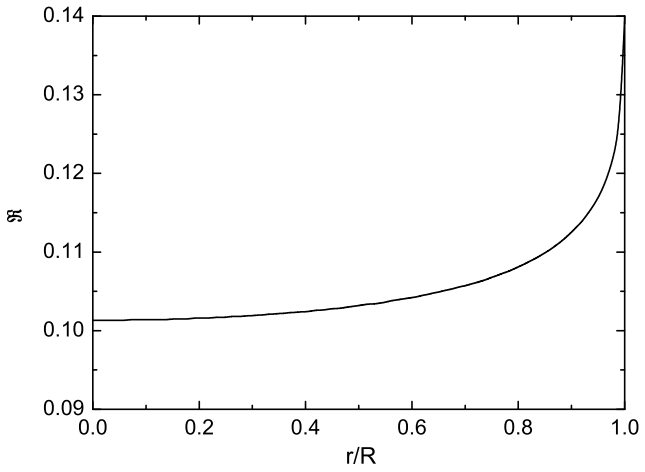

Figure 4.17.: The relative difference between the optimal shapes for frictionless and perfect bonding contact interfaces as a function of r/R.

4.2.5. Optimal shape for fiber cluster

In the above, our discussion on the optimal shape has been just focused on a single fiber. In practice, adhesions involving multiple fibers tend to occur in concert. Under this circumstance, the deformation of the substrate within one contacting region will be affected by the tractions applied on the neighboring regions. Therefore a different optimal shape is needed to achieve the optimal adhesion provided that the fibers are separated not too faraway from one another. In this section, we will discuss the optimal shape for a rigid fiber cluster contacting with an elastic substrate. Let us start with the two-dimensional case.

Two-dimensional array:

As shown in Figure 4.18, a 2D (two-dimensional) fiber array is in contact with a plane substrate. All the fibers are assumed identical and periodically separated by spacing $2L$. For simplicity, frictions are ignored. What we are interested in is the optimal shape of the fiber tips by which optimal adhesion can be achieved.

Obviously, if the fibers are elastic and substrate is rigid, the optimal shape is flat as

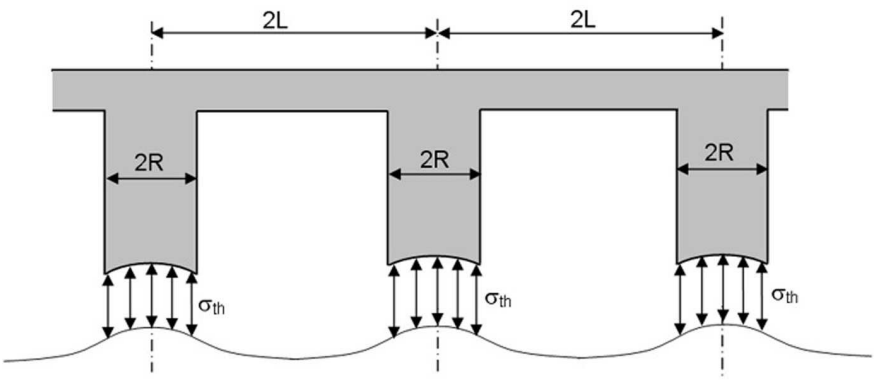

Figure 4.18.: Schematic illustration of 2D fiber array.

we have discussed for the single fiber case. Now let us focus our attention on the case of rigid fibers on elastic substrate. Like the single fiber case, the optimal shape for the fiber array should be conformal to the deformed shape of the elastic substrate under tractions, as shown in Figure 4.18. To evaluate the deformation of the substrate, we first consider the surface displacement produced by a concentrated force of intensity F per unit length distributed in y-axis (out-plane) and acting in a direction normal to the substrate surface (Figure 4.19a). According to the Boussinesq's solution, the normal displacement of the surface can be given by

$$u_z(r,0) = w(r) = \frac{2F}{\pi E^*} \ln r + C, \tag{4.92}$$

where r measures the distance from the loaded point, C is a constant and E^* is the elastic modulus of the substrate defined by $E^* = E/(1-\nu^2)$. Therefore, for an array of such concentrated forces applied periodically on the substrate surface by spacing $2L$ (Figure 4.19b), the normal displacement of the surface can be calculated by summing all the contributions as

$$\begin{aligned} w(r) &= \frac{2F}{\pi E^*} \ln r + \sum_{n=1}^{\infty} \frac{2F}{\pi E^*} \ln(2nL + r) + \sum_{n=1}^{\infty} \frac{2F}{\pi E^*} \ln(2nL - r) + C, \\ &= \frac{2F}{\pi E^*} \left[\ln r + \sum_{n=1}^{\infty} \ln\left(4n^2L^2 - r^2\right) \right] + C. \quad (r \le L) \end{aligned} \tag{4.93}$$

The surface displacement produced by an array of uniform stresses σ_{th} acting period-

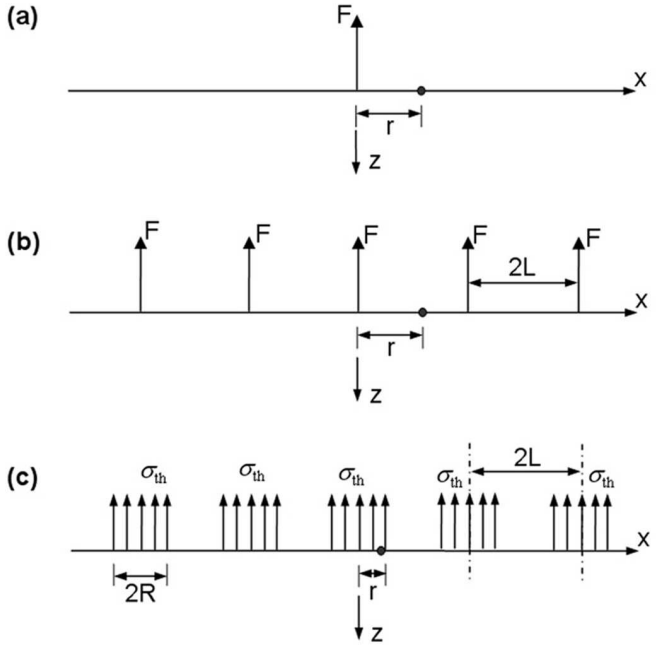

Figure 4.19.: Displacement due to (a) concentrated (line) force (b) periodic concentrated forces (c) periodic tractions.

ically on the substrate can be calculated as

$$
\begin{aligned}
w(r) &= \frac{2\sigma_{\text{th}}}{\pi E^*}\left\{\int_{-R}^{R}\ln|r-r_0| + \sum_{n=1}^{\infty}\ln\left[4n^2L^2-(r-r_0)^2\right]\right\}\mathrm{d}r_0 + C, \quad (r \le R \le L) \\
&= \frac{2\sigma_{\text{th}}}{\pi E^*}\left[(R+r)\ln(R+r)+(R-r)\ln(R-r)-2R\right] \\
&+ \frac{2\sigma_{\text{th}}}{\pi E^*}\sum_{n=1}^{\infty}\left[(2nL+R+r)\ln(2nL+R+r)-(2nL+r-R)\ln(2nL+r-R)\right] \\
&+ \frac{2\sigma_{\text{th}}}{\pi E^*}\sum_{n=1}^{\infty}\left[(2nL+R-r)\ln(2nL+R-r)-(2nL-r-R)\ln(2nL-r-R)\right] + C,
\end{aligned}
\tag{4.94}
$$

where R is the half-width of the stress loading (Figure 4.19c). Considering that the optimal shape of the fiber tip must be conformal to the deformed substrate at pull-off, we have

$$
\begin{aligned}
f_{\text{opt}}(r) = &-\frac{2\sigma_{\text{th}}}{\pi E^*}\left[R\ln\left(\frac{R^2-r^2}{R^2}\right)+r\ln\left(\frac{R+r}{R-r}\right)\right] \\
&-\frac{2\sigma_{\text{th}}}{\pi E^*}\sum_{n=1}^{\infty}\left[R\ln\left(\frac{(2nL+r)^2-R^2}{(2nL)^2-R^2}\right)+(2nL+r)\ln\left(\frac{2nL+r+R}{2nL+r-R}\right)-2nL\ln\left(\frac{2nL+R}{2nL-R}\right)\right] \\
&-\frac{2\sigma_{\text{th}}}{\pi E^*}\sum_{n=1}^{\infty}\left[R\ln\left(\frac{(2nL-r)^2-R^2}{(2nL)^2-R^2}\right)+(2nL-r)\ln\left(\frac{2nL-r+R}{2nL-r-R}\right)-2nL\ln\left(\frac{2nL+R}{2nL-R}\right)\right],
\end{aligned}
\tag{4.95}
$$

where a constant has been added to make $f_{\text{opt}}(0) = 0$.

Letting $\lambda = \dfrac{L}{R}$, $\rho = \dfrac{r}{R}$, $\bar{f}_{\text{opt}}(\rho) = \dfrac{\pi E^*}{2\sigma_{\text{th}}R} f_{\text{opt}}(r)$, Equation (4.95) can be normalized to be

$$
\begin{aligned}
\bar{f}_{\text{opt}}(\rho) = &-\left[\ln\left(1-\rho^2\right)+\rho\ln\left(\frac{1+\rho}{1-\rho}\right)\right] \\
&-\sum_{n=1}^{\infty}\left[\ln\left(\frac{(2n\lambda+\rho)^2-1}{(2n\lambda)^2-1}\right)+(2n\lambda+\rho)\ln\left(\frac{2n\lambda+\rho+1}{2n\lambda+\rho-1}\right)-2n\lambda\ln\left(\frac{2n\lambda+1}{2n\lambda-1}\right)\right] \\
&-\sum_{n=1}^{\infty}\left[\ln\left(\frac{(2n\lambda-\rho)^2-1}{(2n\lambda)^2-1}\right)+(2n\lambda-\rho)\ln\left(\frac{2n\lambda-\rho+1}{2n\lambda-\rho-1}\right)-2n\lambda\ln\left(\frac{2n\lambda+1}{2n\lambda-1}\right)\right],
\end{aligned}
\tag{4.96}
$$

Since

$$
\begin{aligned}
&\lim_{n\to\infty}(2n\lambda)^2\left[\ln\left(\frac{(2n\lambda+\rho)^2-1}{(2n\lambda)^2-1}\right)+(2n\lambda+\rho)\ln\left(\frac{2n\lambda+\rho+1}{2n\lambda+\rho-1}\right)-2n\lambda\ln\left(\frac{2n\lambda+1}{2n\lambda-1}\right)\right. \\
&\left.+\ln\left(\frac{(2n\lambda-\rho)^2-1}{(2n\lambda)^2-1}\right)+(2n\lambda-\rho)\ln\left(\frac{2n\lambda-\rho+1}{2n\lambda-\rho-1}\right)-2n\lambda\ln\left(\frac{2n\lambda+1}{2n\lambda-1}\right)\right]=-2\rho^2,
\end{aligned}
\tag{4.97}
$$

the convergence of the series in Equation (4.96) is ensured. In practice, we just need to sum up the leading N terms of the series to get the optimal shape. For example, taking $N = 20$, Figure 4.20 plots the optimal shapes for different values of L/R in comparison with that for single fiber case, i.e. $L/R = \infty$. As expected, the effect of neighboring contacts upon the optimal shape increases as the fiber spacing decreases. Interestingly, the optimal shape given by Equation (4.96) has been verified recently by molecular dynamics simulation [14].

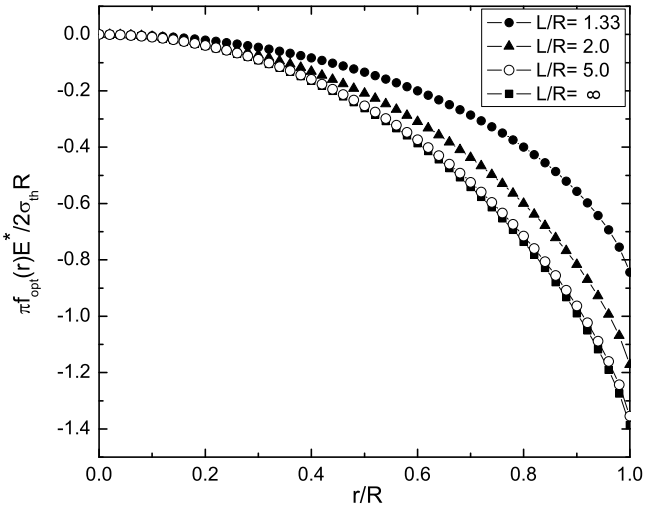

Figure 4.20.: Optimal shapes for 2D fiber array case with different fiber spacings.

Three-Dimensional cluster:

Now, let us extend the concept of optimal shape to the more realistic 3D (three-dimensional) fiber cluster. Consider cylindrical fibers with radius R contacting with substrate, as shown in Figure 4.21. All the fibers are arrayed periodically in a rectangular pattern. The spacings in x-direction and y-direction are $2L_x$, $2L_y$, respectively. Suppose that the fibers are rigid and the substrate is elastic. To determine the optimal shape of the fiber tip, we should calculate the deformation of the substrate under tractions σ_{th} applied on the circular contacting regions (Figure 4.21). Owing to the periodicity,

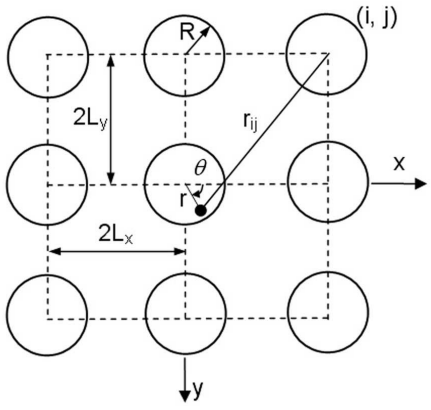

Figure 4.21.: Top view of a 3D fiber cluster.

we just need to find the normal displacement in one contacting region. As shown in Figure 4.21, if we choose the center of one contacting region as the coordinate origin, the distance from a point $(r,\ \theta)$ in this region to any other region center can be expressed as

$$r_{ij} = \sqrt{(x_i - r\cos\theta)^2 + (y_j - r\sin\theta)^2} = \sqrt{(2L_x i - r\cos\theta)^2 + (2L_y j - r\sin\theta)^2} \quad (4.98)$$

with $i,\ j = \pm 1,\ \pm 2,\ \pm 3, \cdots$. Each pair of $(i,\ j)$ corresponds to a contacting region.

It has been shown [60] that the displacement of a half-space surface produced by a uniform tensile stress σ_{th} applied on the circular surface region $(r \leq R)$ is given by

$$\begin{aligned} w(r) = u_z(r,0) &= -\frac{4\sigma_{\text{th}} R}{\pi E^*}\mathbf{E}\left(\frac{r}{R}\right), \quad (r < R) \\ w(r) = u_z(r,0) &= -\frac{4\sigma_{\text{th}} r}{\pi E^*}\left[\mathbf{E}\left(\frac{R}{r}\right) - \left(1 - \frac{R^2}{r^2}\right)\mathbf{K}\left(\frac{R}{r}\right)\right], \quad (r > R) \end{aligned}$$

where $\mathbf{K}(\cdot)$, $\mathbf{E}(\cdot)$ are complete elliptical integrals of first and second kind respectively. Therefore, for our case the displacement of one contacting region can be obtained by superposing the contributions of the tractions applied on all contacting regions

$$w(r) = -\frac{4\sigma_{\text{th}} R}{\pi E^*}\mathbf{E}\left(\frac{r}{R}\right) - \sum_{i=-\infty}^{\infty}\sum_{j=-\infty}^{\infty}\frac{4\sigma_{\text{th}} r_{ij}}{\pi E^*}\left[\mathbf{E}\left(\frac{R}{r_{ij}}\right) - \left(1 - \frac{R^2}{r_{ij}^2}\right)\mathbf{K}\left(\frac{R}{r_{ij}}\right)\right]. \ (|i|+|j| \neq 0)$$

It follows that the optimal shape

$$\begin{aligned} f_{\text{opt}}(r) = {} & \frac{4\sigma_{\text{th}} R}{\pi E^*}\left[\mathbf{E}\left(\frac{r}{R}\right) - \frac{\pi}{2}\right] + \sum_{i=-\infty}^{\infty}\sum_{j=-\infty}^{\infty}\frac{4\sigma_{\text{th}} r_{ij}}{\pi E^*}\left[\mathbf{E}\left(\frac{R}{r_{ij}}\right) - \left(1 - \frac{R^2}{r_{ij}^2}\right)\mathbf{K}\left(\frac{R}{r_{ij}}\right)\right] \\ & - \sum_{i=-\infty}^{\infty}\sum_{j=-\infty}^{\infty}\frac{4\sigma_{\text{th}} r_{ij}^0}{\pi E^*}\left[\mathbf{E}\left(\frac{R}{r_{ij}^0}\right) - \left(1 - \frac{R^2}{r_{ij}^{0\,2}}\right)\mathbf{K}\left(\frac{R}{r_{ij}^0}\right)\right], \quad (|i| + |j| \neq 0) \quad (4.99) \end{aligned}$$

where $r_{ij}^0 = \sqrt{4L_x^2 i^2 + 4L_y^2 j^2}$. Letting $\lambda_x = \dfrac{L_x}{R}$, $\lambda_y = \dfrac{L_y}{R}$, $\rho = \dfrac{r}{R}$, $\bar{f}_{\text{opt}}(\rho) = \dfrac{\pi E^*}{4\sigma_{\text{th}} R} f_{\text{opt}}(r)$, Equation (4.99) can be normalized to be

$$\begin{aligned} \bar{f}_{\text{opt}}(\rho) = {} & \mathbf{E}(\bar{r}) - \frac{\pi}{2} + \sum_{i=-\infty}^{\infty}\sum_{j=-\infty}^{\infty}\bar{r}_{ij}\left[\mathbf{E}\left(\frac{1}{\bar{r}_{ij}}\right) - \left(1 - \frac{1}{\bar{r}_{ij}^2}\right)\mathbf{K}\left(\frac{1}{\bar{r}_{ij}}\right)\right] \\ & - \sum_{i=-\infty}^{\infty}\sum_{j=-\infty}^{\infty}\bar{r}_{ij}^0\left[\mathbf{E}\left(\frac{1}{\bar{r}_{ij}^0}\right) - \left(1 - \frac{1}{(\bar{r}_{ij}^0)^2}\right)\mathbf{K}\left(\frac{1}{\bar{r}_{ij}^0}\right)\right], \quad (|i| + |j| \neq 0) \quad (4.100) \end{aligned}$$

with

$$\bar{r}_{ij} = \sqrt{(2\lambda_x i - \rho\cos\theta)^2 + (2\lambda_y j - \rho\sin\theta)^2},\ \bar{r}_{ij} = \sqrt{4\lambda_x^2 i^2 + 4\lambda_y^2 j^2}.$$

Because

$$\lim_{i\to\infty}(2\lambda_x i)^2 \left\{ \bar{r}_{ij}\left[\mathbf{E}\left(\frac{1}{\bar{r}_{ij}}\right) - \left(1-\frac{1}{\bar{r}_{ij}^2}\right)\mathbf{K}\left(\frac{1}{\bar{r}_{ij}}\right)\right] - \bar{r}_{ij}^0\left[\mathbf{E}\left(\frac{1}{\bar{r}_{ij}^0}\right) - \left(1-\frac{1}{(\bar{r}_{ij}^0)^2}\right)\mathbf{K}\left(\frac{1}{\bar{r}_{ij}^0}\right)\right]\right\} = \rho\cos\theta,$$

$$\lim_{i\to\infty}(2\lambda_y j)^2 \left\{ \bar{r}_{ij}\left[\mathbf{E}\left(\frac{1}{\bar{r}_{ij}}\right) - \left(1-\frac{1}{\bar{r}_{ij}^2}\right)\mathbf{K}\left(\frac{1}{\bar{r}_{ij}}\right)\right] - \bar{r}_{ij}^0\left[\mathbf{E}\left(\frac{1}{\bar{r}_{ij}^0}\right) - \left(1-\frac{1}{(\bar{r}_{ij}^0)^2}\right)\mathbf{K}\left(\frac{1}{\bar{r}_{ij}^0}\right)\right]\right\} = \rho\sin\theta,$$

we have

$$\lim_{i,j\to\infty} \left\{ \bar{r}_{ij}\left[\mathbf{E}\left(\frac{1}{\bar{r}_{ij}}\right) - \left(1-\frac{1}{\bar{r}_{ij}^2}\right)\mathbf{K}\left(\frac{1}{\bar{r}_{ij}}\right)\right] - \bar{r}_{ij}^0\left[\mathbf{E}\left(\frac{1}{\bar{r}_{ij}^0}\right) - \left(1-\frac{1}{(\bar{r}_{ij}^0)^2}\right)\mathbf{K}\left(\frac{1}{\bar{r}_{ij}^0}\right)\right]\right\} = O\left(\frac{1}{i^2 j^2}\right).$$

Therefore, the convergence of the series summation in Equation (4.100) is ensured. Given λ_x and λ_y, optimal shape (4.100) is a function of ρ and θ. Taking $\lambda_x = \lambda_y = 1.33$ and $|i| \le 20$, $|j \le 20|$ as the cut-off of the series summation, Figure 4.22 plots the slices of the optimal shape at $\theta = 0$ and $\theta = 45^\circ$ in comparison with the result for the single fiber case.

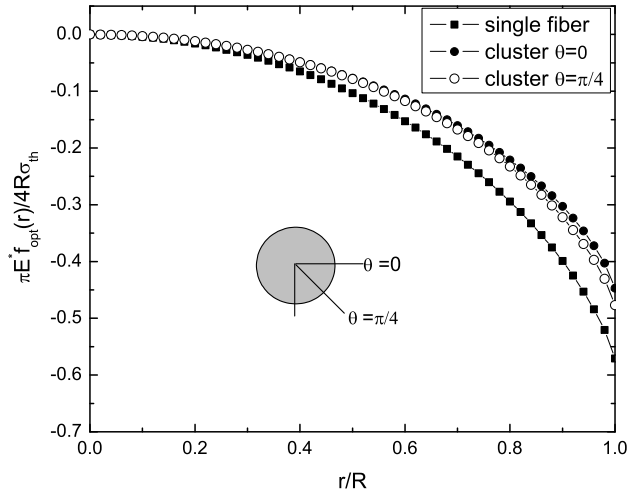

Figure 4.22.: Optimal shape for 3D fiber cluster when $L_x = L_y = 1.33R$

4.3. Spontaneous optimal adhesion

The discussion so far has been focused on how to achieve the theoretical pull-off force by shape optimization. Now, a question arises. Given two optimal-shaped structures, is it always possible to achieve the optimum adhesion spontaneously? In other words, if we put two optimal-shaped structures close to a substrate, can the adhesion force pull them together and form a conjunction spontaneously with theoretical adhesion strength?

To answer these questions we calculate the approaching/receding process between an optimally shaped rigid fiber and an elastic substrate (Figure 4.23a) by using the

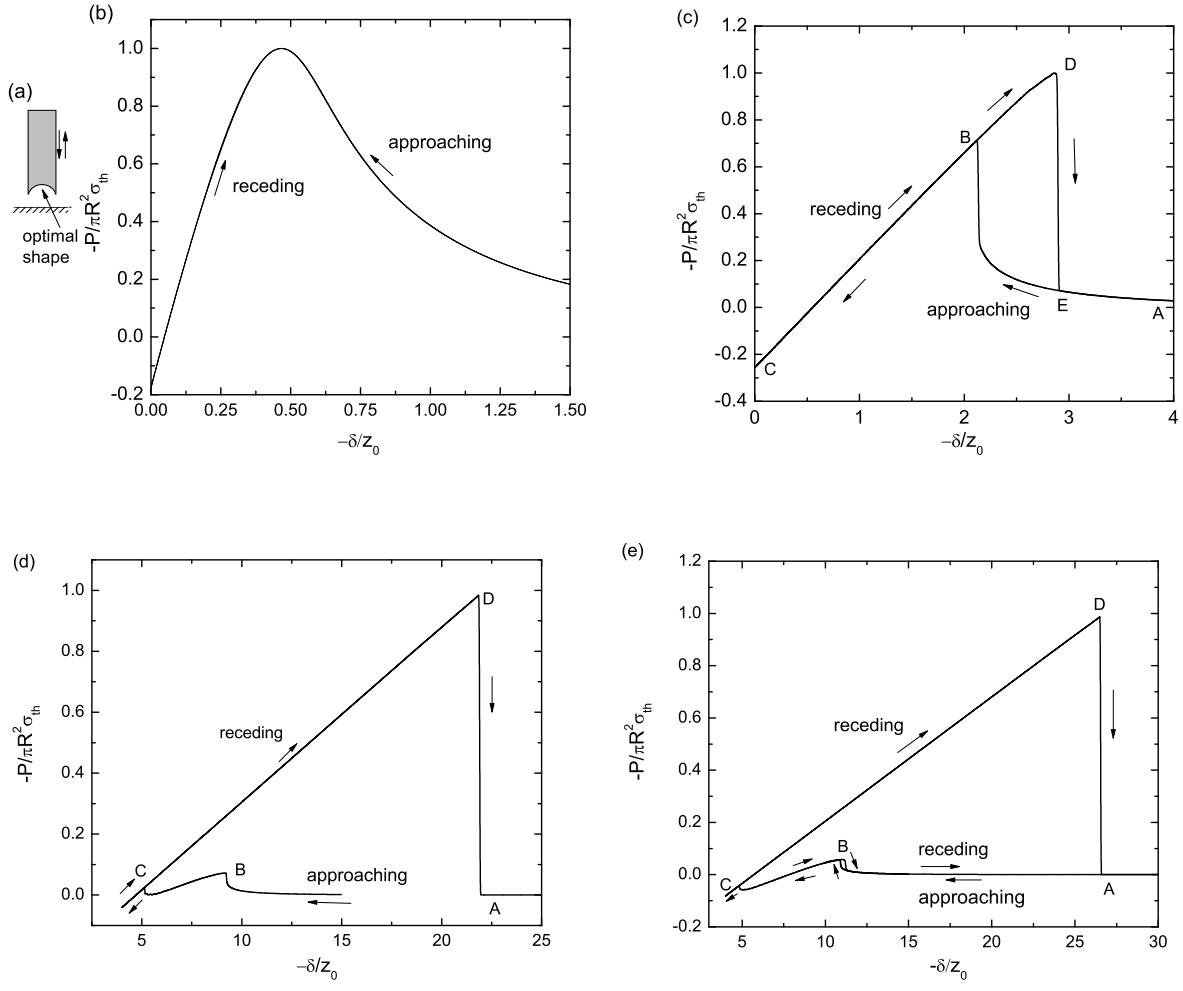

Figure 4.23.: Variation of adhesive force as the optimally shaped rigid fiber approaches or recedes from an elastic substrate. (a) Schematic illustration of the problem. (b-e) different behaviors of fibers with radius equal to (b) $R = 0.13E^*\Delta\gamma/\sigma_{\text{th}}^2$, (c)$R = 1.3E^*\Delta\gamma/\sigma_{\text{th}}^2$, (d)$R = 11.3E^*\Delta\gamma/\sigma_{\text{th}}^2$, (e)$R = 13.7E^*\Delta\gamma/\sigma_{\text{th}}^2$.

numerical Green's function method developed in subsection 3.2.2. For simplicity, friction forces are neglected. With relationship $\sigma_{\text{th}} = 16\Delta\gamma/9\sqrt{3}z_0$ given by Lennard-Jones law, it can be demonstrated that the solution to the Equations (3.89-3.91) for optimal shape of Equation (4.50) depends only on one non-dimensional parameter $R\sigma_{\text{th}}^2/E^*\Delta\gamma$. That is, for a given $R\sigma_{\text{th}}^2/E^*\Delta\gamma$, the adhesive force along the approaching or receding path can be determined.

Figure 4.23(b-e) display the variation of the normalized adhesive force $-P/\pi R^2\sigma_{\text{th}}$ as a function of $-\delta/z_0$, where δ is the penetration of the tip surface centre of the fiber with respect to zero force position and z_0 is the equilibrium distance. Fibers of different sizes are considered. Figure 4.23(b) shows the behavior of a fiber with radius $R = 0.13E^*\Delta\gamma/\sigma_{\text{th}}^2$ (3.2 nm for $\Delta\gamma = 10$ mJ/m^2, $\sigma_{\text{th}} = 20$ MPa and $E^* = 1$ GPa). For this fiber, the approach and recession follow the same path. As the fiber approaches the substrate from a distant position, the adhesive force first increases and then drops to zero at the equilibrium contact position. During this period, the adhesive force is always attractive. Therefore, if we put such a fiber near the substrate the adhesion force will pull the fiber close to the substrate automatically until an equilibrium contact position is reached with zero net interactive force. As the fiber recedes from the equilibrium position, there exists a maximum adhesive force equal to the theoretical pull-off force, confirming that the tip shape is indeed optimized.

Figure 4.23(c) shows the behavior of a larger fiber with $R = 1.3E^*\Delta\gamma/\sigma_{\text{th}}^2$ (32.5 nm for $\Delta\gamma = 10$ mJ/m^2, $\sigma_{\text{th}} = 20$ MPa and $E^* = 1$ GPa). Now the approach and recession follow different paths giving rise to a hysteresis. During approaching, the adhesive force is always positive and the fiber is drawn toward the substrate until equilibrium. Interestingly, the approaching process is unstable. At a critical distance from substrate, there is a sudden increase in adhesive force and the fiber jerks toward the substrate. During recession, the adhesive force increases until reaching the theoretical pull-off force and then abruptly drops to a small value. Similar collapse in adhesion has been termed *adhesive avalanche* [86].

For an even larger fiber with $R = 13.7E^*\Delta\gamma/\sigma_{\text{th}}^2$ (342.5 nm for $\Delta\gamma = 10$ mJ/m^2, $\sigma_{\text{th}} = 20$ MPa and $E^* = 1$ GPa) shown in Figure 4.23(e), the theoretical adhesive strength can not be achieved spontaneously. It can be seen that as the fiber approaches the substrate, the adhesive force vanishes at two equilibrium positions. Only after the second equilibrium position can the fiber achieve the theoretical pull-off force upon recession. If the fiber is pulled back near the first equilibrium position, full contact between the fiber and substrate has not been achieved yet and the adhesive force goes

back along the approaching path BA with a tiny hysteresis and small pull-off value. Between the two equilibrium positions, the adhesive force is actually negative, implying that an externally applied pressure is needed to help the fiber to reach full contact with the substrate. In this case, the theoretical pull-off force can not be achieved unless full contact is achieved by pressing the fiber hard enough against the substrate before recession.

The above analysis indicates that there must exist a threshold radius for spontaneous approaching of substrate, which is calculated to be $R_{\text{spon}} = 11.3E^*\Delta\gamma/\sigma_{\text{th}}^2$ for a rigid fiber interacting with an elastic substrate. The behavior of such a fiber at threshold radius is shown in Figure 4.23(d). Taking $\Delta\gamma = 10$ mJ/m^2, $E^* = 1$ GPa, and $\sigma_{\text{th}} = 20$ MPa, R_{spon} is estimated to be ≈ 282.5 nm. Fibers with radius smaller than R_{spon} can spontaneously achieve full contact and attain the theoretical pull-off force without any externally applied pressure.

In this chapter, we mainly focus our attention on the shape of the contacting surfaces. Although the adhesion strength can in principle be designed to approach the theoretical strength for any contact size, interfacial crack-like flaws due to surface roughness and contaminants are always present to weaken the actual strength. Gao *et al.* [33] performed finite element calculations to show that the adhesion strength of an elastic cylinder in partial contact with a rigid substrate saturates at the theoretical strength at a critical diameter around 200 nm for van der Waals interaction. A similar phenomenon of strength saturation in small contact bodies has been discussed by Persson [77] in the case of a rigid cylinder in frictionless contact with an elastic half-space and by Glassmaker *et al.* [39] in the case of an elastic cylinder in perfect adhesive bonding with a rigid substrate. It is found that the theoretical strength can be achieved either by optimizing the shape of the contact surfaces or by reducing the size of the contact area; the smaller the size, the less important the shape. A shape-insensitive optimal adhesion at the theoretical strength can be realized below a critical size which can be related to the intrinsic capability of a small scale material to tolerate crack-like flaws [29, 31, 32]. Theses studies have provided significant insights into various aspects of adhesive contact mechanics in engineering and biological systems. However, a general understanding is still lacking with respect to a number of critical issues. First, surface roughness should play a very important role in bio-adhesion and needs to be further investigated. Optimizing adhesion at the level of single asperities or fibrils does not automatically address the problem of robust adhesion on rough surfaces at macroscopic scales. Releasable adhesion at the level of single seta does not provide full explanations on how releasable

adhesion is achieved in macroscopic contact on rough surfaces. The existence of smooth attachment systems indicates that the size reduction of contact elements in hairy attachment systems is not the only viable strategy in bio-adhesion. To elucidate these issues, in the next two chapters we will advance further to discuss the mechanics of robust (flaw-tolerant) and releasable adhesion at macroscopic scales.

Chapter 5. Flaw-tolerant adhesion

Although the flexibility of biological attachment pads facilitates, to a great extent, the formation of good contact, crack-like flaws may still exist along the contact interface due to the surface roughness, impurities, contaminants, trapped air bubbles and skewed contact angles, etc. Normally, when two bonded solids are subjected to an external pulling force, such crack-like flaws will induce stress concentration around them. Under increasing load, the intensity of stress concentration ultimately reaches a critical level and the contact is broken by crack propagation. Under this circumstance, the adhesion is not optimal because only a small fraction of material is highly stressed at any instant of loading. However, we recognize that the biological attachment systems seem have never been troubled by adhesion flaws. They even can adhere to the reversed surfaces firmly in spite of the unpredictable roughness. The extraordinary ability of biological attachment systems implies that nature must have evolved a specific solution to deal with the interfacial flaws. What is the basic principle of robust adhesion in biology?

For macroscopic contact, surface roughness has long been recognized as a critically important factor. Greenwood and Williamson [44] developed a statistical approach to contact between elastic or plastic asperities with identical radius of curvature but Gaussian distributed heights. Fuller and Tabor [27] extended this approach to adhesive contact via the JKR model. Maugis [68] discussed a stochastic approach to adhesive contact on rough surfaces based on the DMT model. Morrow *et al.* [69] extended such analysis to the Maugis-Dugdale model and a modification by Kim *et al.* [64]. Fractal surface models with scale-dependent asperity heights, slope and radius of curvature based on the Weierstrass-Mandelbrot fractal function have been developed by Majumdar and Bhushan [65, 66] who expressed contact area and load in terms of fractal dimensions. Such fractal surface models have been coupled with the JKR model [82] and also extended to friction and wear [83]. Some mechanisms of biological attachment on random rough surfaces have been discussed by Persson [78] and Persson and Gorb [79].

Despite of significant research in the past four decades, adhesive contact on rough surfaces remains to be a challenging topic. Instead of directly modeling adhesive contact on

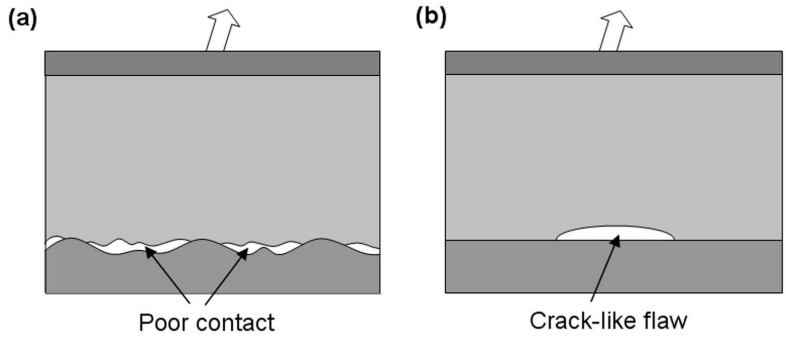

Figure 5.1.: The interfacial crack model. (a) Schematic drawing of adhesion on a rough surface with poor contact regions around asperities. (b) An interfacial crack is used to represent random contact flaws induced by roughness or contaminants.

random or fractal rough surfaces as Greenwood and Williamson [44] and Majumdar and Bhushan [65, 66] did, we shall follow a different approach by considering the behavior of an interfacial crack representing random contact flaws due to surface roughness or contaminant (Figure 5.1). In comparison with the previous contact models on rough surfaces, our approach offers a distinct advantage in addressing questions related to robustness and releasability of adhesion. The crack model greatly simplifies the mathematical problem and allows us to extend the adhesive contact theories to nonhomogeneous (see section 5.3), hierarchical (see section 5.4) and anisotropic contact systems (see Chapter 6). We adopt the viewpoint that robust adhesion on a random rough surface (Figure 5.1a) is equivalent to flaw tolerant adhesion in which the growth of a representative interfacial crack is suppressed irrespective of the crack size (Figure 5.1b). In other words, it is hypothesized that an adhesive material designed to tolerate an interfacial crack of any size will also be able to adhere robustly to any random rough surface, and vice versa. By investigating the conditions under which the representative crack does not grow, we effectively treat the problem of how to prevent randomly occurring poor contact regions from triggering crack-like adhesive failure.

In this chapter, we begin by introducing the fundamental concepts of flaw tolerance. Based on the Dugdale model, we first investigate the condition for flaw tolerance within the context of homogeneous material. Critical length scales for various crack configurations are calculated, under which the representative crack does not grow. To achieve flaw-tolerant adhesion with no size limit, i.e. the so-called generalized flaw tolerance, we extend our discussion to the inhomogeneous material and hierarchical structure. We show that graded elasticity, hierarchical energy dissipation and scale-dependent adhesion strength are three primary strategies that can be used to suppress crack growth and to

achieve flaw tolerant adhesion in all length scales. Our results exhibit a good agreement with the common structural features shared by a variety of biological adhesion systems.

5.1. Definition of flaw tolerance

Consider two dissimilar elastic solids bonded by adhesion along the interface (Figure 5.2a). A crack is assumed to occupy a finite region of the interface to model the imperfect adhesion due to the surface roughness or other kind of flaws. For simplicity, friction effects are neglected at the moment so that no shear stress exists along the interface.

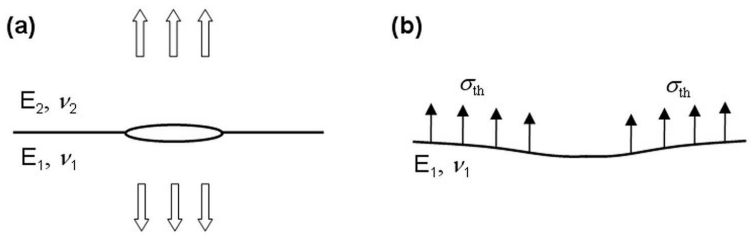

Figure 5.2.: The concept of flaw tolerance in adhesive contact. (a) Adhesion strength between dissimilar elastic solids is often dominated by the crack-like flaws along the interface. (b) In the flaw tolerance state, a pre-existing crack does not participate at all in the failure process and the stress ahead of the crack tip reaches the theoretical strength of the material uniformly.

Dugdale model is adopted to describe the adhesive interaction across the interface in which

$$\sigma(\delta) = \begin{cases} \sigma_{\text{th}}, & \delta \leq \delta_0 \\ 0, & \delta > \delta_0 \end{cases}$$

where σ is the normal traction, δ is the displacement opening across the interface, σ_{th} is the theoretical strength of adhesion and δ_0 is the interaction range. Therefore the work of adhesion would be $\Delta\gamma = \sigma_{\text{th}}\delta_0$.

For the generic crack problem described in Figure 5.2(a), what we are interested in is whether there exists such a state in which pre-existing crack does not propagate before the failure of the interface as the externally applied load increases to separate the adhesion. First let us introduce the following definition:

The state of *flaw tolerance* is defined as such that a pre-existing crack does not propagate and does not participate at all the failure process. The failure occurs by having the normal traction uniformly reach the theoretical

adhesion strength everywhere along the interface except the region occupied by the crack.

The stress distribution at flaw tolerance state is schematically shown in Figure 5.2(b), where, for clarity, only material #1 is plotted. The existence of flaw tolerance implies that the conventional engineering concept of stress concentration near the crack tip becomes invalid. Failure occurs not by crack propagation but by the simultaneous detachment of the whole contacting area, achieving the maximum adhesion strength. In the light of the Dugdale model, the condition for the existence of flaw tolerance solution can be expressed as

$$\delta_{\text{tip}}^{\text{f}} \leq \delta_0 = \Delta\gamma/\sigma_{\text{th}}, \tag{5.1}$$

where $\delta_{\text{tip}}^{\text{f}}$ is the crack tip opening. Since the stress filed in the state of flaw tolerance is uniform, one can easily determine the crack tip opening $\delta_{\text{tip}}^{\text{f}}$ which is normally a monotonic increasing function of crack size. Therefore, from Equation (5.1) we can deduce a critical length scale of the crack size associated with flaw tolerance. In the following, we will show that in a homogeneous material the only way to achieve flaw tolerance is to restrict the size of the flaws to below a critical length scale. The generalized flaw tolerance, in which propagation of any-sized crack is suppressed, can be realized via graded elasticity design, hierarchical energy dissipation and scale-dependent adhesion strength.

5.2. Size-limited flaw tolerance in homogeneous materials

Let us start with the traditional homogeneous material. Various crack configurations will be considered in this section, including penny-shaped crack, circumferential external crack, 2D internal and external cracks.

5.2.1. Size-limited flaw tolerance solution for a penny-shaped crack

Consider two dissimilar elastic homogeneous materials adhering to each other via adhesive interface (Figure 5.3a). A penny-shaped crack with radius a is introduced on the interface to model the crack-like flaw. The materials are considered as elastic half-spaces subjected to remote stress load σ^{∞} which, if sufficiently large, would pull the materials apart. What we are most concerned about is the existence of the flaw tolerant state in such a contact system.

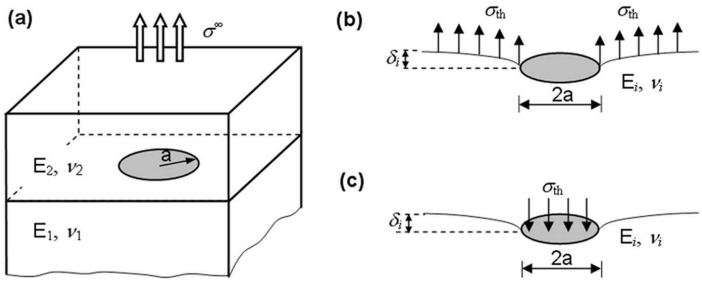

Figure 5.3.: (a) Penny-shaped interfacial crack. (b) Schematic illustration of the flaw tolerance state in which the surface displacement relative to a remote point on the interface is equivalent to that in case (c).

Assuming flaw tolerant state has been achieved, so that at the pull-off instant there should be a uniform distribution of adhesive stress with magnitude σ_{th} outside the crack region (Figure 5.3b), causing an inward deflection of the surface relative to a remote point on the surface. The crack tip opening at pull-off moment thus can be given by

$$\delta_{\text{tip}}^{\text{f}} = \delta_1 + \delta_2, \tag{5.2}$$

where δ_1 and δ_2 are surface deflection at point $r = a$ of material 1 and 2 respectively, as shown in Figure 5.3(b). Actually, the mathematical problem of finding δ_1 and δ_2 can be simplified by superposing a uniform pressure equal to σ_{th} on the entire surface. The problem of Figure 5.3(b) is then converted to an elastic half-space subjected to uniform pressure σ_{th} over $r \leq a$ (Figure 5.3c) while δ_1 and δ_2 remain unaltered. This simplification strategy not only applies to the traditional homogeneous material but also holds for the graded material (see section 5.3) whose Young's modulus is dependent on the distance from the surface. A frequent use of this simplification strategy will be made in our discussion later.

For a homogeneous material, it is easy to attain the tip deflection in Figure 5.3(c) as

$$\delta_1 = \frac{4(1-\nu_1^2)\sigma_{\text{th}} a}{\pi E_1}, \quad \delta_2 = \frac{4(1-\nu_2^2)\sigma_{\text{th}} a}{\pi E_2}, \tag{5.3}$$

where subscripts '1' and '2' denote the quantities pertaining to materials #1 and #2 respectively. Substituting Equation (5.3) into (5.2) and then using Equation (5.1) show that the flaw tolerance solution exists as long as

$$a \leq \frac{\pi E^* \Delta\gamma}{4\sigma_{\text{th}}^2} \tag{5.4}$$

where

$$E^* = \left[(1-\nu_1^2)/E_1 + (1-\nu_2^2)/E_2\right]^{-1}. \tag{5.5}$$

The upper limit of the crack size allowing flaw tolerance is usually termed *critical length scale* for flaw tolerance and denoted by $a_{\rm cr}$. For penny-shaped crack, Equation (5.4) suggests

$$a_{\rm cr} = \frac{\pi E^* \Delta\gamma}{4\sigma_{\rm th}^2}. \tag{5.6}$$

Once the crack size is decreased to below this threshold, flaw tolerance state is achieved.

The above simple analysis gives the critical length at which the adhesion strength saturates at the theoretical strength. However, it has not shown us the evolution of the adhesion strength as the crack size decreases. For this purpose, let us go through the mathematical solution of the three dimensional Dugdale model.

In the Dugdale model of adhesive contact around a penny-shaped crack, the contact area ($r \geq a$) consists of a cohesive zone ($a \leq r < c$) in which the adhesion stress equals the theoretical strength $\sigma_{\rm th}$ and a perfectly bonded region ($r \geq c$) in which the separation between contact surfaces vanishes, as shown in Figure 5.4(a). The mathematical solution to the Dugdale model of a penny-shaped crack has been found by Rice [81] and Olesiak and Wnuk [74]. Here we will present a simpler approach to get the results of concern. Actually, in mechanics this problem can be treated as a superposition of two sub-problems: (a) a penny-shaped crack with radius c undergoing remote tension (Figure 5.4b) and (b) a penny-shaped crack with closure stress $\sigma_{\rm th}$ over a ring-shaped cohesive zone at the tip (Figure 5.4c). For both sub-problems, the corresponding stress intensity factors $K_{\rm I}$ at $r = a$ and crack opening at are given by [94]

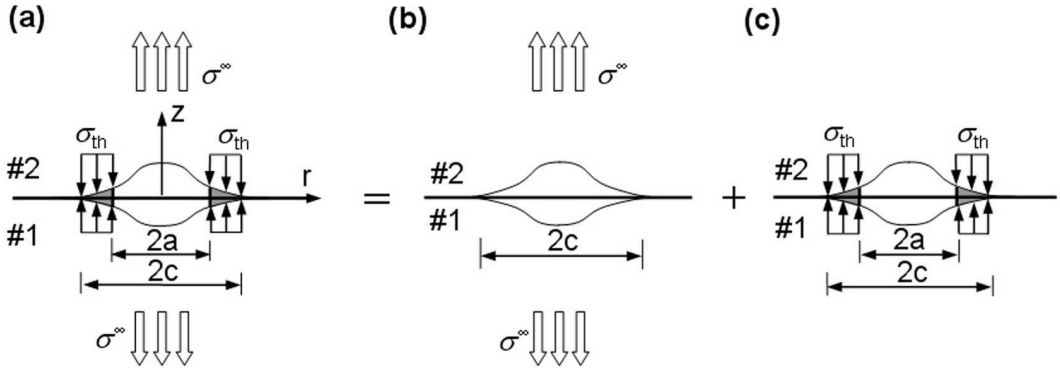

Figure 5.4.: (a) In the Dugdale model of this interfacial crack problem, the contact area is assumed to consist of a cohesive zone ($a \leq r < c$) and a bonded region ($r \geq c$). The problem is equivalent to the superposition of two sub-problems (b) and (c).

$$K_{\mathrm{I}}^{(\mathrm{a})} = 2\sigma^{\infty}\sqrt{\frac{c}{\pi}}, \tag{5.7a}$$

$$\delta^{(\mathrm{a})}(a) = \frac{4\sigma^{\infty}c}{\pi E^{*}}\sqrt{1-a^{2}/c^{2}}, \tag{5.7b}$$

$$K_{\mathrm{I}}^{(\mathrm{b})} = -2\sigma_{\mathrm{th}}\sqrt{\frac{c}{\pi}}\sqrt{1-a^{2}/c^{2}}, \tag{5.8a}$$

$$\delta^{(\mathrm{b})}(a) = -\frac{4\sigma_{\mathrm{th}}c}{\pi E^{*}}\left(1-\frac{a}{c}\right). \tag{5.8b}$$

The stress continuity at the edge of cohesive zone $r = c$ requires that the combined stress intensity factor

$$K_{\mathrm{I}} = K_{\mathrm{I}}^{(\mathrm{a})} + K_{\mathrm{I}}^{(\mathrm{b})} = 0. \tag{5.9}$$

Substitution of Equations (5.7a) and (5.8a) into (5.9) gives rise to

$$\sigma^{\infty} = \sigma_{\mathrm{th}}\sqrt{1-a^{2}/c^{2}}. \tag{5.10}$$

At the critical state of pull-off, the crack opening at the edge of contact $r = a$ reaches the limiting for bond breaking, i.e.,

$$\delta_{\mathrm{tip}}^{\mathrm{f}} = \delta^{(\mathrm{a})}(a) + \delta^{(\mathrm{b})}(a) = \delta_{0} = \Delta\gamma/\sigma_{\mathrm{th}}. \tag{5.11}$$

Substituting Equations (5.7b)(5.8b) into (5.11) and then making use of Equation (5.10) yield

$$\frac{a}{c} = 1 - \frac{\pi E^{*}\Delta\gamma}{4\sigma_{\mathrm{th}}^{2}a}. \tag{5.12}$$

Equation (5.12) gives the outer radius of the cohesive zone c as a function of E^{*}, σ_{th}, $\Delta\gamma$ and a. Substituting Equation (5.12) into (5.10) gives rise to the adhesion strength as

$$\sigma_{\mathrm{cr}}^{\infty} = \sigma_{\mathrm{th}}\sqrt{1-\left(1-\frac{\pi E^{*}\Delta\gamma}{4\sigma_{\mathrm{th}}^{2}a}\right)^{2}}. \tag{5.13}$$

On the other hand, if we directly adopt the Griffith fracture criterion instead of the Dugdale model to the penny-shaped crack, the adhesion strength can be given by

$$\sigma_{\mathrm{cr}}^{\infty} = \sqrt{\frac{\pi E^{*}\Delta\gamma}{2a}}. \tag{5.14}$$

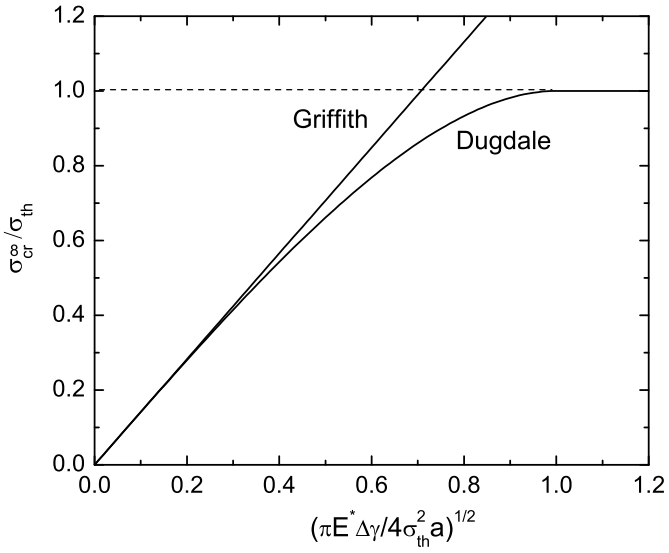

Figure 5.5.: Variation of the adhesion strength with the crack size.

Figure 5.5 displays the normalized adhesion strength as a function of the dimensionless parameter $(\pi E^*\Delta\gamma/4\sigma_{\rm th}^2 a)^{1/2}$. It can be seen that the adhesion strength predicted by the Dugdale model agrees well with the Griffith prediction for large crack sizes and then deviates from it as the crack size decreases. It will eventually saturate at the theoretical strength $\sigma_{\rm th}$ as the crack size is reduced to below the critical length scale

$$a_{\rm cr} = \frac{\pi\Delta\gamma E^*}{4\sigma_{\rm th}^2},$$

which is actually the same as Equation (5.6). Taking typical values for van der Waals interaction $\Delta\gamma = 0.02$ J/m^2, $E^* = 1.0$ GPa, $\sigma_{\rm th} = 20$ MPa, the critical length scale is estimated to be around 40 nm. When $a \leq a_{\rm cr}$ the adhesion strength is a constant equal to the theoretical strength and decreases with a when $a > a_{\rm cr}$. Therefore, a homogeneous material tolerates sufficiently small cracks.

In the analysis so far, we have not considered the effect of friction which may possibly occur on the interface. In effect, friction would unavoidably take place on the interface due to the slip or slip tendency between two contact surfaces. Such friction would cause an additional normal displacement of the surface therefore affect the displacement opening at the crack tip. In this way, the critical length scale for flaw tolerance will be changed. Does the friction force make for or against flaw tolerance? In order to

answer this question, let us assess the critical length scale for the frictional adhesion with penny-shaped crack-like flaw.

The frictional flaw tolerance state is schematically illustrated by Figure 5.6. In addition to the uniform normal stress σ_{th}, now tangential frictional stress is also applied on the surfaces. Assuming the normal traction is only dependent on the surface separation in normal direction and obey the Dugdale law, the condition for flaw tolerance given in Equation (5.1) is still valid. Different from the frictionless case, now the critical crack tip opening $\delta_{\text{tip}}^{\text{f}}$ has two contributions. One is the displacement due to the uniform normal adhesive force σ_{th} and the other is the deformation induced by the tangential friction force whose exact distribution remains to be found.

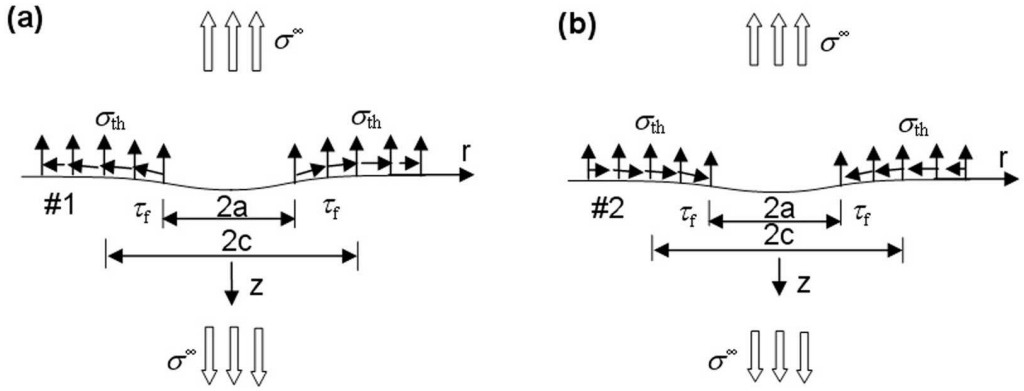

Figure 5.6.: Schematic of frictional flaw tolerance state for (a) material #1 and (b) material #2.

Suppose that slip between two surfaces is allowed whenever the friction stress reaches critical friction strength τ_{f}. Therefore the contact area ($r \geq a$) is divided into a slipping region ($a \leq r \leq c$) in which the friction stress equals the friction strength τ_{f} and a non-slipping region ($r > c$) in which relative tangential displacement between two surfaces vanishes and the tangential stress remains to be found, as shown in Figure 5.6.

This posed mathematical problem is quite similar to that associated with the optimal shape of frictional adhesion (subsection 4.2.4). Likewise, we can express the displacement and stress components in terms of Hankel transforms as

$$\begin{cases} u_r^{(1)}(r,0) = \dfrac{1}{2G_1}\mathcal{H}_1\left[\xi^{-1}C_1;\xi\to r\right] \\ \tau_{zr}^{(1)}(r,0) = -\mathcal{H}_1\left[(1-2\nu_1)A_1 + C_1;\xi\to r\right] \\ \sigma_{zz}^{(1)}(r,0) = -\mathcal{H}_0\left[(2-2\nu_1)A_1 + C_1;\xi\to r\right], \end{cases} \tag{5.15a}$$

for solid #1 and

$$\begin{cases} u_r^{(2)}(r,0) = \dfrac{1}{2G_2}\mathcal{H}_1\left[\xi^{-1}C_2;\xi\to r\right] \\ \tau_{zr}^{(2)}(r,0) = -\mathcal{H}_1\left[(1-2\nu_2)A_2 + C_2;\xi\to r\right] \\ \sigma_{zz}^{(2)}(r,0) = -\mathcal{H}_0\left[(2-2\nu_2)A_2 + C_2;\xi\to r\right], \end{cases} \tag{5.15b}$$

for solid #2, where $G_1,\ G_2$ are shear moduli, $\nu_1,\ \nu_2$ are Poisson's ratios and $A_1,\ A_2,\ C_1,\ C_2$, generally functions of ξ, will be determined by using the boundary conditions; superscripts '(1)' and '(2)' are used to denote the quantities pertaining to the material #1 and #2. Note that the components in Equations (5.15a,b) are referred to the respective coordinate system of each material with z-axis pointing into the materials, as shown in Figure 5.6. The continuity of stress across the interface requires

$$\sigma_{zz}^{(1)}(r,0) = \sigma_{zz}^{(2)}(r,0), \quad \tau_{zr}^{(1)}(r,0) = -\tau_{zr}^{(2)}(r,0). \tag{5.16}$$

Assuming flaw tolerance is achieved, the stresses at pull-off should satisfy

$$\tau_{zr}^{(1)}(r,0) = -\tau_{zr}^{(2)}(r,0) = Q(r/c), \quad (0 \le r \le c) \tag{5.17}$$

$$\sigma_{zz}^{(1)}(r,0) = \sigma_{zz}^{(2)}(r,0) = T(r/c), \quad (r \ge 0) \tag{5.18}$$

with

$$Q(r/c) = \begin{cases} -\tau_{\mathrm{f}} & (a \le r \le c) \\ 0, & (0 \le r < a) \end{cases} \tag{5.19}$$

and

$$T(r/c) = \begin{cases} \sigma_{\mathrm{th}} & (a < r < \infty) \\ 0, & (0 \le r \le a) \end{cases} \tag{5.20}$$

Substituting Equations (5.15a,b) into (5.16) leads to the relationships between functions $A_1,\ C_1$ and $A_2,\ C_2$ as

$$(2-2\nu_1)A_1 + C_1 = (2-2\nu_2)A_2 + C_2 \tag{5.21}$$

$$(1-2\nu_1)A_1 + C_1 = -(1-2\nu_2)A_2 - C_2 \tag{5.22}$$

By eliminating A_2 in Equations (5.21) and (5.22), C_2 can be expressed in terms of A_1 and C_1 as

$$C_2 = -\frac{A_1}{2}(\kappa_1\kappa_2 - 1) - \kappa_2 C_1, \tag{5.23}$$

where $\kappa_i \equiv 3 - 4\nu_i$ $(i = 1, 2)$. Similarly, using Equation (5.15a), the stress boundary conditions of Equations (5.17) and (5.18) for solid #1 can be rewritten in terms of Hankel transforms as

$$\tau_{zr}^{(1)}(r,0) = -\mathcal{H}_1\left[(1-2\nu_1)A_1 + C_1; \xi \to r\right] = Q(r/c), \quad (0 \le r \le c) \tag{5.24}$$

$$\sigma_{zz}^{(1)}(r,0) = -\mathcal{H}_0\left[(2-2\nu_1)A_1 + C_1; \xi \to r\right] = T(r/c). \quad (r \ge 0) \tag{5.25}$$

On the other hand, in the non-slipping region, the continuity of radial displacement requires

$$u_r^{(1)}(r,0) - u_r^{(2)}(r,0) = 0, \quad (r > c) \tag{5.26}$$

which, by using Equations (5.15a,b), can be rewritten as

$$\mathcal{H}_1\left[\xi^{-1}\left(\frac{C_1}{G_1} - \frac{C_2}{G_2}\right); \xi \to r\right] = 0. \quad (r > c) \tag{5.27}$$

On substituting (5.23) into (5.27) to eliminate C_2, we have

$$\mathcal{H}_1\left[\xi^{-1}\left(C_1 + \omega A_1\right); \xi \to r\right] = 0, \quad (r > c) \tag{5.28}$$

where

$$\omega = \frac{(\kappa_1\kappa_2 - 1)G_1}{2(G_2 + G_1\kappa_2)}.$$

Denoting

$$\psi(\xi) = A_1(\xi/c), \ \phi(\xi) = C_1(\xi/c) \tag{5.29}$$

Equations (5.24, 5.25) and (5.28) can be normalized to be

$$\mathcal{H}_1\left[(1-2\nu_1)\psi(\xi) + \phi(\xi); \ \xi \to \rho\right] = -c^2 Q(\rho), \quad (0 \le \rho \le 1) \tag{5.30}$$

$$\mathcal{H}_0\left[(2-2\nu_1)\psi(\xi) + \phi(\xi); \ \xi \to \rho\right] = -c^2 T(\rho), \quad (\rho \ge 0)) \tag{5.31}$$

$$\mathcal{H}_1\left[\xi^{-1}[\phi(\xi) + \omega\psi(\xi)]; \ \xi \to \rho\right] = 0, \quad (\rho > 1) \tag{5.32}$$

where $\rho = r/c$.

With Equation (5.20), inversion of Equation (5.31) gives rise to the relationship between functions $\psi(\xi)$ and $\phi(\xi)$ as

$$(2-2\nu_1)\psi(\xi) + \phi(\xi) = -c^2\sigma_{\text{th}}\int_{a/c}^{\infty} \rho J_0(\rho\xi)\mathrm{d}\rho = ca\sigma_{\text{th}}\xi^{-1}J_1(a\xi/c).$$

It follows that

$$\phi(\xi) = ca\sigma_{\text{th}}\xi^{-1}J_1(a\xi/c) - (2-2\nu_1)\psi(\xi). \tag{5.33}$$

Substituting Equation (5.33) back into (5.30) and (5.32) to eliminate $\phi(\xi)$ yields

$$\mathcal{H}_1\left[\psi(\xi);\xi\to\rho\right] = c^2Q(\rho) + ac\sigma_{\text{th}}\mathcal{H}_1\left[\frac{J_1(a\xi/c)}{\xi};\ \xi\to\rho\right],\ (0\le\rho\le 1) \tag{5.34}$$

$$\mathcal{H}_1\left[\xi^{-1}\psi(\xi);\xi\to\rho\right] = -\frac{a^2\sigma_{\text{th}}}{2[\omega-(2-2\nu_1)]\rho}.\ (\rho>1) \tag{5.35}$$

Equation (5.34) suggests that function $\psi(\xi)$ must have form

$$\psi(\xi) = ac\sigma_{\text{th}}\frac{J_1(a\xi/c)}{\xi} + \bar{\psi}(\xi), \tag{5.36}$$

where function $\bar{\psi}(\xi)$ satisfies, according to (5.34) and (5.35), the dual integral equations

$$\mathcal{H}_1\left[\bar{\psi}(\xi);\xi\to\rho\right] = c^2Q(\rho), \quad (0\le\rho\le 1) \tag{5.37}$$

$$\mathcal{H}_1\left[\xi^{-1}\bar{\psi}(\xi);\xi\to\rho\right] = -\frac{a^2\sigma_{\text{th}}\beta}{2\rho}, \quad (\rho>1) \tag{5.38}$$

with $\beta = \dfrac{(\kappa_1-1)/G_1-(\kappa_2-1)/G_2}{(\kappa_1+1)/G_1+(\kappa_2+1)/G_2}$ being the Dundurs' constant [24]. Without loss of generality, we can assume $\beta\ge 0$, i.e. $(\kappa_1-1)/G_1\ge(\kappa_2-1)/G_2$. Equations (5.37, 5.38) are just a special case of standard dual integral equations (3.40-3.41) with $\mathrm{F}_1(\rho) = c^2Q(\rho)$, $\mathrm{G}_2(\rho) = -a^2\sigma_{\text{th}}\beta/2\rho$. Actually, what we are interested in here is not the solution to $\bar{\psi}$ but the shear stress $\tau_{zr}^{(1)}(r,0)$ which, according to Equations (5.15a, 5.29, 5.36), can be expressed in terms of $\bar{\psi}$ as

$$\tau_{zr}^{(1)} = \frac{1}{c^2}\mathcal{H}_1\left[\bar{\psi}(\xi);\xi\to\rho\right].\ (\rho>1) \tag{5.39}$$

Substituting $\mathrm{G}_2(\rho) = -a^2\sigma_{\text{th}}\beta/2\rho$ into formula (3.45) yields

$$\mathrm{G}^*(\xi) = -\frac{\mathrm{d}}{\mathrm{d}\xi}\int_\xi^\infty \frac{\mathrm{G}_2(s)\mathrm{d}s}{\sqrt{s^2-\xi^2}} = -\frac{\pi a^2\sigma_{\text{th}}\beta}{4\xi^2}. \tag{5.40}$$

With Equation (5.19), substitution of $\mathrm{F}_1(\rho) = c^2Q(\rho)$ and Equation (5.40) into formula

(3.43) gives rise to

$$\begin{aligned}\mathcal{H}_1\left[\bar{\psi}(\xi);\xi\to\rho\right] &= \mathrm{F}_2(\rho)\\ &= \frac{2}{\rho^2\pi}\frac{\mathrm{d}}{\mathrm{d}\rho}\int_1^\rho \xi^3\sqrt{\rho^2-\xi^2}\mathrm{G}^*(\xi)\mathrm{d}\xi - \frac{2}{\pi\rho\sqrt{\rho^2-1}}\int_0^1 \frac{t^2\sqrt{1-t^2}\mathrm{F}_1(t)\mathrm{d}t}{\rho^2-t^2}\\ &= -\frac{a^2\sigma_{\mathrm{th}}\beta}{2\rho\sqrt{\rho^2-1}} + \frac{2c^2\tau_{\mathrm{f}}}{\pi\rho\sqrt{\rho^2-1}}\int_{a/c}^1 \frac{t^2\sqrt{1-t^2}}{\rho^2-t^2}\mathrm{d}t. \end{aligned} \tag{5.41}$$

Inserting Equation (5.41) into Equation (5.39) results in the shear stress

$$\begin{aligned}\tau_{zr}^{(1)}(r,0) &= \frac{1}{c^2}\mathcal{H}_1\left[\bar{\psi}(\xi);\xi\to\rho\right]\\ &= \frac{2\tau_{\mathrm{f}}}{\pi\rho\sqrt{\rho^2-1}}\int_{a/c}^1 \frac{t^2\sqrt{1-t^2}}{\rho^2-t^2}\mathrm{d}t - \frac{a^2\sigma_{\mathrm{th}}\beta}{2c^2\rho\sqrt{\rho^2-1}}. \quad (\rho>1)\end{aligned} \tag{5.42}$$

The continuity of the shear stress at edge of slipping region $\rho = 1$ requires that the stress singularity in Equation (5.42) vanishes, i.e.,

$$\lim_{\rho\to 1}\sqrt{\rho-1}\left[\frac{2\tau_{\mathrm{f}}}{\pi\rho\sqrt{\rho^2-1}}\int_{a/c}^1 \frac{t^2\sqrt{1-t^2}}{\rho^2-t^2}\mathrm{d}t - \frac{a^2\sigma_{\mathrm{th}}\beta}{2c^2\rho\sqrt{\rho^2-1}}\right] = 0.$$

It follows that

$$\frac{2\tau_{\mathrm{f}}}{\pi}\int_{a/c}^1 \frac{t^2}{\sqrt{1-t^2}}\mathrm{d}t = \frac{a^2\sigma_{\mathrm{th}}\beta}{2c^2},$$

namely,

$$\sqrt{\frac{c^2}{a^2}-1} + \frac{c^2}{a^2}\cos^{-1}\left(\frac{a}{c}\right) = \frac{\pi\sigma_{\mathrm{th}}\beta}{2\tau_{\mathrm{f}}}. \tag{5.43}$$

Equation (5.43) determines the radius of the slipping zone c as a function of the theoretical adhesion strength σ_{th}, critical friction strength τ_{f} and Dundurs' constant β. Taking $\tau_{\mathrm{f}} = \sigma_{\mathrm{th}}$, $\nu_1 = 0.3$, $G_2 \to \infty$ (nondeforming), Equation (5.43) gives $c \approx 1.024a$. Inserting Equation (5.43) back into Equation (5.42) yields

$$\begin{aligned}&\tau_{zr}^{(1)}(r,0) =\\ &\frac{2\tau_{\mathrm{f}}\sqrt{\rho^2-1}}{\pi\rho}\cos^{-1}\left(\frac{a}{c}\right) - \frac{\tau_{\mathrm{f}}}{\pi}\left[\cos^{-1}\left(\frac{\rho a-c}{\rho c-a}\right) + \cos^{-1}\left(\frac{\rho a+c}{\rho c+a}\right)\right], \quad (\rho>1)\end{aligned} \tag{5.44}$$

where Equations (A.11) and (A.12) have been used. Taking $c = 1.024a$, the friction stress in the contact area is plotted in Figure 5.7. As expected, the friction stress distribution

is continuous at the edge of the slipping region $r = c$.

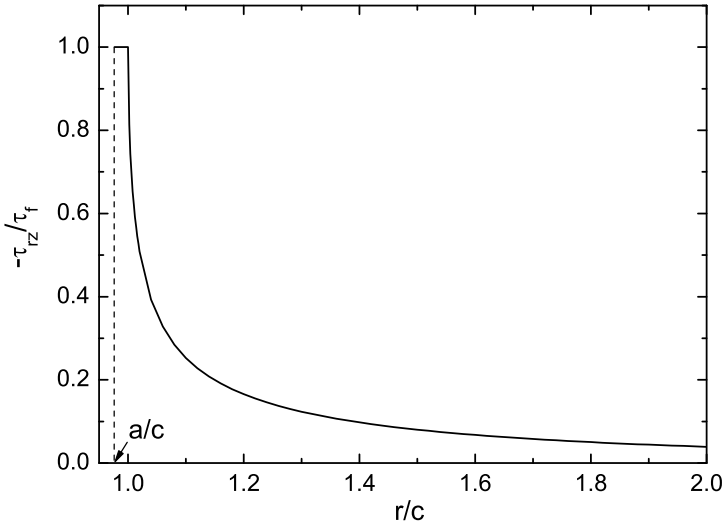

Figure 5.7.: Distribution of friction stress in the contact area.

Now, the normal and tangential tractions applied on the contact area can be summarized as follows,

$$\sigma_{zz}^{(1)}(r,0) = \sigma_{zz}^{(2)}(r,0) = \sigma_{\mathrm{th}}, \quad (0 \le r \le a) \tag{5.45}$$

$$\tau_{zr}^{(1)}(r,0) = -\tau_{zr}^{(2)}(r,0) =$$

$$\frac{\tau_{\mathrm{f}}}{\pi}\left\{\frac{2\sqrt{\rho^2-1}}{\rho}\cos^{-1}\left(\frac{a}{c}\right) - \left[\cos^{-1}\left(\frac{\rho a - c}{\rho c - a}\right) + \cos^{-1}\left(\frac{\rho a + c}{\rho c + a}\right)\right]\right\}, \ (r > c) \tag{5.46}$$

$$\tau_{zr}^{(1)}(r,0) = -\tau_{zr}^{(2)}(r,0) = -\tau_{\mathrm{f}}. \ \ (a \le r \le c) \tag{5.47}$$

The associated displacement in the normal direction at crack tip $r = a$ relative to a surface point at infinity is

$$\delta_1 = \frac{4\sigma_{\mathrm{th}} a(1-\nu_1^2)}{\pi E_1} + \frac{(1-2\nu_1)(1+\nu_1)\tau_{\mathrm{f}} c}{\pi E_1}\cos^{-1}\left(\frac{a}{c}\right), \tag{5.48}$$

$$\delta_2 = \frac{4\sigma_{\mathrm{th}} a(1-\nu_2^2)}{\pi E_2} - \frac{(1-2\nu_2)(1+\nu_2)\tau_{\mathrm{f}} c}{\pi E_2}\cos^{-1}\left(\frac{a}{c}\right). \tag{5.49}$$

Therefore, the crack tip opening

$$\delta_{\text{tip}}^{\text{f}} = \delta_1 + \delta_2 = \frac{4\sigma_{\text{th}} a}{\pi E^*} + \frac{2\beta\tau_{\text{f}} c}{\pi E^*} \cos^{-1}\left(\frac{a}{c}\right), \tag{5.50}$$

where $E^* = \left[(1-\nu_1^2)/E_1 + (1-\nu_2^2)/E_2\right]^{-1}$ is the combined elastic modulus. By using condition of Equation (5.1), the critical length scale for flaw tolerant adhesion now turns to be

$$a_{\text{cr}} = \frac{\pi\Delta\gamma E^*}{4\sigma_{\text{th}}^2}\left[1 + \frac{\tau_{\text{f}}\beta c}{2\sigma_{\text{th}} a}\cos^{-1}\left(\frac{a}{c}\right)\right]^{-1}. \tag{5.51}$$

When $\tau_{\text{f}} \to 0$ or $\beta \to 0$, Equation (5.51) will be reduced to Equation (5.6). Moreover, since $c \geq a$, Equation (5.43) implies that τ_{f} and β have the same sign. Therefore, the factor $\left[1 + \frac{\tau_{\text{f}}\beta c}{2\sigma_{\text{th}} a}\cos^{-1}(a/c)\right]^{-1}$ in Equation (5.51) must be smaller than unity, giving a smaller for frictional adhesion in contrast to that of the frictionless case.

5.2.2. Size-limited flaw tolerance solution for a circumferential external crack

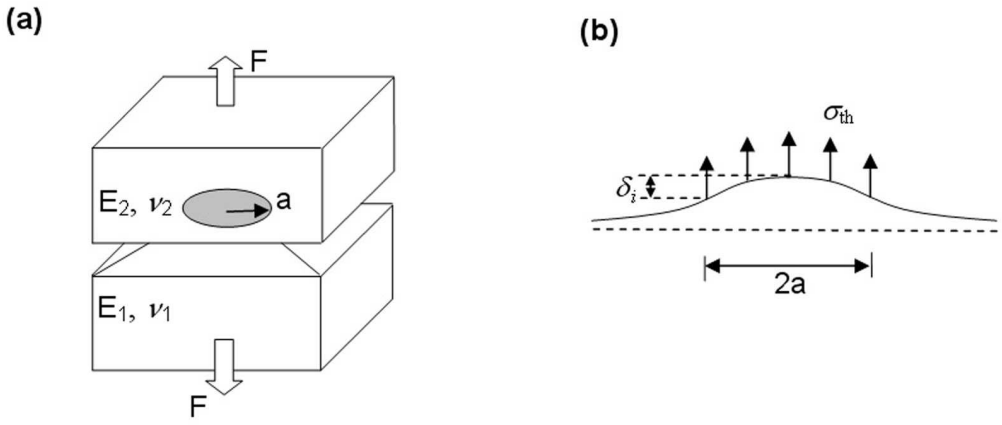

Figure 5.8.: (a) Schematic of a circumferential external crack. (b) At flaw tolerance state, the stress distribution over the contact region is uniformly equal to the theoretical adhesion strength.

Now, let us consider another crack configuration. As shown in Figure 5.8(a), two dissimilar materials adhered to each other over a circular area, forming a circumferential external crack. Similarly, we assume that the flaw tolerance state exists. If no friction is considered, the normal adhesive stress at pull-off will be uniformly equal to the theoretical adhesion strength σ_{th}, as shown in Figure 5.8(b). The crack tip opening $\delta_{\text{tip}}^{\text{f}} = \delta_1 + \delta_2$,

where δ_1 and δ_2 are surface displacement at $r = a$ relative to the surface point $r = 0$. Based on the half-space assumption for the solids, it is easy to obtain [60]

$$\delta_1 = \frac{4\sigma_{\text{th}} a(1-\nu_1^2)}{\pi E_1}\left(\frac{\pi}{2}-1\right), \quad \delta_2 = \frac{4\sigma_{\text{th}} a(1-\nu_2^2)}{\pi E_2}\left(\frac{\pi}{2}-1\right).$$

It follows that

$$\delta_{\text{tip}}^{\text{f}} = \delta_1 + \delta_2 = \frac{4\sigma_{\text{th}} a}{\pi E^*}\left(\frac{\pi}{2}-1\right). \tag{5.52}$$

Applying Equation (5.52) to condition (5.1) immediately leads to the critical length scale for flaw tolerance as

$$a_{\text{cr}} = \frac{\pi \Delta\gamma E^*}{2(\pi-2)\sigma_{\text{th}}^2}. \tag{5.53}$$

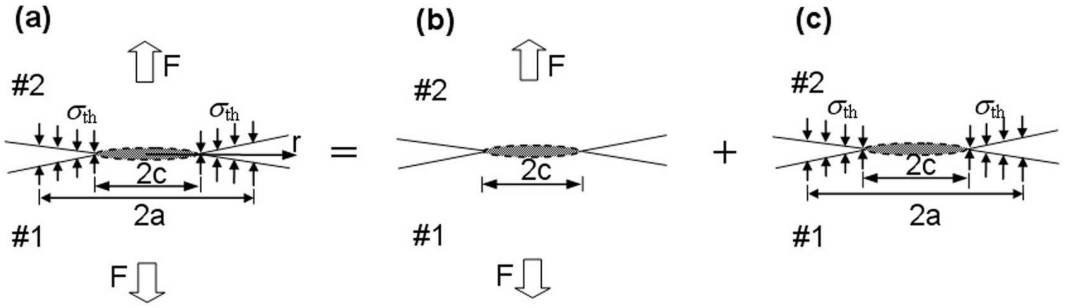

Figure 5.9.: (a) In the Dugdale model of this external crack problem, the contact area is assumed to consist of a cohesive zone ($c \le r \le a$) and a perfectly bonded region ($r < c$). The problem is equivalent to the superposition of two sub-problems (b) an external crack under remote tension and (c) an external crack with closure stress σ_{th} over ring-shaped cohesive zone.

Equation (5.53) provides us the critical length scale for the contact area below which the theoretical adhesion strength can be achieved. In order to obtain more insight into the evolution process of adhesion strength as the size decreases, we need to know the adhesion strength as a function of the crack size. On the basis of Dugdale model, the contact area consists of a cohesive zone ($c \le r \le a$) in which the adhesion stress equals to the theoretical strength σ_{th} and a perfectly bonded region ($r < c$) in which the separation between contact surfaces vanishes, as shown in Figure 5.9(a). In mechanics, this problem can be treated as a superposition of two sub-problems: (a) a circumferential external crack of radius c under remote force F (Figure 5.9b) and (b) a circumferential external crack with closure stress σ_{th} over a ring-shaped cohesive zone at the tip (Figure 5.9c).

For both cases, the stress intensity factors and separations at $r = a$ are given by [94]

$$K_{\mathrm{I}}^{(\mathrm{a})} = \frac{F}{2c\sqrt{\pi c}}, \tag{5.54a}$$

$$\delta^{(\mathrm{a})}(a) = \frac{F}{\pi E^* c}\cos^{-1}\frac{c}{a} = \frac{2K_{\mathrm{I}}^{(\mathrm{a})}\sqrt{\pi c}}{\pi E^*}\cos^{-1}\frac{c}{a}, \tag{5.54b}$$

$$K_{\mathrm{I}}^{(\mathrm{b})} = -\frac{\sigma_{\mathrm{th}}}{\sqrt{\pi c}}\left(\sqrt{a^2-c^2} + \frac{a^2}{c}\cos^{-1}\frac{c}{a}\right), \tag{5.55a}$$

$$\delta^{(\mathrm{b})}(a) = \frac{2}{\pi E^*}K_{\mathrm{I}}^{(\mathrm{b})}\sqrt{\pi a}\cos^{-1}\frac{c}{a} - \frac{4\sigma_{\mathrm{th}}}{\pi E^*}\left[(a-c) - \sqrt{a^2-c^2}\cos^{-1}\frac{c}{a}\right]. \tag{5.55b}$$

The continuity of adhesive stress at $r = c$ requires

$$K_{\mathrm{I}}^{(\mathrm{a})} + K_{\mathrm{I}}^{(\mathrm{b})} = 0,$$

which, by using Equation (5.54a) and (5.55a), gives rise to

$$F = 2a^2\sigma_{\mathrm{th}}\left(\frac{c}{a}\sqrt{1-\frac{c^2}{a^2}} + \cos^{-1}\frac{c}{a}\right). \tag{5.56}$$

It follows that

$$\frac{F}{\pi a^2} = \frac{2}{\pi}\left(\frac{c}{a}\sqrt{1-\frac{c^2}{a^2}} + \cos^{-1}\frac{c}{a}\right)\sigma_{\mathrm{th}}. \tag{5.57}$$

On the other hand, the Dugdale model indicates that at the critical (pull-off) moment the crack tip opening must be equal to the interaction range of the adhesion, i.e.,

$$\delta_{\mathrm{tip}}^{\mathrm{f}} = \delta^{(\mathrm{a})}(a) + \delta^{(\mathrm{b})}(a) = \frac{4\sigma_{\mathrm{th}}}{\pi E^*}\left[\sqrt{a^2-c^2}\cos^{-1}\frac{c}{a} - (a-c)\right] = \frac{\Delta\gamma}{\sigma_{\mathrm{th}}}. \tag{5.58}$$

Equation (5.57), in conjunction with (5.58), determines implicitly the critical adhesive force (pull-off force) F^{f} as a function of E^*, $\Delta\gamma$, σ_{th} and a. Figure 5.10 plots the variation of the normalized adhesion force with $(\pi E^*\Delta\gamma/4a\sigma_{\mathrm{th}}^2)^{1/2}$, in contrast to the prediction based on the Griffith criterion, i.e., $F^{\mathrm{f}}/\pi a^2\sigma_{\mathrm{th}} = \sqrt{8E^*\Delta\gamma/\pi a\sigma_{\mathrm{th}}^2}$. It is observed that as the size of the contact region decreases, the adhesion strength will increase and finally saturates at the theoretical strength σ_{th} when a reaches $\frac{\pi E^*\Delta\gamma}{2(\pi-2)\sigma_{\mathrm{th}}^2}$, a critical value as predicted by Equation (5.53).

Like the penny-shaped crack case, friction can also be taken into account for the flaw tolerance problem of circumferential external crack. Partial slip model is used again, in which slip is allowed whenever the friction stress reaches critical friction strength τ_{f}.

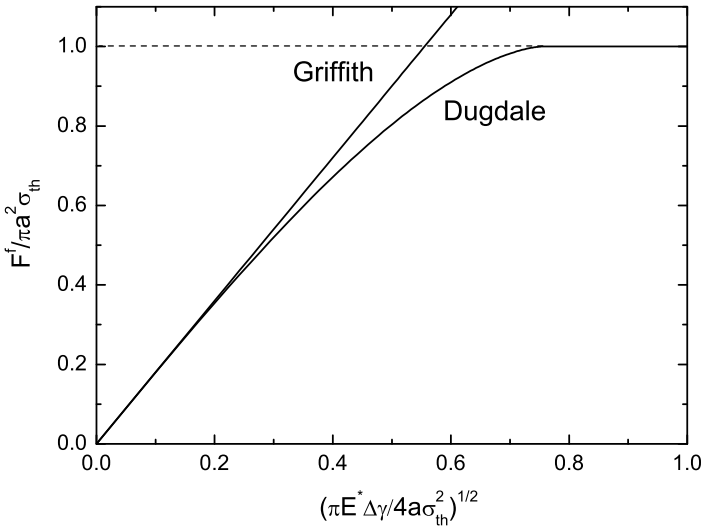

Figure 5.10.: Variation of adhesion strength with crack size.

Therefore, the contact region ($0 \leq r \leq a$) can be divided into two regions, one is slipping zone ($c \leq r \leq a$) in which the friction force is uniformly equal to τ_{f}, and the other is non-slipping zone ($0 \leq r \leq c$) in which no relative slip occur between two surfaces and the friction force remains to be found. Owing to the flaw tolerance state, the normal adhesive force is uniformly equal to the theoretical adhesion strength σ_{th} at pull-off (Figure 5.11). Actually, this boundary condition problem has been solved in subsection 4.2.4. Equations (4.82a,b,c) gives the stresses applied on two surfaces as

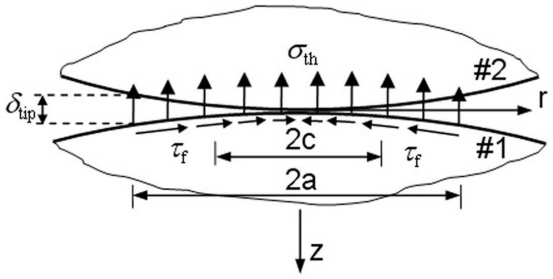

Figure 5.11.: Flaw tolerance state for frictional adhesion (circumferential external crack). For clarity, only the stress applied on material #1 is plotted.

$$\sigma_{zz}^{(1)}(r,0)=\sigma_{zz}^{(2)}(r,0)=\sigma_{\rm th},\quad (0\le r\le a)$$
$$\tau_{zr}^{(1)}(r,0)=-\tau_{zr}^{(2)}(r,0)=\frac{\tau_{\rm f}}{\pi}\left[\sin^{-1}\left(\frac{ar-c^2}{(a-r)c}\right)+\sin^{-1}\left(\frac{ar+c^2}{(a+r)c}\right)\right],\quad (0\le r<c)$$
$$\tau_{zr}^{(1)}(r,0)=-\tau_{zr}^{(2)}(r,0)=\tau_{\rm f}.\quad (c\le r\le a)$$

The outer radius of the non-slipping zone c is determined by

$$\frac{a+\sqrt{a^2-c^2}}{c}=\exp\left(\frac{\sigma_{\rm th}\beta}{\tau_{\rm f}}\right). \tag{5.59}$$

The associated displacement at crack tip $r=a$ relative to the point $r=0$ is given by

$$\delta_1=\frac{2\sigma_{\rm th}a}{E_1^*}\left(1-\frac{2}{\pi}\right)+\frac{2(\kappa_1-1)\tau_{\rm f}a}{\pi(\kappa_1+1)E_1^*}\left[1-\frac{2}{\pi}\sin^{-1}\left(\frac{c}{a}\right)\right], \tag{5.60a}$$
$$\delta_2=\frac{2\sigma_{\rm th}a}{E_2^*}\left(1-\frac{2}{\pi}\right)-\frac{2(\kappa_2-1)\tau_{\rm f}a}{\pi(\kappa_2+1)E_2^*}\left[1-\frac{2}{\pi}\sin^{-1}\left(\frac{c}{a}\right)\right], \tag{5.60b}$$

where $E_1^*=E_1/(1-\nu_1^2)$, $E_2^*=E_2/(1-\nu_2^2)$. The crack tip opening thus can be written as

$$\delta_{\rm tip}^{\rm f}=\delta_1+\delta_2=\frac{2\sigma_{\rm th}a}{\pi E^*}(\pi-2)+\frac{2\tau_{\rm f}a\beta}{\pi E^*}\left[1-\frac{2}{\pi}\sin^{-1}\left(\frac{c}{a}\right)\right], \tag{5.61}$$

with $E^*=[(1-\nu_1^2)/E_1+(1-\nu_2^2)/E_2]^{-1}$. Substituting Equation (5.61) into (5.1) yields

$$a_{\rm cr}=\frac{\pi E^*\delta_0}{2\sigma_{\rm th}(\pi-2)}\left[\frac{\pi-2}{(\pi-2)+2\tau_{\rm f}\beta\cos^{-1}(c/a)/\pi\sigma_{\rm th}}\right]. \tag{5.62}$$

When $\tau_{\rm f}\to 0$ or $\beta\to 0$, Equation (5.62) will be reduced to Equation (5.53). Since $c\le a$, Equation (5.59) indicates that $\tau_{\rm f}$ and β have the same sign. The factor

$$\left[\frac{\pi-2}{(\pi-2)+2\tau_{\rm f}\beta\cos^{-1}(c/a)/\pi\sigma_{\rm th}}\right]$$

in Equation (5.62) therefore must be smaller than unity, giving a smaller critical length scale for frictional adhesion in comparison with that of the frictionless case. Recalling the similar result associated with the penny-shape crack, we conclude that the interfacial friction retards flaw tolerance.

5.2.3. Size-limited flaw tolerance solution for other crack configurations

It should be of interest as well to extend the concept of size-limited flaw tolerance to other possible crack configurations like two-dimensional internal crack (Figure 5.12a) and two-dimensional external crack (Figure 5.12b). For simplicity, frictions are neglected here.

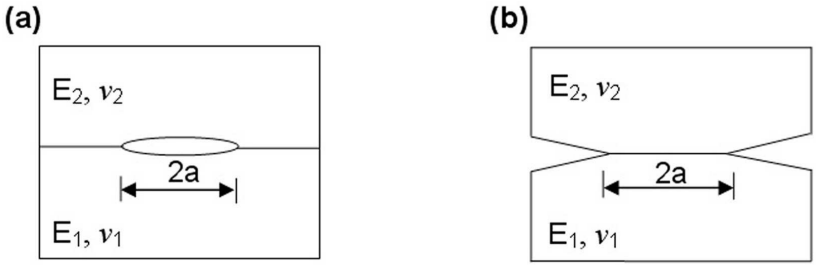

Figure 5.12.: Schematics of other crack configurations: (a) 2D internal crack. (b) 2D external crack.

(a) Two-dimensional internal crack

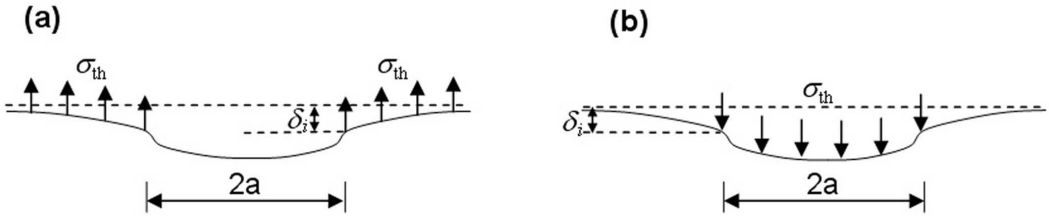

Figure 5.13.: (a) For a half-space subjected to uniform stress on region external to the crack area, the crack tip displacement relative to a remote point on the surface is equivalent to that of case (b) in which the uniform pressure is applied on the crack surface.

Assuming that flaw tolerance is achieved, let us check if the condition of Equation (5.1) can be satisfied. In this case, the crack tip opening equals the summation of δ_1 and δ_2, the surface displacements at $x = a$ relative to a remote surface point, as shown in Figure 5.13(a). The mathematical problem of finding δ_i $(i = 1,\ 2)$ can be simplified by superposing a uniform pressure equal to σ_{th} on the entire surface. The problem of Figure 5.13(a) is then converted to an elastic half-space subjected to uniform pressure σ_{th} over strip $|x| \leq a$ (Figure 5.13b) while δ_i remains unaltered. However, it is found that under such pressure, the normal surface displacement at $|x| = a$ relative to a remote

point on the interface goes to infinity. This is actually an inevitable feature of two-dimensional deformation of an elastic half-space [60]. Therefore, for this case the crack tip opening is infinite no matter how big the crack is, suggesting no solution for flaw tolerance. In this regard, material has "zero tolerance" to the two-dimensional internal crack.

(b) Two-dimensional external crack

For 2D external crack case (Figure 5.14), the existence of the flaw tolerance state depends on the surface displacements at $x = a$ relative to that of point $x = 0$ instead of a remote point. Assuming flaw tolerance state is achieved, the relative displacement for two solids can be easily calculated as [96]

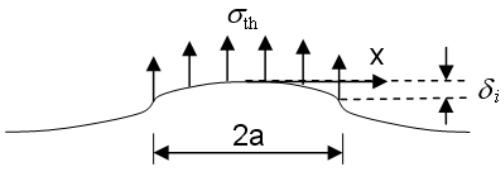

Figure 5.14.: Flaw tolerance state for 2D external crack.

$$\delta_1 = \frac{4(1-\nu_1^2)\sigma_{\text{th}} a \ln 2}{\pi E_1}, \tag{5.63a}$$

$$\delta_2 = \frac{4(1-\nu_2^2)\sigma_{\text{th}} a \ln 2}{\pi E_2}. \tag{5.63b}$$

It follows that the crack tip opening

$$\delta_{\text{tip}}^{\text{f}} = \delta_1 + \delta_2 = \frac{4 \ln 2 \sigma_{\text{th}} a}{\pi E^*}, \tag{5.64}$$

with $E^* = [(1-\nu_1^2)/E_1 + (1-\nu_2^2)/E_2]^{-1}$. Substituting Equation (5.64) into Equation (5.1) yields

$$a_{\text{cr}} = \frac{\pi}{4 \ln 2} \frac{\Delta\gamma E^*}{\sigma_{\text{th}}^2}. \tag{5.65}$$

In addition to the typical crack configurations discussed above, critical length scale for flaw tolerance also has been observed in other configurations like thin film [30]. We note that all the crack configurations, except the 2D internal crack, have critical length

scales for flaw tolerance that can be expressed in a unified form

$$a_{\mathrm{cr}} = \Omega \frac{E^* \Delta\gamma}{\sigma_{\mathrm{th}}^2}, \tag{5.66}$$

where Ω is a geometrical constant typically of order of magnitude unity but varying with flaw geometry. For instance, in the case involving penny-shaped crack-like flaw, $\Omega = \pi/4$. Alternatively, the flaw tolerance condition $a \leq a_{\mathrm{cr}} = \Omega \Delta\gamma E^*/\sigma_{\mathrm{th}}^2$ can also be expressed by

$$\Lambda_{\mathrm{ft}}^a = \frac{\Delta\gamma E^*}{\sigma_{\mathrm{th}}^2 a} \geq \frac{1}{\Omega} \approx 1, \tag{5.67}$$

where Λ_{ft}^a can be referred to as a *flaw tolerance number*. Equation (5.67) suggests that a sufficiently large flaw tolerance number is necessary to achieve the flaw tolerance state. During our previous discussion, we always treat the material as an elastic half-space, implying that the dimension of the material itself is quite larger than that of the contact flaws. This assumption is sound for macroscopic materials. In order to find the material to tolerate crack-like flaws of all sizes, Gao and Chen [29] proposed a strategy of constraining the dimension of material. It is pointed out that the generalized flaw tolerance is achieved when the flaw tolerance number $\Lambda_{\mathrm{ft}}^H = \Delta\gamma E^*/\sigma_{\mathrm{th}}^2 H$ is not less than a quantity on order of 1, where H denotes the characteristic size of the material instead of the flaws. This conclusion does make sense since the flaw size a will never exceed the material dimension H. If $\Lambda_{\mathrm{ft}}^H \geq 1$ is ensured, condition $\Lambda_{\mathrm{ft}}^a \geq 1$ must be met for all possible cracks, resulting in a "generalized" flaw tolerance state. In a word, for traditional homogeneous material, general flaw tolerance can be achieved by small material or structure. But for the macroscopic material, only propagation of very small crack-like flaws can be suppressed.

Now, the question we are most concerned about is whether and how flaw tolerance can be achieved for macroscopic contact with rough surfaces where crack-like flaws with various sizes arise randomly in regions of poor contact. Based on Equation (5.67), the flaw tolerance condition for macroscopic contact would require

$$\frac{\Delta\gamma E^*}{\sigma_{\mathrm{th}}^2 a} \geq 1. \quad (0 < a < \infty) \tag{5.68}$$

While it is obvious that this condition can not be satisfied for a homogeneous material system with constant parameters E^*, $\Delta\gamma$, σ_{th}, Equation (5.68) suggests the following three strategies to achieve flaw tolerant adhesion for macroscopic contact.

Strategy 1: The flaw tolerance condition in Equation (5.68) can be satisfied by

having a material with effective Young's modulus increasing proportional to the crack size, i.e. $E^* \propto a$. Since the zone of stress field affected by an interfacial crack is on the order of the crack size a, the behavior of the crack would also be dominated by the elastic property of the material within a depth on the order of a from the surface. Therefore, this strategy corresponds to an elastically nonhomogeneous material with elastic constant increasing as a function of depth from the surface (see section 5.3).

Strategy 2: The flaw tolerance condition in Equation (5.68) can be satisfied by having a material with work of adhesion increasing proportional to the crack size, i.e. $\Delta\gamma \propto a$. This strategy corresponds to a material with hierarchical (multi-scale) energy dissipation mechanisms (see section 5.4).

Strategy 3: The flaw tolerance condition in Equation (5.68) can be satisfied by having a material with scale-dependent adhesion strength, i.e. $\sigma_{\text{th}} \propto 1/\sqrt{a}$. This strategy corresponds to hierarchically weakening the adhesion strength to increase the fracture process zone along the adhesive interface. However, this strategy by itself leads to vanishing adhesion strength in the limit of large cracks, in which case the concept of flaw tolerance also becomes meaningless. From this point of view, the strategy of scale-dependent reduction of adhesion strength should be used only in combination with graded elasticity and hierarchical energy dissipation in order not to over-degrading the adhesion strength. This will be shown in the later discussion on the bottom-up designed hierarchical structure (see subsection 5.4.3). We do not pursue this point further in this thesis.

While it will be most effective to use a combination of these strategies to achieve optimal result, for conceptual clarity we will discuss them separately in the following sections.

5.3. Flaw tolerance via graded elasticity

Since the stress field around a crack occupies a region on the same order as the crack size, the strategy of having an effective Young's modulus increasing proportional to the crack size, $E^* \propto a$, can be achieved by adopting a nonhomogeneous material with Young's modulus rising as a function of distance from the surface. In this regard, simply increasing E^* in a homogeneous material is not a practical solution for flaw tolerant adhesion since sufficiently flexible material in the vicinity of the surface is necessary to achieve good contact with a rough surface. A compromise between soft surface for conformal contact and stiff bulk for flaw tolerance is to grade the elastic property in such

a way that the average stiffness around a crack is rigid enough to suppress crack growth while the surface remains flexible enough to allow good contact. Graded materials of various kinds have previously been considered to enhance the resistance to frictional sliding-contact and indentation [59, 76, 92]. Here we show that they can also lead to flaw tolerant adhesion.

5.3.1. Theoretical modeling

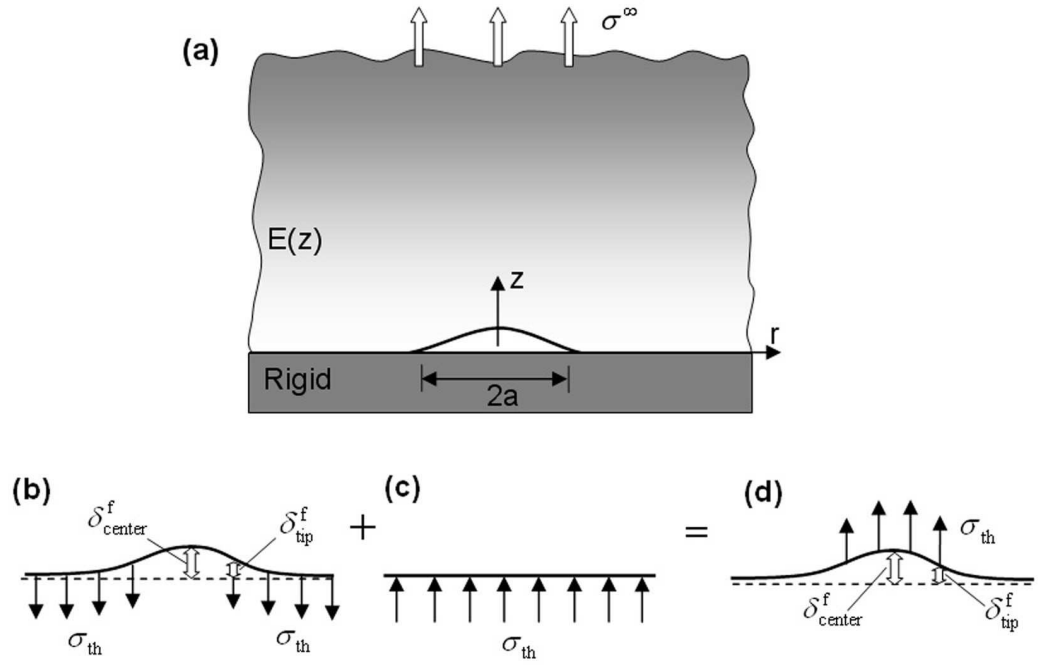

Figure 5.15.: Flaw tolerant adhesion via graded elasticity. (a) A non-homogeneous elastic material with graded Young's modulus $E(z)$ is in contact with a rigid substrate. (b) In the state of flaw tolerance, the adhesive stress outside the crack is uniform and equal to the theoretical strength at the critical state of pull-off. By superposing a uniform pressure of σ_{th} on the entire surface (c), the flaw tolerant adhesion problem is converted into an elastic half-space subjected a uniform pressure over a circular area (d).

To demonstrate the strategy of graded elasticity for flaw tolerant adhesion, we consider an elastic half-space $z \geq 0$ adhering to a rigid substrate, as shown in Figure 5.15(a). We assume that the Young's modulus varies as a function of distance from the surface $E = E(z)$ and Poisson's ratio ν as a constant. A penny-shaped interfacial crack of radius a is used to simulate the random contact flaws along the interface. The question is whether it is possible to select a function $E(z)$ such that cracks of all sizes are tolerated, in which case the stress outside the crack uniformly reaches the theoretical strength σ_{th}

at pull-off while the crack tip separation $\delta_{\text{tip}}^{\text{f}}$ does not exceed δ_0 (Figure 5.15b).

Likewise, the posed mathematical problem can be simplified by superposing a uniform pressure equal to σ_{th} on the entire surface, as shown in Figure 5.15(c). The flaw tolerance solution of Figure 5.15(a) is then converted to an elastic half-space subjected to uniform pressure σ_{th} over $r \leq a$, as shown in Figure 5.15(d). The crack tip separation $\delta_{\text{tip}}^{\text{f}}$ in Figure 5.15(b) is equal to the surface displacement at $r = a$ relative to a surface point at infinity in Figure 5.15(d). The condition for flaw tolerance is that $\delta_{\text{tip}}^{\text{f}}$ should stay within the interaction range of adhesion forces, i.e.,

$$\delta_{\text{tip}}^{\text{f}} \leq \delta_0 = \frac{\Delta\gamma}{\sigma_{\text{th}}} \quad \text{for any crack size } 0 < a < \infty. \tag{5.69}$$

For homogeneous materials, Equation (5.69) can not be satisfied since $\delta_{\text{tip}}^{\text{f}}$ is a monotonically increasing function of a. In the special case of $\nu = 0.5$ (a condition approximately satisfied by many soft biological tissues), an interesting solution to the problem posed in Figure 5.15 and Equation (5.69) is the so-called Gibson soil [37] with

$$E(z) = E_0 z / c_0. \tag{5.70}$$

From the analysis of Gibson [37], one can calculate $(\delta_{\text{tip}}^{\text{f}})_{\text{Gibson}} = 3\sigma_{\text{th}} c_0 / 2E_0$ and obtain from Equation (5.69) the flaw tolerance solution

$$E(z) = \frac{3\sigma_{\text{th}}^2 z}{2\Delta\gamma}, \quad \nu = 0.5. \tag{5.71}$$

The Gibson soil defined in Equation (5.71) is then predicted to tolerate interfacial cracks of all sizes when it is brought into contact with a rigid substrate. According to our hypothesis, it should also adhere robustly on a random rigid rough surface.

The flaw tolerance solution in the form of Gibson's soil can be understood from the following heuristic point of view. As indicated by Equation (5.66), a given homogeneous material can only tolerate cracks below a critical size. We can also interpret this result in a slightly different way that, for a given crack size, there exists a critical Young's modulus for the material above which the crack growth is suppressed. We note that this critical Young's modulus scales up with the crack size, indicating that small cracks can be tolerated by relatively soft material but the tolerance of larger cracks requires stiffer material. Since the zone of stress field affected by an interfacial crack is on the order of the crack size a, the behavior of the crack would also be dominated by the elastic property of the material within a depth on the order of a from the surface. Therefore,

if we distribute stiffer material in the bulk (for flaw tolerance) and softer material near the surface (for good contact with rough surfaces), the requirement for the Young's modulus to increase with crack size can be satisfied. The Gibson soil demonstrates the basic principle of flaw tolerant adhesion via graded elasticity.

In the more general case of $\nu \neq 0.5$, the linearly graded material $E(z) = E_0 z/c_0$, still referred to as the Gibson soil, is no longer flaw tolerant to any crack size as the crack tip separation $\delta^{\mathrm{f}}_{\mathrm{tip}}$ diverges logarithmically with the crack size a. On the other hand, we still expect that the stiffness of a flaw tolerant adhesive material is distributed in a way similar to that of the Gibson soil. Consider a monotonically increasing stiffness function $E(z)$ similar to that of the Gibson soil. While it is difficult to obtain a general solution to $E(z)$, we derive below an asymptotical solution in the limit of large cracks $\delta^{\mathrm{f}}_{\mathrm{tip}}(a \to \infty)$.

To derive the asymptotic solution in the limit of $a \to \infty$, let us first focus on the displacement field in the vicinity of $r = 0$ (Figure 5.15d) which, due to symmetry conditions in this limit, should have only one non-zero displacement component u_z that depends only on z and leads to only one non-zero strain component ε_{zz}. Under this circumstance, the equilibrium equations and Hooke's law are reduced to

$$\frac{\partial \sigma_{zz}}{\partial z} = 0, \tag{5.72}$$

$$\sigma_{zz} = \frac{E(z)(1-\nu)\varepsilon_{zz}}{(1+\nu)(1-2\nu)}. \tag{5.73}$$

Considering the boundary condition $\sigma_{zz} = -\sigma_{\mathrm{th}}$ at $z = 0$, the solutions to Equations (5.72) and (5.73) are $\sigma_{zz} = -\sigma_{\mathrm{th}}$ and

$$\varepsilon_{zz} = -\frac{(1+\nu)(1-2\nu)\sigma_{\mathrm{th}}}{(1-\nu)E(z)}. \tag{5.74}$$

Therefore, the asymptotical solution to the surface deflection at the center of the pressurized region ($z = 0,\ r = 0$) in Figure 5.15(d) is

$$\lim_{a\to\infty} \delta^{\mathrm{f}}_{\mathrm{center}} = \frac{(1+\nu)(1-2\nu)\sigma_{\mathrm{th}}}{(1-\nu)} \int_0^\infty \frac{1}{E(z)} \mathrm{d}z. \tag{5.75}$$

Provided that the integral in Equation (5.75) is integrable, the following relation can be shown appropriate (Appendix B):

$$\lim_{a\to\infty}\delta^{\mathrm{f}}_{\mathrm{tip}}=\frac{1}{2}\lim_{a\to\infty}\delta^{\mathrm{f}}_{\mathrm{center}}=\frac{(1+\nu)(1-2\nu)\sigma_{\mathrm{th}}}{2(1-\nu)}\int_0^\infty\frac{1}{E(z)}\mathrm{d}z. \tag{5.76}$$

Since large cracks are usually more susceptible to growth than small cracks, incorporating Equation (5.76) into Equation (5.69) yields a necessary condition for flaw tolerance via graded elasticity as

$$\int_0^\infty\frac{1}{E(z)}\mathrm{d}z=\frac{2(1-\nu)\Delta\gamma}{(1+\nu)(1-2\nu)\sigma^2_{\mathrm{th}}},\quad(-1<\nu<0.5). \tag{5.77}$$

For example, if we consider Gibson-soil-like modulus grading

$$E(z)=E_0(1+z/c_0)^\alpha, \tag{5.78}$$

where $\alpha>0$, E_0 is the value of Young's modulus at the surface and c_0 is a length parameter, the flaw tolerance condition (with no over-design) according to Equation (5.77) becomes

$$\alpha>1,\ c_0=\frac{2(1-\nu)(\alpha-1)E_0\Delta\gamma}{(1-2\nu)(1+\nu)\sigma^2_{\mathrm{th}}},\quad -1<\nu<0.5. \tag{5.79}$$

Assuming the parameter α remains close to 1, similar to the Gibson soil, the parameter c_0 measures the rate of change of Young's modulus with the depth z. The smaller the c_0, the steeper the rise of $E(z)$ with z. $c_0\to\infty$ corresponds to a homogeneous material. Taking $\alpha=2$, $\sigma_{\mathrm{th}}=20$ MPa, $E_0=1$ GPa, $\nu=0.25$, $\Delta\gamma=0.024$ J/m^2, the critical c_0 is estimated to be 144 nm.

For materials with graded Young's modulus given in the form of Equation (5.78), analytical solutions to the problem described in Figure 5.15(d) have been found for several special cases. For instance, Brown and Gibson [13] presented a solution for $\alpha=1$ with Poisson's ratio ν in the range of $0-1/2$. Chuaprasert and Kassir [17] obtained a solution for any $\alpha>0$ and ν satisfying the relation $\alpha\nu=1-2\nu$ (e.g., $\alpha=2$, $\nu=0.25$). Based on these existing solutions for nonhomogeneous elastic solids, Figure 5.16 shows the evolution of the normalized energy release rate $\mathcal{G}E_0/\sigma^2_{\mathrm{th}}c_0=E_0\delta^{\mathrm{f}}_{\mathrm{tip}}/\sigma_{\mathrm{th}}c_0$ with the crack size a for $\alpha=$0, 1 and 2. In the well-known homogeneous case $\alpha=0$, $\mathcal{G}$ grows linearly with the crack size. In fact, $\mathcal{G}$ grows unboundedly with increasing crack size as long as $\alpha\le1$ (linearly when $\alpha=0$ and logarithmically when $\alpha=1$). For $\alpha=2$ and $\nu=0.25$, $\mathcal{G}$ is seen to asymptotically approach a constant value $5\sigma^2_{\mathrm{th}}c_0/12E_0$. That is, $\delta^{\mathrm{f}}_{\mathrm{tip}}$ has an asymptotical limit of $5\sigma_{\mathrm{th}}c_0/12E_0$ which agrees with the asymptotical solution given by Equation (5.76) and confirms that this material can be made flaw tolerant by

choosing parameters satisfying Equation (5.79).

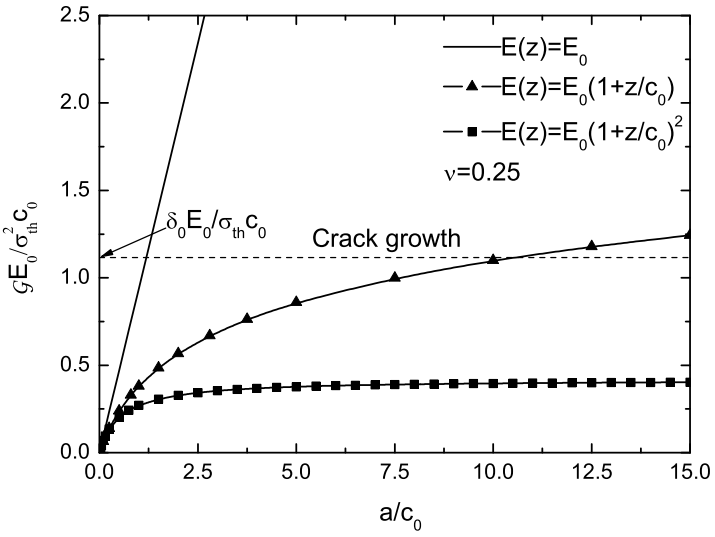

Figure 5.16.: The variation of normalized energy release rate $\mathcal{G}E_0/\sigma_{\rm th}^2 c_0$ as a function of the normalized crack size a/c_0 for a graded material with $E(z) = E_0(1 + z/c_0)^\alpha$ ($\alpha = 0, 1, 2$) and $\nu = 0.25$. The dotted line indicates the crack growth criterion.

5.3.2. Numerical simulations

To further verify the strategy of flaw tolerant adhesion via graded elasticity, we have also performed numerical simulations using Tahoe. The simulation system involves an elastic cylindrical punch of finite dimension (radius×height=$6a \times 6a$) in contact with a rigid substrate (Figure 5.17a). A penny-shaped interfacial crack of radius a is introduced at the central region of contact. A uniform vertical displacement is applied on the top surface of the cylinder. The net force F at a given displacement load is calculated by summing up all the nodal forces on the top surface. We consider a graded material of the type $E = E_0(1 + z/c_0)^2$ with $E_0 = 1.0$ GPa and $c_0 = 144$ nm; the latter is evaluated according to Equation (5.79) by taking $\sigma_{\rm th} = 20$ MPa, $\Delta\gamma = 0.024$ J/m^2 and $\nu = 0.25$. The results are compared to the homogeneous case $E \equiv E_0$. The pull-off force $F^{\rm f}$ is calculated for three different punch sizes: 50 nm, 500 nm and 1000 nm. The normalized adhesion strength $F^{\rm f}/A\sigma_{\rm th}$, where A is the actual contact area, is plotted as a function of the non-dimensional parameter $(\sigma_{\rm th}^2 a/E_0\Delta\gamma)^{1/2}$ in Figure 5.17(b). As expected, the adhesion strength in the homogeneous case decreases as the contact size increases, while

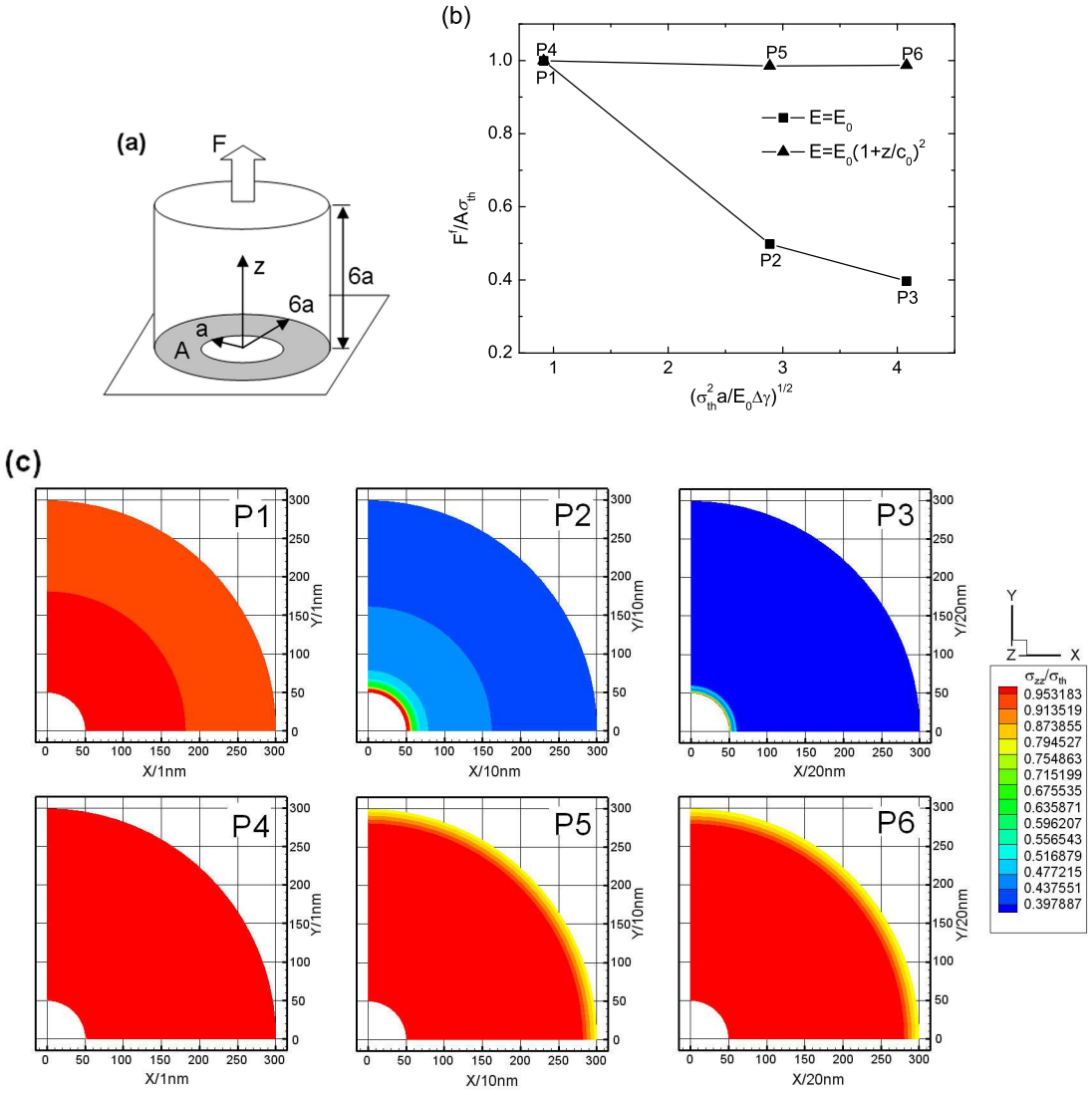

Figure 5.17.: FEM simulations of an elastic cylindrical punch adhering to a rigid substrate. (a) Schematic of the simulation model. (b) The normalized adhesion strength $F^{\mathrm{f}}/A\sigma_{\mathrm{th}}$ as a function of the size parameter $(\sigma_{\mathrm{th}}^2 a/E_0\Delta\gamma)^{1/2}$; A being the actual contact area. (c) The distribution of adhesion stress within the contact region for six pull-off states, P1-P6. Due to the axial symmetry, only a quarter of the contact area is shown.

in the graded case the adhesion strength is maintained at the theoretical strength σ_{th} independent of the punch size. Figure 5.17(c) shows the stress distribution inside the contact area for the six different pull-off states, P1-P6, shown in Figure 5.17(b). The top three figures in Figure 5.17(c) show that pull-off in the homogeneous cases occurs increasingly by crack propagation via stress concentration near the crack tip as the contact size increases. In this situation, size reduction helps to homogenize the stress distribution inside the contact area and change the failure mode from crack growth to uniform detachment near the theoretical strength of adhesion. In contrast, the bottom three figures in Figure 5.17(c) indicate that pull-off in the graded material occurs by uniform detachment at the theoretical strength irrespective of the size, confirming the strategy of flaw tolerant adhesion via graded elasticity.

5.4. Flaw tolerance via hierarchical energy dissipation

In the discussions so far, we have assumed that the work of adhesion consists only of surface energy contribution $\Delta\gamma$ which is typically on the order of $0.01 - 0.05$ J/m^2 for van der Waals interaction. This assumption is appropriate if no bulk dissipation occurs during the break of adhesion. In fact, biological adhesion systems rely heavily on energy dissipation mechanisms based on various mechanisms such as viscoelastic deformation [51, 57] and irreversible loss of elastic strain energy [31, 58, 78]. In the following, this point is illustrated by using a simple hairy surface model. It is demonstrated that the work of adhesion can be increased greatly via fibrillar structures. But such increment is limited by the fiber stability condition against self-bunching. To overcome this constraint, we design a hierarchical fibrillar structure by which a scale-dependent work of adhesion is achieved, resulting in a generalized flaw tolerance state.

5.4.1. High work of adhesion in fibrillar structures

As mentioned in section 2.1.2, if two smooth solid surfaces are brought into contact (Figure 5.18a), surface adhesion will occur, which, according to the Lennard-Jones potential, can be described as a function of the interfacial separation h:

$$\sigma(h) = \frac{8\Delta\gamma}{3z_0}\left[\left(\frac{z_0}{h}\right)^3 - \left(\frac{z_0}{h}\right)^9\right],$$

where $\Delta\gamma$ is the work of adhesion representing the work required to separate two unit surfaces from the equilibrium place $h = z_0$ to $h = \infty$. In this regard, the work of

adhesion can be visualized as the area below the $\sigma - h$ curve ranging from $h = z_0$ to $h = \infty$.

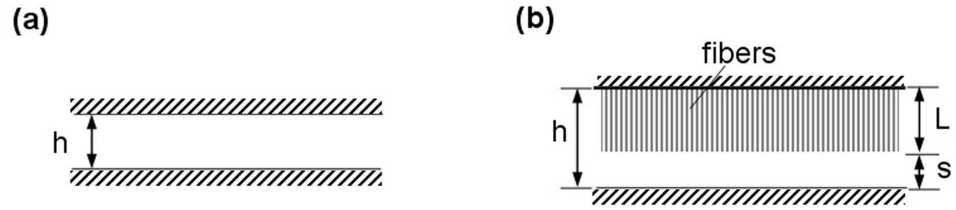

Figure 5.18.: Schematic of contact between (a) two smooth surfaces and (b) a hairy surface and smooth substrate.

Now, let us have one surface extrude into a great number of identical thin fibers and bring it into contact with a smooth substrate, as shown in Figure 5.18(b). We assume that: (1) two surfaces are separated so far that the direct interaction can be ignored; (2) the diameter of the fibers meets the condition for robust adhesion.

Let L and s denote the fiber length and the separation between fiber tip and substrate respectively, the apparent surface-surface separation now can be given by

$$h = L + s. \tag{5.80}$$

According to the Hooke's law, we have

$$L = L_0(1 + \sigma/E_{\mathrm{f}}), \tag{5.81}$$

where L_0 is the original length of the fibers, E_{f} is the Young's modulus and σ is the tensile stress correlated with s by Lennard-Jones law

$$\sigma(s) = \frac{8\Delta\gamma}{3z_0}\left[\left(\frac{z_0}{s}\right)^3 - \left(\frac{z_0}{s}\right)^9\right]. \tag{5.82}$$

Equations (5.80-5.82) define the adhesion stress σ as a function of apparent surface-surface h implicitly. Given $\Delta\gamma L_0/E_{\mathrm{f}}z_0^2$, the variation of σ with apparent separation h is plotted in Figure 5.19. We can see that the $\sigma - h$ curve is tilted as $\Delta\gamma L_0/E_{\mathrm{f}}z_0^2$ increases, resulting in unstable adhesion stress on the separating path. Under this circumstance, pull-off will occur accompanied by an abrupt drop in adhesion stress and the strain energy stored in the fiber is dissipated, giving an additional component to the work

done per unit surface area of fracture advance, i.e.

$$W_{\mathrm{ad}} = \Delta\gamma + W_{\mathrm{diss}} = (\Delta\gamma + \sigma_{\mathrm{th}}^2 L_0/2E_{\mathrm{f}})\varphi, \tag{5.83}$$

where φ denotes the area fraction of fibers. Taking $\Delta\gamma = 0.01$ J/m^2, $\sigma_{\mathrm{th}} = 20$ MPa, $L_0 = 100$ μm, $E_{\mathrm{f}} = 1.0$ GPa, $\varphi = 0.5$, the work of adhesion is calculated to be $W_{\mathrm{ad}} \approx 10$ J/m^2, a value much larger than $\Delta\gamma$. Such enhancement in work of adhesion by fibrillar structures has been reported and/or discussed by Jagota and Bennison [58], Persson [78] and Tang *et al.* [95].

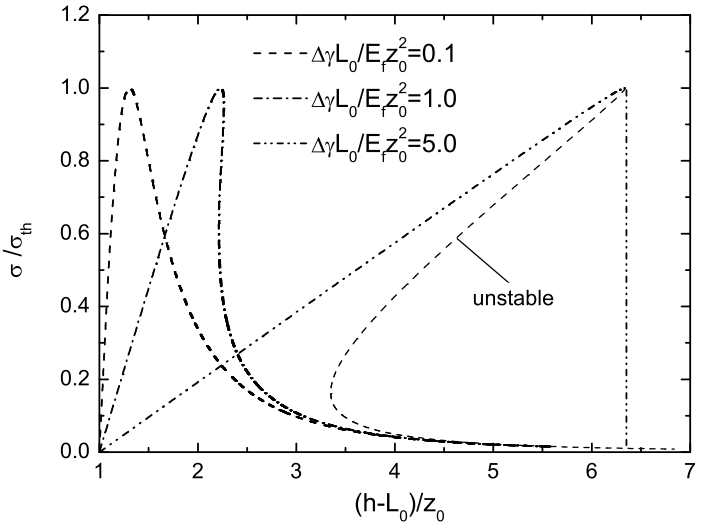

Figure 5.19.: Effective stress-separation curve in fibrillar structures with different fiber lengths.

If we apply such hairy structure to the tip of a stalk fiber, as shown in Figure 5.20, a two-levelled fibrillar structure or a "brush" will be designed. According to Equation (4.52), now the condition for flaw tolerant adhesion of this hairy tipped fiber can be described as

$$R \leq \frac{8W_{\mathrm{ad}}E_{\mathrm{f}}}{\pi(1-\nu_{\mathrm{f}}^2)(\varphi\sigma_{\mathrm{th}})^2}, \tag{5.84}$$

where ν_{f} denotes the Poisson's ratio of the fiber and W_{ad} is the work of adhesion given by Equation (5.83). For most of the discussions in following, we shall take the equality sign in Equation (5.84) corresponding to the optimal condition with no over-design. Normally, since W_{ad} is much greater than $\Delta\gamma$, Equation (5.84) in comparison with Equation (4.52) reveals that flaw tolerant adhesion can be extended to a larger length

scale by using hairy structure. From the viewpoint of robustness, slender hairs with large aspect ratio can significantly increase the work of adhesion and contribute to the robustness of adhesion at higher structural levels. However, the length of the fibrils cannot be too long as there is an instability leading to fiber bunching as the aspect ratio of the fibrils increase. This point will be discussed in the following.

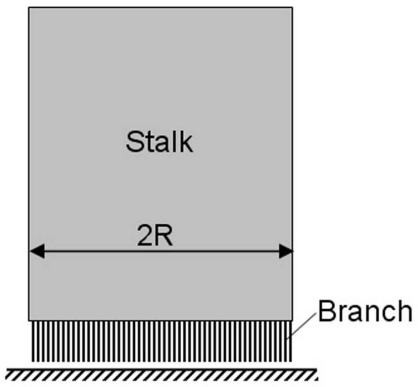

Figure 5.20.: Schematic of a brush structure.

5.4.2. Anti-bunching condition for fibrillar structures

In an array of slender hairs on a surface, the van der Waals interaction among neighbouring fibers can cause them to bundle together [33, 35, 40, 52, 78, 85]. The anti-bunching condition is an important factor in the design of hairy adhesion structures. The exact form of the anti-bunching condition depends on the geometry of the fiber. For example, the anti-bunching condition for fibers of square cross section has been derived by Hui *et al.* [52] and Gao *et al.* [33]. In this paper, we focus on cylindrical fibers as has been considered by Glassmaker *et al.* [40].

Consider two neighboring identical cylindrical fibers with circular cross-sections. When the separation $2w$ becomes small, the surface adhesive force between them will cause to bundle together, as shown Figure 5.21(a). In other words, given separation $2w$ and radius R, there exists a critical length beyond which lateral bunching of neighbouring fibers becomes stable configurations. For two identical cylindrical fibrils adhering to one anther in parallel, the 2D JKR theory [53] gives the externally applied force as

$$P = \frac{\pi E_{\mathrm{f}} b^2}{4(1-\nu_{\mathrm{f}}^2)R} - \sqrt{2b\pi E_{\mathrm{f}}\gamma_{\mathrm{f}}/(1-\nu_{\mathrm{f}}^2)}, \tag{5.85}$$

where γ_f is the surface energy of the fiber material. In our case, since no end constraint occurs, with $P = 0$ the half-width of contact (Figure 5.21b) can be estimated from Equation (5.85) as

$$b = \left[\frac{32R^2(1-\nu_f^2)\gamma_f}{\pi E_f}\right]^{1/3}. \tag{5.86}$$

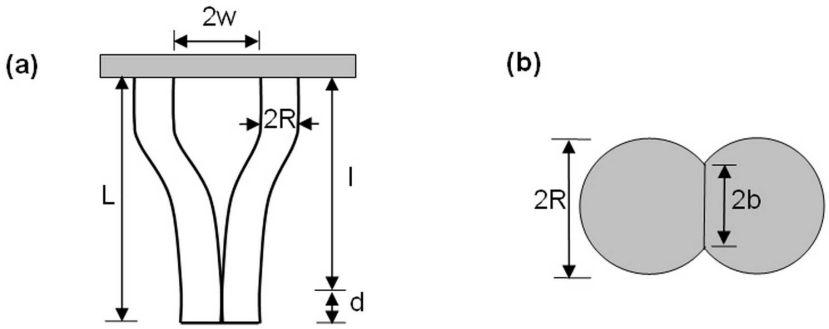

Figure 5.21.: Anti-bunching condition of a fibrillar structure. (a) Configuration of self-bunching in fiber cluster. (b) A bottom-up view of the sticking ends.

Due to the local deformation of the contact region, there is an accompanying stored elastic energy U_c in the fibrils. At equilibrium, we have [40]

$$\frac{\partial U_c}{\partial b} = 4\gamma_f. \tag{5.87}$$

Substituting Equation (5.86) into Equation (5.87) yields

$$\frac{\partial U_c}{\partial b} = \frac{b^3\pi E_f}{8(1-\nu_f^2)R^2}.$$

It follows that

$$U_c = \frac{b^4\pi E_f}{32(1-\nu_f^2)R^2} = \frac{b\pi E_f}{32(1-\nu_f^2)R^2}b^3 = \gamma_f b. \tag{5.88}$$

On the other hand, the strain energy associated with bending can be calculated by using the elementary beam theory [18]

$$U_b = 2\times\frac{6E_f I w^2}{l^3} = \frac{12E_f I w^2}{l^3}, \quad I = \frac{\pi R^4}{4}.$$

The length of the non-contact region l is determined by using the equilibrium condition

$$\mathrm{d}\left[U_b + (U_c - 2\gamma_f 2b)(L-l)\right]/\mathrm{d}l = 0,$$

which results in

$$l = \left[\frac{36E_{\mathrm{f}}Iw^2}{4\gamma_{\mathrm{f}}b - U_{\mathrm{c}}}\right]^{1/4}. \tag{5.89}$$

Substituting Equation (5.88) into Equation (5.89) gives rise to

$$l = \left[\frac{36E_{\mathrm{f}}Iw^2}{3\gamma_{\mathrm{f}}b}\right]^{1/4} = \left[\frac{3\pi E_{\mathrm{f}}R^4w^2}{\gamma_{\mathrm{f}}b}\right]^{1/4} = \left[\frac{\pi^4E_{\mathrm{f}}R}{2^{11}\gamma_{\mathrm{f}}(1-\nu_{\mathrm{f}}^2)}\right]^{1/12}\left[\frac{12E_{\mathrm{f}}R^3w^2}{\gamma_{\mathrm{f}}}\right]^{1/4}. \tag{5.90}$$

Assuming that the fibers are distributed in a regular lattice pattern, half-separation w and radius R thus can be correlated by the area fraction φ as

$$w = (\sqrt{\varphi_{\max}/\varphi} - 1)R, \quad (0 < \varphi < \varphi_{\max}) \tag{5.91}$$

where $\varphi_{\max}$ stands for the maximum area fraction of a given hair pattern. It can be shown that $\varphi_{\max} = \pi/2\sqrt{3}$ for a triangular pattern (Figure 5.22a), $\varphi_{\max} = \pi/4$ for a square lattice (Figure 5.22b) and $\pi/3\sqrt{3}$ for a hexagonal lattice (Figure 5.22c). Substituting Equation (5.91) into (5.90) leads to

$$l = R\alpha\left(\frac{E_{\mathrm{f}}R}{\gamma_{\mathrm{f}}}\right)^{1/3}\left(\sqrt{\varphi_{\max}/\varphi} - 1\right)^{1/2}, \tag{5.92}$$

where $\alpha = \left[\frac{3^3\pi^4}{2^5(1-\nu_{\mathrm{f}}^2)}\right]^{1/12}$. Equation (5.92) gives the upper limit of the fibril length over which lateral bunching between two fibrils will take place. The anti-bunching condition thus can be expressed as

$$L \geq L_{\mathrm{cr}} = l = R\alpha\left(\frac{E_{\mathrm{f}}R}{\gamma_{\mathrm{f}}}\right)^{1/3}\left(\sqrt{\varphi_{\max}/\varphi} - 1\right)^{1/2}. \tag{5.93}$$

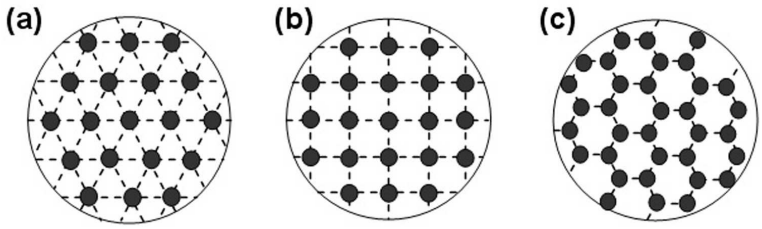

Figure 5.22.: Possible layout patterns of fibers: (a) triangular pattern (b) square pattern and (c) hexagonal pattern.

Equation (5.93) has been derived for the lateral sticking between two neighboring fibrils. Similar analysis can also be carried out for other possible bunching configurations involving multiple neighbouring fibers, as shown in Figure 5.23. We find that the critical fiber length for multiple fiber bunching is no less than that given by Equation (5.93). It seems that the anti-bunching condition between two fibers is the most critical condition against bunching involving multiple fibers.

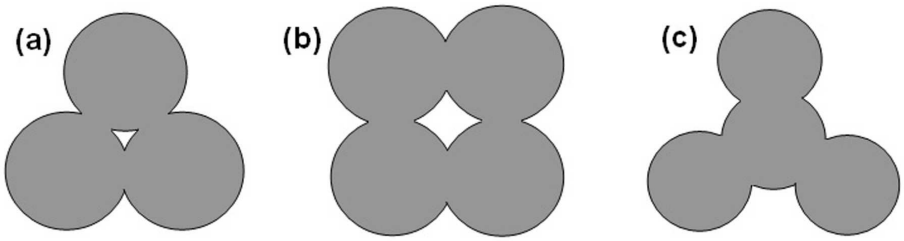

Figure 5.23.: Other possible bunching configurations involving multiple neighboring fibers in (a) triangular pattern (b) square pattern and (c) hexagonal pattern.

5.4.3. Bottom-up designed hierarchical structures

Given that the work of adhesion can be increased to a larger value by adopting a "hairy" structure [31, 58, 78, 95], the critical length for flaw tolerant adhesion can also be extended to a larger scale, according to Equation (5.84). Meanwhile, the increase in work of adhesion with each level of added hierarchy should be limited by the maximum length of the fibers allowed by the anti-bunching condition. In other words, bunching between fibers provides an upper limit on how much the flaw tolerant length scale can be extended by one level of hierarchy. In order to achieve flaw tolerant adhesion at macroscopic length scales, multiple levels of hierarchy may be needed. To demonstrate the principle of flaw tolerance via structure hierarchy, we propose a "fractal gecko hairs" model, in which a hierarchical fibrillar structure is made from multiple levels of self-affine "brush"structures, as shown in Figure 5.24. In this fractal structure, the tips of fibers at each level of hierarchy are assumed to be coated with a "brush" structure consisting of smaller fibrils from one level below. The flaw tolerance and anti-bunching conditions are applied to all hierarchical levels from bottom and up to ensure robustness and stability at all levels. That is, the robustness principle of flaw tolerance and the stability principle of anti-bunching are used to determine the fiber geometry at different scales. The bottom-up construction of the desired hierarchical structure is described in detail below.

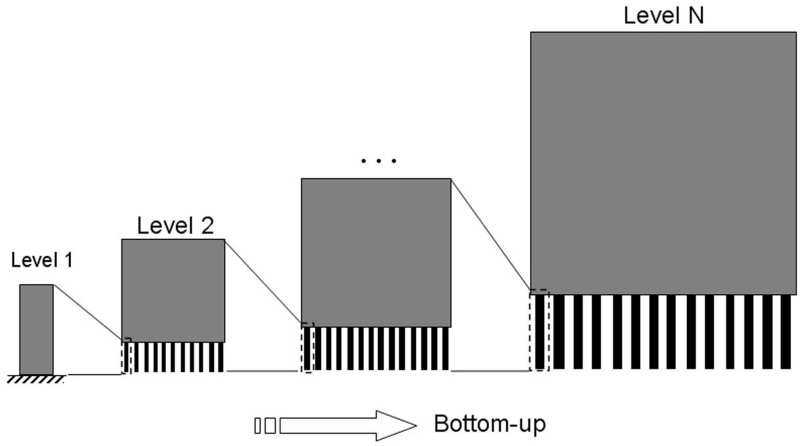

Figure 5.24.: Schematic of the bottom-up design scheme for a hierarchical structure. At each level, the fibers depend on smaller fibrils form the lower hierarchical levels as effective "adhesive bonds" with a surface. Interestingly, the fibers themselves act as "adhesive bonds" for larger fibers from higher hierarchical levels.

At the lowest level of hierarchy, the failure process is governed by the van der Waals interaction between the smallest fibers (ultrastructure) and a solid surface. In this case, the maximum fiber radius ensuring flaw tolerant adhesion is given by

$$R_1 = \frac{8\Delta\gamma E_\mathrm{f}}{\pi(1-\nu_\mathrm{f}^2)\sigma_\mathrm{th}^2}, \tag{5.94}$$

where the work of adhesion is simply equal to the surface energy $\Delta\gamma$ due to van der Waals interaction and σ_th is the theoretical strength of van der Waals forces.

In light of the anti-bunching condition of Equation (5.93), the maximum fiber length of the bottom level can be expressed as a function of the area fraction φ_1 of this level as

$$L_1(\varphi_1) = R_1\alpha\left(\frac{E_\mathrm{f}R_1}{\gamma_\mathrm{f}}\right)^{1/3}\left(\sqrt{\varphi_\mathrm{max}/\varphi_1}-1\right)^{1/2}. \tag{5.95}$$

With these parameters, the work of adhesion associated with the next (second) level is given by

$$W_2^\mathrm{ad}(\varphi_1) = \left(\frac{\sigma_\mathrm{th}^2 L_1}{2E_\mathrm{f}} + \Delta\gamma\right)\varphi_1, \tag{5.96}$$

which is a function of the area fraction φ_1. This function exhibits a maximum at a specific value of φ_1 due to the opposing trends of variation of the parameters L_1 and φ_1: denser fibers with larger φ_1 require smaller L_1 for stability against bunching. Therefore, we can choose the fiber area fraction φ_1 to maximize the work of adhesion at the next level

according to Equation (5.96). After φ_1 is calculated, the fiber length L_1 is immediately determined by Equation (5.95). In this way, all the structural parameters characterizing the first level R_1, L_1, φ_1 have been determined. In addition, the work of adhesion for the second level W_2^{ad} is given by Equation (5.96).

We now advance to the design of the second (next) level. The fiber radius is again chosen to ensure flaw tolerant adhesion,

$$R_2 = \frac{8W_2^{\mathrm{ad}}E_{\mathrm{f}}}{\pi(1-\nu_{\mathrm{f}}^2)(S_2)^2} = \frac{8W_2^{\mathrm{ad}}E_{\mathrm{f}}}{\pi(1-\nu_{\mathrm{f}}^2)(\varphi_1\sigma_{\mathrm{th}})^2}, \tag{5.97}$$

where $S_2 = \varphi_1\sigma_{\mathrm{th}}$ is the effective adhesion strength of the second level. Similarly, the anti-bunching condition allows the fiber length to be determined as a function of the area fraction φ_2 as

$$L_2(\varphi_2) = R_2\alpha\left(\frac{E_{\mathrm{f}}R_2}{\gamma_{\mathrm{f}}}\right)^{1/3}\left(\sqrt{\varphi_{\max}/\varphi_2}-1\right)^{1/2}, \tag{5.98}$$

upon which the work of adhesion for the third level can be determined,

$$W_3^{\mathrm{ad}}(\varphi_2) = \left[W_2^{\mathrm{ad}} + \frac{(S_2)^2L_2}{2E_{\mathrm{f}}}\right]\varphi_2 = \left[W_2^{\mathrm{ad}} + \frac{(\varphi_1\sigma_{\mathrm{th}})^2L_2}{2E_{\mathrm{f}}}\right]\varphi_2. \tag{5.99}$$

Next, the area fraction φ_2 is determined by maximizing $W_3^{\mathrm{ad}}(\varphi_2)$. Once φ_2 is known, the fiber length L_2 is determined from Equation (5.98). Hence all the structural parameters, R_2, L_2, φ_2, for the second hierarchical level, as well as the work of adhesion W_3^{ad} for the third level, have been determined.

A general iterative procedure can now be formulated to determine the structural parameters at all hierarchical levels, starting from the lowest level. Assuming we have completed the design from the first to $(n-1)$th levels so that R_i, L_i, φ_i, W_i^{ad} $(i = 1, 2, \cdots, n-1)$ as well as W_n^{ad} have been determined, for the nth level $(n > 1)$, the (maximum) fiber radius ensuring flaw tolerant adhesion is given by

$$R_n = \frac{8W_n^{\mathrm{ad}}E_{\mathrm{f}}}{(1-\nu_{\mathrm{f}}^2)(S_n)^2} = \frac{8W_n^{\mathrm{ad}}E_{\mathrm{f}}}{(1-\nu_{\mathrm{f}}^2)\pi(\sigma_{\mathrm{th}}\Phi_{n-1})^2}, \tag{5.100}$$

where

$$S_n = \sigma_{\mathrm{th}}\Phi_{n-1},\ \ \Phi_{n-1} = \varphi_1\varphi_2\cdots\varphi_{n-1} = \prod_{i=1}^{n-1}\varphi_i, \tag{5.101}$$

is the effective adhesion strength of the nth level. The (maximum allowable) fiber length

of the nth level can then be expressed, according to the anti-bunching condition, as a function of the area fraction φ_n,

$$L_n(\varphi_n) = \alpha R_n \left(\sqrt{\varphi_{\max}/\varphi_n} - 1\right)^{1/2} \left(\frac{E_{\mathrm{f}} R_n}{\gamma_{\mathrm{f}}}\right)^{1/3}, \tag{5.102}$$

The work of adhesion for the $(n+1)$th level is

$$W_{n+1}^{\mathrm{ad}}(\varphi_n) = \left[W_n^{\mathrm{ad}} + \frac{(S_n)^2 L_n}{2E_{\mathrm{f}}}\right] \varphi_n = \left[W_n^{\mathrm{ad}} + \frac{(\sigma_{\mathrm{th}}\, \Phi_{n-1})^2 L_n}{2E_{\mathrm{f}}}\right] \varphi_n. \tag{5.103}$$

The area fraction for the nth level φ_n can now be determined by maximizing $W_{n+1}^{\mathrm{ad}}(\varphi_n)$, upon which L_n and W_{n+1}^{ad} can be readily calculated. This iterative, bottom-up design procedure can be repeated until the desired size scale for flaw tolerant adhesion is reached. Upon the knowledge of the fiber radius and area fraction of each level, we can calculate the number of fibrils on the tip of a fiber at the next higher level,

$$N_n^{\mathrm{f}} = \varphi_n \left(R_{n+1}/R_n\right)^2, \tag{5.104}$$

as well as the net pull-off force at each hierarchical level,

$$F_n^{\mathrm{f}} = \pi R_n^2 S_n. \tag{5.105}$$

Figure 5.25 shows the calculated hierarchical fibrillar structures following the bottom-up design procedure described above. In the calculations, we have taken the material properties of keratin as $E_{\mathrm{f}} = 1.0$ GPa, $\nu_{\mathrm{f}} = 0.3$, $\Delta\gamma = 10$ mJ/m^2, $\gamma_{\mathrm{f}} = 5$ mJ/m^2 and $\sigma_{\mathrm{th}} = 20$ MPa. Three lattice patterns, triangular, square and hexagonal, for the fiber cluster are considered. As shown in Figure 5.25(a) and (b), both the fiber radius and length increase exponentially with the hierarchy level. Under the selected parameters, the critical fiber radius of flaw tolerant adhesion is only around 100 nm at the lowest level of structure. With hierarchical design, the flaw tolerant radius increases to 1 μm with 2 levels, 1 mm with 3 levels, 1 m with 4 levels of hierarchy. With 8 levels, the dimension of flaw tolerant radius has reached 10^{26} m, which is an astronomical size! These calculations demonstrate the enormous potential of a hierarchical structure for flaw tolerant adhesion. Figure 5.25(c) displays the variation of the area fraction with the number of hierarchy levels. Interestingly, the area fraction converges to a constant after the third hierarchy level for each fiber layout pattern. Figure 5.25(d) shows the work of adhesion at different hierarchical levels. In the first 6 levels, the triangular fiber

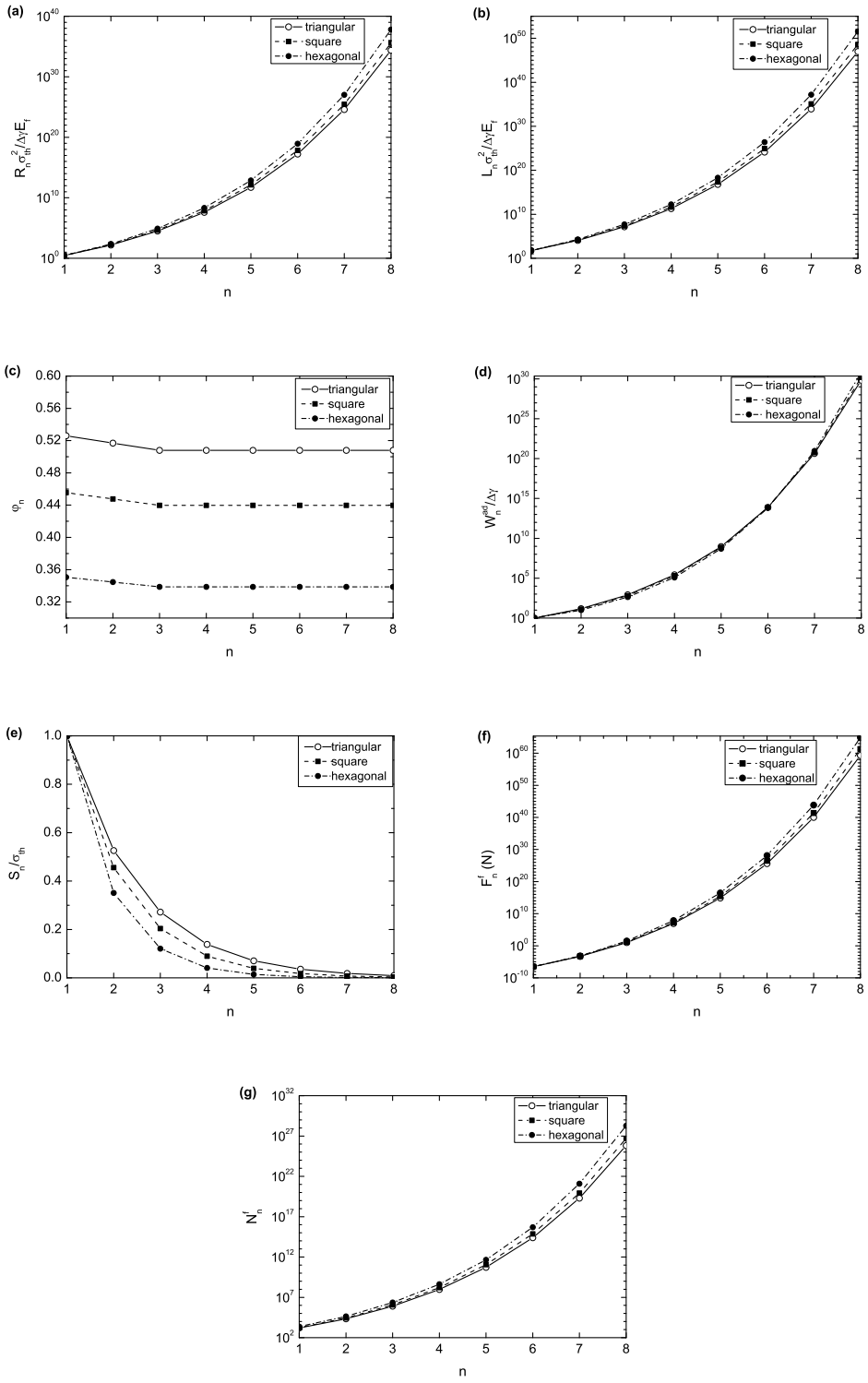

Figure 5.25.: Variations of (a) fiber radius R_n, (b) fiber length L_n, (c) area fraction φ_n, (d) work of adhesion W_n^{ad}, (e) adhesion strength S_n, (f) pull-off force F_n^{f} and (g) the number of fibers N_n^{f} as a function of the hierarchical level n.

pattern exhibits higher work of adhesion than the other two patterns. With further increase in hierarchy levels, this advantage is taken over by the hexagonal fiber pattern. Figure 5.25(e) shows the effective adhesion strength which decreases and asymptotically approaches zero with the increasing hierarchy level. Therefore, the strategy of scale-dependent adhesion strength also exists in this fractal structure. On the other hand, the pull-off force F_n^{f}, as shown in Figure 5.25(f), increases exponentially with the hierarchy level. Figure 5.25(g) illustrates the number N_n^{f} of fibrils on the tip of a fiber at the next level. We see that N_n^{f} increases sharply with increasing hierarchy levels. Most results in Figure 5.25 are presented in the normalized form. The quantitative estimates based on the assumed materials properties are tabulated in Table 5.1.

Table 5.1.: Calculated geometrical and mechanical properties of a bottom-up designed fractal hair structure.

n	R_n(m)	L_n(m)	φ_n	W_n^{ad}(J/m^2)	S_n(MPa)	F_n^{f}(N)	N_n^{f}
Triangular							
1	7.00×10^{-8}	1.37×10^{-6}	0.5260	0.01	20	3.08×10^{-7}	1.539×10^{3}
2	3.78×10^{-6}	2.86×10^{-4}	0.5169	0.15	10.52	4.73×10^{-4}	2.2032×10^{4}
3	7.81×10^{-4}	0.36	0.5079	**8.26**	**5.44**	10.43	7.9914×10^{5}
4	0.98	4.80×10^{3}	0.5079	2.67×10^{3}	2.76	8.33×10^{6}	9.2685×10^{7}
5	1.32×10^{4}	1.55×10^{9}	0.5079	9.31×10^{6}	1.4026	7.72×10^{14}	5.2558×10^{10}
6	4.26×10^{9}	3.41×10^{16}	0.5079	7.72×10^{11}	0.7123	4.06×10^{25}	2.4676×10^{14}
7	9.39×10^{16}	2.11×10^{26}	0.5079	4.39×10^{18}	0.3618	1.00×10^{40}	1.9399×10^{19}
8	5.80×10^{26}	2.39×10^{39}	0.5079	7.0×10^{27}	0.1837	1.94×10^{59}	6.5330×10^{25}
Square							
1	7.00×10^{-8}	1.37×10^{-6}	0.4555	0.01	20	3.08×10^{-7}	1.777×10^{3}
2	4.37×10^{-6}	3.46×10^{-4}	0.4477	0.13	9.11	5.47×10^{-4}	2.7977×10^{4}
3	1.10×10^{-3}	0.56	0.4398	6.49	4.08	15.50	1.1534×10^{6}
4	1.7691	1.06×10^{4}	0.4398	2.03×10^{3}	1.79	1.76×10^{7}	1.5865×10^{8}
5	3.36×10^{4}	5.35×10^{9}	0.4398	7.47×10^{6}	0.79	2.80×10^{15}	1.1291×10^{11}
6	1.70×10^{10}	2.16×10^{17}	0.4398	7.33×10^{11}	0.35	3.16×10^{26}	7.1761×10^{14}
7	6.88×10^{17}	3.0×10^{27}	0.4398	5.72×10^{18}	0.15	2.27×10^{41}	8.4482×10^{19}
8	9.53×10^{27}	9.97×10^{40}	0.4398	1.53×10^{28}	0.067	1.91×10^{61}	4.8744×10^{26}
Hexagonal							
1	7.00×10^{-8}	1.37×10^{-6}	0.3507	0.01	20	3.08×10^{-7}	2.309×10^{3}
2	5.68×10^{-6}	4.91×10^{-4}	0.3446	0.10	7.01	7.10×10^{-4}	4.3203×10^{4}
3	2.00×10^{-3}	1.25	0.3386	4.20	2.42	30.37	2.2486×10^{6}
4	5.18	4.42×10^{4}	0.3386	1.24×10^{3}	0.82	6.90×10^{7}	4.2178×10^{8}
5	1.83×10^{5}	5.12×10^{10}	0.3386	5.02×10^{6}	0.28	2.91×10^{16}	4.5376×10^{11}
6	2.12×10^{11}	6.23×10^{18}	0.3386	6.66×10^{11}	0.0938	1.32×10^{28}	5.0028×10^{15}
7	2.57×10^{19}	3.75×10^{29}	0.3386	9.27×10^{18}	0.0318	6.61×10^{43}	1.2276×10^{21}
8	1.55×10^{30}	8.85×10^{43}	0.3386	6.40×10^{28}	0.0108	8.14×10^{64}	1.8860×10^{28}

It should be of interest to make a comparison between our calculated results with the observed hierarchical structure in nature. Under the selected parameters, our results show that the diameter and length of the first level fiber are 140 nm and 1.37 μm. These

values are not inconsistent with the dimension of the topmost spatula hairs (stalk) of Tokay gecko (*Gekko gecko*) which is around 100-200 nm wide and $0.5-3$ μm long[3] [3, 101]. The dimension of the second level of our bottom-up constructed structure is around $7.56 - 11.34$ μm wide and $286 - 491$ μm long, depending upon the pattern of the fiber cluster, while the size of a seta on gecko's feet is about 5 μm in width and 110 μm in length [101]. In addition, our calculation predicts that the number of the lowest level fibrils accommodated by a fiber of the second level is around 1539-2309, which is qualitatively similar to the observation of 100-1000 spatulae/seta [4]. Furthermore, from our calculated results we evaluate the density $N_2^{\mathrm{f}}/\pi R_3^2$ of the second level fiber to be $11,494,\ 7363,\ 3439$ mm^{-2} for triangular, square and hexagonal patterns, respectively. This is also comparable to the observed density of seta around $14,400$ mm^{-2} [4]. Therefore, it seems that gecko only adopts a few levels of hierarchical fibrillar structures to achieve robust adhesion. A question then is why nature has not evolved more hierarchical levels, thus larger adhesion species heavier than gecko? A possible answer to this question is addressed in the next subsection.

5.4.4. Fiber fracture: an upper limit on flaw tolerant adhesion design

In the preceding discussions, we have focused on the failure along an adhesion interface and implicitly assumed that the fibers themselves do not fracture. In practice, as the adhesion strength is enhanced by introducing hierarchical fibrillar structures, the fracture of fibers eventually rises to become the dominant issue for failure at the system level. In other words, a robust adhesion system must be robust against not only adhesion failure but also fiber fracture.

Consider a single fiber at hierarchy level n. A penny-shaped crack is introduced in the center of the cross-section as a possible internal flaw. Other configurations of crack-like flaws, such as edge/corner cracks/singularities, can be considered without affecting the basic idea. The maximum tensile stress that this fiber can sustain can be determined from the Griffith's criterion [45] for crack growth as (see [94]),

$$\sigma_n^{\max} = \sqrt{\frac{E_{\mathrm{f}}^* \Gamma_{\mathrm{f}}}{R_n}} \frac{\sqrt{\pi R_n/2a}}{g(a/R_n)}, \tag{5.106}$$

[3]These values are estimated from the micrographs in the references.

where a is the crack radius, $E_{\mathrm{f}}^{*} = E_{\mathrm{f}}/(1-\nu_{\mathrm{f}}^{2})$, Γ_{f} is the fracture energy and

$$g(a/R_n) = \frac{1 - 0.5a/R_n + 0.148(a/R_n)^3}{\sqrt{1 - a/R_n}} \tag{5.107}$$

is a geometrical parameter [94]. Considering a crack half the size of the fiber, i.e. $a/R_n = 0.5$, Equation (5.106) can be further reduced to

$$\sigma_n^{\max} = 1.63\sqrt{E_{\mathrm{f}}^{*}\Gamma_{\mathrm{f}}/R_n}. \tag{5.108}$$

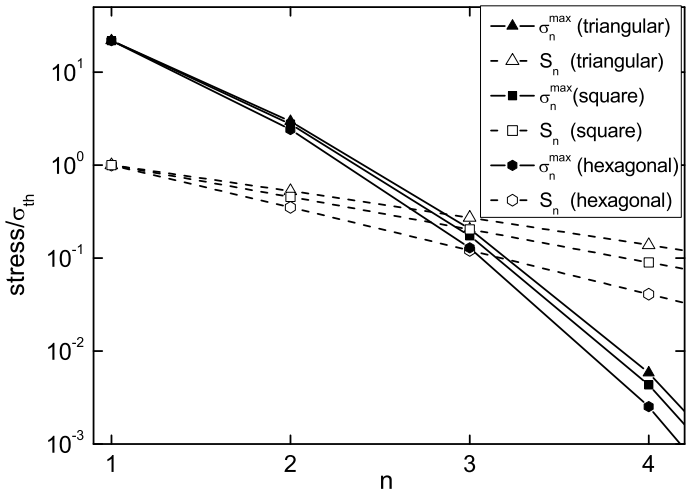

Figure 5.26.: Comparison between the fracture strength $\sigma_n^{\max}$ of a cracked fiber and the nth level adhesion strength S_n of the bottom-up designed fractal hairs. If $\sigma_n^{\max} > S_n$, adhesion failure is regarded as the principal failure mode, otherwise ($\sigma_n^{\max} < S_n$) fiber fracture is thought of as the principal failure mode.

The relative significance of fiber fracture can be measured by a comparison between $\sigma_n^{\max}$ and the effective adhesion strength S_n at the nth hierarchical level. If $\sigma_n^{\max} > S_n$, adhesion failure is regarded as the dominant issue and further increase in hierarchical levels can be considered. On the other hand, if $\sigma_n^{\max} < S_n$, fiber fracture is regarded as the dominant failure mode, which imposes an upper limit on the hierarchical design. Taking $\Gamma_{\mathrm{f}} = 5.0$ J/m^2 and $E_{\mathrm{f}}^{*} = 1.0$ GPa, we compare $\sigma_n^{\max}$ and S_n for the fractal hair structures constructed above. As shown in Figure 5.26, for triangular and square fiber layout, only fibers within the first two levels satisfy the condition $\sigma_n^{\max} > S_n$; for the hexagonal layout, this condition is satisfied for the first three levels. Hence, although

there is no upper bound for flaw tolerant adhesion via fractal hairs design, crack-like flaws in the hairs themselves would impose a practical limit upon the usefulness of this strategy.

In this chapter, we have studied some basic principles of robust adhesion on rough surfaces within the framework of continuum interfacial failure mechanics. Instead of directly modeling the adhesive contact on random or fractal rough surfaces as in some of the previous studies in the literature, we have adopted a different modeling approach by considering an interfacial crack as a representative contact flaw. In comparison with previous contact models on rough surfaces, the crack model is mathematically more tractable and allows us to consider adhesive contact in hierarchical and nonhomogeneous elastic materials, which is crucially important for biological systems. We have assumed that robust adhesion on random rough surfaces is equivalent to flaw tolerant adhesion in which the growth of a representative interfacial crack is suppressed for any crack size. By using the concept of flaw tolerant adhesion, we have shown that graded elasticity, hierarchical energy dissipation [104] and scale-dependent adhesion strength are three basic strategies to make the system insensitive to crack-like contact flaws due to roughness or contaminants. The strategy of graded elasticity tends to ensure that the average property of material around a crack is rigid enough to suppress the crack growth while the surface remains sufficiently compliant to achieve good contact with a rough surface. The strategy of hierarchical energy dissipation tends to increase the work of adhesion in proportion to the flaw size. The scale-dependent adhesion strength strategy trades the strength for toughness. Based on a bottom-up scheme, a hierarchical fibrillar structure is constructed for tolerating crack-like flaws of all sizes. This conclusion is appropriate provided that the fibers themselves will not fracture before the failure of the adhesion. Further consideration of crack-like flaws in the hairs themselves results in an upper size limit for flaw tolerant design. Therefore, Flaw tolerance can be achieved by a combination of graded elasticity, hierarchical energy dissipation and scale-dependent adhesion strength. For biological adhesion systems, it seems even necessary to adopt a combination of these strategies. For example, it seems difficult to achieve flaw tolerant adhesion via graded elasticity alone. If we take $E = E_0(1+z/c_0)^2$ and $c_0 = 144$ nm as we have assumed in our numerical simulation, the Young's modulus at a depth of $z = 5$ μm (typical size of bio-adhesion system is one hundred microns or so) would already exceed 1200 times of that on the surface. Achieving such a sharp grading of elasticity may be difficult especially for biological systems. Therefore, the strategy of hierarchical energy dissipation plays a more important role in the biological attachments than the other

two.

A quantitative comparison of the present findings with biological adhesion systems is still difficult due to the lack of accurate measurement data for local elastic properties of biological attachment pads. On the other hand, some qualitative remarks can be readily made. The nanoscale spatulae on the toe of gecko exhibits hierarchical hairy structures which effectively induce hierarchical energy dissipation with graded elastic property (Figure 1.1a). The attachment pad of cicada contains a foam-like structure with variable cell size and wall thickness (Figure 1.1b). Since the Young's modulus of a foam-like material is proportional to $(t/l)^3$, where t and l denote the wall thickness and size of the cell respectively [36], the variation of $(t/l)^3$ with distance from the surface could result in a graded Young's modulus. Furthermore, because these foams are normally filled with viscous liquid, the varying cell sizes could also introduce hierarchical energy dissipation due to viscoelastic deformation around an interfacial crack. These different microstructural designs seem to share a common feature of nonhomogeneous material property with an ability to dissipate energy in scale with crack size.

In the next chapter, we will turn our attention from robust adhesion to releasable adhesion.

Chapter 6. Releasable adhesion

For geckos and insects, robust adhesion alone is insufficient for survival as these animals also need to move swiftly on walls and ceilings; the reversibility of attachment is just as important as the robustness. One conceivable way for reversible adhesion is to design an orientation-controlled switch between attachment and detachment, with adhesion strength varying strongly with the direction of pulling. An ideal scenario of robust and releasable adhesion is that the adhesion strength would be maintained near the theoretical strength insensitive to crack-like flaws when pulled in some range of directions, but then dramatically reduced when pulled in another range of directions. The switch between attachment and detachment thus can be accomplished simply by changing the pulling angles (e.g., by exerting different muscles). Some known examples of anisotropic adhesion systems in which the pull-off force varies strongly with the direction of pulling include an elastic tape on substrate [50, 63, 89] and a single seta of gecko sticking to a wall [3, 33]. In these single contact systems, the anisotropic behaviors of the pull-off force are due to the asymmetric structure of the material. A different theory will be needed to explain how bio-adhesion can be released in macroscopic contact with rough surfaces.

In the following, we will address the question of releasable adhesion on rough surfaces within the framework of continuum interfacial failure mechanics. This generalization is also necessary for explaining how adhesion is released in the smooth attachment systems in biology. The previous studies on the behavior of a single seta of gecko [3, 33] or spatula [50] can not explain why adhesion can also be released in smooth attachment systems with no fibrillar contact structure. We perform theoretical modeling and numerical simulations to show that strong elastic anisotropy on the continuum level induces a strong orientation dependence of the pull-off force similar to the behavior of a single seta observed by Autumn *et al.* [3] in experiment and Gao *et al.* [33] in simulation.

6.1. Orientation-dependent adhesion of an anisotropic elastic material

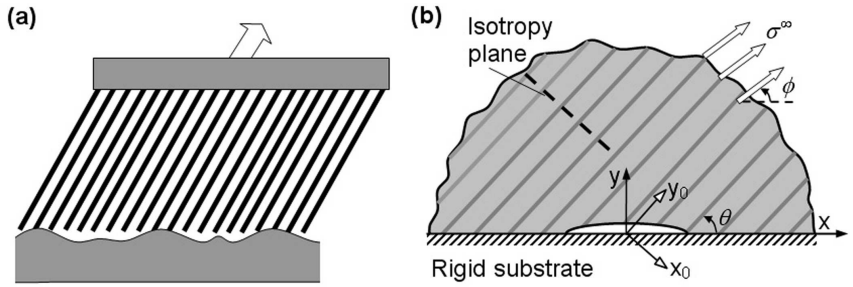

Figure 6.1.: The interfacial crack model for releasable adhesion. (a) A transversely isotropic solid contacting a rough surface. (b) An interfacial crack is used to represent random contact flaws.

To facilitate the theoretical analysis of releasable adhesion on rough surfaces schematically shown in Figure 6.1(a), we consider a plane-strain adhesion problem shown in Figure 6.1(b) where a transversely isotropic elastic half-space ($y \geq 0$) contacts a rigid substrate. A plane-strain interfacial crack of size $2a$ is used to simulate the random contact flaws due to surface roughness or contaminants. Although the actual adhesion strength depends on the crack size, the ratio between the maximum and minimum pull-off stresses as the pulling angle varies will be shown to be independent of the crack geometry and used as a measure for the releasability of adhesion.

In this interfacial crack model, the longitudinal direction of the material (y_0-axis) is tilted at the angle θ from the tangent of the substrate plane (x-axis). A remote uniaxial tensile stress σ^∞ is applied at an angle ϕ ($0 < \phi < \pi$) with respect to the x-axis. The transversely isotropic material is characterized by five independent elastic constants: E_t, E_l, ν_t, ν_l and G. E_t and E_l stand for the transverse (x_0 direction) and longitudinal (y_0 direction) Young's moduli; ν_t, ν_l are Poisson's ratios associated with transverse (x_0 direction) and longitudinal (y_0 direction) loading, respectively; G denotes the shear modulus in the $x_0 - y_0$ plane.

We are interested in the pull-off stress of the above adhesion system as a function of the pulling direction. This problem can be solved as a classical interfacial crack between two dissimilar anisotropic elastic solids [28, 42, 55, 91, 97, 102]. A general solution for the interfacial crack problem between two dissimilar anisotropic materials has been considered by many authors [28, 55, 91, 98] based on the Stroh formalism [90]. In this

field of research, several different groups of notations have been used in the literature. Here we just summarize the results immediately relevant to our present study by using the notations in [55].

For a finite interfacial crack between two dissimilar anisotropic elastic solids, the stress intensity factor at the right crack tip induced by remotely applied loading $\mathbf{t}^{\infty} = \left[\begin{array}{ccc} \sigma_{xy}^{\infty} & \sigma_{yy}^{\infty} & \sigma_{yz}^{\infty} \end{array}\right]^{\mathrm{T}}$ can be expressed as

$$\mathbf{K} = \left[\begin{array}{c} K_{\mathrm{II}} \\ K_{\mathrm{I}} \\ K_{\mathrm{III}} \end{array}\right] = \sqrt{\pi a}\boldsymbol{\Lambda}\langle\langle(1+2\mathrm{i}\varepsilon_{\alpha})(2a/\ell)^{-\mathrm{i}\varepsilon_{\alpha}}\rangle\rangle\boldsymbol{\Lambda}^{-1}\mathbf{t}^{\infty}, \tag{6.1}$$

$$\boldsymbol{\Lambda} = [\boldsymbol{\lambda}_1 \ \ \boldsymbol{\lambda}_2 \ \ \boldsymbol{\lambda}_3], \quad \varepsilon_{\alpha} = \mathrm{Im}(\delta_{\alpha}), \quad \mathrm{i} = \sqrt{-1}, \tag{6.2}$$

where the angular bracket $\langle\langle\cdot\rangle\rangle$ stands for the diagonal matrix, i.e. $\langle\langle f_{\alpha}\rangle\rangle = \mathrm{diag}[f_1,\ f_2,\ f_3]$; $\mathrm{Im}(\cdot)$ denotes the imaginary part of a complex variable; $2a$ is the width of the interface crack; ℓ is a length parameter which can be chosen arbitrarily; δ_{α} and $\boldsymbol{\lambda}_{\alpha}$ $(\alpha = 1, 2, 3)$ are eigenvalues and eigenvectors of the following problem

$$\left(\mathbf{M}^{*} + e^{2\mathrm{i}\pi\delta}\overline{\mathbf{M}}^{*}\right)\boldsymbol{\lambda} = \mathbf{0}. \tag{6.3}$$

Here, $\overline{\mathbf{M}}^{*}$ is the complex conjugate of the bimaterial matrix $\mathbf{M}^{*}$ which is defined as

$$\mathbf{M}^{*} = \mathbf{D} - \mathrm{i}\mathbf{W}, \tag{6.4}$$

$$\mathbf{D} = \mathbf{L}_1^{-1} + \mathbf{L}_2^{-1}, \quad \mathbf{W} = \mathbf{S}_1\mathbf{L}_1^{-1} - \mathbf{S}_2\mathbf{L}_2^{-1}, \tag{6.5}$$

where $\mathbf{S},\ \mathbf{L}$ are the *Barnett-Lothe* tensors [98]; subscripts '1' and '2' are used to denote the quantities pertaining to the materials 1 and 2. The explicit solution to the eigenvalues of problem Equation (6.3) have been obtained as [97]

$$\begin{aligned} &\delta_{\alpha} = -\frac{1}{2} + \mathrm{i}\varepsilon_{\alpha}, \ (\alpha = 1, 2, 3) \\ &\varepsilon_1 = \varepsilon = \frac{1}{2\pi}\ln\frac{1+\beta}{1-\beta}, \ \varepsilon_2 = -\varepsilon, \ \varepsilon_3 = 0, \ \beta = \left[-\frac{1}{2}\mathrm{tr}\left(\mathbf{W}\mathbf{D}^{-1}\right)^2\right]^{1/2}, \end{aligned} \tag{6.6}$$

where 'tr' stands for the trace of a matrix.

The influence of the material properties on the solutions is reflected through the Barnett-Lothe tensors $\mathbf{S},\ \mathbf{L}$ whose matrix expressions are composed of elastic constants [22]. For a given bimaterial, once the matrices $\mathbf{S},\ \mathbf{L}$ of each material are obtained,

the stress intensity factor can be deduced from Equations (6.1-6.6) and the corresponding energy release rate then can be evaluated according to the formula

$$\mathcal{G} = \frac{1}{4}\mathbf{K}^{\mathrm{T}}\mathbf{E}\mathbf{K}, \tag{6.7}$$

where

$$\mathbf{E} = \mathbf{D} + \mathbf{W}\mathbf{D}^{-1}\mathbf{W}. \tag{6.8}$$

Substitution of Equation (6.1) into Equation (6.7) yields

$$\begin{aligned}&\mathcal{G}(\mathbf{t}^{\infty}) = \\ &\frac{\pi a}{4}\left[(\mathbf{t}^{\infty})^{\mathrm{T}}(\mathbf{\Lambda}^{-1})^{\mathrm{T}}\langle\langle(1+2\mathrm{i}\varepsilon_{\alpha})(2a/\ell)^{-\mathrm{i}\varepsilon_{\alpha}}\rangle\rangle\mathbf{\Lambda}^{\mathrm{T}}\right]\mathbf{E}\left[\mathbf{\Lambda}\langle\langle(1+2\mathrm{i}\varepsilon_{\alpha})(2a/\ell)^{-\mathrm{i}\varepsilon_{\alpha}}\rangle\rangle\mathbf{\Lambda}^{-1}\mathbf{t}^{\infty}\right].\end{aligned} \tag{6.9}$$

For our problem proposed in Figure 6.1(b), we first consider the case of $\theta = \pi/2$ in which the material coordinates $(x_0,\ y_0)$ is coincident with the fixed spatial coordinates $(x,\ y)$. According to Equation (6.9), the energy release rate induced by a remote load $\mathbf{t}^{\infty}$ can be written as

$$\begin{aligned}&\mathcal{G}_0(\mathbf{t}^{\infty}) = \\ &\frac{\pi a}{4}\left[(\mathbf{t}^{\infty})^{\mathrm{T}}(\mathbf{\Lambda}_0^{-1})^{\mathrm{T}}\langle\langle(1+2\mathrm{i}\varepsilon_{\alpha})(2a/\ell)^{-\mathrm{i}\varepsilon_{\alpha}}\rangle\rangle\mathbf{\Lambda}_0^{\mathrm{T}}\right]\mathbf{E}_0\left[\mathbf{\Lambda}_0\langle\langle(1+2\mathrm{i}\varepsilon_{\alpha})(2a/\ell)^{-\mathrm{i}\varepsilon_{\alpha}}\rangle\rangle\mathbf{\Lambda}_0^{-1}\mathbf{t}^{\infty}\right].\end{aligned} \tag{6.10}$$

where subscript '0' stands for quantities referred to the material coordinates $(x_0,\ y_0)$. With the help of the relevant explicit expressions given by [55] for orthotropic bimaterials, the energy release rate (plane strain) of Equation (6.10) can be explicitly expressed as

$$\mathcal{G}_0(\mathbf{t}^{\infty}) = \frac{\pi a(1+4\varepsilon^2)}{4\cosh^2\pi\varepsilon}\left[D_{22}(\sigma_{yy}^{\infty})^2 + D_{11}(\sigma_{xy}^{\infty})^2\right], \tag{6.11}$$

with

$$\varepsilon = \frac{1}{2\pi}\ln\frac{1+\beta}{1-\beta},\ \beta = \left|W_{21}(D_{11}D_{22})^{-1/2}\right|, \tag{6.12}$$

$$D_{11} = \frac{1}{E_{\mathrm{t}}}\sqrt{\frac{E_{\mathrm{t}}}{E_{\mathrm{l}}}}(1-\nu_{\mathrm{t}}^2)^{1/2}\left\{\frac{E_{\mathrm{l}}}{G} + 2\left[\sqrt{(1-\nu_{\mathrm{t}}^2)\left(\frac{E_{\mathrm{l}}}{E_{\mathrm{t}}} - \nu_{\mathrm{l}}^2\right)} - \nu_{\mathrm{l}}(1+\nu_{\mathrm{t}})\right]\right\}^{1/2}, \tag{6.13}$$

$$D_{22} = \frac{1}{E_{\mathrm{l}}}\left(1 - \frac{\nu_{\mathrm{l}}^2}{E_{\mathrm{l}}}E_{\mathrm{t}}\right)^{1/2}\left\{\frac{E_{\mathrm{l}}}{G} + 2\left[\sqrt{(1-\nu_{\mathrm{t}}^2)\left(\frac{E_{\mathrm{l}}}{E_{\mathrm{t}}} - \nu_{\mathrm{l}}^2\right)} - \nu_{\mathrm{l}}(1+\nu_{\mathrm{t}})\right]\right\}^{1/2}, \tag{6.14}$$

$$W_{21} = -\sqrt{\frac{1}{E_{\mathrm{t}}E_{\mathrm{l}}}}\left[\sqrt{(1-\nu_{\mathrm{t}}^2)\left(1-\frac{\nu_{\mathrm{l}}^2 E_{\mathrm{t}}}{E_{\mathrm{l}}}\right)} - (1+\nu_{\mathrm{t}})\nu_{\mathrm{l}}\sqrt{\frac{E_{\mathrm{t}}}{E_{\mathrm{l}}}}\right], \tag{6.15}$$

where we only consider the in-plane load, i.e. $\mathbf{t}^{\infty} = \begin{bmatrix}\sigma_{xy}^{\infty} & \sigma_{yy}^{\infty} & 0\end{bmatrix}^{\mathrm{T}}$.

When $\theta \neq \pi/2$, the material coordinates $(x_0,\ y_0)$ do not coincide with the fixed coordinate system $(x,\ y)$ any more. The transformations of the Barnett-Lothe tensors between these two coordinate systems are

$$\mathbf{S} = \boldsymbol{\Omega}\mathbf{S}_0\boldsymbol{\Omega}^{\mathrm{T}},\ \mathbf{L} = \boldsymbol{\Omega}\mathbf{L}_0\boldsymbol{\Omega}^{\mathrm{T}}, \tag{6.16}$$

where $\boldsymbol{\Omega}$ is the transform matrix from (x_0, y_0) to (x, y) and

$$\boldsymbol{\Omega} = \begin{bmatrix} \sin\theta & \cos\theta & 0 \\ -\cos\theta & \sin\theta & 0 \\ 0 & 0 & 1 \end{bmatrix} \tag{6.17}$$

Based on (6.16), one can get the transformations for other related matrices as

$$\mathbf{D} = \boldsymbol{\Omega}\mathbf{D}_0\boldsymbol{\Omega}^{\mathrm{T}},\ \mathbf{W} = \boldsymbol{\Omega}\mathbf{W}_0\boldsymbol{\Omega}^{\mathrm{T}},\ \mathbf{M}^{*} = \boldsymbol{\Omega}\mathbf{M}_0^{*}\boldsymbol{\Omega}^{\mathrm{T}},\ \mathbf{E} = \boldsymbol{\Omega}\mathbf{E}_0\boldsymbol{\Omega}^{\mathrm{T}},\ \boldsymbol{\Lambda} = \boldsymbol{\Omega}\boldsymbol{\Lambda}_0, \tag{6.18}$$

where the orthotropic condition of the transformation matrix, $\boldsymbol{\Omega}^{-1} = \boldsymbol{\Omega}^{\mathrm{T}}$, have been used. Substituting the last relation of (6.18) into (6.1), we obtain the stress intensity factor for $\theta \neq \pi/2$ as

$$\mathbf{K} = \begin{bmatrix} K_{\mathrm{II}} \\ K_{\mathrm{I}} \\ K_{\mathrm{III}} \end{bmatrix} = \sqrt{\pi a}\boldsymbol{\Omega}\boldsymbol{\Lambda}_0\langle\langle(1+2\mathrm{i}\varepsilon_\alpha)(2a/\ell)^{-\mathrm{i}\varepsilon_\alpha}\rangle\rangle\boldsymbol{\Lambda}_0^{-1}\boldsymbol{\Omega}^{\mathrm{T}}\mathbf{t}^{\infty}. \tag{6.19}$$

The corresponding energy release rate then is given by

$$\mathcal{G} = \frac{1}{4}\mathbf{K}^{\mathrm{T}}\mathbf{E}\mathbf{K} = \\ \frac{\pi a}{4}\left[(\hat{\mathbf{t}}^{\mathrm{T}}(\boldsymbol{\Lambda}_0^{-1})^{\mathrm{T}}\langle\langle(1+2\mathrm{i}\varepsilon_\alpha)(2a/\ell)^{-\mathrm{i}\varepsilon_\alpha}\rangle\rangle\boldsymbol{\Lambda}_0^{\mathrm{T}}\right]\mathbf{E}_0\left[\boldsymbol{\Lambda}_0\langle\langle(1+2\mathrm{i}\varepsilon_\alpha)(2a/\ell)^{-\mathrm{i}\varepsilon_\alpha}\rangle\rangle\boldsymbol{\Lambda}_0^{-1}\hat{\mathbf{t}}\right]. \tag{6.20}$$

where

$$\hat{\mathbf{t}} = \boldsymbol{\Omega}^{\mathrm{T}}\mathbf{t}^{\infty} = \begin{bmatrix} \sin\theta & -\cos\theta & 0 \\ \cos\theta & \sin\theta & 0 \\ 0 & 0 & 1 \end{bmatrix}\begin{bmatrix} \sigma_{xy}^{\infty} \\ \sigma_{yy}^{\infty} \\ 0 \end{bmatrix} = \begin{bmatrix} \sigma_{xy}^{\infty}\sin\theta - \sigma_{yy}^{\infty}\cos\theta \\ \sigma_{xy}^{\infty}\cos\theta + \sigma_{yy}^{\infty}\sin\theta \\ 0 \end{bmatrix}. \tag{6.21}$$

Comparing (6.10) with (6.20) shows that the latter can be evaluated simply by replacing $\mathbf{t}^\infty$ with $\hat{\mathbf{t}}$ in the former. If only in-plane load is considered, after some straightforward calculations we obtain

$$\mathcal{G} = \frac{\pi a(1+4\varepsilon^2)}{4\cosh^2 \pi\varepsilon}\left[D_{22}\left(\sigma_{xy}^\infty \cos\theta + \sigma_{yy}^\infty \sin\theta\right)^2 + D_{11}\left(\sigma_{xy}^\infty \sin\theta - \sigma_{yy}^\infty \cos\theta\right)^2\right], \quad (6.22)$$

with ε, D_{11}, D_{22} are constants given by Equations (6.12-6.15). Although Equation (6.22) is the energy release rate corresponding to the right crack tip, similar analysis leads to an identical expression associated with the left crack tip.

For the uniaxial pulling stress σ^∞ applied at an inclined angle ϕ, as shown in Figure 6.1(b), the components σ_{xy}^∞ and σ_{yy}^∞ can be expressed as

$$\sigma_{xy}^\infty = \sigma^\infty \sin\phi\cos\phi,\ \ \sigma_{yy}^\infty = \sigma^\infty \sin\phi\sin\phi. \quad (6.23)$$

Substituting (6.23) into (6.22) and then applying the Griffith criterion for crack initiation $\mathcal{G} = W_{\text{ad}}$ lead to the following prediction of adhesion strength in the presence of the interfacial crack,

$$\sigma_{\text{cr}}^\infty(\theta,\phi) = \frac{\sqrt{W_{\text{ad}}/\pi a}}{\sin\phi\sqrt{C[D_{22}\cos^2(\theta-\phi) + D_{11}\sin^2(\theta-\phi)]}}, \quad (6.24)$$

where

$$C = \frac{(1+4\varepsilon^2)}{4\cosh^2\pi\varepsilon}. \quad (6.25)$$

Given material constants and the anisotropy direction θ, Equation (6.24) indicates that the adhesion strength varies as a function of the pulling angle ϕ. To calculate the critical (maximum and minimum) values as well as the corresponding directions, we try to solve equation $\partial\sigma_{\text{cr}}^\infty(\theta,\phi)/\partial\phi = 0$ and obtain

$$\frac{1+D_{22}/D_{11}}{1-D_{22}/D_{11}}\cos\phi = \cos(3\phi-2\theta),\ \ D_{22}/D_{11} = \sqrt{\frac{E_{\text{t}}(E_{\text{l}}-\nu_{\text{l}}^2 E_{\text{t}})}{E_{\text{l}}^2(1-\nu_{\text{t}}^2)}}. \quad (6.26)$$

If the Young's modulus in the longitudinal direction (e.g., along a fiber axis) is much larger than that in the transverse direction (e.g. transverse to the fiber direction), i.e. $E_{\text{l}}/E_{\text{t}} \gg 1$, Equation (6.26) has two roots

$$\phi_1 = \theta,\ \ \phi_2 = \theta/2 + \pi/2, \quad (6.27)$$

corresponding to the directions of the maximum and minimum pull-off stress, respectively. The adhesion releasability thus can be measured by the ratio of the maximum to the minimum pull-off stresses:

$$\frac{(\sigma_{\mathrm{cr}}^{\infty})_{\max}}{(\sigma_{\mathrm{cr}}^{\infty})_{\min}} = \frac{(1+\cos\theta)}{2\sin\theta}\left(\frac{D_{11}}{D_{22}}\right)^{1/2} = \frac{(1+\cos\theta)}{2\sin\theta}\left[\frac{E_{\mathrm{l}}^2(1-\nu_{\mathrm{t}}^2)}{E_{\mathrm{t}}(E_{\mathrm{l}}-\nu_{\mathrm{l}}^2 E_{\mathrm{t}})}\right]^{1/4}. \tag{6.28}$$

For small Poisson's ratios, Equation (6.28) suggests that the releasability of adhesion mainly depends on the stiffness ratio $E_{\mathrm{l}}/E_{\mathrm{t}}$ and the anisotropy direction θ. The stronger the anisotropy, the higher the releasability of adhesion. Assuming $\nu_{\mathrm{l}} = \nu_{\mathrm{t}} = 0.3$, $\theta = 30^{\circ}$ and $E_{\mathrm{l}}/E_{\mathrm{t}} = 10^4$, Figure 6.2 plots the normalized pull-off stress as a function the pulling angle ϕ. We can see that the elastic anisotropy causes about an order of magnitude change in adhesion strength as the pulling angle varies. A switch between attachment and detachment can thus be accomplished just by shifting the pulling angle between these two directions. In contrast, the adhesion strength of an isotropic material with $E_{\mathrm{l}} = E_{\mathrm{t}}$ and $\nu_{\mathrm{l}} = \nu_{\mathrm{t}}$ is much less sensitive to the pulling direction. We conclude that strong elastic anisotropy can result in an orientation-controlled switch between attachment and detachment.

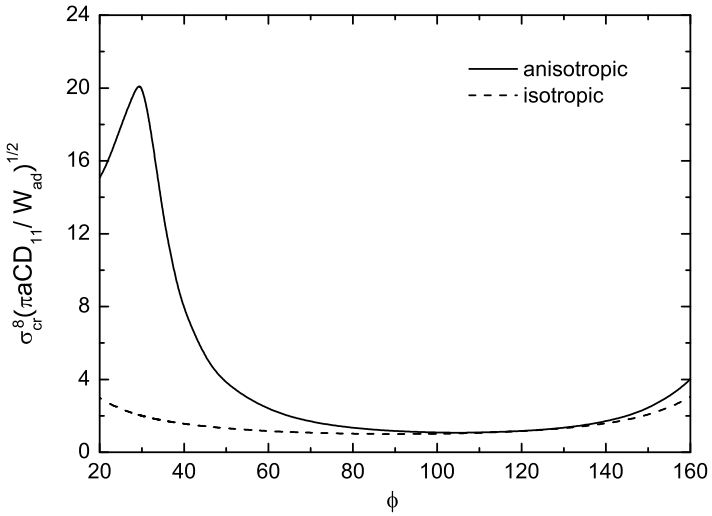

Figure 6.2.: Variation of the normalized adhesion strength as a function of the pulling angle ϕ for the anisotropic case ($\nu_{\mathrm{t}} = \nu_{\mathrm{l}} = 0.3$, $\theta = 30^{\circ}$ and $E_{\mathrm{l}}/E_{\mathrm{t}} = 10^4$) and the isotropic case.

One might note that Equation (6.24) implies an infinite adhesion strength in the limit of $\phi = 0$. This is caused by the assumed loading by a uniaxial tensile stress. Actually,

the limit $\phi = 0$ should be characterized as sliding under an applied shear stress. If, instead of pulling, we apply a remote shear stress σ_{xy}^{∞}, the critical shear stress becomes

$$(\sigma_{xy}^{\infty})_{\mathrm{cr}} = \frac{\sqrt{W_{\mathrm{ad}}/\pi a}}{\sqrt{C(D_{22}\cos^2\theta + D_{11}\sin^2\theta)}}, \tag{6.29}$$

which can be reduced to

$$(\sigma_{xy}^{\infty})_{\mathrm{cr}} = \frac{2\sqrt{W_{\mathrm{ad}}/\pi a}}{\sqrt{CD_{11}}} \tag{6.30}$$

when $D_{22} \ll D_{11}$ and $\theta = 30°$, and to

$$(\sigma_{xy}^{\infty})_{\mathrm{cr}} = \frac{\sqrt{W_{\mathrm{ad}}/\pi a}}{\sqrt{CD_{11}}} \tag{6.31}$$

when $D_{22} = D_{11}$ for the isotropic case.

6.2. Orientation-dependent adhesion of an attachment pad: numerical simulations

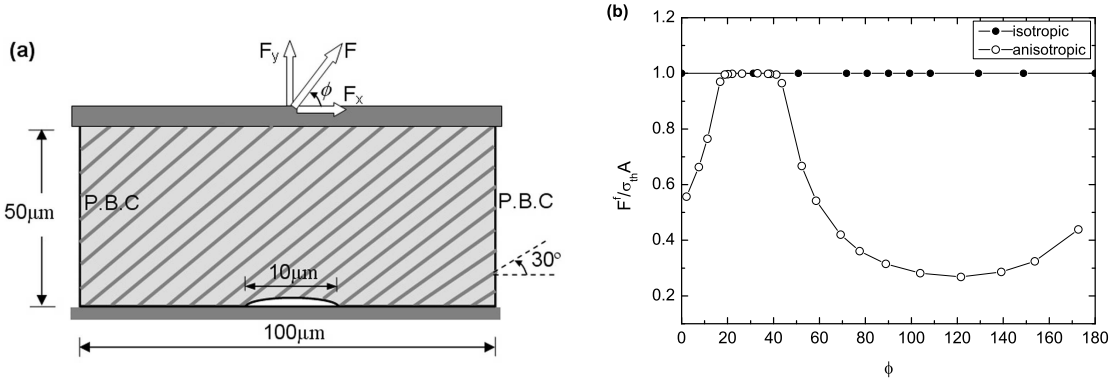

Figure 6.3.: Releasable adhesion in an attachment pad. (a) Geometry of the attachment pad used in FEM calculations. (b) Variation of the normalized pull-off force with the pulling angle. P.B.C.: Periodic boundary condition.

To further verify the principle of orientation-controlled adhesion switch via strong elastic anisotropy, we have also performed numerical simulations of the adhesion of a strongly anisotropic attachment pad (mimicking the hairy structured tissue on gecko's feet) via Tahoe.

The simulation system consists of a plane-strain anisotropic (transversely isotropic) elastic pad adhering to a rigid substrate with a crack situated at the central region of the contact interface (representing an adhesion flaw due to surface roughness), as shown in Figure 6.3(a). A displacement-controlled load is applied on the upper surface. At a given displacement, summation of all the nodal forces on the upper surface gives the pulling force F with components F_x, F_y. The pulling angle is then calculated via $\phi = \tan^{-1}(F_y/F_x)$. Periodic boundary conditions are applied on the left and right sides of the simulation domain. For comparison, both isotropic case and anisotropic case are considered. The material constants and potential parameters for each simulation case are listed in Table 6.1 where we adopt the calculated parameters S_3 and W_3^{ad} of the triangular hair pattern (see Table 5.1) as the effective adhesion strength and work of adhesion in simulating the detaching process of the pad.

Table 6.1.: Parameters used in FEM simulations.

Isotropic case	$E = 1.0$ GPa, $\nu = 0.3$
Anisotropic case	$E_{\mathrm{t}} = 0.1$ MPa, $E_{\mathrm{l}} = 1.0$ GPa, $\nu_{\mathrm{t}} = \nu_{\mathrm{l}} = 0.3$, $G = 10$ MPa, $\theta = 30^\circ$
Parameters for Tvergaard-Hutchinson model:	
$\Lambda_1 = 0.1$, $\Lambda_2 = 0.9$, $\sigma_{\mathrm{th}} = 5.44$ MPa, $\delta_{\mathrm{cn}} = \delta_{\mathrm{ct}} = 1.687$ μm.($W_{\mathrm{ad}} = 8.26$ J/m^2)	

Figure 6.3(b) plots the normalized pull-off stress $F^{\mathrm{f}}/\sigma_{\mathrm{th}}A$ as a function of the pulling angle ϕ. In the anisotropic case, saturation of adhesion strength is observed in the vicinity of $\phi = \theta = 30^\circ$, corresponding to a plateau of the curve in the range of $20^\circ < \phi < 40^\circ$. If the pulling angle deviates from this range in either direction, the adhesion strength decreases quickly to a lower plateau, illustrating the anisotropy-induced releasability of adhesion. This two-plateau adhesion strength is ideal for rapid switch between attachment and detachment during animal movement. The ratio between the maximum and minimum strengths reaches four for the given geometry, giving rise to significant releasability. In contrast, for the isotropic cases, no variation in pull-off force is observed as the pulling angle varies. Therefore, we conclude that strong elastic anisotropy leads to releasable adhesion via an orientation-controlled switch between strong and weak adhesion.

In this chapter, we have studied the mechanics principle of releasable adhesion. It has been shown that strong elastic anisotropy allows the adhesion strength to vary strongly with the direction of pulling. This orientation-dependent pull-off force enables robust attachment in the stiff direction of the material to be released by pulling in the soft direction. This strategy, conveniently summarized as "stiff-adhere, soft-release" principle, can be interpreted in a simple way as follows. When pulled in the stiff direction,

less elastic energy can be stored in the material (much like a stiff spring can store less energy compared to a soft spring), leading to lower energy release rate to drive random crack-like flaws induced by surface roughness. On the other hand, much more elastic energy can be stored in the material when pulled in the soft direction, especially when the material is strongly anisotropic, leading to much higher energy release rate to drive the roughness induced crack-like flaws.

Chapter 7. Discussions

We have systematically investigated the mechanical principles of robust and releasable adhesion within the framework of continuum mechanics. The studies include

- shape effect on adhesion,
- flaw tolerant (robust) adhesion and
- releasable adhesion.

Although the work is motivated by the biological attachment systems, the results we obtained can be interpreted extensively as the general principles governing the adhesion.

In this chapter, the important results obtained in this thesis will be summarized. Then, we will discuss the potential application of our results in the fabrication of the synthetic adhesion devices. Finally, the whole thesis will be concluded with an outlook to the future work.

7.1. Summary and discussion

It is the superior adhesion capability of biological attachment systems that motivates the studies reported in this thesis. Our objective is to elucidate the mechanics principles accounting for the robust and releasable adhesion of these natural attachment systems.

When two solid surfaces are brought into adhesive contact, a critical force, normally termed pull-off force, is required to pull them apart. Since the pull-off force is affected by the size of the contact area, adhesion strength is defined more often by the pull-off force per unit contact area. This definition allows us to compare the adhesion strength between two joints even thought their contact areas are different. On the other hand, the traction between two surfaces is limited by the theoretical strength σ_{th}. Given two solids, is it possible to achieve the theoretical adhesion via structural optimization? To answer this question, we first investigated the effect of size and shape on the adhesion strength for a single contact asperity. It has been found that the optimal adhesion

with theoretical adhesion strength can be realized either by size reduction or by shape optimization. The smaller the size, the less important the shape [34]. At larger contact sizes, optimal adhesion could still be achieved if the shape can be manufactured to a sufficiently high precision. Under this circumstance, however, the optimal adhesion is not robust because a small variation in the contact shape could leads to large decrease in the adhesion strength. The robust design of optimal adhesion can be obtained at nanoscale, in which case the contact shape is not a dominant issue any more. This finding provides a plausible explanation to the convergent evolution of hairy attachment systems in biology.

However, optimizing adhesion at the level of single asperities or fibrils does not automatically address the problem of robust adhesion on rough surfaces at macroscopic scales. To solve this problem, we have studied the adhesion strength between rough surfaces. Instead of directly modeling adhesive contact on random or fractal rough surfaces as in the pervious works, we have adopted a different modeling approach by considering an interfacial crack as a representative contact flaw. In comparison with previous contact models on rough surfaces, the crack model is more tractable in mathematics and allows us to deal with adhesive contact associated with hierarchy, elasticity grading and anisotropy that are crucially important for biological systems. We have hypothesized that robust adhesion on random rough surfaces is equivalent to flaw tolerant adhesion in which the growth of a representative interfacial crack is suppressed for any crack size. By using the concept of flaw tolerant adhesion, we have shown that graded elasticity and hierarchical energy dissipation are two important strategies to make the system insensitive to crack-like contact flaws. But these two strategies have distinct theoretical bases. The strategy of graded elasticity works because it ensures that the average property of material around a crack is rigid enough to suppress crack growth while the surface remains sufficiently compliant to achieve good contact with a rough surface. The strategy of hierarchical energy dissipation operates because it makes the work of adhesion scale up with the flaw size. In principle, these two strategies are equivalently effective in promoting the flaw tolerance. However, for adhesion due to van der Waals interaction as in the biological attachment systems, the graded elasticity strategy by itself seems less practical because flaw tolerance needs such a steep gradient in elasticity that can not be realized in reality easily. In practice, therefore, flaw tolerance can be achieved by a combination of graded elasticity and hierarchical energy dissipation.

In addition to the robustness, adhesion releasability is also important for animals. How to release an attachment designed for robust adhesion becomes the topic that we

are most concerned about. Instead of modeling the microscopic structure of a specific adhesion device as in some of previous studies, in this thesis we focus our attention on the general mechanical principle of releasable adhesion. Motivated by the common feature observed in the various biological attachment systems, we proposed that strong elastic anisotropy may allow the adhesion strength to vary with the direction of pulling force, achieving an orientation-controlled switch between attachment and detachment. This proposition has been demonstrated by theoretical modeling and numerical simulation within the framework of continuum fracture mechanics. The orientation-dependent pull-off stress induced by the elastic anisotropy allows robust attachment in the stiff direction of the material to be released by pulling in the soft direction. In this regard, it can be summarized as "stiff-adhere, soft-release". This finding provides a plausible explanation for the adhesion releasability and agrees well with the common anisotropy feature observed in the biological attachment systems with different microscopic structures.

Table 7.1.: Parameters used in FEM simulations.

	Homogeneous	Graded
Isotropic	$E = 1.0$ GPa, $\nu = 0.3$	$E(y) = E_0(1 + y/c_0)^2$, $E_0 = 1.0$ GPa, $c_0 = 1$ μm, $\nu = 0.3$
Anisotropic	$E_\mathrm{t} = 0.1$ MPa, $E_\mathrm{l} = 1.0$ GPa, $\nu_\mathrm{t} = \nu_\mathrm{l} = 0.3$, $G = 10$ MPa, $\theta = 30°$	$E_\mathrm{l}(y) = E_\mathrm{l0}(1 + y/c_0)^2$, $E_\mathrm{l0} = 1.0$ GPa, $c_0 = 1$ μm, $E_\mathrm{t} = 0.1$ MPa, $G = 10$ MPa, $\nu_\mathrm{t} = \nu_\mathrm{l} = 0.3$, $\theta = 30°$
Parameters for the Tvergaard-Hutchinson model: $\sigma_\mathrm{th} = 10$ MPa, $\Lambda_1 = 0.1$, $\Lambda_2 = 0.9$, $\delta_\mathrm{cn} = \delta_\mathrm{ct} = 5$ nm, ($W_\mathrm{ad} = 0.045$ J/m^2)		

For conceptual clarity, our discussions for the adhesion robustness and releasability have been carried out separately. This does not mean these two aspects are completely independent. On the contrary, they affect each other. To illustrate this point, we calculate the adhesion strength for an anisotropic graded material by using the same simulation system illustrated in Figure 6.3(a). For comparison, we consider three control cases in addition to the anisotropic homogeneous case: isotropic homogeneous case, isotropic graded case and anisotropic graded case. The material constants and potential parameters for each simulated case are listed in Table 7.1 in terms of a combination of two classes of properties "isotropic/anisotropic" and "homogeneous/graded". Here we ignore the effect of energy dissipation for the moment by taking a typical value of surface energy (0.045 J/m^2) as the work of adhesion. The effects of graded elasticity and anisotropy on the pull-off stress as a function of the pulling angle are shown in Figure 7.1. For the isotropic homogeneous case, it can be seen that introduction of

graded elasticity enhances the adhesion strength toward the theoretical strength for all directions of pulling. In particular, adhesion stress saturates at the theoretical value in the vertical direction $\phi = 90°$. The unsaturation of adhesion stress in the other directions might be attributed to the relatively smaller elasticity gradient in these directions. On the other hand, introduction of anisotropy increases the adhesion releasability but it simultaneously reduces the adhesion strength in all directions. The joint anisotropic graded material combines these two effects together and results in a "robust" and releasable adhesion, although the associated maximum adhesion strength can not reach the theoretical value. We can make it up by increasing the elasticity grading or by adopting energy dissipation strategy.

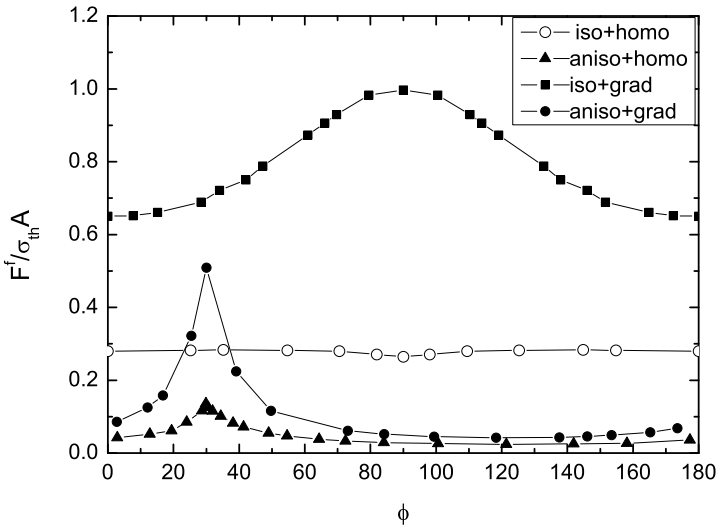

Figure 7.1.: Variation of the normalized pull-off force as a function of the pulling angle; iso+homo: isotropic homogeneous case; iso+grad: isotropic graded case; aniso+homo: anisotropic homogeneous case; aniso+grad: anisotropic graded case.

In addition, work of adhesion W_{ad} also has an effect on the adhesion releasability. For the anisotropic case defined in Table 6.1, if we replace the work of adhesion with a lower value $W_{\text{ad}} = 7.83$ J/m^2 or a higher value $W_{\text{ad}} = 48.96$ J/m^2 while keep all the other parameters unchanged, the variations of the pull-off force are plotted in Figure 7.2 as a function of the pulling angle. One can see that while a higher work of adhesion decreases the releasability, a lower work of adhesion will make the pull-off stress around the robust direction too sensitive to the pulling angle even though optimal adhesion is achieved there. An effective attachment system therefore needs a proper work of adhesion which

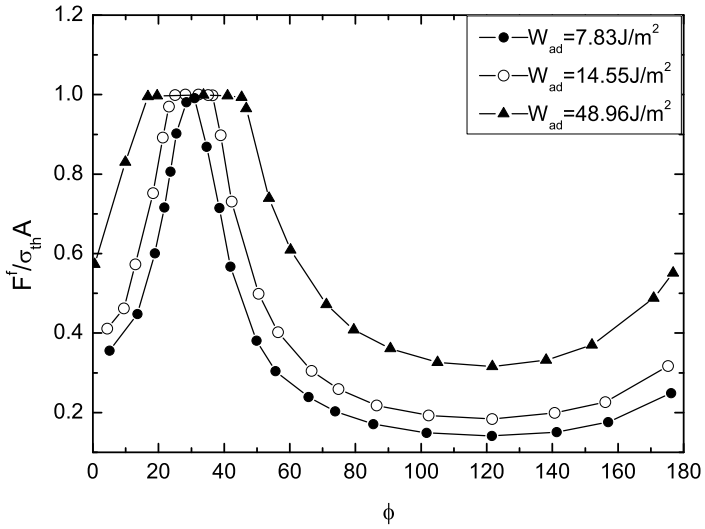

Figure 7.2.: Variation of the normalized pull-off force with the pulling angle for different work of adhesion.

not only can ensure optimal adhesion in a certain range of pulling angle but also can maintain sufficient releasability.

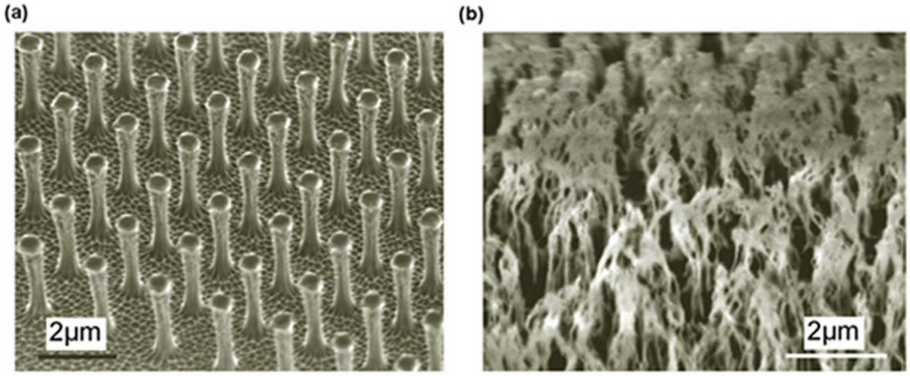

Figure 7.3.: Synthetic attachment systems. (a) Array of submicron pillars (adapted from [35]) (b) Multi-scaled conformal system (adapted from [73].

Biological adhesion devices are complex systems which provide a rich source of inspirations for industrial applications. Some novel synthetic attachment systems have been produced in laboratory by mimicking the fibrillar structure of gecko. For instance, Geim *et al.* [35] fabricated arrays of polymeric nanopillars on solid substrate (Figure 7.3a). A considerable adhesion force was obtained via such man-made hairy structures. More

recently, Northen and Turner [73] made use of massively parallel MEMS processing technology to produce hierarchical hairy adhesive materials containing single slender pillars coated with polymer nanorods (Figure 7.3b), and reported significantly improved adhesion in this multi-scale system. All these synthetic adhesion materials or structures have been designed to achieve strong adhesion. With the guidance of the results reported in this thesis, maybe we can develop a flaw-tolerant and releasable attachment device in the near future. While we usually do not expect to capture all the bio-complexities in simple models, the essence of bio-inspired mechanics is to break a complex problem into many comprehensible sub-problems that can be understood using mechanics principles. In this thesis, we have considered the effects of graded elasticity, hierarchical dissipation energy, scale-dependent adhesion strength and elastic anisotropy on robust and releasable adhesion. Many other important aspects of the problem, such as viscoelasticity and large nonlinear deformation have not been taken into account. Much further work will be needed to advance our current understanding of bio-adhesion mechanisms. The studies on such problems should be of interest not only to the mechanics community but also to a variety of other disciplines including materials science, biology and nanotechnology.

7.2. Outlook to the future research

On the basis of the work reported in the thesis, two prospective projects are proposed. *Project 1* Investigates the condition for robust (flaw tolerant) adhesion between fractal rough surfaces. *Project 2* models the twist-induced releasable adhesion.

Project 1. Robust adhesion between fractal rough surfaces

In our previous modeling, we have reduced the contact problems to the crack problems by neglecting the profile of the roughness asperities. This approximation is appropriate when the roughness wave amplitude is quite small in comparison with the wave length. If it is not the case, the non-planar profile of the roughness asperities will become the essential feature which distinguishes a contact problem from a fracture problem. For example, in the crack problem, the area of the contact (bonded) region is invariant before fracture, while in a typical contact problem the contact area is shrunk as the external pulling load increases until detachment occurs. In essence, this dissimilarity can be attributed to the non-planar roughness profile.

In the future research, we plan to take the roughness protrusion into account so as to investigate the condition for robust (flaw tolerant) adhesion between real rough surfaces.

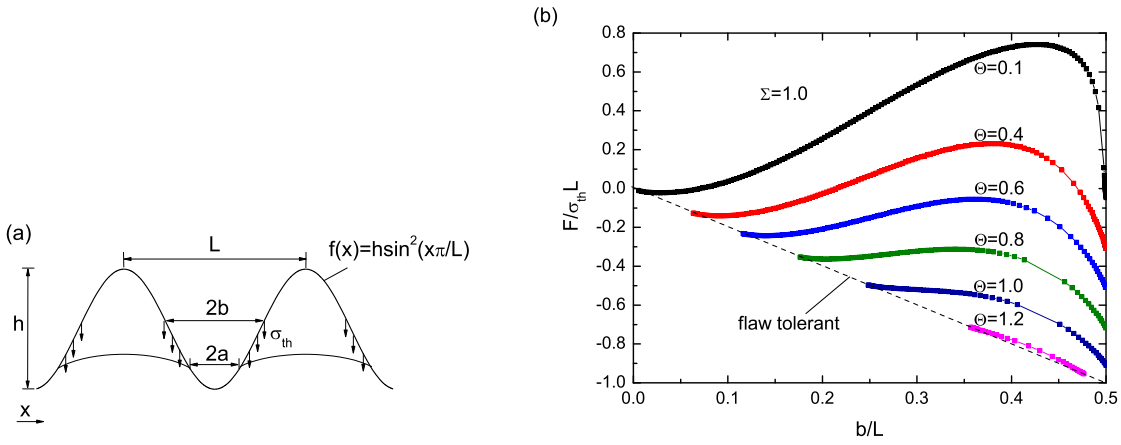

Figure 7.4.: (a) Schematic of a rigid solid with sinusoidal roughness in contact with an elastic flat substrate. (b) Variation of the adhesion force with the contact area for $\Sigma = 1.0$ and different Θ.

We will begin with a simple model in which a rigid solid with sinusoidal roughness is in contact with a flat substrate (Figure 7.4a). Actually, this problem has been solved by Hui *et al.* [54]. We will apply the relative results into our discussion on the flaw tolerant adhesion between solids with periodic roughness. Given materials, the roughness height h and periodicity L are two important factors that dominate the behavior of adhesion. Denoting

$$\Sigma = \frac{2\sigma_{\mathrm{th}} L}{\pi E^* h}, \quad \Theta = \left(\frac{8L\Delta\gamma}{h^2\pi^2 E^*}\right)^{1/2}$$

with σ_{th} being the theoretical adhesion strength, $\Delta\gamma$ the adhesion energy and $E^* = E/(1-\nu^2)$ with E, ν being the Young's modulus and Poisson's ratio of the substrate, the variation of the adhesion force with the contact area is fully determined by these two dimensionless parameters. Taking $\Sigma = 1.0$, Figure 7.4(b) shows the variation of the adhesion force with the contact area for different Θ. The dash line stands for the flaw tolerant state in which the adhesive force equals $2b\sigma_{\mathrm{th}}$. One can see that for a given Σ, large Θ, corresponding to large aspect ratio L/h, small roughness height h or small modulus E^*, facilitates flaw tolerant adhesion. Based on these preliminary results, in this project we plan to extend the discussion further to the three-dimensional case. First, we can assume that roughness asperities are uniform and distributed periodically. Then, we will consider a more sophisticated but realistic case in which the roughness is not simply periodic but obeys a certain statistic distribution. After that, the discussion

can be advanced to the contact between two surfaces with fractal roughness [15]. Besides robust adhesion, other interesting concepts like spontaneous adhesion [34] are also worth studying within the framework proposed above.

Project 2. Twist-induced releasable adhesion

It has been pointed out that materials with strong anisotropy can produce orientation-dependent adhesion strength. Switch between attachment and detachment thus can be accomplished by changing the pulling angles (e.g., by exerting different muscles) (Figure 7.5a). Under this circumstance, the releasability of adhesion can be measured by ratio of the maximum pull-off force to the minimum $F^{\mathrm{f}}_{\mathrm{max}}/F^{\mathrm{f}}_{\mathrm{min}}$. The higher the ratio, the more efficient the releasable adhesion.

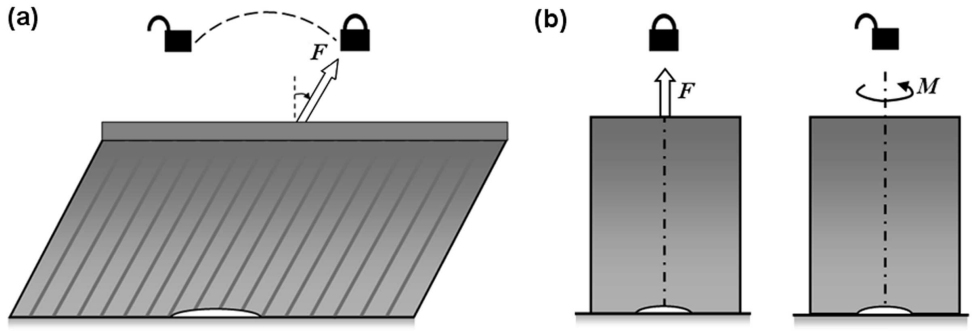

Figure 7.5.: Two possible strategies for achieving releasable adhesion: (a) via strong anisotropy and (b) via twisting.

Motivated by the movement feature of gecko's feet at the detachment moment here we propose another possible mechanism for releasable adhesion. We hypothesize that robust adhesion may be easily released by applying a torque, as shown in Figure 7.5(b). The problem of designing releasable adhesion thus can be stated as to find such an attachment system that can withstand strong tensile force but small torque. So that strong adhesion can be easily detached via twisting.

The work of this project will begin by studying the adhesive contact between single asperities like a sphere or a fiber. Different from our previous studies, now we will focus our attentions on the failure of adhesion under torque loading. The magnitude of the critical torque M_{c}, i.e. the moment required to twist two surfaces apart, reflects the ability of the attachment to withstand torsion loading. How does the magnitude of M_{c} rely on the factors such as contact size, shape and material properties (e.g. Young's modulus)? How to optimize M_{c} by controlling these factors? All these questions will

be discussed systematically in the present project. For the twist-induced releasable adhesion, the releasability can be measured by ratio of $F^{\mathrm{f}}\ell/M_{\mathrm{c}}$, where F^{f} is the pull-off force and ℓ is the characteristic length scale of the contact area. Our objective is to find such a design that has a small M_{c} and a large pull-off force F^{f}, resulting in a large releasability $F^{\mathrm{f}}\ell/M_{\mathrm{c}}$. In addition, we can extend our investigation from single asperities to rough surfaces. For simplicity, we can begin by modeling the adhesion defects due to roughness as the interfacial cracks. Then, other complex factors like the protrusion of the roughness, the statistic distribution of the roughness can be incorporated into our model gradually. Moreover, it will be an interesting research topic to combine the twist-induced releasable adhesion with concepts of elasticity grading or hierarchy [104].

Our discussions so far have been limited within the linear elastic materials. A point of particular interest is to extend the studies to the nonlinear and time-dependent elasticity. This viscoelasticity, as it is called, is actually most common to the biological materials. Such extension could shed much light on the problem of biological attachment. Meanwhile, our previous studies mainly focus on the dry adhesion. It should be quite interesting as well to extend the existing discussions to the regime of wet adhesion in which a certain amount of liquid is existent between two contact surfaces. Under this circumstance, the effect of liquid surface tension should be taken into account.

Understanding the engineering principles of biological systems can play an important role in helping address some of the major challenges in materials science and engineering in the 21$^{\mathrm{st}}$ century. We believe that the development of nanotechnology will eventually open up enormous possibilities in developing multi-functional and hierarchical material systems. What we have reported in this thesis regarding the adhesion in biological attachment systems is just a tentative step of this grand endeavor. In some cases, such as the biological attachment systems discussed in this thesis, convergent evolutions occur when genetically unrelated biological systems have adopted the same strategies to achieve the same goal or properties or functions. In other cases, genes associated with a given set of properties or functions of the same biological system may be found to be strongly conserved over the history of evolution. Whenever convergent evolutions occur, we may look for hints on property optimization. We have discussed in this thesis adhesion strength in connection with the principle of flaw tolerance. Similar investigations may be conducted with respect to other properties including friction, fatigue, corrosion and hydrophobicity. There is still a long way to go before the complexities of hierarchical structures of biological systems and their associated functions are fully understood.

References

[1] E. Arzt, S. Enders, and S. Gorb. Towards a micromechanical understanding of biological surface devices. *Z. Metallk.*, 93:345–351, 2002.

[2] E. Arzt, S. Gorb, and R. Spolenak. From micro to nano contacts in biological attachment devices. *Proc. Natl. Acad. Sci. USA*, 100:10603–10606, 2003.

[3] K. Autumn, Y.A. Liang, S.T. Hsieh, W. Zesch, W.P. Chan, T.W. Kenny, R. Fearing, and R.J. Full. Adhesive force of a single gecko foot-hair. *Nature*, 405:681–685, 2000.

[4] K. Autumn and A.M. Peattie. Mechanisms of adhesion in geckos. *Integr. Compar. Biol.*, 42:1081–1090, 2002.

[5] K. Autumn, M. Sitti, Y.A. Liang, A.M. Peattie, W.R. Hansen, S. Sponberg, T.W. Kenny, R. Fearing, J.N. Israelachvili, and R.J. Full. Evidence for van der Waals adhesion in gecko setae. *Proc. Natl. Acad. Sci. USA*, 99:12252–12256, 2002.

[6] J.M. Baney and C.Y. Hui. A cohesive zone model for the adhesion of cylinders. *J. Adhesion Sci. Technol.*, 11:393–406, 1997.

[7] M. Barquins. Adherence and rolling kinetics of a rigid cylinder in contact with a natural rubber surface. *J. Adhesion*, 26:1–12, 1988.

[8] E. Barthel. On the description of the adhesive contact of spheres with arbitrary interaction potentials. *J. Colloid Interface Sci.*, 200:7–18, 1998.

[9] W. Barthlott and C. Neinhuis. Purity of the sacred lotus, or escape from contamination in biological surfaces. *Planta*, 202:1–8, 1997.

[10] R.G. Beutel and S. Gorb. Ultrastructure of attachment specializations of hexapods (arthropoda): evolutionary patterns inferred from a revised ordinal phylogeny. *J. Zool. Syst. Evol. Research*, 39:177–207, 2001.

[11] J. Boussinesq. *Application des Potentials à l'etude de l' équilibre et du movement des solids é lastiques*. Gauthier-Villar, Paris, 1885.

[12] R.S. Bradley. The cohesive force between solid surface and the surface energy of solids. *Phil. Mag.*, 13:853–862, 1932.

[13] P.T. Brown and R.E. Gibson. Surface settlement of a deep elastic stratum whose modulus increases linearly with depth. *Can. Geotech. J.*, 9:467–476, 1972.

[14] M.J. Bühler, H. Yao, B. Ji, and H. Gao. Cracking and adhesion at small scales: Atomistic and continuum studies of flaw tolerant nanostructures. *Modeling and Simulation in Materials Science and Engineering*. submitted.

[15] R. Buzio, C. Boragno, F. Biscarini, F.B. De Mongeot, and U. Valbusa. The contact mechanics of fractal surfaces. *Nature Mater.*, 2:233–236, 2003.

[16] R.W. Carpick, D.F. Ogletree, and M. Salmeron. A general equation for fitting contact area and friction vs load measurements. *J. Colloid Interface Sci.*, 211:395–400, 1999.

[17] M.F. Chuaprasert and M.K. Kassir. Displacements and stresses in nonhomogeneous solid. *J. Eng. Mech. Div. ASCE*, 100:861–872, 1974.

[18] S.H. Crandall, N.C. Lardner, and T.J. Lardner. *An introduction to the mechanics of solids*. McGrawHill, Kogakusha, 1978.

[19] J.H. de Boer. The influence of van der Waals' forces and primary bonds on binding energy, strength and orientation, with special reference to some artificial resins. *Trans. Faraday Soc.*, 32:10–36, 1936.

[20] B.V. Derjaguin. Theorie des anhaftens kleiner teilchen. *Koll. Z.*, 69:155–164, 1934.

[21] B.V. Derjaguin, V.M. Muller, and Y.P. Toporov. Effect of contact deformations on the adhesion of particle. *J. Colloid Interface Sci.*, 53:314–326, 1975.

[22] C. Dongye and T.C.T. Ting. Explicit expressions of Barnett-Lothe tensors and their associated tensors for orthotropic materials. *Q. Appl. Math.*, 47:723–734, 1989.

[23] D.S. Dugdale. Yielding of steel sheets containing slits. *J. Mech. Phys. Solids*, 8:100–108, 1960.

[24] J. Dundurs. *Mathematical Theory of Dislocations*, chapter Elastic interactions of dislocations with inhomogeneities, pages 70–115. ASME, New York, 1969.

[25] F. Erdogan and G.D. Gupta. Numerical solution of singular integral-equations. *Q. Appl. Math.*, 29:525–534, 1972.

[26] F. Erdogan, G.D. Gupta, and T.S. Cook. *Methods of Analysis and Solutions of Crack Problems*, pages 368–425. Leyden, Noordhoff, 1973.

[27] K.N.G. Fuller and D. Tabor. The effect of surface roughness on adhesion of elastic solids. *Proc. R. Soc. Lond. A*, 345:327–342, 1975.

[28] H. Gao, M. Abbudi, and D.M. Barnett. On interfacial crack-tip field in anisotropic elastic solids. *J. Mech. Phys. Solids*, 40:393–416, 1992.

[29] H. Gao and S. Chen. Flaw tolerance in a thin strip under tension. *J. App. Mech.*, 72:732–737, 2005.

[30] H. Gao and B. Ji. Modeling fracture in nanomaterials via a virtual internal bond method. *Eng. Frac. Mech.*, 70:1777–1791, 2003.

[31] H. Gao, B. Ji, M.J. Buehler, and H. Yao. Flaw tolerant bulk and surface nanostructures of biological systems. *Mech. Chem. Biosys.*, 1:37–52, 2004.

[32] H. Gao, B. Ji, I.L. Jaeger, E. Arzt, and P. Fratzl. Materials become insensitive to flaws at nanoscale: lessons from nature. *Proc. Natl. Acad. Sci. USA*, 100:5597–5600, 2003.

[33] H. Gao, X. Wang, H. Yao, S. Gorb, and E. Arzt. Mechanics of hierarchical adhesion structure of gecko. *Mechanics of Materials*, 37:275–285, 2005.

[34] H. Gao and H. Yao. Shape insensitive optimal adhesion of nanoscale fibrillar structures. *Proc. Natl. Acad. Sci. USA*, 101:7851–7856, 2004.

[35] A.K. Geim, S.V. Dubonos, I.V. Grigorieva, K.S. Novoselov, A.A. Zhukov, and S.Y. Shapoval. Microfabricated adhesive mimicking gecko foot-hair. *Nature Mater.*, 2:461–463, 2003.

[36] L.J. Gibson and M.F. Ashby. The mechanics of three-dimensional cellular materials. *Proc. R. Soc. Lond. A*, 382:43–59, 1982.

[37] R.E. Gibson. Some results concerning displacements and stresses in a non-homogeneous elastic half-space. *Géotechnique*, 17:58–67, 1967.

[38] G.M. Gladwell. *Contact problems in the classical theory of elasticity*. Sijthoff and Noordhoff, Netherlands, 1980.

[39] N.J. Glassmaker, A. Jagota, and C.Y. Hui. Adhesion enhancement in a biomimetic fibrillar interface. *Acta Biomater.*, 1:367–375, 2005.

[40] N.J. Glassmaker, A. Jagota, C.Y. Hui, and J. Kim. Design of biomimetic fibrillar interfaces: 1. making contact. *J. R. Soc. Lond. Interface*, 1:23–33, 2004.

[41] S. Gorb, Y. Jiao, and M. Scherge. Ultrastructural architecture and mechanical properties of attachment pads in tettigonia viridissima (orthoptera tettigoniidae). *J. Comp. Physiol. A*, 186:821–831, 2000.

[42] M. Gotoh. Some problems of bonded anisotropic plates with cracks along the bond. *Int. J. Fract. Mech.*, 3:253–265, 1967.

[43] J.A. Greenwood. Adhesion of elastic spheres. *Proc. R. Soc. Lond. A*, 453:1277–1297, 1997.

[44] J.A. Greenwood and J.B.P. Wiliamson. Contact of nominally flat surfaces. *Proc. R. Soc. Lond. A*, 295:300–319, 1966.

[45] A.A. Griffith. The phenomena of rupture and flow in solids. *Phil. Trans. Roy. Soc. Lond. A*, 221:163–198, 1921.

[46] G. Haiat, M.C.P. Huy, and E. Barthel. The adhesive contact of viscoelastic spheres. *J. Mech. Phys. Solids*, 51:69–99, 2003.

[47] J.W. Harding and I.N. Sneddon. The elastic stresses produced by the indentation of the plane surface of a semi-infinite elastic solid by a rigid punch. *Proc. Camb. Phil. Soc.*, 41:16–26, 1945.

[48] H.C. Harmaker. The London - van der Waals attraction between spherical particles. *Physica*, 4:1058–1072, 1937.

[49] H. Hertz. Über die berührung fester elastischer körper (on the contact of elastic solids). *J. Reine Angew. Math.*, 92:156–171, 1882.

[50] G. Huber, S. Gorb, R. Spolenak, and E. Arzt. Resolving the nanoscale adhesion of individual gecko spatulae by atomic force microscopy. *Biol. Lett.*, 1:2–4, 2005.

[51] C.Y. Hui, J.M. Baney, and E.J. Kramer. Contact mechanics and adhesion of viscoelastic spheres. *Langmuir*, 14:6570–6578, 1998.

[52] C.Y. Hui, A. Jagota, Y.Y. Lin, and E.J. Kramer. Constraints on microcontact printing imposed by stamp deformation. *Langmuir*, 18:1394–1407, 2002.

[53] C.Y. Hui, Y.Y. Lin, J.M. Baney, and A. Jagota. The accuracy of the geometric assumptions in the JKR (Johnson-Kendall-Roberts) theory of adhesion. *J. Adhes. Sci. Technol.*, 14:1297–1319, 2000.

[54] C.Y. Hui, Y.Y. Lin, J.M. Baney, and E.J. Kramer. The mechanics of contact and adhesion of periodically rough surfaces. *J. Polym. Sci., Pt. B, Polym. Phys.*, 39:1195–1241, 2001.

[55] C. Hwu. Fracture parameters for the orthotropic bimaterial interface cracks. *Engr. Fract. Mech.*, 45:89–97, 1993.

[56] J.N. Israelachvili. *Intermolecular and surface forces*. Academic Press, San Diego, 2nd edition, 1992.

[57] J.N. Israelachvili. Irreversibility, energy-dissipation, and time effects in intermolecular and surface interactions. *Isr. J. Chem.*, 35:85–91, 1995.

[58] A. Jagota and S.J. Bennison. Mechanics of adhesion through a fibrillar microstructure. *Intergr. Comp. Biol.*, 42:1140–1145, 2002.

[59] J. Jitcharoen, N.P. Padture, A.E. Giannakopoulos, and E. Suresh. Hertzian-crack suppression in ceramics with elastic-modulus-graded surfaces. *J. Amer. Ceram. Soc.*, 81:2301–2308, 1998.

[60] K.L. Johnson. *Contact mechanics*. Cambridge Univ. Press, Cambridge, U.K.

[61] K.L. Johnson and J.A. Greenwood. An adhesion map for the contact of elastic spheres. *J. Colloid Interface Sci.*, 192:326–333, 1997.

[62] K.L. Johnson, K. Kendall, and A.D. Roberts. Surface energy and contact of elastic solids. *Proc. R. Soc. Lond. A*, 324:301–313, 1971.

[63] K. Kendall. Thin-film peeling-elastic term. *J. Phys. D: Appl. Phys.*, 8:1449–1452, 1975.

[64] K.S. Kim, R.M. McMeeking, and K.L. Johnson. Adhesion, slip, cohesive zones and energy fluxes for elastic spheres in contact. *J. Mech. Phys. Solids*, 46:243–266, 1998.

[65] A. Majumdar and B. Bhushan. Role of fractal geometry in roughness characterization and contact mechanics of surfaces. *J. Tribology*, 112:205–216, 1990.

[66] A. Majumdar and B. Bhushan. Fractal model of elastic-plastic contact between rough surfaces. *J. Tribology*, 113:1–11, 1991.

[67] D. Maugis. Adhesion of spheres: the JKR-DMT transition using dugdale model. *J. Colloid Interface Sci.*, 150:243–269, 1992.

[68] D. Maugis. *Contact, Adhesion and Rupture of Elastic Solids.* Springer-Verlag, Berlin, 2000.

[69] C. Morrow, M.R. Lovell, and X.G. Ning. A JKR-DMT transition solution for adhesive rough surface contact. *J. Phys. D: Appl. Phys.*, 36:534–540, 2003.

[70] W. Nachtigall. *Biological mechanisms of attachment.* Springer-Verlag, Berlin, 1974.

[71] H. Neuber. Ein neuer ansatz zur lösung räumlicher probleme der elastizitätstheorie. *Z. Angew. Math. Mech.*, 14:203–212, 1934.

[72] S. Niegeregger, S. Gorb, and Y. Jiao. Contact behaviour of tenent setae in attachment pads of the blowfly calliphora vicina (diptera, calliphoridae). *J. Comp. Physiol. A*, 187:961–970, 2002.

[73] M.T. Northen and K.L. Turner. A batch fabricated biomimetic dry adhesive. *Nanotech.*, 16:1159–1166, 2005.

[74] Z. Olesiak and M. Wnuk. Plastic energy dissipation due to a penny-shaped crack. *Int. J. Fract. Mech.*, 4:383–396, 1968.

[75] P.F. Papkovich. Solution générale des équations diffrentielles fondamentales de l'élasticité exprimée partrois fonctions harmoniques. *Comput. Rend.*, 195:513–515, 1932.

[76] D.C. Pender, N.P. Padture, A.E. Giannakopoulos, and S. Suresh. Gradients in elastic modulus for improved contact-damage resistance. Part I: the silicon nitride-oxynitride glass system. *Acta Mater.*, 49:3255–3262, 2001.

[77] B.N.J. Persson. Nanoadhesion. *Wear*, 254:832–834, 2003.

[78] B.N.J. Persson. On the mechanism of adhesion in biological systems. *J. Chem. Phys.*, 118:7614–7621, 2003.

[79] B.N.J. Persson and S. Gorb. The effect of surface roughness on the adhesion of elastic plates with application to biological systems. *J. Chem. Phys.*, 119:11437–11444, 2003.

[80] O. Pietrement and M. Troyon. General equations describing elastic indentation depth and normal contact stiffness versus load. *J. Colloid Interface Sci.*, 226:166–171, 2000.

[81] J.R. Rice. *Treatise on Fracture*, chapter Mathematical analysis in the mechanics of fracture, page 266. Academic Press, 1968.

[82] P. Sahoo and S.K.R. Chowdhury. A fractal analysis of adhesion at the contact between rough solids. *Proc. Instn. Mech. Engrs.*, 210:269–279, 1996.

[83] P. Sahoo and S.K.R. Chowdhury. A fractal analysis of adhesive wear at the contact between rough solids. *Wear*, 253:924–934, 2002.

[84] M. Scherge and S. Gorb. *Biological Micro and Nano-Tribology.* Spinger-Verlag, New York, 2001.

[85] M. Sitti and R.S. Fearing. Synthetic gecko foot-hair micro/nano-structures as dry adhesives. *J. Adhesion Sci. Technol.*, 17:1055–1073, 2003.

[86] J.R. Smith, g. Bozzolo, A. Banerjea, and J. Ferrante. Avalanche in adhesion. *Phys. Rev. Lett.*, 63:1269–1272, 1989.

[87] I.N. Sneddon. The relation between load and penetration in the axisymmetric boussinesq problem for a punch of arbitrary profile. *Int. J. Eng. Sci.*, 3:47–57, 1965.

[88] I.N. Sneddon. *Mixed boundary value problems in potential theory.* North-Holland publishing company, Amsterdam, 1966.

[89] R. Spolenak, S. Gorb, H. Gao, and E. Arzt. Effects of contact shape on the scaling of biological attachments. *Proc. R. Soc. A*, 461:305–319, 2005.

[90] A.N. Stroh. Dislocations and cracks in anisotropic elasticity. *Phil. Mag.*, 3:625–646, 1958.

[91] Z. Suo. Singularities, interfaces and cracks in dissimilar anisotropic media. *Proc. R. Soc. Lond. A*, 427:331–358, 1990.

[92] S. Suresh, M. Olsson, A.E. Giannakopoulos, N.P. Padture, and J. Jitcharoen. Engineering the resistance to sliding-contact damage through controlled gradients in elastic properties at contact surfaces. *Acta Mater.*, 47:3915–3926, 1999.

[93] D. Tabor. Surface forces and surfaces interactions. *J. Colloid Interface Sci.*, 58:2–23, 1976.

[94] H. Tada, P.C. Paris, and G.R. Irwin. *The stress analysis of cracks handbook.* ASME Press, New York, 2000.

[95] T. Tang, C.Y. Hui, and N.J. Glassmaker. Can a fibrillar interface be stronger and tougher than a non-fibrillar one? *J. R. Soc. Interface*, 2:505–516, 2005.

[96] S.P. Timosheko and J.N. goodier. *Theory of elasticity.* McGraw-Hill, New York, 1987.

[97] T.C.T. Ting. Explicit solution and invariance of the singularities at an interface crack in anisotropic composites. *Int. J. Solids Struct.*, 22:965–983, 1986.

[98] T.C.T. ting. *Anisotropic Elasticit.* Oxford Univ. Press, New York, 1996.

[99] E.C. Titchmarsh. *Introduction to the theory of Fourier integrals.* Clarendon Press, Oxford, 2nd edition.

[100] V. Tvergaard and J.W. Hutchinson. The relation between crack growth resistance and fracture process parameters in elastic-plastic solids. *J. Mech. Phys. Solids*, 40:1377–1397, 1992.

[101] E.E. Williams and J.A. Peterson. Convergent and alternative designs in the digital adhesive pads of scincid lizards. *Science*, 215:1509–1511, 1982.

[102] J.R. Willis. Fracture mechanics of interfacial cracks. *J. Mech. Phys. Solids*, 19:353–368, 1971.

[103] X.P. Xu and A. Needleman. Numerical simulations of fast crack growth in brittle solids. *J. Mech. Phys. Solids*, 42:1397–1434, 1994.

[104] H. Yao and H. Gao. Mechanics of robust and releasable adhesion in biology: bottom-up designed hierarchical structures of gecko. *J. Mech. Phys. Solids*, 54(6):1120–1146, 2006.

[105] H. Yao and H. Gao. Optimal shapes for adhesive binding between two elastic bodies. *J. Colloid and Interface Sci.*, 298(2):564–572, 2006.

Appendix

A. Useful Integrals and Relations

$$\int_0^\infty \cos(\xi t) J_0(\xi\rho)\mathrm{d}\xi = \begin{cases} 0, & (0<\rho<t) \\ \frac{1}{(\rho^2-t^2)^{1/2}}, & (\rho>t) \end{cases} \tag{A.1}$$

$$\int_0^\infty \sin(\xi t) J_0(\xi\rho)\mathrm{d}\xi = \begin{cases} \frac{1}{(t^2-\rho^2)^{1/2}}, & (0<\rho<t) \\ 0, & (\rho>t) \end{cases} \tag{A.2}$$

$$\int_0^\infty \cos(\xi t) J_1(\xi\rho)\mathrm{d}\xi = \begin{cases} \frac{1}{\rho}\left[1-\frac{t}{(t^2-\rho^2)^{1/2}}\right], & (0<\rho<t) \\ 1/\rho, & (\rho>t) \end{cases} \tag{A.3}$$

$$\int_0^\infty \sin(\xi t) J_1(\xi\rho)\mathrm{d}\xi = \begin{cases} 0, & (0<\rho<t) \\ \frac{t}{\rho(\rho^2-t^2)^{1/2}}, & (\rho>t) \end{cases} \tag{A.4}$$

$$\int_0^\infty \xi^{-1}\sin(\xi t) J_0(\xi\rho)\mathrm{d}\xi = \begin{cases} \pi/2, & (0<\rho<t) \\ \sin^{-1}(t/\rho), & (\rho>t) \end{cases} \tag{A.5}$$

$$\int_0^\infty \xi^{-1}\sin(\xi t) J_1(\xi\rho)\mathrm{d}\xi = \begin{cases} \frac{1-\sqrt{1-\rho^2/t^2}}{\rho}, & (0<\rho<t) \\ t/\rho, & (\rho>t) \end{cases} \tag{A.6}$$

$$\int_0^\infty \xi\sin(\xi t) J_0(\xi\rho)\mathrm{d}\xi = \begin{cases} 0, & (0<\rho<t) \\ -\frac{t}{(\rho^2-t^2)^{3/2}}, & (\rho>t) \end{cases} \tag{A.7}$$

$$\int_0^\infty \xi\sin(\xi t) J_1(\xi\rho)\mathrm{d}\xi = \begin{cases} -\frac{\rho}{(t^2-\rho^2)^{3/2}}, & (0<\rho<t) \\ 0, & (\rho>t) \end{cases} \tag{A.8}$$

$$\int \frac{\mathrm{d}t}{(t-\rho)\sqrt{t^2-1}} = \frac{1}{\sqrt{1-\rho^2}} \sin^{-1}\left(\frac{\rho t - 1}{t-\rho}\right) \quad (\rho \leq 1 \leq t) \tag{A.9}$$

$$\int \frac{\mathrm{d}t}{(t+\rho)\sqrt{t^2-1}} = -\frac{1}{\sqrt{1-\rho^2}} \sin^{-1}\left(\frac{\rho t + 1}{t+\rho}\right) \quad (\rho \leq 1 \leq t) \tag{A.10}$$

$$\int \frac{\mathrm{d}t}{(\rho-t)\sqrt{1-t^2}} = \frac{1}{\sqrt{\rho^2-1}} \sin^{-1}\left(\frac{\rho t - 1}{\rho-t}\right) \quad (t \leq 1 \leq \rho) \tag{A.11}$$

$$\int \frac{\mathrm{d}t}{(\rho+t)\sqrt{1-t^2}} = \frac{1}{\sqrt{\rho^2-1}} \sin^{-1}\left(\frac{\rho t + 1}{\rho+t}\right) \quad (t \leq 1 \leq \rho) \tag{A.12}$$

$$\frac{\mathrm{d}}{\mathrm{d}z}[z^\nu J_\nu(z)] = z^\nu J_{\nu-1}(z) \tag{A.13}$$

$$\frac{\mathrm{d}}{\mathrm{d}z}[z^{-\nu} J_\nu(z)] = -z^{-\nu} J_{\nu+1}(z) \tag{A.14}$$

$$\ln\left[\frac{c}{t} + \sqrt{\frac{c^2}{t^2} - 1}\right] = \int_t^c \frac{\mathrm{d}\tau}{\sqrt{\tau^2 - t^2}} \tag{A.15}$$

$$\int_{-1}^{1}\int_{-1}^{1} \left[\frac{\sqrt{1-x^2}}{\sqrt{1-y^2}} + \frac{\sqrt{1-y^2}}{\sqrt{1-x^2}}\right] \frac{1}{x-y} \ln\left(\frac{1+x}{1-x}\right) \mathrm{d}x\mathrm{d}y = 2\pi^2 \tag{A.16}$$

$$\ln\frac{1+x}{1-x} = 2\tanh^{-1}(x) \tag{A.17}$$

B. Proof of relationships $\lim_{a\to\infty} \delta^{\mathrm{f}}_{\mathrm{tip}}(a) = 1/2 \lim_{a\to\infty} \delta^{\mathrm{f}}_{\mathrm{center}}(a)$

Consider the problem shown in Figure 5.15(d) where an elastic half-space with graded Young's modulus $E(z)$ is subjected to a uniform pressure σ_{th} over a circular surface region $r \leq a$. The surface depressions at the center $r = 0$ and the edge $r = a$ of the loaded region are denoted by $\delta^{\mathrm{f}}_{\mathrm{center}}(a)$ and $\delta^{\mathrm{f}}_{\mathrm{tip}}(a)$ respectively.

Theorem:

If $\lim_{a\to\infty} \delta^{\mathrm{f}}_{\mathrm{center}}(a) < +\infty$, then $\lim_{a\to\infty} \delta^{\mathrm{f}}_{\mathrm{tip}}(a) = 1/2 \lim_{a\to\infty} \delta^{\mathrm{f}}_{\mathrm{center}}(a)$

Proof:

The surface depression at the edge $r = a$ can be calculated by integrating the over the loaded region,

$$\delta^{\mathrm{f}}_{\mathrm{tip}} = 2\int_0^{\pi/2} \mathrm{d}\theta \int_0^{2a\cos\theta} \sigma_{\mathrm{th}} G(r) r \mathrm{d}r, \tag{B.1}$$

where $G(r)$ is the Green's function. Interchanging the order of integration yields

$$\delta^{\mathrm{f}}_{\mathrm{tip}}(a) = 2\int_0^{2a} G(r) r \mathrm{d}r \int_0^{\cos^{-1}(r/2a)} \sigma_{\mathrm{th}} \mathrm{d}\theta = 2\sigma_{\mathrm{th}} \int_0^{2a} \cos^{-1}\left(\frac{r}{2a}\right) G(r) \mathrm{d}r. \tag{B.2}$$

Similarly, the surface depression at the center $r = 0$ can be expressed as

$$\delta^{\mathrm{f}}_{\mathrm{center}}(a) = 2\pi\sigma_{\mathrm{th}} \int_0^{a} G(r) r \mathrm{d}r. \tag{B.3}$$

If $\delta^{\mathrm{f}}_{\mathrm{center}}$ converges to a finite value as $a \to \infty$, i.e.

$$\lim_{a\to\infty} \delta^{\mathrm{f}}_{\mathrm{center}}(a) = 2\pi\sigma_{\mathrm{th}} \lim_{a\to\infty} \int_0^{a} G(r) r \mathrm{d}r < +\infty, \tag{B.4}$$

the following relation should exist

$$\lim_{a\to\infty} \delta^{\mathrm{f}}_{\mathrm{center}}(a) = 2\pi\sigma_{\mathrm{th}} \lim_{a\to\infty} \int_0^{a} G(r) r \mathrm{d}r = 2\pi\sigma_{\mathrm{th}} \lim_{a\to\infty} \int_0^{2a} G(r) r \mathrm{d}r < +\infty. \tag{B.5}$$

Therefore, according to Equations (B.2) and (B.5),

$$\lim_{a\to\infty} \left[\delta^{\mathrm{f}}_{\mathrm{tip}} - \frac{1}{2}\delta^{\mathrm{f}}_{\mathrm{center}}\right] = 2\sigma_{\mathrm{th}} \lim_{a\to\infty} \int_0^{2a} \left[\cos^{-1}\left(\frac{r}{2a}\right) - \frac{\pi}{2}\right] G(r) r \mathrm{d}r. \tag{B.6}$$

Introducing dimensionless parameter $\hat{a} = 2a/\ell$, Equation (B.6) can be rewritten as

$$\lim_{a\to\infty}\left[\delta^{\mathrm{f}}_{\mathrm{tip}} - \frac{1}{2}\delta^{\mathrm{f}}_{\mathrm{center}}\right] = 2\sigma_{\mathrm{th}} \lim_{\hat{a}\to\infty}\left\{\int_0^{\ell\sqrt{\hat{a}}}\left[\cos^{-1}\left(\frac{r}{\ell\hat{a}}\right) - \frac{\pi}{2}\right] G(r) r \mathrm{d}r + \int_{\ell\sqrt{\hat{a}}}^{\ell\hat{a}}\left[\cos^{-1}\left(\frac{r}{\ell\hat{a}}\right) - \frac{\pi}{2}\right] G(r) r \mathrm{d}r\right\}, \tag{B.7}$$

where ℓ is an arbitrary length scale. Letting $r/\ell = \xi\sqrt{\hat{a}}$, the first term of the right-hand of Equation (B.7) is recast as

$$2\sigma_{\mathrm{th}}\ell^2 \lim_{\hat{a}\to\infty}\int_0^1\left[\cos^{-1}\left(\xi/\sqrt{\hat{a}}\right) - \frac{\pi}{2}\right]\hat{a}G(\xi\ell\sqrt{\hat{a}})\xi \mathrm{d}\xi. \tag{B.8}$$

As Equation (B.4) implies that

$$\lim_{\hat{a}\to\infty}\int_0^{\ell\sqrt{\hat{a}}} G(r) r \mathrm{d}r = \ell^2 \lim_{\hat{a}\to\infty}\hat{a}\int_0^1 G(\xi\ell\sqrt{\hat{a}})\xi \mathrm{d}\xi < +\infty, \tag{B.9}$$

$G(\xi\ell\sqrt{\hat{a}})$ must have the same order as $1/\hat{a}$ when $\hat{a}\to\infty$, namely

$$G(\xi\sqrt{\hat{a}}) \sim O(1/\hat{a}).\ (\hat{a}\to\infty) \tag{B.10}$$

Substituting Equation (B.10) into Equation (B.8), we have

$$2\sigma_{\mathrm{th}} \lim_{\hat{a}\to\infty}\int_0^{\ell\sqrt{\hat{a}}}\left[\cos^{-1}\left(\frac{r}{\ell\hat{a}}\right) - \frac{\pi}{2}\right] G(r) r \mathrm{d}r = 0. \tag{B.11}$$

For the second term on the right-hand side of Equation (B.7),

$$\left|\lim_{\hat{a}\to\infty}\int_{\ell\sqrt{\hat{a}}}^{\ell\hat{a}}\left[\cos^{-1}\left(\frac{r}{\ell\hat{a}}\right) - \frac{\pi}{2}\right] G(r) r \mathrm{d}r\right| \le \frac{\pi}{2}\lim_{\hat{a}\to\infty}\int_{\ell\sqrt{\hat{a}}}^{\ell\hat{a}}|G(r)| r \mathrm{d}r = 0, \tag{B.12}$$

where the following additional assumption has been employed

$$\lim_{\hat{a}\to\infty}\int_0^{\ell\hat{a}}|G(r)| r \mathrm{d}r < +\infty. \tag{B.13}$$

Substitution of Equations (B.11) and (B.12) into Equation (B.7) yields

$$\lim_{a\to\infty}\delta^{\mathrm{f}}_{\mathrm{tip}} = 1/2 \lim_{a\to\infty}\delta^{\mathrm{f}}_{\mathrm{center}}. \tag{B.14}$$

C. Zusammenfassung (in German)

Über Milliarden von Jahren hat die Natur viele erfinderische Wege gefunden, Materialien mit hochwertigen mechanischen Eigenschaften herzustellen. In dieser Dissertation richten wir die Aufmerksamkeit auf die trockene Haftung, die als ein spezifisches Phänomen häufig in vielen Tierarten in der Natur zu finden ist, wie Gecko, Fliegen und Insekten. Unser Ziel ist, die Haftungsmechanismen aufzuklären, die in diesen professionellen Kletterern verborgen sind. Diese Untersuchung könnte Richtlinie für die Entwicklung neuartiger Materialen oder Vorrichtungen für industrielle Anwendungen sein.

Die Dissertation ist in drei Teilen organisiert. Im ersten Teil bestehend aus den Kapiteln 1-3 stellen wir zunächst in Kapitel 1 die Motivation der Forschung und die Organisation der Dissertation vor. Der theoretische Hintergrund der Kontaktmechanik wird in Kapitel 2 wiederholt. Danach beschreiben wir in Kapitel 3 die Methoden, die in dieser Dissertation verwendet werden. Der Schwerpunkt richtet sich dabei auf die mathematischen Grundlagen und die verwendeten numerischen Verfahren.

Robustheit und Freilassung sind zwei wesentliche Eigenschaften der biologischen Haftung. Der zweite Teil dieser Dissertation (Kapitel 4-6) ist auf das Ergründen der mechanischen Prinzipien dieser zwei Eigenschaften gerichtet. Bei gegebener Kontaktfläche wird die Haftkraft durch die Größe der Abreißkraft gezeichnet, d.h. die Kraft, die notwendig ist, um zwei abgebundene Körper auseinander zuziehen. Je größer diese Abreißkraft, desto stärker ist die haftende Verbindung. Im Rahmen dieser Dissertation beschäftigen wir uns mit der Frage, wie diese Haftkraft maximiert werden kann.

In Kapitel 4 diskutieren wir die Haftung zwischen zwei einzelnen Kontaktunebenheiten. Es zeigt sich, daß die Haftkraft von der geometrischen Form und der Größe der Kontaktflächen abhängt und durch die theoretischen Festigkeit begrenzt ist. Es ergibt sich eine spezifische Form, die optimale Form, durch die die theoretische Festigkeit erzielt werden kann. Eine allgemeine Methode für die Bestimmung der optimalen Form wird entwickelt, mit der analytische Ausdrücke für einige Beispielfälle entwickelt werden. Jedoch zeigt die Formoptimierung hinsichtlich optimaler Haftung, daß das Design für die optimale Haftung besonders auf der Makroskala unzuverlässig ist, da dort die Haftskraft sehr empfindlich gegenüber kleinen Unregelmäßigkeiten in der Geometrie der Haftkontakte verhält. Ein robustes Design für formunempfindliche, optimale Haftung ist nur möglich, wenn die charakteristische Größe der Kontaktfläche auf einen Bereich von 100 nm verringert wird. Allgemein kann die optimale Haftung durch eine Kombination von

Miniaturisierung und Formoptimierung erzielt werden. Je kleiner der Haftkontakt, desto unwesentlicher wird seine Form. Aus diesem Grund besitzen biologische, feinfaserige Nanostrukturen eine hohe Haftkraft.

Die in Kapitel 4 erzielten Ergebnisse lassen den Schluss zu, daß Materialien die intrinsische Fähigkeit besitzen, ziemlich kleine Kontaktfehler tolerieren. In der Wirklichkeit neigen Kontaktflächen jedoch dazu, auf verschiedenen Längenskalen rauh zu sein, was zu multiskaligen Kontaktfehlern führt. Auf der Makroskala wird robuste Haftung auf rauhen Oberflächen nicht automatisch durch die optimale Haftung der einzelnen Kontakte oder der Feinfaser erzielt. Um dieses Problem zu lösen, untersuchen wir in Kapitel 5 die Haftkraft zwischen rauhen Oberflächen. Anstatt einen haftenden Kontakt auf willkürlichen oder fraktalen rauhen Oberflächen direkt zu modellieren, betrachten wir das Verhaltens eines Grenzflächenrisses, der die gelegentlichen Kontaktfehler aufgrund von Oberflächenrauheit oder Verunreinigungen repräsentiert. Indem wir die Bedingungen untersuchen, unter denen dieser repräsentative Riss nicht wächst, behandeln wir im Sinne einer statistischen Mittelung das Problem des Riss initiierten Haftversagens aufgrund eines zufällig auftretenden, schwachen Kontaktbereiches. So wird ein Zustand der Fehlertoleranz erzielt, in dem bereits existierende Risse nicht mehr wachsen, selbst wenn das Material bis zum Versagen nahe der theoretischen Festigkeit belastet wird. In diesem Kapitel werden Strategien für das Erzielen fehlertoleranter Haftung systematisch diskutiert. Die Untersuchungen zeigen, daß die Fehlertoleranz in klassischen, homogenen Materialien nur erhalten werden kann, wenn die Strukturgröße unter eine kritischen Längenskala verringert wird. Um die allgemeine Fehlertoleranz zu erzielen, in der rissähnlicher Fehler aller Größen zugelassen werden können, müssen wir uns den Gradientenwerkstoffen oder einem hierarchischen Design zuwenden. Theoretische Modelle und numerische Simulationen zeigen, daß Gradientenwerkstoffe in Verbindung mit hierarchischen, Energie aufnehmenden Mechanismen entworfen werden können, um das Wachstum von Grenzenflächenrisse jeglicher Größe zu unterdrücken. So kann eine Fehlertoleranz von der kleinsten Längenskala bis zur makroscopischen Ebene erzielt werden. Solche Konstruktionsprinzipien stimmen auch gut mit den allgemeinen, strukturellen Eigenschaften überein, die bei einer Vielzahl der biologischen Haftsysteme beobachtet werden.

Für die meisten Tiere ist jedoch die robuste Haftfähigkeit nicht allein für ihre Mobilität auf vertikalen Flächen und auf den Unterseiten von Flächen ausreichend. Für diese Situationen ist die Freilassung(die Lösbarkeit) der haftenden Vorrichtungen genauso wichtig wie ihre Robustheit. Unsere Diskussion in Kapitel 6 richtet sich auf das Problem des leichten Freigebens (der Lösbarkeit) einer robusten Haftung. Inspiriert durch

die allgemeinen strukturellen Eigenschaften biologischer Haftsysteme untersuchen wir die Effekte der Materialanisotropie auf die Abhängigkeit der Haftkraft von der Orientierung des Kontaktes. Die Untersuchungen zeigen, daß bei Materialien mit starker Anisotropie die Haftkraft mit Änderung der Zugrichtung stark variiert. Die resultierende orientierungsabhängige Zugkraft ermöglicht das Lösen robuster Haftung in der steifen Richtung des Materials durch das Ziehen in die weiche Richtung und ermöglicht einen orientierungskontrollierten Schalter zwischen Haftung und Trennung.

Biologische Haftvorrichtungen sind sehr komplizierte Systeme und liefern einen ganzen Zoo von Ideen für die Entwicklung industrieller Anwendungen. Das in dieser Dissertation entwickelte Konzept sollte vom allgemeinen Wert für das Verständnis biologischer Haftvorrichtungen und das Design künstlicher Haftsysteme für die Technik sein. Im letzten Teil dieser Dissertation (Kapitel 7) werden die wichtigsten Ergebnisse kurz zusammengefasst. Den Schluss bildet ein Ausblick auf zukünftige Arbeiten.